UNDERSTANDING THE FINE GRINDING OF CALCIUM CARBONATE

By

SOPHIE BIANCA RIMMER

A thesis submitted to the University of Birmingham for the Degree of

DOCTOR OF PHILOSOPHY

Centre for Doctoral Training in Formulation Engineering

School of Chemical Engineering

College of Engineering and Physical Sciences

University of Birmingham

October 2021

ABSTRACT

Stirred media mills are commonly used in industry for the fine grinding of many materials, including calcium carbonate. Since stirred media mills are composed of a vessel equipped with a stirrer, they can be considered analogous to stirred tanks. This thesis looks at key differences between stirred tanks and stirred media mills and considers how established literature theories for stirred tanks can be adapted for successful application to stirred media mills. A focus is placed on assessing different methods of predicting power draw based on the dimensionless Power number and Reynolds number. The most successful method proposed utilises the vane rheometer to measure a combined viscosity of the slurry and grinding media. However, some experimental data does not fit well to the proposed correlation models.

Using Positron Emission Particle Tracking (PEPT), it was found that the cases that do not fit well to the power prediction correlations exhibit a significantly wider vortex than the cases that are a good fit to the correlations. The vortex shape is challenging to predict, but it was observed that cases with both a low fluid viscosity and low grinding media amount showed the most significant vortexing which lead to power draw being over predicted. To develop an enhanced understanding of flow patterns inside stirred media mills and compliment PEPT findings, high-speed imaging was utilised to observe grinding media. Although only the grinding media at the walls of the vessel can be observed, this technique provides the advantage that close-to-instantaneous flow patterns can be obtained.

To consider the most important scale-up parameters and compare them with those important for standard mixing applications, experiments were conducted at three different equipment scales. Since lab-scale milling is frequently operated as a batch whilst larger scale milling is operated continuously, a semi-continuous lab-scale system was developed and compared to the batch system. Lab-scale residence time distributions are presented and suitable methods of determining pilot-scale residence time distributions experimentally are proposed and suggested as further study. At lab-scale, it was found that the solid and liquid phases have similar residence time distributions, close to that of a continuous stirred tank reactor (CSTR).

ACKNOWLEDGEMENTS

I would like to thank the EPSRC and Imerys for funding this project, enabling me to learn from the project and present my research at conferences. I am grateful for all of the support throughout the project from my academic supervisors, Dr Andy Ingram and Dr Federico Alberini and my industrial supervisor Dr Richard Tamblyn. I would also like to thank Nigel Rowe from Imerys for the initial lab training and supplying of materials, and Joseph Cambisano for the running of pilot plant trials. Thanks also go to Dr Richard Greenwood for encouragement and support at conferences and Professor David Parker for the preparation of PEPT tracers. I would also like to thank Douglas Wattleworth and Kessigen Mooroogen for their contribution to setting up and operating the continuous lab-scale mill during their masters project.

Finally yet importantly, I would also like to thank my family, friends and Michael for their continued support.

TABLE OF CONTENTS

1. INTRODUCTION 1

1.1. Project Background 1

1.1.1. Calcium Carbonate 1

1.1.2. Stirred Media Mills 1

1.1.3. Analogy to Mixing 3

1.2. Aims and Objectives 4

1.3. Business Case 4

1.4. Thesis Layout 5

1.5. Conference Presentations 6

2. LITERATURE REVIEW 7

2.1. Introduction 7

2.2. Stirred Media Mill Operating Principles 7

2.2.1. Breaking Particles 7

2.2.2. Defining Energy Efficiency 11

2.2.3. Factors Influencing Energy Efficiency 13

2.2.3.1. Grinding Media Properties 13

2.2.3.2. Impeller Speed 15

2.2.3.3. Dispersant Amount 16

2.2.3.4. Slurry Solids Content 17

2.2.3.5. Equipment Set-Up and Geometry 17

2.2.3.6. Continuous Milling Circuit Parameters 19

2.3. Analogy with Mixing 20

2.3.1. Rheology 20

2.3.1.1. Measuring the Viscosity of Particulate Systems 22

2.3.1.2. Calcium Carbonate Slurry Viscosity 24

2.3.1.3. Measuring the Viscosity of Large Particulate Systems 25

2.3.1.4. Predicting Slurry Viscosity 27
2.3.1.5. Apparent Viscosity of Non-Newtonian Fluids 30
2.3.1.5.1. Metzner-Otto Correlation 30
2.3.2. Predicting Power Draw 32
2.3.3. Residence Time Distributions (RTDs) 35
2.3.4. Scale-Up 40
2.4. Flow Visualisation Methods 42
2.4.1. Positron Emission Particle Tracking (PEPT) 42
2.4.2. DEM and CFD Modelling 44
2.5. Summary of Literature Review 45
3. MATERIALS AND METHODS 46
3.1. Introduction 46
3.2. Materials 46
3.2.1. Calcium Carbonate 46
3.2.2. Dispersant 47
3.2.3. Grinding Media 47
3.2.4. Glycerol 48
3.2.5. SiLi Beads 48
3.3. Methods 48
3.3.1. Milling Calcium Carbonate 49
3.3.1.1. Batch Operation 50
3.3.1.1.1. Recording Power Draw 51
3.3.1.1.2. Taking Slurry Samples 51
3.3.1.2. Continuous Milling 52
3.3.1.3. Using a Dye Tracer to Determine the RTD 52
3.3.1.3.1. Ultraviolet Visible Spectroscopy (UV/Vis) 54
3.3.1.4. Using a Titanium Dioxide Tracer to Determine the RTD 55
3.3.1.4.1. X-Ray Fluorescence (XRF) 56

3.3.1.5. Small-Scale and Large-Scale Milling 57
3.3.1.5.1. Smaller Scale Experiments – Rheometer-Scale 57
3.3.1.5.2. Larger Scale Experiments – Pilot-Scale 59
3.3.2. Slurry and Grinding Media Characterisation Methods 60
3.3.2.1. Particle Size Measurement – Wet Laser Diffraction 60
3.3.2.2. Viscosity Measurement – Rotational Rheometry 62
3.3.2.3. Fluid Friction Measurement - Tribology 63
3.3.3. Flow Visualisation 64
3.3.3.1. High Speed Imaging (HSI) 64
3.3.3.2. Endoscopic Camera 67
3.3.3.3. Positron Emission Particle Tracking (PEPT) 68
4. PREDICTING THE POWER DRAW IN STIRRED MEDIA MILLS 72
4.1. Introduction 72
4.2. Power Draw During Batch Grinding 72
4.3. Predicting Power Draw Using the Power Number and Reynolds Number 75
4.3.1. Measuring Slurry Viscosity 76
4.3.1.1. The Effect of Temperature 78
4.3.1.2. The Effect of Slurry Solids Content 79
4.3.1.3. Using Newtonian Mimic Fluids in Place of Slurries 83
4.3.2. Measuring Combined Fluid + Grinding Media Viscosity 83
4.3.2.1. Comparing Grinding Media Types 89
4.3.3. Predicting Power Draw: Assuming Grinding Media are a Part of the Equipment 90
4.3.3.1. Glycerol-Water Solutions 91
4.3.3.2. Calcium Carbonate Slurries 99
4.3.3.3. The Metzner-Otto Correlation 100
4.3.3.3.1. Using Metzner-Otto in Power Number Correlations 101
4.3.4. Predicting Power Draw: Assuming Grinding Media are a Part of the Fluid 109
4.3.5. Testing and Comparing the Models 114
4.3.6. Comparing Glycerol-Water Solutions and Calcium Carbonate Slurries 119

4.4. Tribology 120

4.5. Summary 123

5. GRINDING MEDIA MOTION IN STIRRED MEDIA MILLS 125

5.1. Introduction 125

5.2. High Speed Imaging (HSI) 126

5.2.1. Grinding Media Motion at the Wall in a 71% Glycerol-Water Solution (0.02 Pa s) 126

5.2.1.1. Surface Plots – Considering the Impeller Position 132

5.2.1.2. Investigating the Transition Zone 138

5.2.2. The Effect of Changing Fluid Properties on Bead Motion 144

5.2.2.1. Comparing Fluids of Different Viscosities – Glycerol-Water Solutions 146

5.2.2.2. Comparing Slurries at Different Stages of Grinding 149

5.2.2.2.1. Changes During Batch Grinding 152

5.2.2.2.2. Micron Sized Glass Beads in 71% Glycerol 154

5.3. PEPT 157

5.3.1. Flow Pattern Development During Batch Grinding 158

5.3.2. Bead Motion with Time 160

5.3.3. Visualising the Vector Flow Field 162

5.3.4. The Effect of the Irradiated Bead Size 164

5.3.5. The Effect of Impeller Speed 168

5.3.6. The Effect of Grinding Media Amount and Solids Content 172

5.3.6.1. Varying Slurry Solids Content 172

5.3.6.2. Varying Newtonian Fluid Viscosity - Glycerol 175

5.3.6.3. Varying Grinding Media Amount 177

5.3.6.4. The Coupling of Fluid Properties and Grinding Media Amount 179

5.3.7. Using Higher Density Grinding Media Beads 181

5.4. Comparison of PEPT and HSI 185

5.5. Summary 188

6. COMPARING STIRRED MEDIA MILLS AT THREE SCALES 190

6.1. Introduction 190
6.2. Comparing Batch and Continuous Operation 190
6.3. Lab-scale Residence Time Distributions (RTDs) 192
6.3.1. Glycerol RTDs in Stirred Media Mill 193
6.3.2. Calcium Carbonate RTDs in Stirred Media Mills 199
6.3.3. Comparing Glycerol and Calcium Carbonate RTDs in Stirred Media Mill 204
6.3.4. Potential Application of RTD Measurement Methods to Pilot-Scale 206
6.4. Investigating Key Parameters Affecting Scale-Up 207
6.4.1. Tip Speed, Torque and Specific Power Draw 208
6.4.2. Stress Energy and Stress Number 210
6.4.3. Froude Number 213
6.4.4. Reynolds Number and Power Number 214
6.4.4.1. Metzner-Otto k_s = 13 – Slurry Only Viscosity 216
6.4.4.2. Metzner-Otto k_s = 13 – Slurry + Grinding Media Viscosity 217
6.4.4.3. Metzner-Otto $k_s = 10.7\ n^{-0.15}$ (Optimal k_s from Chapter 4) – Slurry + Grinding Media Viscosity 219
6.4.4.4. Shear Rate is Proportional to Square Root of Energy Dissipation Rate – Slurry + Grinding Media Viscosity 220
6.4.5. Predicting Power Draw at Different Scales 222
6.4.6. Comparing Power Measurement Methods at Each Scale 223
6.4.7. Variability Considerations 224
6.5. Summary 226
7. CONCLUSIONS 228
8. FURTHER STUDY SUGGESTIONS 231
8.1. Improving Power Prediction Methods 231
8.2. Flow Pattern Analysis Development 232
8.3. Further Scale-Up Studies 233
9. REFERENCES 235
10. APPENDIX 254

10.1. Appendix A 254

10.2. Appendix B 254

10.3. Appendix C 255

10.4. Appendix D 257

LIST OF FIGURES

Figure 1.1: Diagram of a Typical Vertical Stirred Media Mill Used for Fine Grinding of Calcium Carbonate.....2

Figure 2.1: (a) Particle Breakage Mechanisms, and (b) Particle Size Distributions Resulting from Different Breakage Mechanisms[10] 8

Figure 2.2: Flow Curves for Common Fluid Types[43] 21

Figure 3.1: Lab-Scale Stirred Media Mill (a) Inside Vessel Configuration (b) Sealed vessel 49

Figure 3.2: Diagram of Lab-Scale Stirred Media Mill (a) front view, (b) top down view 49

Figure 3.3: Continuous Set-Up for Glycerol RTD 53

Figure 3.4: Continuous Set-Up for Calcium Carbonate RTD.....55

Figure 3.5: Lab-Scale Impeller (left) and 3D Printed Impeller (right) 58

Figure 3.6: Vane Rheometer Geometry with Trios Rheometer.....62

Figure 3.7: PCS Instruments Mini Traction Machine with Stainless Steel Ball and Plate[149].....64

Figure 3.8: Diagram of High Speed Camera Set-Up 65

Figure 3.9: ‘U’, ‘V’ and ‘Z’ Directions 66

Figure 3.10: Application of Mask and Interrogation Windows to High Speed Camera Data.....66

Figure 3.11: Diagram of Endoscopic Camera Set-Up 67

Figure 3.12: Stirred Media Mill Between Detectors 68

Figure 3.13: Illustration of Lines of Response for a Single Particle[151] 69

Figure 3.14: (a) Cartesian Co-Ordinate System (b) Cylindrical Co-Ordinate System 70

Figure 4.1: Particle Size of Calcium Carbonate Particles in 72 wt% Slurries Ground with 0.8-1.2 mm Mullite Grinding Media at 9.8 m s^{-1} After Different Mill Energy Consumptions 73

Figure 4.2: Power Draw and Temperature Evolving Over Batch Milling at 9.8 m s^{-1} (72 wt% Calcium Carbonate Slurry in Mullite 0.8-1.2 mm Grinding Media) 74

Figure 4.3: 72 wt% Slurry Viscosity Over the Course of a Batch Grind Using 0.8-1.2 mm Mullite Grinding Media Measured Using 28 mm Vane in a 30 mm Diameter Cup at 25 ° C. Error Bars Indicate the Standard Deviation of Three Consecutive Flow Ramps. 77

Figure 4.4: 72 wt% Slurry Viscosity Over the Course of a Batch Grind Using 0.8-1.2 mm Mullite Grinding Media Measured Using 28 mm Vane in a 30 mm Diameter Cup Measured at Approximate Mill Temperature When Slurry Sample Was Taken and At 25 °C 79

Figure 4.5: Slurry Viscosity with Same Particle Size but Different $CaCO_3$ Solids Content (Ground Samples Diluted by Water Addition) Measured Using Vane Geometry at 25 °C - 200 kWh/tonne (2.8 μm d_{80}). Error Bars Indicate the Standard Deviation of Three Consecutive Flow Ramps.....80

Figure 4.6: Viscosity of 72 wt% Surries or Glycerol-Water Solutions with 52 vol% Mullite Grinding Media 0.8 – 1.2 mm at 25 °C. Error Bars Show Standard Deviation of Three 'Up' Flow Sweeps.....84

Figure 4.7: Rheometer Torque for Vane Impeller and Custom 3D Printed Pin Geometry at Constant Rheometer Fill Level – 0 kWh/tonne 72 wt% $CaCO_3$ Slurry with 52 vol% 0.8-1.2 mm Mullite Grinding Media.....87

Figure 4.8 Consecutive Up and Down Flow Sweeps Conducted Using Vane Geometry – 0 kWh/tonne 72 wt% $CaCO_3$ Slurry with 52 vol% 0.8-1.2 mm Mullite Grinding Media 89

Figure 4.9: Viscosity of 0 kWh/tonne 72 wt% Surry with Different Grinding Media Types at 25 °C. Error Bars Show Standard Deviation of Three 'Up' Flow Sweeps.....90

Figure 4.10: Po-Re Curve for Glycerol-Grinding Media Systems with 52 vol% Grinding Media, Assuming the Grinding Media are a Part of the Tank Set-Up. Dashed lines indicate the transition to the vortexing region. 91

Figure 4.11: Best Fit Relation Between Power Number and Reynolds and Froude Numbers for Glycerol and 52 vol% Grinding Media Systems, Entire Range of Fr.....95

Figure 4.12: Best Fit Relation Between Power Number and Reynolds and Froude Numbers for Glycerol and 52 vol% Grinding Media Systems, Fr >0.5 96

Figure 4.13: Best Fit Relation Between Power Number, Reynolds Number, Froude Number and Stokes Number for Glycerol and 52 vol% Grinding Media Systems 97

Figure 4.14: Best Fit Relation Between Power Number, Reynolds Number, Froude Number and Stokes Number for Glycerol and 52 vol% Grinding Media Systems – Grinding Media are Included in Density Terms.....98

Figure 4.15: Power Draw for Grinding of 72 wt% Calcium Carbonate Slurry in 52 vol% Mullite 0.8 – 1.2 mm Grinding Media.....99

Figure 4.16: Po-Re Curve for Slurry-Grinding Media Systems, Assuming the Grinding Media are a Part of the Tank Set-Up, k_s=13.....102

Figure 4.17: Best Fit Relation Between Power Number and Reynolds Number for Calcium Carbonate Slurries with Grinding Media, k_s=13.....103

Figure 4.18: Best Fit Relation Between Power Number and Reynolds and Froude Numbers for Calcium Carbonate Slurries with Grinding Media, k_s=13 103
Figure 4.19: Best Fit Relation Between Power Number, Reynolds Number, Froude Number and Stokes Number for Slurry and Grinding Media Systems, Grinding Media Assumed to be Part of System, k_s = 13 104
Figure 4.20: Best Fit Relation Between Power Number, Reynolds Number, Froude Number and Stokes Number for Slurry and Grinding Media Systems - Grinding Media are Included in All Density Terms, Grinding Media Assumed to be Part of System, k_s = 13 105
Figure 4.21: Best Fit Relation Between Power Number, Reynolds Number, Froude Number, Grinding Media Amount and Slurry Solids Content for Slurry and Grinding Media Systems, k_s = 13 (a) Grinding Media Excluded From Density Term (b) Grinding Media Included In Density Term.....107
Figure 4.22: Po-Re Curve for Slurry-Grinding Media Systems, Assuming the Grinding Media are a Part of the Fluid, Metzner-Otto Constant, $k_s = 10.7\ n^{-0.15}$.....111
Figure 4.23: Best Fit Relation Between Power Number and Reynolds Number for Slurry and Grinding Media Systems, $k_s = k_s = 10.7\ n^{-0.15}$.....112
Figure 4.24: Best Fit Relation Between Power Number, Reynolds Number and Froude Number for Slurry and Grinding Media Systems, $k_s = k_s = 10.7\ n^{-0.2}$.....113
Figure 4.25: Best Fit Relation Between Power Number, Reynolds Number, Froude Number and Stokes Number for Slurry and Grinding Media Systems, for slurry and grinding media, $k_s = 12\ n^{-0.12}$ for slurries only, k_s =13.....113

Figure 4.26: Experimental Power Number and Power Number Predicted Using Each Model (Model Test Conditions Defined in Table 4.8 for (a) to (d)). Error bars indicate fluctuations over a 10 second measurement 117
Figure 4.27: Power – Reynolds Number Curve for Slurries and Glycerol-Water Solutions with 52 vol% Grinding Media – Viscosity of Fluid and Grinding Media Combination Measured with Vane Rheometer Geometry 119
Figure 4.28: Stribeck Curves at 3 N for Glycerol-Water Solutions and Slurries with Stainless Steel Ball and Plate. Error bars show the standard deviation of 6 sweeps of entrainment speed.....121
Figure 5.1: Average Dimensionless Velocity of 52 vol% 0.8-1.2 mm Mullite Beads in 71% Glycerol at the Vessel Wall Over One Complete Impeller Revolution at Increasing Impeller Speeds (a) Horizontal 'U' Velocity and (b) Vertical 'V' Velocity (Note that –ve 'V' velocity indicates upward motion).....127
Figure 5.2: Velocity Vectors of Grinding Media at Vessel Wall for 52 vol% 0.8 – 1.2 mm Mullite Beads in 71% Glycerol at Different Impeller Tip Speeds – Average Over One Complete Impeller Revolution 129
Figure 5.3: Average Peak Dimensionless 'U' Velocity Over One Full Impeller Revolution for 52 vol%0.8-1.2 mm Mullite Beads in 71% Glycerol in the Wall Regions Adjacent to the Top and Bottom Impellers. Error bars represent one standard deviation for 5 impeller revolutions. The absence of error bars indicates that the standard deviation is very low 130
Figure 5.4: Kinetic Energy at Wall for 52 vol% 0.8 – 1.2 mm Mullite Beads in 71% Glycerol. Horizontal error bars represent fluctuation in power over 10 seconds. Vertical error bars represent standard deviation of velocity for 5 impeller revolutions.....132

Figure 5.5: Surface Plots Demonstrating Change in Dimensionless ‘U’ Velocity at Wall as Impeller Rotates for 52 vol% 0.8 – 1.2 mm Mullite Beads in 71% Glycerol at Impeller Tip Speeds (a) 3.9 m s^{-1} (b) 6.5 m s^{-1} (c) 9.2 m s^{-1} 133

Figure 5.6: Surface Plots Demonstrating Change in Dimensionless ‘V’ Velocity at Wall as Impeller Rotates for 0.8 – 1.2 mm Mullite Bead Velocity in 71% Glycerol at Impeller Tip Speeds (a) 3.9 m s^{-1} (b) 6.5 m s^{-1} (c) 9.2 m s^{-1} 135

Figure 5.7: Vector Plots for Grinding Media Beads at Wall for 0.8 – 1.2 mm Mullite Bead Velocity in 71% Glycerol at Impeller Tip Speeds (a) 3.9 m s^{-1} (b) 6.5 m s^{-1} (c) 9.2 m s^{-1} Note that 0 ° is where the top impeller directly passes the window of beads being observed.....137

Figure 5.8: Average Velocity Magnitude at Vessel Wall for 52 vol% 0.8 – 1.2 mm Mullite Beads in 71% Glycerol at Vessel Wall Over 5 Impeller Revolutions 138

Figure 5.9: ‘U’ Velocities at Vessel Wall for 52 vol% 0.8 – 1.2 mm Mullite Beads in 71% Glycerol in the Impeller Region – Variation Over Three Impeller Revolutions.140

Figure 5.10: ‘U’ Velocities at Vessel Wall for 52 vol% 0.8 – 1.2 mm Mullite Beads in 71% Glycerol– Variation Over Three Impeller Revolutions (a) in Top Impeller Region (b) in Bottom Impeller Region.....141

Figure 5.11: Endoscope Images of Vortex with 52 vol% 0.8 – 1.2 mm Mullite in 71% Glycerol Grinding Media at Tip Speeds (a) 3.9 m s^{-1}, (b) 6.5 m s^{-1} and (c) 7.9 m s^{-1} 143

Figure 5.12: Velocity Magnitude at Vessel Wall for 52 vol% 0.8 – 1.2 mm Mullite Beads in Glycerol-Water Solutions of Different Viscosities and a 72 wt% Calcium Carbonate Slurries at Different Stages of Grinding 144

Figure 5.13: Kinetic Energy at Vessel Wall for 52 vol% 0.8 – 1.2 mm Mullite Beads at Vessel Wall in Glycerol-Water Solutions and Calcium Carbonate Slurries at Different Stages of Grinding. Y direction error bars show the standard deviation in velocity measurements occurring over 5 consecutive impeller revolutions. X direction error bars show power fluctuation occurring over 10 seconds. 145
Figure 5.14: Surface Plots Demonstrating Change in Dimensionless 'U' Velocity at Vessel Wall for 52 vol% 0.8 – 1.2 mm Mullite Beads in 87% Glycerol at Impeller Tip Speeds (a) 3.9 m s^{-1} (b) 6.5 m s^{-1} (c) 9.2 m s^{-1} 147
Figure 5.15: Surface Plots Demonstrating Change in Dimensionless 'U' Velocity at Vessel Wall for 52 vol% 0.8 – 1.2 mm Mullite Beads in 95% Glycerol at Impeller Tip Speeds (a) 3.9 m s^{-1} (b) 6.5 m s^{-1} (c) 9.2 m s^{-1} 148
Figure 5.16: Surface Plots Demonstrating Change in Dimensionless 'U' Velocity at Vessel Wall for 52 vol% 0.8 – 1.2 mm Mullite Beads in Calcium Carbonate Slurries at 3.9 m s^{-1} - (a) Start of milling, (b) 100 kWh/tonne, (c) 200 kWh/tonne 150
Figure 5.17: Surface Plots Demonstrating Change in Dimensionless 'U' Velocity at Vessel Wall for 52 vol% 0.8 – 1.2 mm Mullite Beads in Calcium Carbonate Slurries at 6.5 m s^{-1} - (a) Start of milling, (b) 100 kWh/tonne, (c) 200 kWh/tonne 151
Figure 5.18: Average Bead Velocity at Wall During Batch Milling with Temperature and Power Draw. 52 vol% 0.8 – 1.2 mm Mullite Beads in 72 wt% Calcium Carbonate Slurry at 7.8 m s^{-1}. Error Bars Show the Standard Deviation of 5 Consecutive Impeller Revolutions.....153
Figure 5.19: Raw High Speed Camera Images at 6.5 m s^{-1} (a) 100 kWh $tonne^{-1}$ Calcium Carbonate Slurry (49 vol%) (b) Glass Beads in 71% Glycerol (40 vol%) 154

Figure 5.20: Surface Plots for 71% Glycerol-Water Solutions with Different Glass Particle Contents at 3.9 m s^{-1} – (a) 5 vol% (b) 20 vol% (c) 40 vol% 155
Figure 5.21: Surface Plots for 71% Glycerol-Water Solutions with Different Glass Particle Contents at 6.5 m s^{-1} – (a) 5 vol% (b) 20 vol% (c) 40 vol% 156
Figure 5.22: Occupancy and Velocity Plots for 52 vol% 0.8 – 1.2 mm Mullite Grinding Media with 72 wt% Calcium Carbonate Slurry at 6.5 m s^{-1}.....159
Figure 5.23: Height and Radial Position of Irradiated Bead Over 400 Seconds of Milling for 52 vol% 0.8 – 1.2 mm Mullite Grinding Media with 72 wt% Calcium Carbonate Slurry at 6.5 m s^{-1} 161
Figure 5.24: Histogram Showing the Amount of Time the Irradiated Bead Spends Above the Impellers Before Dropping into the Bottom Flow Loop – For 72 wt% Slurry in 52 vol% 0.8 – 1.2 mm Mullite Grinding Media 162
Figure 5.25: Velocity Vectors (Radial and Vertical) for 52 vol% 0.8 – 1.2 mm Mullite Grinding Media with 72 wt% Calcium Carbonate Slurry at 6.5 m s^{-1} 163
Figure 5.26: Occupancy and Velocity Plots for 52 vol% 1.4 – 2.4 mm Mullite Grinding Media with 72 wt% Calcium Carbonate Slurry at 7.9 m s^{-1}.....164
Figure 5.27: Height and Radial Position of Irradiated Small Bead Over 400 Seconds of Milling for 52 vol% 1.4 – 2.4 mm Mullite Grinding Media with 72 wt% Calcium Carbonate Slurry at 7.9 m s^{-1} Note that for radial position, 0 m is centre of vessel and 0.07 m is wall of vessel. 165
Figure 5.28: Height and Radial Position of Irradiated Large Bead Over 400 Seconds of Milling for 52 vol% 1.4 – 2.4 mm Mullite Grinding Media with 72 wt% Calcium Carbonate Slurry at 7.9 m s^{-1} 166

Figure 5.29: Histogram Showing the Amount of Time the Irradiated Bead Spends Above the Impellers Before Dropping into the Bottom Flow Loop – For 72 wt% Slurry in 52 vol% 1.4 – 2.4 mm Mullite Grinding Media (a) Small Bead Tracer (b) Large Bead Tracer 167

Figure 5.30: Velocity Vectors for 52 vol% 1.4 – 2.4 mm Mullite Grinding Media with 72 wt% Calcium Carbonate Slurry at 7.9 m s^{-1} - (a) Small Bead (b) Large Bead 168

Figure 5.31: Occupancy Plots for 52 vol% 0.8 – 1.2 mm Mullite Grinding Media with 72 wt% Calcium Carbonate Slurry at Different Tip Speeds 170

Figure 5.32: Maximum Height of Vortex at Increasing Froude Number – 72 wt% Calcium Carbonate Slurry in 52 vol% 0.8-1.2 mm Mullite Grinding Media 171

Figure 5.33: Occupancy and Velocity Plots for Slurries of Different Solids Contents with 52 vol% 0.8-1.2 mm Mullite Grinding Media at 6.5 m s^{-1} 173

Figure 5.34: Occupancy and Velocity Plots for Glycerol-Water Solutions of Different Concentrations with 52 vol% 0.8-1.2 mm Mullite grinding Media at 6.5 m s^{-1}.....176

Figure 5.35: Occupancy and Velocity Plots of 72 wt% Slurries with Different Amounts of 0.8-1.2 mm Mullite Grinding Media at 6.5 m s^{-1}.....178

Figure 5.36: (a) Occupancy and (b) Velocity Plots for 35 vol% 0.8-1.2 mm Mullite Grinding Media Beads with 52 wt% Calcium Carbonate Slurry at 6.5 m s^{-1} (Power = 52 W).....180

Figure 5.37: Velocity Vector Plot for 35 vol% 0.8-1.2 mm Mullite Grinding Media Beads with 52 wt% Calcium Carbonate Slurry at 6.5 m s^{-1} 180

Figure 5.38: Occupancy and Velocity Plots of 87% Glycerol-Water Solutions with 52 Different Grinding Media Types at 6.5 m s^{-1} 182

Figure 5.39: Occupancy and Velocity Plots of Different Fluids and Grinding Media Amounts at 6.5 m s^{-1} 184
Figure 5.40: Diagram of the Three Regions in a Stirred Media Mill Proposed by Barley[28] 186
Figure 5.41: Vector Plot for Vessel Edge for 0.8 – 1.2 mm Mullite Beads in Calcium Carbonate Slurries at 6.5 m s^{-1} from PEPT Data 187
Figure 6.1: Power Draw and Temperature During Lab-scale Grinding at Impeller Tip Speed 9.8 m s^{-1} and Flowrate 1 ml s^{-1} (a) Batch Operation (b) Continuous Operation 191
Figure 6.2: RTDs of a Dye Tracer in 71% Glycerol with Varying Amounts of 0.8-1.2 mm Mullite Grinding Media in the Stirred Media Mill. Error bars indicate the standard deviation from the average of three tracer pulses added to mill 194
Figure 6.3: Normalised RTDs of a Dye Tracer in Glycerol with Varying Amounts of 0.8-1.2 mm Mullite Grinding Media in the Stirred Media Mill – E Curves 197
Figure 6.4: Dimensionless Plots of Glycerol RTDs 198
Figure 6.5: RTDs of a Titanium Dioxide Tracer in Calcium Carbonate with Varying Amounts of 0.8-1.2 mm Mullite Grinding Media in the Stirred Media Mill. Error bars indicate the standard deviation from the average of three tracer pulses added to mill. 200
Figure 6.6: Normalised RTDs of a Titanium Dioxide Tracer in Calcium Carbonate with Varying Amounts of 0.8-1.2 mm Mullite Grinding Media in the Stirred Media Mill – E Curves 201
Figure 6.7: Dimensionless Plots of Calcium Carbonate RTDs Using Titanium Dioxide Tracer 202

Figure 6.8: Dimensionless RTDs – Comparison Between Nigrosin Dye in Glycerol and Titanium Dioxide in Slurry 204
Figure 6.9: Power Draw in Pilot-scale Continuous Operation Milling with approx 42 vol% 0.8-1.2 mm Mullite Grinding Media in 75 wt% Slurry 208
Figure 6.10: Specific Power Draw for Small Rheometer Scale Tests, Lab-scale Batch Milling and Pilot-scale Semi-Continuous Milling 209
Figure 6.11: Maximum Stress Energy at Each Equipment Scale 211
Figure 6.12: Froude Numbers at A Range of Tip Speeds for Each Equipment Scale 213
Figure 6.13: Po-Re Plot for Lab and Pilot-scale Milling – $k_s = 13$ - Viscosity and Density Terms Exclude Grinding Media and Assume They are a Part of the System 216
Figure 6.14: Po-Re Plot for Small Rheometer, Lab and Pilot-scale Milling – $k_s = 13$ - Viscosity and Density Terms Include Grinding Media 218
Figure 6.15: Po-Re Plot for Lab and Pilot-scale Milling – $k_s = 10.7\ n^{-0.15}$ (optimal from Chapter 4) -Viscosity and Density Terms Include Grinding Media 219
Figure 6.16: Po-Re Plot for Lab and Pilot-scale Milling – Shear Rate Estimated to be Proportional to Square Root of Power per Unit Mass ($\boldsymbol{shear\ rate} = \boldsymbol{100 power\ per\ unit\ mass}$).....220
Figure 6.17: Po-Re Plot for Lab and Pilot-scale Milling – Shear Rate Estimated to be Proportional to Square Root of Power per Unit Mass for Turbulent Pilot-scale and Estimated Using Metzner-Otto for Lab and Rheometer Scale - Viscosity and Density Terms Include Grinding Media 221

Figure 6.18: Mill and Rheometer Power Draw Data for 75 wt% Slurry in 42 vol% 0.8-1.2 mm Mullite Grinding Media – Data is Average of 3 Mill or Rheometer Runs, Error Bars Indicate Standard Deviation (a) Mill Lab-scale (b) Rheometer-Scale.....224
Figure 6.19: Mass of Material in Mill Changes with Impeller Speed During Pilot-Scale Continuous Grinding with approx 42 vol% 0.8-1.2 mm Mullite Grinding Media in 75 wt% Slurry.....225
Figure 10.1: A plot Showing the Conversion from Signal to Power Draw Using Picolog 254
Figure 10.2: Calibration Curve for Spectrophotometer at 910 nm Wavelength 254
Figure 10.3: 'V' Velocities of 0.8 – 1.2 mm Mullite Beads in 71% Glycerol in the Impeller Region – Variation Over Three Impeller Revolutions 255
Figure 10.4: 'V' Velocities of 0.8 – 1.2 mm Mullite Beads in 71% Glycerol in Top Impeller Region – Variation Over Three Impeller Revolutions.....255
Figure 10.5: 'V' Velocities of 0.8 – 1.2 mm Mullite Beads in 71% Glycerol in Bottom Impeller Region – Variation Over Three Impeller Revolutions.....256
Figure 10.6: Velocity Vector Plots for 72 wt% Calcium Carbonate Slurry in 52 vol% 0.8-1.2 mm Mullite Grinding Media – (a) 3.9 m s^{-1}, (b) 5.2 m s^{-1}, (c) 6.5 m s^{-1}, (d) 7.8 m s^{-1}, (e) 9.2 m s^{-1}.....257

LIST OF TABLES

Table 1.1: Conference Presentations During PhD.....6

Table 2.1: Equations Describing Flow Behaviour for Common Fluid Types[43].....21

Table 2.2: Relationship between Power Number and Reynolds number in Different Flow Regimes.....33

Table 2.3: Types of Tracer Utilised in Chemical Processes.....36

Table 3.1: Grinding Media Types.....48

Table 3.2: Normal Operating Parameters Used During Grinding.....51

Table 3.3: Geometries of Rheometer and Lab-Scale Mill Set-Ups.....58

Table 4.1: Power Law Equations for 200 kWh tonne^{-1} Ground Calcium Carbonate Slurries with Different Solids Contents.....82

Table 4.2: Glycerol Concentrations Selected and Justification for Use.....83

Table 4.3: Power Law of Different Glycerol-Water Solutions and Slurries with 0.8-1.2 mm Mullite Grinding Media.....86

Table 4.4: Mill Conditions for Mullite 1.4 – 2.4 mm Grinding Media with Glycerol at Reynolds Number 3000.....92

Table 4.5: Error Associated with Power Number Correlations, Assuming Grinding Media are a Part of the System.....108

Table 4.6: Error Associated with Power Number Correlations, Assuming Grinding Media are a Part of the System – Grinding Media Included In Density Terms Only 108

Table 4.7: Error Associated with Power Number Correlations, Assuming Grinding Media are a Part of the Fluid.....114

Table 4.8: Summary of Tests Conducted to Test Model.....115

Table 4.9: Average % Error Using Each Model for Each Test.....118

Table 6.1: Actual and Experimentally Fitted Values for Constants in Ideal CSTR RTD – Dye Tracer in Glycerol.....195
Table 6.2: Comparing the Experimental and Predicted Amounts of Dye Exiting the Mill Over 5 Residence Times.....197
Table 6.3: Actual and Experimentally Fitted Values for Constants in Ideal CSTR RTD – Titanium Dioxide Tracer in Calcium Carbonate.....201
Table 6.4: Actual and Experimentally Fitted Values for Constants in Ideal CSTR RTD + Constant – Titanium Dioxide Tracer in Calcium Carbonate.....203
Table 6.5: Average Residence Times Measured Using the Two RTD Methods.....205

NOMENCLATURE

a	Weibull distribution shape parameter	[-]
Abs	Absorption of light	[-]
B	Weibull distribution scale parameter	[-]
c	Concentration of dye	[mol m^{-3}]
C	Impeller geometry constant	[-]
C_{A0}	Initial concentration	[-]
C_b	Titanium dioxide base level concentration	[-]
C_v	Slurry solids concentration	[-]
C(t)	Concentration function	[-]
D	Impeller diameter	[m]
d_{GM}	Diameter of grinding media beads	[m]
d_v	Volume equivalent sphere diameter	[m]
E	Energy	[J]
E(t)	Residence time distribution function	[s^{-1}]
$E(\theta)$	Dimensionless residence time distribution function	[-]
Fr	Froude number	[-]
GM	Volume ratio of grinding media in mill	[-]
I	Path length of light	[m]

k_s	Metzner-Otto constant	[-]
KE	Kinetic energy	[J]
m	Mass of grinding media beads	[kg]
n	Flow behaviour index	[-]
N	Rotational speed	[s^{-1}]
N_c	Amount of grinding media contacts	[-]
N_p	Number of feed particles in mill	[-]
P	Power	[W]
Po	Power number	[-]
P_s	Probability a particle is broken at a grinding media contact	[-]
Q	Volume flowrate out of mill	[ml s^{-1}]
Re	Reynolds number	[-]
SC	Solids content of slurry	[wt %]
SE	Stress energy	[J]
SE_{max}	Maximum stress energy	[J]
St	Stokes number	[-]
t	Time	[s]
t_m	Mean residence time	[s]
T	Torque	[N m]

Tr	Transmittance (% light passed through sample)	[%]
v	Velocity of grinding media beads	[m s^{-1}]
V_{fluid}	Total volume of fluid in mill	[L]
V_p	Volume of particle	[m^3]
v_t	Impeller tip speed	[m s^{-1}]
X	Particle size	[m]
$\in$	Molar absorption coefficient	[m^2 mol^{-1}]
ε	Grinding media porosity	[-]
$\dot{\gamma}$	Shear rate	[s^{-1}]
μ_f	Viscosity of fluid	[Pa s]
μ_{f+GM}	Combined viscosity of fluid and grinding media	[Pa s]
ρ_f	Density of fluid	[kg m^{-3}]
ρ_{f+GM}	Combined density of fluid and grinding media	[kg m^{-3}]
ρ_{GM}	Density of grinding media	[kg m^{-3}]
ρ_{GM-f}	Density difference between fluid and grinding media	[kg m^{-3}]
τ	Shear stress	[Pa]
τ_0	Yield stress	[Pa]
τ_t	Average residence time	[s]
φ_{GM}	Grinding media fill ratio	[-]

1. INTRODUCTION

1.1. Project Background

Imerys is a world leader in the minerals industry - there are approximately 230 Imerys sites across 50 countries[1]. One of the major products supplied by Imerys is calcium carbonate, which is sold as small particles (on the micron scale) for a range of product applications.

1.1.1. Calcium Carbonate

Calcium carbonate is a naturally occurring material that accounts for around 4% of the world's crust[2]. It has many uses, including being the most widely used mineral in the paint and paper industries, where it is used as a filler or extender[3]. Ground calcium carbonate is extracted from a mineral feedstock and subsequently processed using a series of crushing, fine grinding and separation stages. This thesis will focus on the fine grinding stage, where particles are typically between 2 μm (final product) and 50 μm (feed). Small calcium carbonate particles can alternatively be formed using a precipitation mfethod, where calcium oxide is hydrated to form calcium hydroxide, which is subsequently carbonated to form calcium carbonate[4]. However, this production method is outside the scope of this research.

1.1.2. Stirred Media Mills

Fine grinding typically occurs in stirred media mills, which are formed of a stationary grinding chamber and an agitator. They can be mounted horizontally or vertically, with

grinding media motion differing due to gravitational forces. This thesis focuses on vertical stirred media mills, with a typical set-up illustrated in Figure 1.1.

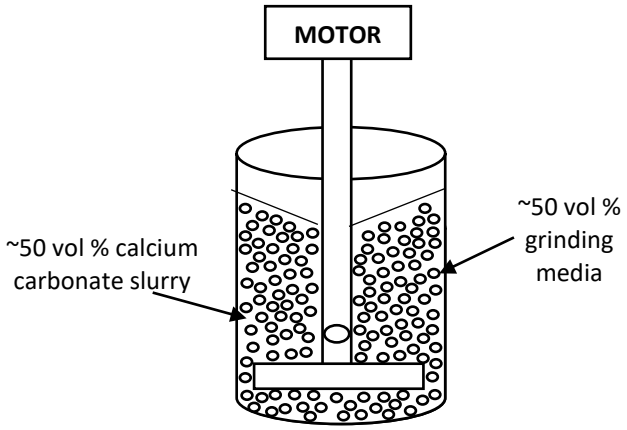

Figure 1.1: Diagram of a Typical Vertical Stirred Media Mill Used for Fine Grinding of Calcium Carbonate

A slurry of mineral particles, water and a dispersant is added to the grinding chamber. Also in stirred media mills are free moving grinding media, which are typically made from metals, glass or ceramics[5]. When the grinding media beads collide, particles trapped between them will break, provided that there is enough energy in the collision for this to happen.

For industrial operations, stirred media mills are operated continuously with a series of separation and recirculation stages. The product from each milling unit passes through a classifier and any coarse product is returned to the mill to be reground. However, lab-scale experiments are often conducted batch wise since continuous lab-scale operation remains a challenge to monitor and control.

It is estimated that only 3-5% of the energy consumed by stirred media mills is used for breaking particles, with the remaining energy being dissipated as heat, noise or

vibrational energy[6]. This high energy requirement means that it is a particularly important research area - improvements could help reduce the energy costs associated with fine grinding as well as reducing the environmental impact of the process. To improve stirred media mills, changes could be made to many different parameters, including:

- The geometry of the stirred media mill and impeller.
- The impeller speed.
- The type and amount of grinding media.
- The type and amount of dispersant.
- The separation and recirculation stages between mills in continuous set-ups.

1.1.3. Analogy to Mixing

Changes can be made to design or operating parameters to improve the energy efficiency in stirred media mills. To determine suitable changes to make, a detailed understanding of what happens inside a stirred media mill is required. Stirred media mills can be considered analogous to stirred tanks. However, the vessel contents are more complex than in the case of stirred tanks due to the large amounts of different solids in the mill. The large amount of grinding media makes the rheology complex and challenging to measure or predict. This makes the application of equations and correlations for stirred tanks a challenge to apply to stirred media mills. As the aim in a stirred media mill is to break particles rather than give a well-mixed system, higher rotational speeds are used in stirred media mills than in typical mixing operations, which gives rise to different flow patterns.

1.2. Aims and Objectives

Due to the complex nature of stirred media mills and key differences between stirred tanks and stirred media mills, this research aims to increase the understanding of the operation of stirred media mills. The key objectives of this thesis are:

- To determine the extent to which theories typically applied to stirred tanks can be applied to stirred media mills. The focus will be on methods of predicting power draw using the dimensionless Power Number and Reynolds number.
- To understand how flow inside a stirred media mill is affected by key operating parameters and relate this to the effect of these operating parameters on power draw. This includes utilising the techniques High Speed Imaging (HSI) and Positron Emission Particle Tracking (PEPT).
- To compare important scale-up parameters in stirred media mills to those of stirred tanks and determine key differences between lab-scale and pilot-scale operation.

1.3. Business Case

The industrial sponsor of this project was Imerys, who operate a large number of stirred media mills for grinding calcium carbonate at lab, pilot and processing plant scales. The main issue with grinding is that the energy efficiency is low due to heat, noise and vibrational energy dissipation. The aims of this thesis relate to gaining an understanding of the important operating parameters in stirred media mills, which can lead to new ideas for changes to the mill operating parameters, which may in turn lead to improved energy efficiency. Stirred tanks are well researched and hence there is a

clear usefulness of being able to apply stirred tank theories presented in literature to stirred media mills and understand the key differences.

A deeper understanding of the parameters affecting scale-up is also desirable since this will make research methods more efficient. It is significantly more time and resource efficient to conduct trials at a smaller scale than the processing scale. Since lab-scale mills are often batch operated, this thesis will also explore some of the key differences between batch and continuous grinding and discuss how results from batch lab-scale mills can be related to larger scale continuously (or semi-continuously) operated mills.

1.4. Thesis Layout

This thesis contains an introduction, literature review, details of methods, three results chapters, conclusions and suggestions for further research.

- **Chapter 1** – introduction to the research area and relevance to Imerys.
- **Chapter 2** – a review of existing literature surrounding stirred media mills and analogies between stirred tanks and stirred media mills, as well as existing research into flow patterns.
- **Chapter 3** – details of the materials and experimental methods used throughout the results chapters. This chapter describes milling methods, slurry analysis techniques and flow visualisation methods.
- **Chapter 4** – first results chapter comparing methods of predicting power draw in stirred media mills, and proposing a new method where the combined

viscosity of the slurry and grinding media is measured using the vane rheometer.

- **Chapter 5** – second results chapter looking at the flow of grinding media beads in the mill using both PEPT and HSI. A particular focus is placed on the shape and development of the vortex in the lab-scale mill since this appears to affect the power draw. The potential benefits of using HSI to look at (close to) instantaneous flow patterns are discussed.
- **Chapter 6** – third results chapter comparing pilot-scale experimental data with the lab-scale and a smaller rheometer-scale. Lab-scale RTDs are presented and potential methods of measuring pilot-scale RTDs are proposed.
- **Chapter 7** – a summary of the main findings of this thesis and how they relate to the initial objectives.
- **Chapter 8** – suggestions for further research in the area of understanding the operation of stirred media mills.

1.5. Conference Presentations

Sections of this PhD were presented at conferences, as detailed in Table 1.1

Table 1.1: Conference Presentations During PhD

Conference	Presentation Title
International Congress on Particle Technology – April 2019	Understanding the Fine Grinding of Calcium Carbonate in Stirred Media Mills
European Symposium on Comminution and Classification – September 2019	Understanding the Flow of Calcium Carbonate in Stirred Media Mills
American Institute of Chemical Engineers Annual Meeting – November 2019	Understanding the Flow of Materials in Stirred Media Mills

2. LITERATURE REVIEW

2.1. Introduction

This section reviews existing knowledge of stirred media mill operation, including ways in which they are analogous to stirred tanks, parameters affecting scale-up and flow pattern assessments.

2.2. Stirred Media Mill Operating Principles

Stirred media mills are used for the fine grinding of many materials, including minerals, pharmaceuticals and foods. The idea of stirred mills was first proposed by Klein and Szegvari in 1928, before being used industrially by Du Pont in 1948[7]. Recent developments focus on improving the efficiency of these mills as well as adapting them to be able to handle different feed sizes and form products of different sizes. This section discusses the key operating principles, including how particles break and how energy efficiency can be defined or estimated.

2.2.1. Breaking Particles

Particles break when they are exposed to a stress exceeding their fracture strength. The fracture mechanism is dependent on the nature of the particle, the type of force (e.g. compressive or shear) and the rate of force[8]. For particle breakage in a stirred media mill, there are three possible scenarios[9]:

- Particles are stressed by grinding media being accelerated from the impeller to the vessel walls and can hence break from impact with the impeller or walls.

- Particles are pressed against the vessel wall due to centrifugal forces.
- Particles are moving in the tangential direction and collide with slower moving grinding media.

Due to varied flow patterns within stirred mills, there is a combination of breakage mechanisms occurring. The types of breakage are abrasion, compression and impact, which can be visualised in Figure 2.1a[10]. Each of these mechanisms of breakage results in a different shape of particle size distribution, shown in Figure 2.1b[10].

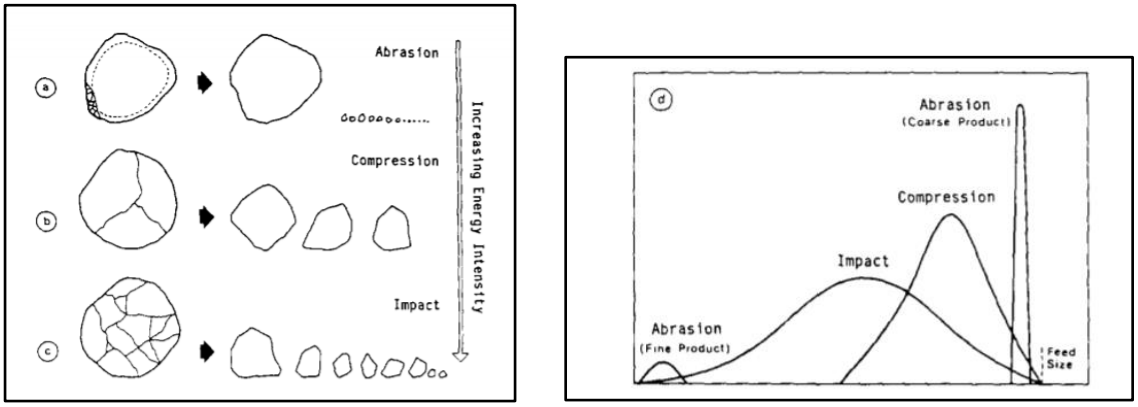

(a) **(b)**

Figure 2.1: (a) Particle Breakage Mechanisms, and (b) Particle Size Distributions Resulting from Different Breakage Mechanisms[10]

The breakage mechanism occurring depends on the energy intensity of the collision. If multiple particles are captured between the colliding grinding media, Kwade[9] determined that only the first particle would break, with any additional particles involved wearing down by abrasion.

Ideally, in a stirred media mill there should be a large number of collisions involving enough force to break particles. To quantify the effect of different operating conditions

on the number of collisions and the stress exerted by collisions, the concepts of stress energy (SE) and stress number (SN) were introduced[11].

Stress energy is a measure of the amount of energy in a collision – there is a distribution of stress energies throughout the mill due to flow patterns[11]. Stress energy is related to the kinetic energy of grinding media and can be calculated from Equation (2.1)[11], where d_{GM} is the grinding media size, v_t is the tip speed, and ρ_{GM} is the grinding media density. It is assumed that the velocity of the grinding media is proportional to the tip speed.

$$SE \propto SE_{max} = d_{GM}^3 v_t^2 \rho_{GM} \tag{2.1}$$

Stress number is defined as the average number of stress events of each feed particle (and its resulting fragments) and can be calculated using Equation (2.2)[12].

$$SN = \frac{N_C P_S}{N_P} \tag{2.2}$$

By considering the terms involved in N_c (number of grinding media collisions), P_s (probability of a particle being trapped in a collision) and N_p (number of feed particles in mill), a stress number proportionality relationship was determined in Equation (2.3)[12], where φ_{GM} is the grinding media fill ratio, ε is the grinding media porosity, N is the impeller speed, t is the time, C_v is the solids content of the slurry and d_{GM} is the diameter of the grinding media beads.

$$SN \propto \frac{\varphi_{GM}(1-\varepsilon)}{(1-\varphi_{GM}(1-\varepsilon))C_v} \frac{Nt}{d_{GM}^2} \tag{2.3}$$

When grinding media beads collide, it is likely that there will be more than one particle trapped between them. As the beads approach, the fluid is squeezed out of the gap and some of the particles remain trapped to be potentially broken. The smaller a particle is, the more faithfully it follows the path of the fluid and the more likely it is to be carried out of the gap instead of being trapped. The volume of particles trapped in a collision is important since the energy of a collision is shared between breaking all of these particles. The concept of stress intensity considers this by dividing the stress energy by the volume of trapped particles[13]. The stress intensity is therefore proportional to the stress energy[14].

Stress energy and stress number can be related to operating parameters shown in Equation (2.1) and Equation (2.2) have hence been used for the scale-up of mills[15]. This scale-up process uses the assumption that if the mean stress energy and specific energy transferred to the particles is constant, the product quality obtained will be constant[16]. However, there is a distribution of stress energies throughout the mill. In order to have a large number of collisions with sufficient energy to cause particle breakage, the grinding media should spend a long time in zones of the mill with the highest energy density, and the high energy density zones should be large. Stress intensities and the number of stress events for each mechanism have been compared to determine that most particles are broken by colliding with slower moving grinding media. Stress events near the wall have lower stresses due to the lower velocities away from the impeller[9] and may also have a lower local grinding media density due to the effect of the wall on packing efficiency.

For the maximum number of particle breakages, there should be a high number of collisions and sufficient stress imparted in each collision to lead to breakage. These requirements can be contradictory; large grinding media beads impart more stress since the bead mass is greater and there is more momentum, but the total number of beads in a given volume will be smaller, resulting in fewer collisions[17].

In order to have many collisions with sufficient energy to cause particle breakage, the grinding media should spend a long time in zones of the mill with the highest energy density. Blecher et al.[18] showed theoretically that the zones with highest energy density are at the wall and in the vicinity of the impeller. However, these zones only make up around 10% of the total mill volume. A limitation of this research is that calculations used to find energy densities and velocities are based off the stirring of a Newtonian fluid at laminar flow, which is not representative of a mill containing grinding media at high speeds. Nevertheless, this research shows that the flow patterns obtained during grinding are important and mill improvements can potentially be made by expanding the zones with high energy density. Flow patterns are discussed further in section 2.4.

2.2.2. Defining Energy Efficiency

The energy efficiency of the mill is a measure of how much of the energy supplied is used usefully to break particles and create new surfaces as opposed to being dissipated as heat, noise or vibrational energy. It is also possible that some energy can be used to modify the surface chemistry or crystal structure of the minerals, which can be useful for downstream separation processes. However, the energy use and benefit

of this is rarely considered when estimating the grinding efficiency[14]. It is a challenge to calculate the energy efficiency of a stirred media mill since the energy used for creating new surfaces is difficult to measure directly.

Energy efficiency has been defined in several ways for a stirred media mill. The product size at a given energy input is commonly used as a milling efficiency. Kwade found that there is an optimum stress intensity that gives a minimum particle size for a given energy input[18]. This is useful because operating parameters of the mill can be adjusted to give this optimum stress intensity. However, due to the distribution of product particle sizes produced during milling, it can be difficult to compare energy efficiencies directly using this method. Similarly, the energy efficiency could be defined based on the desired industrial use, such as for the paper industry, the main required particle size characteristic is that 90% of particles are less than 2 μm[19], so the percentage of particles less than 2 μm for a given energy input could be used to compare energy efficiencies.

Ballantyne et al.[20] introduced the size-specific energy (SSE) as a measure of the amount of energy used to generate particles below 75 μm and found that for different ores, the relationship between specific breakage energy and generation of sub 75 μm material is linear. The SSE is measured as an amount of energy per tonne of particles that are less than 75 μm. This method is thought to accurately reflect the energy used in generating new surface area for the fine particles, which relates to Rittinger's 1867 proposal that the work done in crushing is proportional to the new surface area

produced[21]. Although 75 μm was used by Ballantyne et al., this size can be adapted depending on the stirred media milling application.

2.2.3. Factors Influencing Energy Efficiency

There are many operating parameters affecting grinding performance. For optimal performance, the required particle size should be obtained using minimal energy whilst also having a short residence time in the mill. This means that production rates will be high and operating costs low. A high power draw is therefore desirable. Many operating and physical equipment parameters strongly affect the rate of particle size reduction and the power draw of the mill, including but not limited to[22]:

- Grinding media size, density and shape
- Impeller speed
- Slurry particle size, density and hardness

Although the above parameters were found to be of high importance when considering milling efficiency, there are a large number of other parameters having an effect.

2.2.3.1. Grinding Media Properties

The grinding media size is important in stirred media milling. As a general rule of thumb, it is suggested that grinding media should be 20 times bigger than the feed particle size[23]. According to the concept of stress energy, increasing the grinding media size has a cubic impact on the stress energy. Furthermore, larger grinding media beads have less curvature, making it easier to trap particles between two beads[24].

The size of grinding media beads not only affects the stationary packing of grinding media beads but also the fluidisation and packing of the mill whilst the impeller is in operation. It remains a challenge to quantify the packing density at different levels in the mill. Some indication of where grinding media reside in the mill can be obtained from PEPT (Positron Emission Particle Tracking). However, PEPT can only be used to track one (or in some cases a few) grinding media beads per experiment, which makes it difficult to compare the flow patterns of different sized grinding media beads within the mill. Most PEPT research in literature uses an irradiated grinding media bead of average size to investigate flow patterns. Grinding media motion and flow patterns within the mill are discussed in greater detail in section 2.4.1.

The size distribution of the grinding media has had limited consideration - grinding media is typically sold as a monomodal range of sizes due to the production methods used. Patel et al.[25] considered the effect of mixing grinding media of different sizes to produce bimodal size distributions and found that less energy was required to produce smaller particles when a mix of fine and coarse grinding media was used. However, due to the high cost of small grinding media, costs are higher than using coarse grinding media are used alone.

Additionally, Yue and Klein[23] related the effect of using a bimodal distribution of grinding media beads to the particle packing density. The packing density increases when the voids between larger grinding media beads are filled with smaller beads. The maximum packing density is achieved when the large grinding media beads are at least 10 times the size of the smaller beads and the smaller beads occupy 30% of the

fill volume. This particle packing density also affects the viscosity of suspensions of a fixed solids concentration; viscosity reduces when smaller beads are added, which leads to a smaller power draw from the mill. However, it was concluded that although the use of a bimodal size distribution of grinding media beads decreases power draw, it does not have a desired effect on the product particle size or the rate of particle breakage. Additionally, a ball bearing effect was identified, where fine beads behave as bearings and alter the direction of any adjacent larger grinding media beads, which reduces their kinetic energy and hence reduces the collision force.

As well as the size of grinding media beads, the material is important. The material should be sufficiently hard as not to result in rapid wear of the grinding media beads. Due to the large cost of grinding media, wear in milling operations is a well researched and discussed topic[26]. As well as having different hardness and wear properties, different bead materials have different densities, which also has an impact on grinding.

2.2.3.2. Impeller Speed

The effect of impeller speed on milling is relatively well understood. Up to a point, the increase in speed increases the efficiency of milling due to the larger amount of energy in collisions. After this point, energy is wasted and dissipated as heat because the energy in collisions is greater than that required to break particles[27]. In terms of flow patterns, the impeller speed has a big effect on the packing of the grinding media and the speed at which they move. This was visualised by Conway-Baker et al.[28] using PEPT, again only for a small lab-scale mill as opposed to a plant scale mill where the tip speed vs the revolution speed of the impeller will be very different.

2.2.3.3. Dispersant Amount

During wet milling, a dispersant is used to reduce the yield stress of the slurry and enable a larger percentage of solids to be used. Without a dispersant, the maximum solids concentration is around 50 wt%, while this can be increased to around 80 wt% if an optimum dispersant is used[29]. Increasing the amount of dispersant increases the milling efficiency by altering the slurry rheology. However, past a certain point, the milling efficiency decreases again because the excess dispersant surrounding the grinding media acts as a cushion and lowers the stress intensities[30].

Forssberg and Wang[31] investigated the effect of adding dispersant periodically during batch milling. This periodic addition compensates for the rheological changes occurring and the new surface area exposed as the particle size decreases. It was found that an increase in milling efficiency could be obtained by this periodic addition. Most large-scale milling operations are continuous and the slurry flows through a series of mills. To make this periodic addition relevant to continuous milling, more dispersant is added at each consecutive mill.

There is an optimum dispersant concentration. Electroacoustics has successfully been used to measure the zeta potential and from this determine the optimum dispersant choice and concentration when grinding calcium carbonate in a stirred media mill[29]. The optimum dispersant amount has a large zeta potential when the dispersant covers all particles since this means there are repulsive forces between particles. When adding more dispersant does not give any further change in zeta potential, no more dispersant can adsorb onto the particles.

2.2.3.4. Slurry Solids Content

The impact of slurry solids content on grinding has been reported in literature. Increasing the solids content increases efficiency but only to a certain point - there lies an optimum[22,32]. Higher solids content slurries have a higher viscosity, which affects power draw also cushions collisions. However, higher solids contents also mean that it is more likely a particle will be broken in a collision[22].

2.2.3.5. Equipment Set-Up and Geometry

The type and size of stirred media mills has an effect on energy efficiency since it effects the distribution of stress energy within the grinding chamber and the energy dissipation mechanisms. For scale-up, a characteristic mean stress energy and an efficiency is required since wall effects are strongly dependent on the mill diameter[11].

Yang et al.[33] used PEPT to investigate how different impeller types affect the flow field during milling within a batch lab-scale stirred media mill. The impeller type affects the acceleration of particles and hence the forces achieved in collisions, which in turn determines whether particles will break and the efficiency of particle breakage. It was found that by adding more pins to the impeller, a greater power draw is required but it does not break more particles, likely due to heat dissipation. Pitched blade impellers were seen to be favourable in terms of energy efficiency. This data is valid for a small 2 L batch scale mill. However, it is unclear whether the performance enhancements achieved using a pitched blade impeller will translate to a much larger scale where the flow field is different due to wall effects and a different distribution of stress energies, as well as other dimensional differences such as aspect ratios.

Conway-Baker et al.[28] also found the pitched blade turbine to give good milling results, with the grinding media being more densely packed in the region adjacent to and surrounding the impellers, resulting in a narrower particle size distribution of particles. Altun[34] researched dry horizontal mills at the pilot-scale, confirming that at larger scale there are large difference in power requirements for mills with different impeller types. The stirrer type has a large impact on the power requirement - when the same rotational speed is used, a higher power draw is required for pin-counter-pin stirrers than disc stirrers[35]. A high power draw will result in faster grinding, provided that the energy is used usefully to break particles rather than being dissipated as heat.

Daraio et al.[36] varied the diameter of the impeller in DEM models to determine how it affects the motion of grinding media inside stirred media mill and found that greater diameter impeller arms give more effective media agitation but a higher hydrostatic pressure at the bottom of the mill, which can lead to powder compaction at the bottom and along the walls of the mill. However, DEM does not allow the fluid phase to be studied for the case of wet milling and only considers the motion of the dry grinding media.

Stender et al.[11] researched the impact of chamber size on efficiency and related this to the stress energy distribution within the mill by looking at the median product particle size compared with the specific energy. The impact of changing the chamber size depends on other operating parameters in the mill. For the smallest grinding media used, the smallest grinding chamber gave more efficient grinding, whereas when larger grinding media were used the largest grinding chamber gave more efficient grinding.

This was explained using stress energies; smaller grinding media in smaller chambers have the same mean stress energy as larger grinding media in larger chambers.

2.2.3.6. Continuous Milling Circuit Parameters

The overall energy efficiency of industrial milling is also related to operating parameters of a continuous milling circuit. In industrial grinding where it is important to reach a desired particle size, there can be other issues such as overgrinding, where some particles are ground to a smaller size than is required. Industrial mills often operate continuously, such as in closed circuit mode, where the product of the mill passes through a classifier and the coarse product is returned to the mill. This means that fine particles are removed from the mill and overgrinding is prevented. The type of classifier selected and the efficiency of the classification unit can have big impacts on grinding; it is estimated that the use of more efficient classification technology could increase the grinding circuit capacity by 15-25% when compared with using single stage cyclones[37]. The size range of the particles returning to the mill is also important and prevents overgrinding[38]. The circulating load is the amount of material returning to the mill from a separator and it affects the grinding efficiency and the circuit capacity. Bond[39] determined that the optimum circulating load of a closed ball mill circuit with a cyclone is approximately 250%, demonstrating that the operation of a milling operation is not purely governed by the milling parameters - other parameters, such as those of the classification circuit must also be considered.

2.3. Analogy with Mixing

Horizontal stirred media mills can be described as a vessel equipped with an impeller and can therefore be considered analogous to stirred tanks. This suggests that factors that are important in mixing such as rheology, Power Number, Reynolds number and residence time distributions (RTDs) are also important in milling. The stirred vessels are filled with grinding media and can be operated either dry with a powder or wet with a slurry, which means that there are differences between stirred tanks and stirred media mills. The extent to which theories developed for stirred tanks have been applied to mills is discussed in this section. When considering dimensionless numbers, mixing and flow patterns rheology is of particular importance.

2.3.1. Rheology

Rheology is indicative of the level of interparticular interactions and aggregation[40]. When grinding media collide, viscous energy is dissipated into the fluid. Many process parameters alter the slurry rheology in milling. The main factors are[41]:

- Solid concentration
- Particle size distribution
- Shear rate
- Temperature

Non-Newtonian fluids have a viscosity that is dependent on the shear rate. Time independent fluids have a viscosity that has no dependence on the amount of time for which they have been sheared[42]. Figure 2.2 shows the relationship between shear rate and shear stress for some of the most common fluid types. Equations describing

the relationship between shear stress (τ) and shear rate ($\dot{\gamma}$) for some common fluid types are shown in Table 2.1, where τ_0 is the yield stress.

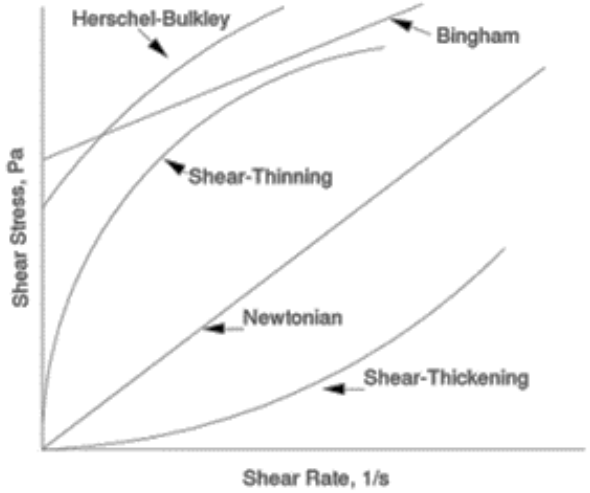

Figure 2.2: Flow Curves for Common Fluid Types[43]

Table 2.1: Equations Describing Flow Behaviour for Common Fluid Types[43]

Fluid Type	General Relationship
Newtonian	$\tau = \mu\dot{\gamma}$
Shear Thinning	$\tau = \mu\dot{\gamma}^n$ (where n < 1)
Shear Thickening	$\tau = \mu\dot{\gamma}^n$ (where n > 1)
Bingham	$\tau = \mu\dot{\gamma} + \tau_0$
Herschel-Bulkley	$\tau = \mu\dot{\gamma}^n + \tau_0$

When the fluid is a suspension of solid particles dispersed in a liquid phase, both the liquid properties and dispersed phase properties affect the suspension rheology. If particles are small enough (similar to the solvent molecule size), they are subject to Brownian motion and interact due to attractive Van der Waals forces or repulsive electrostatic forces, whilst if they are large, they are subject to movement due to

gravitational forces. In the fine grinding of calcium carbonate, particles reduce in size to sub-micron and hence which of these forces dominate depends on the amount of milling that has been performed. Dispersants are added during grinding to overcome the attractive forces and prevent aggregation and ensure the product is well dispersed[44].

2.3.1.1. Measuring the Viscosity of Particulate Systems

Slurry viscosities are challenging to measure due to particle settling and wall slip. When cone and plate or parallel plate geometries are used, the gap size must be sufficient - if the particles are relatively large compared to the gap width or the solids content is high, there will be slip at the wall. For suspensions with up to 25% solids, a gap size of 10 times the maximum particle size is typically required. With greater solids contents up to 50%, a gap size of 100 times the maximum particle size is required [45]. Large gap sizes result in the assumption that shear stress is constant across the gap being invalid. To overcome this, vane rheometers can be used to analyse non-Newtonian fluids of fluids with large particles[46]. They have been utilised for determining the viscosity of materials such as concrete and paste like slurries[47].

Some literature explores methods of overcoming this slip issue using standard geometries. Zarraga et al.[48] used parallel plate and cone and plate rheometer geometries to measure the rheology of concentrated suspensions of solid glass spheres (approx 44 μm) in Newtonian fluids. A dimensionless slip correction factor was applied due to the large solids concentration attributing to wall slip. At high solids loading, the suspensions showed shear thinning behaviour with all Newtonian fluids

tested. At lower concentrations, some shear thickening behaviour was observed at the lowest shear rates. This behaviour is common and expected and has been reported as early as 1979 by Ferrini et al.[49] who also investigated the effects of glass beads of different solids contents in Newtonian liquids and found that they show shear thinning behaviour, with increasing the solids content increasing the extent of shear thinning behaviour.

As well as the vane geometry or adaptations to standard geometry methods, other methods have been developed to measure slurry viscosities. Faitli et al.[50] developed an online method of monitoring the rheology of the stirred media slurry using a tube rheometer. This is useful because the slurry rheology changes rapidly during milling as the particles get smaller. The online monitoring method was deemed both fast and reliable, having been validated by conducting tests using a rotational rheometer.

In addition to this, Mangesana[51] found the viscosity distribution in the main regions of a tumbling mill using an online tube rheometer method. However, because of the temperature changes during milling, the viscosity measurements had to be corrected to the same temperature. It is difficult to measure the rheology of slurries with a high solid content because the particles settle rapidly and there are particle packing variations as well as wall slip. Hence, the experiments were only conducted at relatively low solids contents where the solids did not settle out in the pipes or plug the rheometer (<60 wt% in this case). This is less useful for standard milling applications which often utilise a higher solids content.

Instead of using rheometers, several authors have related the power draw of the mill itself to slurry viscosity. Zheng et al.[52] determined that the power draw (P) was related to the slurry viscosity (μ) by Equation (2.4), where C is the impeller geometry constant, D is the impeller diameter and N is the impeller speed. It is assumed that:

- The fluid viscosity follows the power law.
- Shear rate is proportional to impeller speed.
- Shear stress is proportional to torque.

$$\mu = \frac{P}{CN^2D^3} \tag{2.4}$$

Fuerstenau et al.[53] measured the torque of a ball mill and modelled torque (and hence mill power) as a function of the changing viscosity of the slurry inside by assuming that the torque reflects the motion of the grinding media. It is thought that a similar concept could be applied to stirred media mills.

2.3.1.2. Calcium Carbonate Slurry Viscosity

Calcium carbonate slurries are common due to the wide range of uses of calcium carbonate. Hence, their viscosity has been measured and reported by many authors for a range of solid contents, particle sizes and dispersant amounts.

Garcia et al.[44] found calcite suspensions with solids contents 8-14 vol% to be shear thinning with a yield stress (a Herschel Bulkley fluid). A cone and plate rheometer geometry was used, which means that the occurrence of wall slip limits measurements

to low solid concentrations. The viscosity was also shown to increase as particle size decreased due to the increase in attractive interparticular forces. When a polyacrylate dispersant was added, the viscosity decreased notably for all shear rates investigated as particle interaction is reduced, which decreases aggregation and viscosity. If the dispersant amount is sufficient to cover the whole particle surface area, Newtonian behaviour is observed, which results in improved grinding efficiency. However, the maximum solids content used in this work was 14 vol%, which is lower than is typically used for grinding.

To measure higher solids concentrations, Koltka et al.[54] used a vane geometry. At solids contents of 50, 60 and 70 wt%, the slurries showed shear thickening behaviour, which was explained by most of the liquid being trapped in the pores and showing flow resistance. As the solids content of the slurry increases to 80 wt%, they are shear thinning with a yield stress. The shear thickening behaviour observed here is different to that observed by other authors investigating high solid content slurries, which have often been found to be shear thinning[44,55,56]. However, this behaviour is dependent on the calcium carbonate particle size; Shi et al.[57] found slurries to be shear thickening with a low yield stress after passing through a primary ball mill but shear thinning with a high yield stress after the secondary ball mill. This indicates that the particle size has a large impact on flow behaviour.

2.3.1.3. Measuring the Viscosity of Large Particulate Systems

In stirred tanks, the viscosity term represents the fluid being stirred. In the case of stirred media mills, the material being stirred is a combination of slurry and grinding

media. To measure the viscosity of this combination of slurry and grinding media, advanced rheological methods are required due to the large particle size of the grinding media beads. Although there is currently no literature specifically looking at the rheology of grinding media in mineral suspensions using a rheometer, other large particle suspensions have been investigated.

When wall slip is a problem in fluids (such as when there are a large amount of particles), the vane rheometer can be used to measure viscosity. It has however been found that some slip can still occur in the smooth outer cup of the vane, and this surface can be roughened to minimise this[46]. Savarmand et al.[58] used 3D finite element simulations to investigate the distribution of shear stress and velocity streamlines. It was shown that there is a small stress peak at the tips immediately next to the vane, but the stress is close to uniform throughout the rest of the gap between the vane and the wall. It was also found that for power law fluids with an index of 0.5, the fluid between the vane blades does not exchange with the fluid in the gap between the vane and the wall; the fluid between the blades moves as a solid body at a similar speed to the vane moves. This creates a rotating cylindrical surface. The vane has been utilised for measuring many structured liquids and solid suspensions[46].

Mahaut et al.[59] investigated the behaviour of non-colloidal particles in yield stress fluids, including an emulsion, a gel and a colloidal suspension using the vane rheometer. The non-colloidal particles added to these fluids were monodisperse polystyrene beads or higher density glass beads of a range of sizes up to 2 mm. Solid volume fractions up to 50 vol% were used, which is similar to the grinding media bead

content during stirred milling. This work focused on identifying the yield stress and elastic modulus instead of steady shear rheometry, so is not useful in calculating the Reynolds number.

In a second paper, Mahaut et al.[60] suspended 2 mm glass beads in a cement paste as a way of modelling the rheology of concrete. The particles in the paste are so much smaller than the glass beads, so the paste is seen as a continuous medium. This set-up is similar to grinding media beads in a mineral slurry. Again, this paper focuses on the yield stress and time dependency - the suspensions were found to be time independent and shear thinning.

When a large number of beads are used in a vane rheometer, they can be subject to sticking and slipping, particularly when there is no continuous phase. This behaviour is similar to the process of fault slip in earthquakes. Higashi et al.[61] used glass beads in a vane rheometer and looked at stick slip behaviour by looking at how the spindle jams and releases again due to the bulk friction of the glass beads. The effect of the fluid viscosity was found to resemble the Stribeck curve since friction is of high importance when the glass beads are moving against each other. Increasing the particle size or decreasing the fluid viscosity there is more stick slip occurring.

2.3.1.4. Predicting Slurry Viscosity

The viscosity of fluids with particles can be predicted since the effect of spherical solids volume concentration on slurry rheology is well documented in the literature. Einstein's equation (Equation (2.5)) can be used to predict the viscosity (η) when there is a small

volume fraction ($\emptyset$) of particles (<0.1) in a Newtonian liquid of viscosity, η_0. B is the Einstein coefficient and is usually 2.5[62].

$$\eta = \eta_0(1 + B\emptyset) \tag{2.5}$$

This is not applicable to mineral slurries since solids contents are usually much higher to give fast and efficient grinding. To enable the prediction of the viscosity for higher solid content slurries, there have been many extensions to Einstein's equation, including Krieger-Dougherty shown in Equation (2.6). The Krieger-Dougherty equation includes the additional parameter $\emptyset_m$, which is the densest possible packing that can be achieved in the system[62]. The exponent constant 2.5 is the intrinsic viscosity of spheres.

$$\eta = \eta_0 \left(1 - \frac{\emptyset}{\emptyset_m}\right)^{-2.5\emptyset_m} \tag{2.6}$$

The main adjustable parameter in these equations is usually the volume fraction of solids, since this has a significant impact on rheology. However, other factors not considered in this equation also have an effect on slurry rheology, including the particle size distribution, particle size and temperature. Smaller particles result in a greater amount of particle-particle interactions and a narrower PSD shape means that the particles do not pack as well and hence have a larger void space and a higher viscosity.

Some empirical models incorporate the particle size and distribution shape[63,64]. Tangsathitkulchai et al.[63] used a cup and bob geometry to investigate the effect of

particle size and distribution on viscosity of coal and quartz slurries with solids contents between 30 and 60 vol%. The Rosin-Rammler size and distribution moduli were used to quantify the particle size and distribution range and develop an empirical equation for predicting room temperature viscosity. In mathematical terms, the Rosin Rammler distribution function (R(X)) is the same as the Weibull distribution used to describe material fatigue and is shown in Equation (2.7)[65], where a is the shape parameter, D is the scale parameter and X is the particle size. This, amongst other functions can be used to describe the particle size distribution[66].

$$\mathrm{R}(X) = e^{(-\frac{X}{D})^{a}} \tag{2.7}$$

He et al.[64] investigated the effect of particle size on the viscosity of limestone slurries, again using the Rosin-Rammler size distribution moduli. When no dispersant was used, the PSD shape and size had an effect on viscosity. However, the effect decreased with increasing dispersant amounts by decreasing the interparticular interactions.

Additionally, most of the equations for predicting viscosity are only applicable at a fixed shear rate. It can be desirable to be able to predict the whole flow curve for non-Newtonian mineral slurries. Shi and Napier-Munn[67] used a calibration algorithm to predict the flow curve of mineral slurries. The slurry temperature, solids concentration and particle size were considered in an empirical correlation. However, the shape of particles and extreme particle sizes (e.g. fines) were not considered.

The particle shape, PSD shape and temperature are all very important during stirred media milling, the solids content is extremely high and a dispersant is used, which makes predicting viscosity a challenge. Direct measurements are more reliable.

2.3.1.5. Apparent Viscosity of Non-Newtonian Fluids

High solids content fluids such as slurries are usually non-Newtonian, which means that the viscosity varies with shear rate, making it challenging to determine which viscosity should be used in calculating Reynolds number. Additionally, in vessels such as stirred media mills the shear rate is not constant throughout the volume. This difference in shear rate also occurs in mixers, leading to the formation of caverns in yield stress fluids, where the shear rate at the wall of the vessel is not sufficient to overcome the fluid's yield stress. Similarly, pseudo-caverns can form in yield stress fluids, where the low shear rate at the wall causes the fluid viscosity to be much higher in this region [68].

2.3.1.5.1. Metzner-Otto Correlation

The Metzner-Otto correlation is commonly used to estimate an apparent viscosity in power law fluids, assuming that the shear rate near the impeller can be characterised by an average shear rate ($\dot{\gamma}_e$), which is proportional to the rotation speed of the impeller (N), as shown in Equation (2.8), where k_s is a function of the impeller geometry[69].

$$\dot{\gamma}_e = k_s N \tag{2.8}$$

Equation (2.8) assumes that k_s is independent of fluid properties[70]. Wu et al.[71] found experimentally that in the laminar regime, an increase in viscosity reduces k_s. However, the effect of Reynolds number on k_s was not quantified. It has also been suggested that the power law index, n, has an effect on k_s, particularly in shear thickening or shear thinning fluids [72,73].

The estimated k_s for common impeller types can be found in literature[74]. However, values outside this range do exist for some impeller types[75]. For new impeller designs, it is possible to estimate k_s either experimentally[76] or using CFD[77].

The Metzner-Otto equation is generally limited to the laminar shear region. The apparent shear rate in the turbulent region would be significantly higher than the average shear rate predicted using the Metzner-Otto equation - it has been instead proposed that in the turbulent region, the shear rate is proportional to the local energy dissipation rate[72].

It is possible to estimate shear rates in mills using modelling or experimental methods to compare with the Metzner-Otto average shear rate. For a ball mill, Shi and Napier-Munn[78] estimated the shear rates using models, considering both cascading and cataracting grinding media in a ball mill. For a tumbling mill, Govender et al.[79] characterised the shear rate profile based on the trajectory fields obtained using PEPT (positron emission particle tracking). However, there remains debate on the most suitable methods for predicting shear rate.

2.3.2. Predicting Power Draw

The power draw of the mill is an important factor to consider and be able to predict since it determines the mill throughput rate for achieving a given product particle size. However, it is a challenge to find the viscosity of slurries in grinding applications because of difficulties in determining the shear rate in the mill[80].

A high power draw will ideally produce the required particle size in less time, however only if the energy is being used efficiently. Predicting the power draw in a stirred media mill is more difficult than in the case of stirred tanks due to the presence of grinding media. There have been numerous attempts of estimating the power draw in stirred media mills based on using the Power number and Reynolds number or computational fluid dynamics (CFD) and discrete element method (DEM) modelling[81]. This section focuses on utilising the Power number and Reynolds number. CFD/DEM is discussed in section 2.4.2.

In stirred tanks, the Power number (Equation (2.9)) and Reynolds number (Equation (2.10)) are commonly used to predict the power draw, where N is the impeller speed, D is the impeller diameter and μ and ρ are the viscosity and density of the fluid respectively.

$$\mathrm{Po} = \frac{P}{\rho N^3 D^5} \tag{2.9}$$

$$Re = \frac{\rho N D^2}{\mu} \tag{2.10}$$

The Reynolds number of a stirred tank is important since the flow regime at which the stirred tank is operating will indicate what the relation between Power number and Reynolds number is, as indicated in Table 2.2.

Table 2.2: Relationship between Power Number and Reynolds number in Different Flow Regimes

Regime	Significance
Laminar	Power number is inversely proportional to Reynolds number
Transitional	No direct correlation between Power and Reynolds numbers
Turbulent	Power number is independent of Reynolds number

In the case of Newtonian fluids, it is simple to calculate the Reynolds number and predict the power draw due to the constant viscosity term. However, for non-Newtonian fluids, the Metzner-Otto correlation can be applied (Section 2.3.1.5.1).

In the case of unbaffled tanks where air is drawn in and there is a significant vortex, the Power number is dependent on the Froude number as well as the Reynolds number[82]. The Froude number (Fr) is defined as the ratio of inertial to gravitational forces (g) and can be calculated from Equation (2.11).

$$Fr = \frac{N^2 D}{g} \tag{2.11}$$

For the case of stirred media mills, the presence of large grinding media beads mean that the power prediction methods used in stirred tanks cannot be directly applied to stirred media mills. In 1987 Weit and Schwedes proposed a method of predicting the

power draw of Newtonian fluids in a stirred media mill by assuming the grinding media are a part of the equipment set-up and hence discounted from the fluid viscosity and density terms, like how baffles are considered in stirred tank scenarios[83]. In this case, since the grinding media were not considered in the correlation, a new Po-Re curve must be formed for each grinding media type or fill volume. In a stirred tank, baffles transform the flow field in order to improve mixing. This therefore has an effect on the power draw of the vessel and hence effects the turbulent Power number of the system. Many baffle parameters such as the number of baffles, length or curvature have an effect on the Power number[84]. Grinding media behave in the same way and hence the amount of and properties of the grinding media affect the Power number.

Kwade[85] developed this further to form one overall equation that considers more parameters associated with milling:

- Filling ratio of grinding media
- Stirrer tip speed
- Slurry viscosity
- Slurry density
- Grinding media diameter
- Stirrer diameter

However, five different flow regimes were identified and the contribution of each of these parameters was highly dependent on the flow regime. The exponent for each of these factors is also dependent on the system geometry[11].

This method has since been adapted to account for the non-Newtonian nature of the fluid with grinding media. Zheng, Harris and Somasundaran[52] estimated the viscosity

of the fluid and grinding media by assuming that shear stress is proportional to torque and applying the Metzner-Otto correlation to estimate shear rate. Although this method does consider an estimate of the viscosity of the slurry and grinding media combination, this viscosity has not been directly measured using a rheometer to test the validity of the assumptions made.

Mannheim[86] used dimensional analysis to find the power draw of stirred media mills. The dimensionless Reynolds number and Froude number were deemed important. However, the Froude number was subsequently neglected in this work since the stirrer was operated slow enough to avoid vortexing caused by introducing air into the suspension.

Other empirical models for predicting power draw exist. However, the range of scenarios for which the empirical correlations are valid is limited by the range of tests that were conducted in forming the empirical formulation. Due to the complex nature of mill motion, it is impossible to cover all combinations of parameter variation[87,88].

2.3.3. Residence Time Distributions (RTDs)

Industrial stirred media mills operate continuously. The amount of time each particle spends inside the mill affects its chances of being involved in numerous grinding media collisions and hence the chances of it being broken. This means that the residence time affects both the size and particle size distribution of the particles in the product feed. The particle size distributions measured from batch grinding tests weighted with

respect to the RTD for the continuous mill can be used to predict the particle size distribution of the product in the continuously operated mill[89–91].

RTDs are commonly analysed and well understood for reactors and stirred tanks. They are measured using different methods based around injecting tracer pulse or introducing a tracer step change and taking samples of the outlet feed at regular intervals and measuring the concentration of a tracer in each sample. Examples of different types of tracers used successfully to measure the RTD in various chemical process operations are summarised in Table 2.3.

Table 2.3: Types of Tracer Utilised in Chemical Processes

Tracer Type and Measurement Method	Key Points	Literature Examples Using this Tracer Type
Dye – a UV spectrometer measures colour intensity	Cannot be used for opaque/coloured fluids.	[92]
Fluorescent dye – a fluorometric detector measures fluorescence	Can be used for opaque fluids.	[93–95]
Solid minerals – XRF measures elemental composition	Large amount of solids required to exceed lower limit of XRF measurements.	[96]
Radioactive isotopes measured using radiation detector	High cost and requires authorisation.	[97–99]
Salts	The background concentration of salts is sometimes high.	[100,101]
Magnetic tracers – anisotropic magnetoresistive sensors measure electrical resistance	Significantly lower cost than radioactive tracer methods.	[102,103]

It is important to note that some of these methods measure the RTD of the solid phase, whilst others measure that of the liquid phase. Where a vessel comprises of a suspension of solids and liquids, such as a stirred media mill, the liquid and solid phases may have different residence times. Stehr[89] compared the RTDs of the solid and liquid phases in a limestone slurry using the following methods:

- Am impulse of salt solution was used to measure the RTD of the liquid phase. After collecting samples, they were centrifuged and the liquid phase was heated to evaporate water and weigh the mass of salt in each sample.
- A step change in solids concentration was used. A radiometric density meter to measure the RTD of the solid phase at the mill outlet.

It was found that the solid and liquid phases had such similar RTDs that they can be considered to be one phase[89]. However, it is possible that the salt tracer used caused flocculation of the solids within the ball mill which could affect the RTD. Chen et al.[104] found that the salinity and dispersant both affect the zeta potential of limestone solutions. Salts cause the thickness of the diffuse layer to decrease, which decreases the range of repulsive forces and reduces the zeta potential, which causes a suspension to coagulate. The zeta potential can be measured - a decrease in zeta potential indicates that flocculation is occurring. However, zeta potential measurements can only be used for very dilute suspensions, which are not similar to those used during milling[105]. As an alternative, rheology could be used to test for flocculation. The viscosity of the limestone slurry with and without the salt added could be compared; a different viscosity is likely to affect the RTD. A high viscosity can

indicate a lower zeta potential due to flocculation[106]. Yianatos et al.[107] also found the solid and liquid residence times to be very similar using a radioactive tracer.

The analysis of RTDs uses several types of distribution function[108]. The most basic plot of raw data is a C-curve, which is a plot of measured concentration vs the time at which the sample was taken. Equation (2.12) shows the concentration function (C(t)) for a perfectly mixed tank, where C_{A0} is the concentration at the start, t is the time and τ_t is the time constant.

$$C(t) = C_{A0} e^{\frac{-t}{\tau_t}} \tag{2.12}$$

C-curves for different scenarios and measurement methods are difficult to compare since they are dependent on the concentration of dye added to the mill and the outlet flowrate. E-curves are a useful analysis tool; by dividing by the area under the C-curve (as shown in Equation (2.13)), the effects of the amount of dye added and the flowrate of the mill are incorporated. The area under the C curve, found using integration, is equal the total mass of tracer inputted to the system.

$$E(t) = \frac{C(t)}{\int_0^\infty C(t)dt} \tag{2.13}$$

The E-curve can be further normalised to create a dimensionless time (θ) (Equation (2.14)) and a dimensionless E-curve (Equation (2.15)), where τ_t is the residence time. This enables a good comparison between mills of different sizes to be made since every ideal CSTR should have the same dimensionless RTD.

$$\theta = \frac{t}{\tau_t} \tag{2.14}$$

$$E(\theta) = \tau_t E(t) \tag{2.15}$$

The mean residence time (t_m) is calculated using Equation (2.16) and should be equal to the time constant, τ_t, if the volume flowrate is constant.

$$t_m = \int_0^\infty tE(t)dt \tag{2.16}$$

As well as changing the operating parameters within the mill, the RTD can be altered by changing other aspects of the milling circuit, such as through the use of cyclones after the mill. Closed circuit operation is common, where large particles are separated and sent through the mill for another pass to increase their chances of being broken to a smaller particle size (See section 2.2.3.6).

Varinot et al.[90] showed experimentally that using multiple passes through the mill but with the same overall residence time results in a narrower particle size distribution compared with that obtained for a single pass. This is hence concluded to be a good, relatively low cost way of controlling the size of particles.

As well as experimental methods of investigating the RTD of a mill, there have been some attempts at modelling the RTDs. Yianatos et al.[107] measured the RTD for an industrial scale Vertimill using a radioactive tracer and found that the large and small tanks in series model described well the RTD of the solid and liquid phase. Frances[109]

found that for a small-scale stirred media mill, the RTD was very close to that of a perfectly mixed reactor. However it was suggested by the authors that this may be due to the small scale of the mill; larger mills would be likely to show a different RTD more similar to the axial dispersion or cells model.

2.3.4. Scale-Up

Scale-up is an important concept in both mixing and milling since it is desirable to conduct lab-scale trials and be able to achieve the same results at larger scales. Many scale-up methods depend on geometric similarity between the vessels at different scales. However, this is not always practical.

In typical fluid mixing applications, scale-up is relatively well understood. It is commonly based on constant tip speed or constant power per unit mass. When scaling up by constant tip speed, the same mixing time is usually obtained. However, this results in the need for a significantly higher motor power, which may not be acceptable. When scaling up by constant power per unit mass, the tip speed decreases greatly which results in an increased mixing time[74]. To assess how well different scale-up methods work in stirred tanks, experimental research has been conducted to assess the mixing progress at different scales. An example of this include using coloured powder to assess the degree of mixedness at different scales[110].

Usually during scale-up, the Reynolds number is significantly larger at large-scale due to the larger impeller diameter term, which means that flow patterns differ greatly at each scale. It has been suggested that the flow patterns at large-scale are more similar

to smaller scale equipment with a lower viscosity fluid (as this has a more similar Reynolds number)[111].

The scale up of stirred media mills is more complex than in the case of stirred tanks because it is important to keep the stress intensity and stress number constant to ensure the resulting particle size distribution is the same[16]. Due to the different equipment sizes, the distribution of stress energies throughout the mill differs. Provided that either the specific energy and stress intensity or the relative number of stress events and stress intensity are kept constant, the achieved particle size distribution after grinding should not change[112]. Purely keeping the specific energy itself constant is not sufficient. Mazzinghy et al.[113] also showed that keeping just the energy input the same does not give the same particle size with scale-up and proposed a method of considering the different energy efficiencies of the different scale mills to consider the difference in energy dissipation between units.

Scale-up based on a constant Froude number has been suggested for some mixing processing applications, particularly for granulation[114,115]. However, scale-up based on using the Froude number often results in over-mixing since keeping the Froude number constant between the two scales gives increased power per unit volume[116]. In mixing applications, overmixing is not a significant issue in terms of product quality, but energy is wasted. This is of greater importance in stirred media mills, where if overgrinding occurs the particle size may be too small for the application and furthermore, a large amount of energy is being wasted. Since large-scale stirred media

mills are typically operated continuously, rigorous control methods and the use of classification loops can prevent overgrinding.

2.4. Flow Visualisation Methods

Flow visualisation is useful for gaining further understanding of how stirred media mills operate. Most works use positron emission particle tracking (PEPT) to do this[33,117,118]. There have been a small number of attempts to use laser techniques such as particle image velocimetry (PIV)[119,120]. However, the application of this technique to milling is more complex and requires more assumptions to be made due to the requirement for a transparent system.

For other Chemical Engineering applications such as mixing and pipe flow, techniques such as electrical resistance tomography (ERT)[121,122], planar laser induced fluorescence (PLIF)[123–125] and high speed imaging (HSI) have been successfully applied to look at motion in vessels. These techniques have had little to no published research relating to stirred media mills[126].

2.4.1. Positron Emission Particle Tracking (PEPT)

Positron emission particle tracking (PEPT) is a technique based on medical positron emission tomography (PET) used to look at flow patterns in opaque systems by irradiating a tracer particle[127]. The use of PEPT for engineering applications was described in 1993 by Parker et al.[128]. Further details about the methods associated with this technique can be found in Methods section 3.3.3.3.

Significant research has been conducted to investigate algorithms and processing methods to convert the raw PEPT data to tracer locations[129–131]. There are recent attempts at developing new algorithms to track multiple particles simultaneously[130,132,133]. However, distinguishing between particles remains a key difficulty of this.

To use PEPT in stirred media mills, a grinding media bead must be irradiated. If a particle being ground were irradiated, there would be problems when the particle breaks since the whole vessel would become irradiated. Hence, it is not possible to obtain information about the flow of the slurry and shear rates within the slurry using PEPT.

Recent published works attempt to visualise the flow inside stirred media mills and determine the main flow regions[118]. This has been expanded on by determining how changes in operating parameters and configuration affect the flow patterns and distribution of kinetic energy within the mill[117]. The stresses exerted by the grinding media can be determined based on their velocities (found using PEPT) and compared with the strength of the particles being ground. Skuse[32] used PEPT analysis, but focused on using velocities to calculate stresses inside the mill and determine where stresses are high enough to break calcium carbonate particles. The stress required to break a single calcium carbonate particle was found using micromanipulation, but this varied due to the presence of flaws and cracks in particles, which greatly reduce their strength. It was found that stresses were highest in the impeller region but that process

parameters such as impeller speed, slurry loading and calcium carbonate particle size had a big effect on the stress distribution.

The distribution of kinetic energy throughout the mill is also deemed important and has been investigated by looking at velocities and occupancies in different regions of the mill. The distribution of kinetic energy was found to depend greatly on the impeller tip speed[134].

2.4.2. DEM and CFD Modelling

The numerical modelling of stirred media mills is useful for looking at the motion of the slurry and grinding media at high resolution. These numerical models can then be validated using experimental results, such as those obtained using PEPT. Discrete element method (DEM) models can be used to model systems based on Newton's second law of motion and the force-displacement law[135]. There have been numerous attempts to simulate the motion of grinding media in a stirred media mills using this technique[136–138]. However, these DEM models assume the milling is dry milling. To incorporate the impact of the slurry flow, the DEM can be coupled with computational fluid dynamics (CFD), which uses the locally averaged Navier-Stokes equation to simulate fluid flow[139]. Although these models provide valuable information about stirred mill motion[140,141], they should ideally be backed up by experimental data to determine the impact of assumptions made in the models.

Jayasundara et al.[142] compared CFD/DEM simulations with PEPT data for an Isamill™ and found the results to be in reasonable agreement, with key differences

attributed to the lower resolution of PEPT data compared to simulation data and simplifications made in the set-up of the model. It was deemed that the CFD/DEM model is a valid method of gaining a more detailed understanding of motion in stirred media mills. Yang[143] also compared PEPT results with DEM results and found them to be in general close agreement. The main discrepancy lies in the region close to the impeller, since grinding media beads here are not at steady state and do not move in a stable or predictable pattern.

2.5. Summary of Literature Review

Stirred media mills are similar to stirred tanks but due to key differences such as the large amount of grinding media beads mean that correlations applied to stirred tanks are not directly applicable to stirred media mills. Further understanding of rheology and factors affecting the flow patterns and power draw in stirred media mills is required. Scale-up is complex due to the importance of the stress energy and the stress number. Current scale-up methods suggested are based on combining a lab-scale batch PSD with an RTD to predict a continuous large-scale PSD.

3. MATERIALS AND METHODS

3.1. Introduction

This section describes the materials and methods used for batch lab grinding, the characterisation of calcium carbonate slurries and the monitoring of grinding media motion. Additionally, methods associated with operating the lab-scale mill continuously and determining RTDs are defined as well as methods of operation for mills at different scales.

3.2. Materials

Calcium carbonate was ground in a lab-scale stirred media mill in slurry form. Typically 72 wt% calcium carbonate slurries are milled, with the remainder of the slurry comprising of water and a dispersant. A range of grinding media types were used to break up the calcium carbonate particles. In some cases, glycerol-water solutions were used as a mimic fluid, in place of the slurry in the mill, due to their Newtonian behaviour.

3.2.1. Calcium Carbonate

Calcium carbonate is a naturally occurring material commonly found as chalk, limestone or marble. For this project, Imercarb 10 was supplied by Imerys. This product is sold by Imerys to industrial customers, including paint and coating industries. It is the marble form of calcium carbonate and has been ground by Imerys to have a d_{50} of 13 μm with a normal distribution. This is tested by Imerys and deviations from this are small.

3.2.2. Dispersant

To aid the dispersion of calcium carbonate particles, reduce aggregation and reduce the viscosity of the slurry, Sokalan NR-2555 was used, which is a BASF dispersant. It is a 50% neutralised sodium polyacrylate with an activity of 45% and is commonly used for grinding fine calcium carbonate at several Imerys sites. Sodium polyacrylate is a sodium salt of polyacrylic acid. The carboxylic groups in the main chain are negatively charged – these groups are neutralised by sodium ions. The sodium polyacrylate dispersants stabilise by electrostatic repulsions, imparting negative charge to the calcium carbonate particles, as well as steric repulsions[144]. For slurries used in this work, an active dispersant content of 0.8% of the calcium carbonate mass is sufficient to reduce viscosity and prevent aggregation.

Due to supply and availability, a different dispersant, Rheosperse 5074, was used for scale-up experiments in Chapter 6 with a dispersant content of 0.4% of the calcium carbonate mass. Rheosperse 5074 is a polycarboxylate in aqueous solution. The different dispersant types affect the rheology of the slurry and hence may affect grinding performance. Different dispersants have different optimum concentrations.

3.2.3. Grinding Media

Grinding media were supplied by Imerys. In this thesis, grinding media amounts of 35-52 vol% were used (where vol% is the % of the fill volume occupied by grinding media); lower amounts lead to extreme vortexing and overflowing whilst higher amounts cause excessively high power draw at high speeds. Key grinding media properties are outlined in Table 3.1.

Table 3.1: Grinding Media Types

Brand Name	Material	Density (g cm^{-3})	Size Range (mm)
Carbolite (16-20)	Mullite	2.7	0.8 – 1.2
Carbolite (08-14)	Mullite	2.7	1.4 – 2.4
HD Bitossi	Aluminium Oxide	3.6	0.75 – 1.25

3.2.4. Glycerol

Glycerol –water solutions of various concentrations were used in the mill. Glycerol tech was supplied by SLS (Scientific Laboratory Supplies). Glycerol is a Newtonian fluid and by diluting the glycerol with water, the viscosity can be selected to be within the range of viscosities encountered during the milling of calcium carbonate slurries. The viscosity of glycerol is also highly temperature dependent[145].

3.2.5. SiLi Beads

To make the glycerol-water solutions increasingly representative of calcium carbonate slurries, different amounts of 0-50 μm SiLi beads supplied by Sigmund Linder and consisting mainly of SiO_2 were added.

3.3. Methods

Calcium carbonate slurries were ground in a stirred media mill, both batch-wise and semi-continuously. The particle size distribution, tribology and viscosity of the resulting slurries were measured as well as the residence time distribution (RTD) for continuous milling operations. This section details the equipment and methods used to do this. Smaller and larger scale milling operations used for scale-up are also described.

3.3.1. Milling Calcium Carbonate

A lab-scale Imerys stirred media mill produced by GT Jones (shown in Figure 3.1) was used for the fine grinding of calcium carbonate. Dimensions are detailed in Figure 3.2.

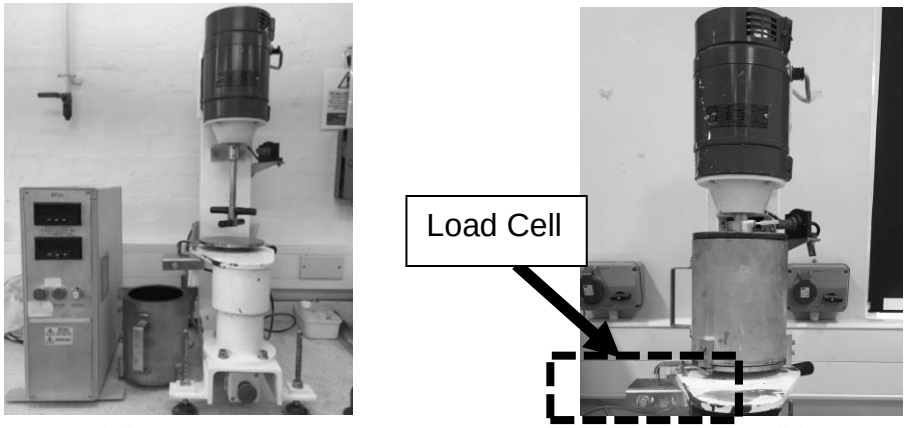

(a) **(b)**

Figure 3.1: Lab-Scale Stirred Media Mill (a) Inside Vessel Configuration (b) Sealed vessel

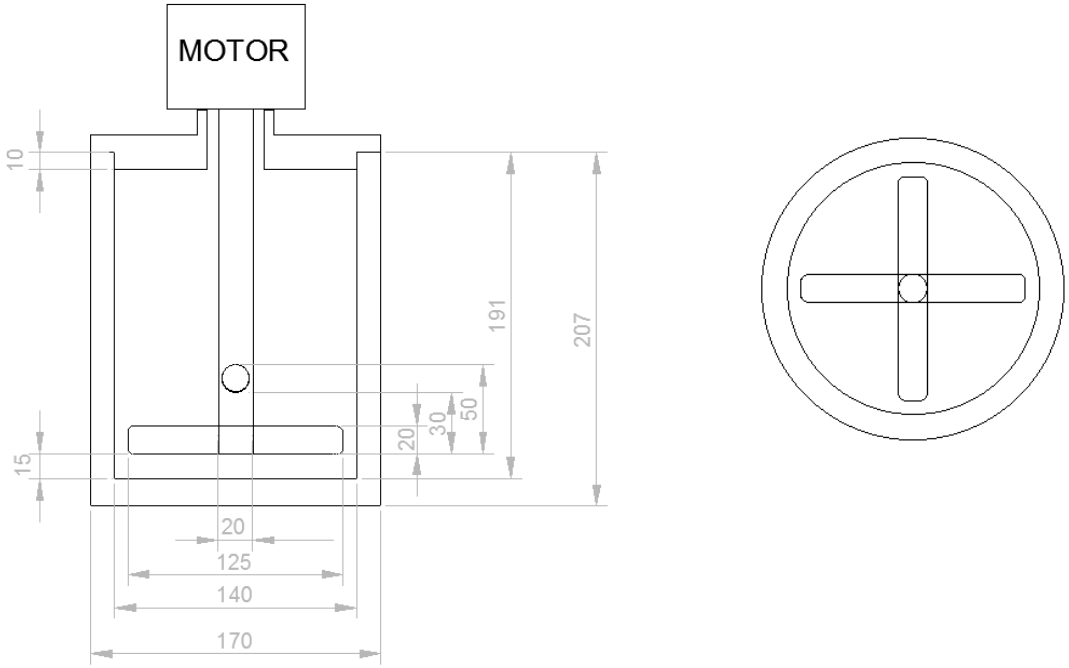

(a) **(b)**

Figure 3.2: Diagram of Lab-Scale Stirred Media Mill (a) front view, (b) top down view

`

The milling vessel is lined with polyurethane for temperature and wear resistance and is equipped with a 0.55 kW motor. The calibration of the impeller speed and load cell were tested - a tachometer was used to confirm the calibration of the impeller speed and known masses were used to determine the linearity and offset of the load cell for use in calibration. A graph of the voltage signal to power conversion for the Datalogger can be found in Appendix A (section 10.1).

Equations (3.1) and (3.2) were used to calculate the associated power draw (P) and cumulative energy consumption (E) of the mill from the torque (T) measured by the load cell (shown in Figure 3.1) and the impeller speed (N). The temperature of the mill was monitored and recorded using a k-type thermocouple with a Picolog TC-08.

$$P = \frac{2\pi NT}{60} \quad (3.1)$$

$$E = \int_0^{t_f} P \, dt \quad (3.2)$$

3.3.1.1. Batch Operation

The dry, unmilled calcium carbonate powder and grinding media were mixed by hand in a sealed bag before being added to the milling vessel. The water and dispersant were then added before the lid was placed on the unit and the mill was turned on. It was confirmed that the order of material addition has no impact on particle sizes achieved. The k-type thermocouple was attached to a Picolog TC-08 and inserted through a small opening in the mill lid. The power draw measured from the load cell was recorded using Picolog. Normal grinding conditions are summarised in Table 3.2.

However, impeller speeds from 200 – 1500 rpm were utilised in experiments – this covers the entire operable range of the unit.

Table 3.2: Normal Operating Parameters Used During Grinding

Parameter	Normal Value
Volume Concentration of Media	52 %
Solids wt% in Slurry	72 %
Dispersant Dose	0.017 g / g $CaCO_3$
Impeller speed	1500 rpm / 9.8 m s^{-1}
Grinding media volume	616 ml
Slurry volume	568 ml

3.3.1.1.1. Recording Power Draw

The power draw of the mill was measured at different impeller speeds at different stages of grinding. To measure the power draw at the start of grinding (0 kWh/tonne), the mill was operated at 1500 rpm for 30 seconds to reach a steady, mixed state. The impeller speed was then systematically varied to record the power draw at each speed for 15 seconds, or until the power became constant if this took longer than 15 seconds. To find the power draw at different stages of grinding (after different energy input), the mill was operated until the desired energy input was reached. Once this happened, the impeller speed was systematically varied to record the power draw at each speed, using the same procedure as at 0 kWh/tonne.

3.3.1.1.2. Taking Slurry Samples

To take ground samples of slurry from the mill for particle size measurement, the mill motor was temporarily turned off, a 1 – 2 ml sample was drawn up in a syringe and

then the mill motor was promptly restarted. By limiting the sample size to 1-2 ml, slurry removal had minimal impact on the overall mill composition. Where larger samples were required for viscosity measurements (35-50 ml per measurement), the mill run was aborted immediately after sample taking and a new mill run was conducted for each slurry sample required. This prevents the reduced amount of slurry in the mill from influencing the grinding behaviour.

3.3.1.2. Continuous Milling

For continuous operation of the lab-scale mill, a steady state flowrate of 1 ml s^{-1} slurry was used; this is equivalent to an average residence time of 10 minutes or an average energy input of approximately 55 kWh/tonne. An 850 μm mesh fixed to the mill outlet hole allowed fluids to flow out of the mill whilst keeping the grinding media contained. The outlet tubing was elevated to enable some control of the level inside the mill. The slurry output was sent to a storage container and was not recirculated back to the mill.

3.3.1.3. Using a Dye Tracer to Determine the RTD

To find the liquid phase residence time, a dye tracer was used. This method could potentially be used with calcium carbonate slurries by centrifuging the slurry and die mixture exiting the mill. However, the amount of slurry required to give a large enough liquid and dye sample to measure the dye concentration is large enough to result in the RTD resolution being poor due to the high solids content of the slurries. To overcome this, glycerol-water solutions in a similar viscosity range to the slurries were used in place of the slurry. The set-up shown in Figure 3.3 was used, where a water-soluble Nigrosin dye supplied by Alfa Aesar was used as the tracer.

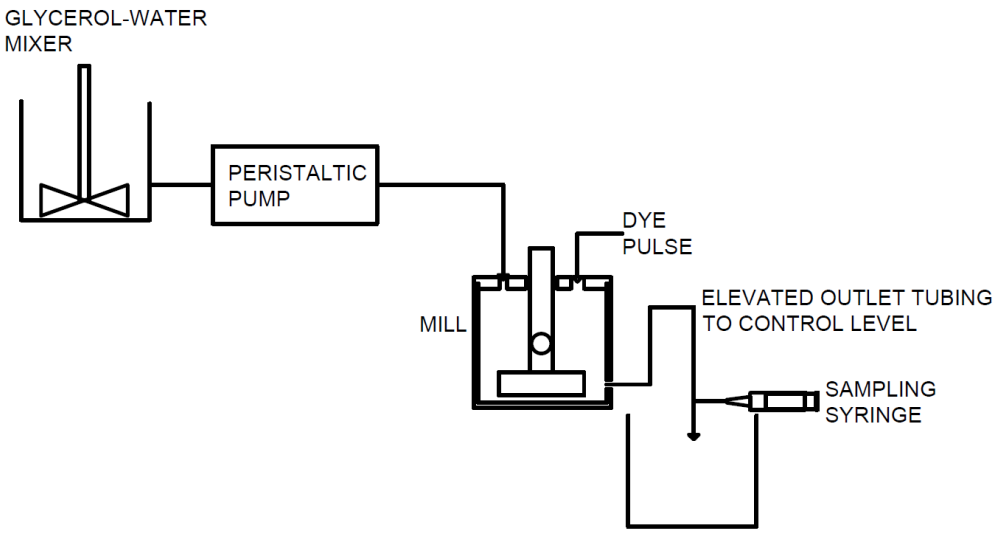

Figure 3.3: Continuous Set-Up for Glycerol RTD

Only 71% glycerol-water solutions were used. With higher glycerol concentrations, the glycerol exited the mill significantly more slowly due to not flowing easily through the mesh designed to stop the grinding media flowing out of the mill, which caused operational problems.

Samples were taken from the outflow of the mill and the amount of light passing through them was measured using, Ultraviolet Visible Spectroscopy (UV/Vis), as is described in section 3.3.1.3.1. To obtain experimental repeats, the mill was allowed to reach steady state, a pulse of dye was added to the mill and samples were taken for UV/vis analysis. After five residence times (and when the glycerol-water solution had returned to being transparent), a new zero measurement was taken and a second pulse was added for new samples to be taken and analysed. This was subsequently repeated for a third pulse of dye.

3.3.1.3.1. Ultraviolet Visible Spectroscopy (UV/Vis)

To measure the concentration of dye in glycerol at the outlet of the mill, the syringed 2 ml samples were added to a cuvette before the concentration of dye was measured in a Jenway 6300 spectrophotometer, which measures the absorbance of light at a defined wavelength. The Beer-Lambert law, Equation (3.3), describes the linear relationship between absorbance (A) and concentration (c), where $\in$ is the molar absorption coefficient and I is the path length of the light[146].

$$Abs = \in Ic \tag{3.3}$$

Equation (3.3) is not valid at high concentrations, since a measurable amount of light needs to pass through the sample to give a valid reading. To overcome this, where the dye concentrations were high, samples were diluted using a known amount of glycerol and subsequently re-measured.

Within the Jenway 6300 Spectrophotometer, there is a halogen light and a grating to separate this light into different wavelengths. This light then passes through the sample. The light that has passed through the sample enters a collection lens on the other side of the sample and is measured by a photo-diode signal detector to give a transmittance (Tr), which can be related to absorbance (abs) using Equation (3.4).

$$Abs = -\log(Tr) \tag{3.4}$$

A wavelength of 900 nm was deemed acceptable for the range of dye concentrations used in measuring the RTD. A calibration line was produced using known concentrations of dye in glycerol to enable the Spectrophotometer's absorbance

reading to be related to an actual dye concentration using Equation (3.3). This can be found in Appendix B (section 10.2).

3.3.1.4. Using a Titanium Dioxide Tracer to Determine the RTD

To measure the solid RTD, a titanium dioxide tracer was used and the concentration relative to the calcium carbonate amount was measured using X-Ray Fluorescence, described in section 3.3.1.4.1.

The continuous set-up used with glycerol-water solutions is not suitable for use with calcium carbonate slurries. Before the slurries have been milled, the particles settle within the pump, causing unsteady flowrates. Hence, a peristaltic pump is not suitable for these slurries. Instead of pumping the slurry, the liquid and solid feed were fed separately to the mill using a peristaltic pump and powder feeder respectively, as shown in Figure 3.4.

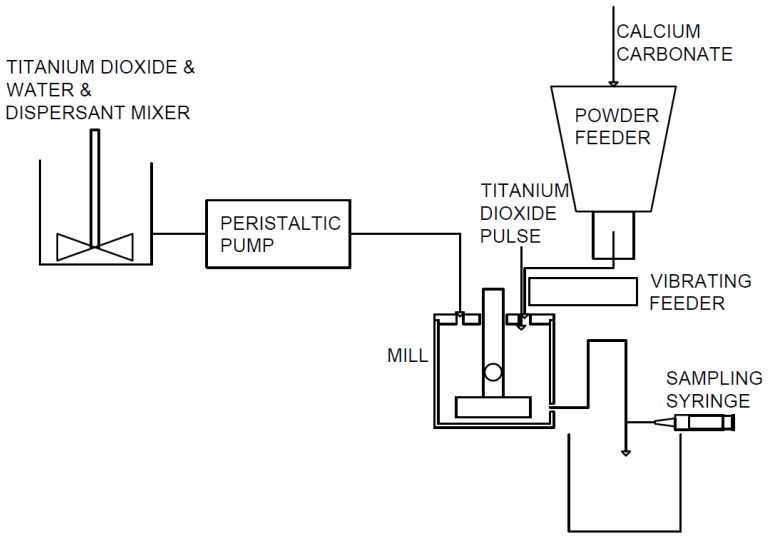

Figure 3.4: Continuous Set-Up for Calcium Carbonate RTD

The water was pre-mixed with the dispersant and a background amount of titanium dioxide before being added to the mill. The background amount of titanium dioxide (0.01 g TiO_2 / g $CaCO_3$) is required to ensure the amount of titanium dioxide in the outflow was sufficiently above the lower limit of detection of the XRF instrument (See section 3.3.1.4.1).

3.3.1.4.1. X-Ray Fluorescence (XRF)

XRF can be used to determine the elemental composition of materials. The sample is bombarded with X-Rays, causing it to ionise. If the radiation energy is high enough, the atom becomes unstable as an inner electron is displaced. An outer electron then replaces this electron and energy is released in this binding. The amount of energy released (known as the fluorescence) when the electron moves between orbitals is characteristic of a particular element, enabling the element to be identified and the relative amount of it to be determined[147].

XRF measurements were conducted using a Niton XL3t handheld analyser, which uses energy dispersive spectrometry. The handheld device is equipped with an X-Ray generator, a solid-state X-Ray detector and a signal processor. In the detector, photons ionise the atoms and produce electrical pulses proportional to the amount of energy detected. The pulses are amplified so that a computer within the XRF unit can determine the amounts of each element present in the sample.

The samples for XRF must be in the form of dry, small particles. The wet slurry samples from the mill were therefore dried in aluminium dishes and subsequently broken up

manually. The resulting powder was added to the XRF sample containers and placed into the device measurement chamber for the elemental composition to be determined. Samples of known concentrations were measured initially to ensure the calibration of the equipment and determine the lower measurable limit.

3.3.1.5. Small-Scale and Large-Scale Milling

To compare mills at different scales, three equipment scales were utilised:

- A 3D printed pin impeller (the same as the lab impeller) in a 50 mm rheometer cup, operated using the rheometer discussed in section 3.3.1.5.1.
- Lab-scale milling discussed in section 3.3.1
- Pilot-scale milling conducted at Imerys pilot plant in Liege, Belgium by Imerys pilot plant manager Joseph Cambisano discussed in section 3.3.1.5.2.

3.3.1.5.1. Smaller Scale Experiments – Rheometer-Scale

To consider a smaller scale of operation, which is fast and easy to set up and operate, a smaller impeller was created and used in conjunction with the Trios Discovery HR-1 rheometer. Due to the rheometer set-up limitations and difficulties in process control at such a small scale, experiments at this scale were conducted as batch experiments. The impeller was designed in Autocad and 3D printed in a tough resin and is shown in Figure 3.5 with the lab-scale impeller.

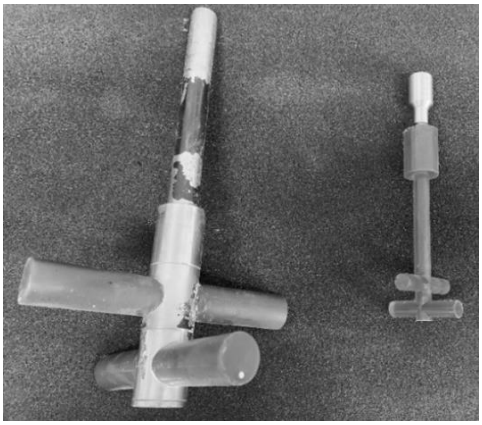

Figure 3.5: Lab-Scale Impeller (left) and 3D Printed Impeller (right)

The rheometer impeller was designed to be approximately 17 times smaller than the lab impeller by volume. It should be noted that because of some of the fixed constraints of the rheometer set-up, there were some deviations from geometric similarity, including the size of the gap between the bottom of the vessel and the impeller and the height to width ratio of the vessel. Table 3.3 shows some of these key geometry values for comparison.

Table 3.3: Geometries of Rheometer and Lab-Scale Mill Set-Ups

	Rheometer Scale	Lab Scale	Lab Scale/ Rheometer Scale
Vessel Diameter (mm)	50	140	2.8
Vessel Height (mm)	80	181	2.3
Impeller Diameter (mm)	42	125	2.9
Impeller Pin Diameter (mm)	9	20	2.2
Shaft Diameter (mm)	9	20	2.2
Clearance from Base (mm)	5.4	15	2.8
Vessel Volume (ml)	157	2800	17.8
Fill Volume (ml)	76	1184	15.6

Due to it being a custom geometry, the relationship between the impeller geometry and the shear stress and shear rate are unknown, so it is not possible to find the viscosity directly. However, it is possible to measure the rotational speed of the impeller and the torque, which can be compared with data for the vane rheometer and data from the lab-scale and pilot-scale. To find the torque at a range of impeller speeds in the rheometer, peak holds were conducted by holding several different impeller speeds for 20 seconds. 20 seconds was deemed sufficient because there was little variation of torque with time after the first few seconds.

3.3.1.5.2. Larger Scale Experiments – Pilot-Scale

Due to Covid travel restrictions, pilot plant trials were conducted at Imerys pilot plant in Liege by Joseph Cambisano.

The pilot plant mill is comprised of a 0.8 m diameter octagonal vessel equipped with baffles and three layers of six-pin impellers. A Historian datalogger was used to monitor processing conditions, including the motor power and the mass of material in the mill (as the mill sits on a load cell). It should be noted that the mass measured by the load cell does not consider the thrust of the impeller, which may affect the reliability of the measurements.

The mill was operated continuously - feed material was constantly added to the top of the mill and there was one open outlet at the bottom of the mill for slurry to exit. This outlet was covered by a mesh to keep the grinding media beads within the mill. The temperature and flowrate of the slurry exiting the mill were measured in a flowmeter.

The flowrate out of the mill is predominantly dependent on a level control system. However, when the impeller speed in the mill is reduced and the materials are more densely packed in the mill, the flowrate exiting the mill reduces causing the level in the mill to rise and the ratio of slurry to grinding media to change. This was considered when results were analysed in Chapter 6.

The pilot mill was operated for 20 minutes at each rotational speed to allow a new steady state to be reached. In some cases at the slowest impeller speeds, the level of the mill rose to a critical level due to the slurry flowrate decreasing, so the trial was stopped.

3.3.2. Slurry and Grinding Media Characterisation Methods

Methods used to characterise the calcium carbonate particles and slurry are detailed in this section.

3.3.2.1. Particle Size Measurement – Wet Laser Diffraction

The particle size distribution of calcium carbonate was measured using the Mastersizer 2000, which uses wet laser diffraction. The angle and intensity of scattered light is measured and Mie theory is used to determine the particle size distribution, where larger particles scatter light at smaller angles than smaller particles. At a given angle, the greater the intensity of light, the more particles of that size there are. To increase resolution, the Mastersizer 2000 uses both red and blue light wavelengths. Blue light has a shorter wavelength and is therefore used for measuring smaller particles, whilst longer wavelength red light is used for measuring the larger particles.

To calculate the particle size using Mie theory, the refractive index and absorption are required. Calcite has a refractive index of 1.5 and an absorption of 0.01 is generally suitable for milled materials[148].

Particle sizes presented by the Mastersizer are the volume equivalent sphere diameter (d_v). The volume equivalent sphere diameter, d_v, is the diameter of a sphere that would have the same volume as the particle, V_p, and is shown in Equation (3.5).

$$d_v = \left(\frac{6V_p}{\pi}\right)^{\frac{1}{3}} \tag{3.5}$$

The calcium carbonate slurry sample was diluted by adding 1-2 drops to approximately 7 ml water for ease of controlling the amount added to the Mastersizer. To prevent multiple scatterings whilst ensuring there are enough particles to give a representative measurement, tests were conducted to determine a suitable target obscuration. A suitable target obscuration was found to be 1.5 – 3% by measuring the same sample at a range of obscuration values. Within this range, adjusting the obscuration had no effect on the measured PSD. With higher obscuration, the PSD differed due to multiple scatterings, where the light from the laser is scattered by more than one particle before being detected, hence leading to a larger contact angle and an underestimated particle size. Due to the small particle size, there is good sample representation with a small sample size. However, to ensure the measurement signal is above the background signal, only laser obscuration values greater than 1.5% were used.

A stirrer speed of 1500 rpm was used to disperse the sample through the entire solution passing through the Mastersizer. This speed is sufficient for dispersion whilst not

causing any new particle breakage. Each sample added to the Mastersizer was measured three times. The average of the three measurements was used for plotting and data analysis. As the errors are small, error bars are omitted for clarity.

3.3.2.2. Viscosity Measurement – Rotational Rheometry

Rotational rheometers control and systematically vary either shear rate or shear stress. They are equipped with air bearings, which allow very small changes to shear rate and shear stress to be made. Non-Newtonian fluids have an apparent viscosity, μ_{app}, which can be determined from the shear rate ($\dot{\gamma}$) and shear stress (τ) using Equation (3.6).

$$\mu_{app} = \frac{\tau}{\dot{\gamma}} \tag{3.6}$$

Measurements were made using a TA Instruments Discovery HR1 Rheometer with a 4 blade vane geometry with a 28 mm diameter, shown in Figure 3.6.

Figure 3.6: Vane Rheometer Geometry with Trios Rheometer

The measurement cup used to measure the viscosity of the calcium carbonate slurries has a diameter of 30 mm. In order to measure the combined viscosity of the calcium slurry with the grinding media, a larger gap is required between the vane and the wall to allow the grinding media to fit through, so a cup with a diameter of 50 mm was used in this case.

For viscosity measurements, a relatively large sample was used (35 ml for 30 mm cup or 100 ml for 50 mm diameter cup) to ensure the entirety of the vane is covered. For measurements conducted at elevated temperatures, a solvent trap was used to minimise the drying out of the slurry.

Flow ramps were conducted between 1 – 400 s^{-1}. At higher shear rates, vortexing occurs. An equilibrium time of 10 seconds was deemed suitable by conducting peak hold tests. To ensure the particles were well mixed and homogeneously distributed, the 0 kWh/tonne (unmilled) samples were mixed in the mill with grinding media for 30 seconds and all samples were further mixed by hand immediately before measurement. This hand mixing was to ensure there were no settled particles at the bottom of the container.

3.3.2.3. Fluid Friction Measurement - Tribology

To investigate the friction coefficient of the slurries and glycerol-water solutions, a PCS Instruments mini-traction machine (MTM) was used (shown in Figure 3.7).

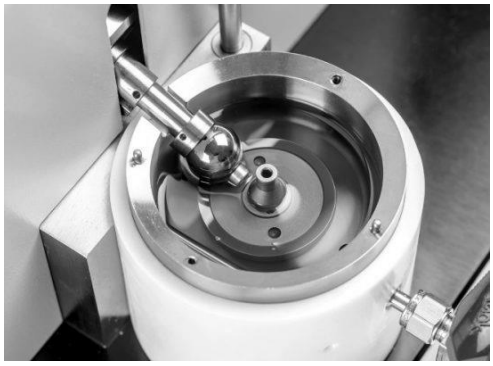

Figure 3.7: PCS Instruments Mini Traction Machine with Stainless Steel Ball and Plate[149]

The fluid was placed onto the stainless steel plate and the stainless steel ball rotates around the plate at a constant force of 3 N, sweeping a range of entrainment speeds to produce a Stribeck curve. The frictional test results are highly dependent on the surfaces used, so the surfaces were regularly inspected for scratches or damage and replaced. For each fluid sample, six consecutive speed sweeps were performed, where the entrainment speed was swept up and down alternatively.

3.3.3. Flow Visualisation

To visualise flow patterns within the mill, Positron Emission Particle Tracking (PEPT) and High Speed Imaging (HSI) were used and compared.

3.3.3.1. High Speed Imaging (HSI)

To observe the motion of grinding media beads at the wall of the vessel, a high-speed camera (Photron Fastcam SA3) was used to capture sequential images of the grinding media at the wall of a custom made transparent Perspex vessel using the set-up indicated in Figure 3.8.

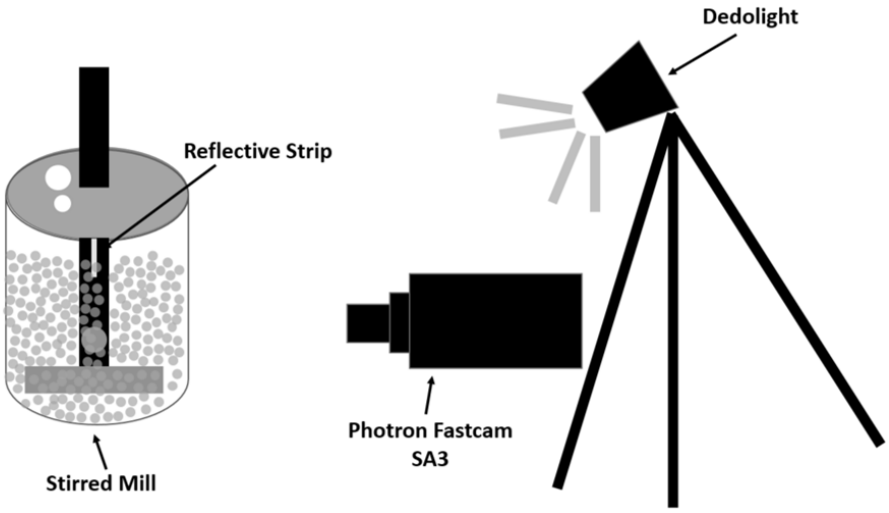

Figure 3.8: Diagram of High Speed Camera Set-Up

The grinding media bead velocities are highly dependent on the position of the impeller; the grinding media moves faster when the impeller directly passes. To be able to determine the image frame at which the top impeller directly passes perpendicular to the section being analysed, a reflective tape marker was added to the impeller shaft at this position whilst black tape was placed around the rest of the shaft. When the light marker is observed, it indicates that in this frame, the top impeller blade was perpendicular to the camera.

Images were captured at a rate of 2000 fps and data was subsequently analysed using PIVLab software, which is a Matlab package[150]. The captured images only show motion in the 'U' and 'V' directions respectively (See Figure 3.9 for direction definitions and note that the origin is at the vessel wall). CLAHE (contrast-limited adaptive histogram equilisation) was applied within PIVLab to enhance the contrast of the images and make the beads more visible[150].

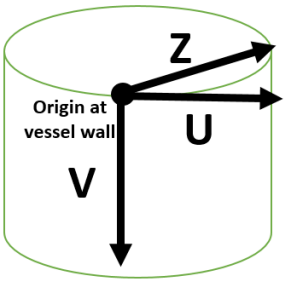

Figure 3.9: 'U', 'V' and 'Z' Directions

The vessel is cylindrical, which means that data moving along the wall will also move in the 'Z' direction. Hence, when data was analysed, only the strip of data from the centre of the vessel was used - a mask was applied to the data to ensure only the region of interest was analysed. The width of this strip was selected to be large enough that the grinding media do not move out of the strip between two frames but small enough that 'Z' motion is considered negligible. The data was analysed in two passes, with the size of the interrogation window getting smaller for each pass (passes are illustrated in Figure 3.10).

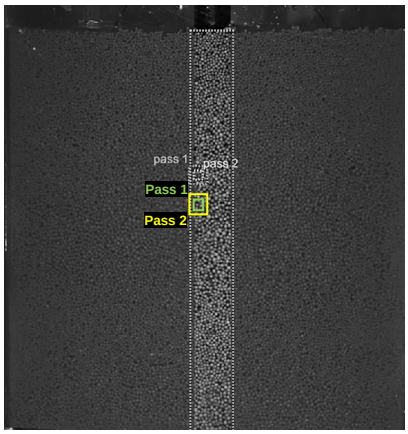

Figure 3.10: Application of Mask and Interrogation Windows to High Speed Camera Data

The first pass (32 pixel interrogation window) calculates displacement reliably and gives robust calculations and less signal to noise ratio due to the larger window size,

whilst the second pass (16 pixel interrogation window) gives better vector resolution[150].

To calibrate the velocities, converting from pixel s^{-1} to m s^{-1}, calibration images with known distances were utilised. To post-process the data, filters were applied to remove any outlier velocities. Within PIVLab, these outliers were replaced with interpolated values. Processed velocity data was extracted from PIVlab and subsequently plotted using Matlab.

3.3.3.2. Endoscopic Camera

To observe the vortex inside the vessel, a Sumgott IP68 endoscopic camera equipped with eight LED lights surrounding the camera was placed inside the mill and a video of the vortex was recorded for a range of conditions and impeller speeds – the set-up can be seen in Figure 3.11.

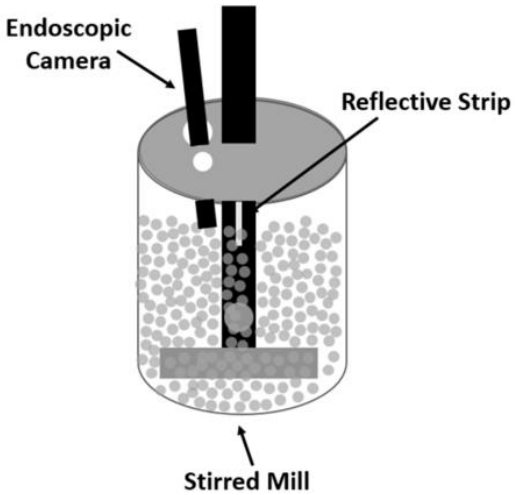

Figure 3.11: Diagram of Endoscopic Camera Set-Up

The videos obtained using the set-up in Figure 3.11 were used for qualitative data analysis to help explain the motion throughout the vessel rather than for any form of quantitative data analysis.

3.3.3.3. Positron Emission Particle Tracking (PEPT)

Grinding media beads were directly irradiated using the University of Birmingham's MC40 cyclotron, where a ^{3}He beam is accelerated at energy high enough to convert ^{16}O occurring within the tracer to radioactive ^{18}F[151]. For each experimental run, a radioactively labelled grinding media bead's motion was tracked throughout the vessel.

The mill was operated as described in section 3.3.1.1. The radioactive grinding media tracer was added to the mill, which was placed between the detectors, as illustrated in Figure 3.12, and allowed to run for 20 minutes for each set-up to ensure the tracer had sufficient time to travel in all regions of the mill.

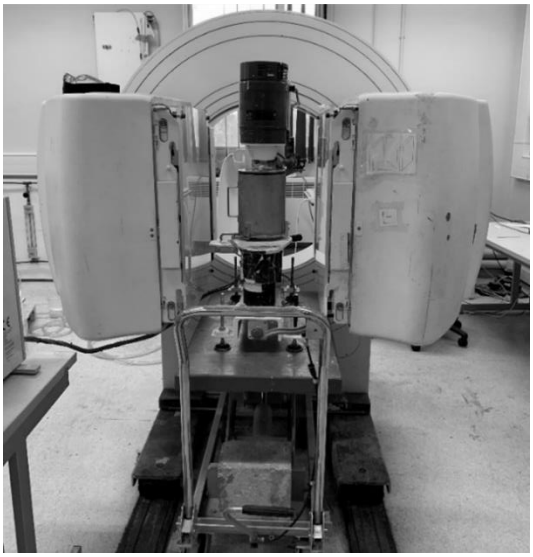

Figure 3.12: Stirred Media Mill Between Detectors

The detector is an ADAC forte gamma camera, which detects up to 100,000 gamma rays per second. As ^{18}F decays, positrons are emitted which collide with electrons, releasing anti-parallel gamma rays. The gamma rays are simultaneously detected by two cameras so that lines of response can be plotted and used to determine the location of the tracer particle[151]. This requires the use of algorithms, which triangulate the position of the tracer from the intersection of many lines of response, as illustrated in Figure 3.13.

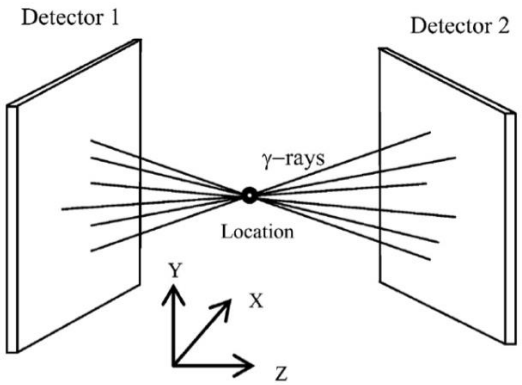

Figure 3.13: Illustration of Lines of Response for a Single Particle[151]

In this thesis, the Birmingham method[152] was used to process the data. Each tracer location is determined from a defined number of events (N_{events}) and some of the data is discarded as corrupted paths (e.g. due to scattered photons or random coincidences) - f_{opt} is the percentage of data that is remaining after events are discarded. N_{events} is an important parameter - as the tracer is constantly moving, fast moving tracers move further in fewer events, meaning that a smaller N_{events} is required for faster moving tracers to give a more accurate location.

It was assumed that the optimum f_{opt} was the same for each experiment with the same grinding media type, since it is predominantly dependent on the system surrounding

the tracer. To find f_{opt} for each grinding media type, the standard deviation of the errors was minimised using a trial and error approach proposed by Chiti[131].

Once the tracer locations at given times were determined using the Birmingham Method in the 'Track' programme, Matlab was used to process and plot the data. Due to the cylindrical geometry of the stirred media mill, Cartesian co-ordinates were converted into polar co-ordinates (defined in Figure 3.14), enabling the flow fields of a radial slice of the mill to be observed.

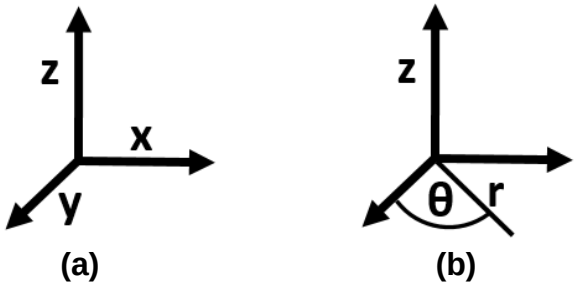

Figure 3.14: (a) Cartesian Co-Ordinate System (b) Cylindrical Co-Ordinate System

Some of the locations may be corrupt and lie apart from other locations. This data was removed using a Matlab filtering function developed by Chiti[131]. In this function, a histogram of distances between each location is plotted and from this, an acceptable distance can be determined. Any points with a larger distance than this are removed and classified as corrupt data[131].

To account for the high speed of the grinding media bead, a second Matlab function, also developed by Chiti[131], was applied to the data. This function assesses the distance between two points and applies linear interpolation between the points if the

distance is larger than a specified value related to the size of each cell to ensure the grinding media bead is accounted for in each cell that it passes through.

The locations of the tracer at a given time were then used to find the velocity of the tracer bead. This was done by considering 5 consecutive tracer locations and finding the line of best fit for each set of five data points and determining the velocity as the gradient of the line[131]. After calculating the velocities, the velocity data was put into cells to show the Eulerian flow field. The mill volume was broken down into cells of an equal 3D volume. In the vertical y direction, each grid cell is approximately 1.6 mm high, which is 1.5 – 2 times the size of the grinding media beads, whilst the width of each grid varies to ensure the 3D volume of each cell is the same; cells have a smaller width near the walls than the impeller. In addition, information about the areas of the mill where the tracer spends most time were obtained by considering the fraction of time the grinding media bead spends in each equal volume cell of the mill.

4. PREDICTING THE POWER DRAW IN STIRRED MEDIA MILLS

4.1. Introduction

As was outlined in the Literature Review (Chapter 2), there are several differences between stirred tanks and stirred media mills, which mean that key mixing equations in literature must be adapted for successful application to stirred media mills. This chapter aims to investigate how the Power number concept can be applied to stirred media mills to predict power draw and understand the key factors affecting the power draw in stirred media mills. The vane rheometer will be used for viscosity measurements to determine if the use of this improves upon existing power prediction methods.

4.2. Power Draw During Batch Grinding

Lab-scale grinding is typically operated batch wise due to the challenges in setting up and operating small-scale semi-continuous milling equipment. A key issue with comparing between batch and continuous grinding is that during batch grinding, the particle size of calcium carbonate decreases, whilst with continuous grinding, there is a broader steady state particle size distribution. The size distribution of the calcium carbonate particles in the 72 wt% slurries resulting from batch grinding at 9.8 ms^{-1} with 52 vol% 0.8 – 1.2 mm mullite grinding media is shown in Figure 4.1. Although the tip speed was fixed at 9.8 m s^{-1} here, tip speeds has an impact on the PSD since it affects the rate of collisions and forces involved. This has been investigated in published works[22].

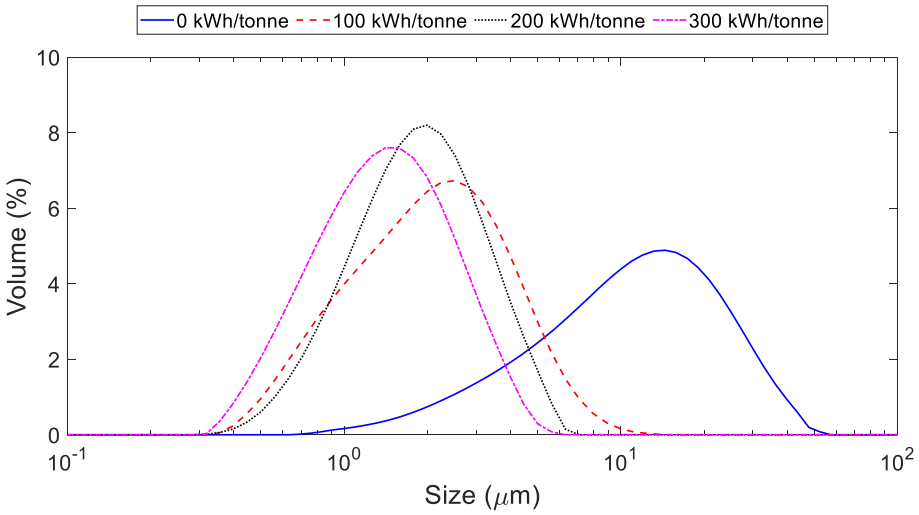

Figure 4.1: Particle Size of Calcium Carbonate Particles in 72 wt% Slurries Ground with 0.8-1.2 mm Mullite Grinding Media at 9.8 m s^{-1} After Different Mill Energy Consumptions

Figure 4.1 shows that both the mean particle size and the maximum particle size decrease as the sample is milled further. The particle size distribution remains monomodal, but the span decreases with increased milling. This results in differences in viscosity at different points during grinding. In addition to this, there are further viscosity changes occurring since friction causes the temperature of the mill to increase rapidly during grinding. To determine the extent to which these changes occurring during batch grinding affect the power draw of the lab-scale mill, the power and temperature were recorded using a data logger and are shown in Figure 4.2.

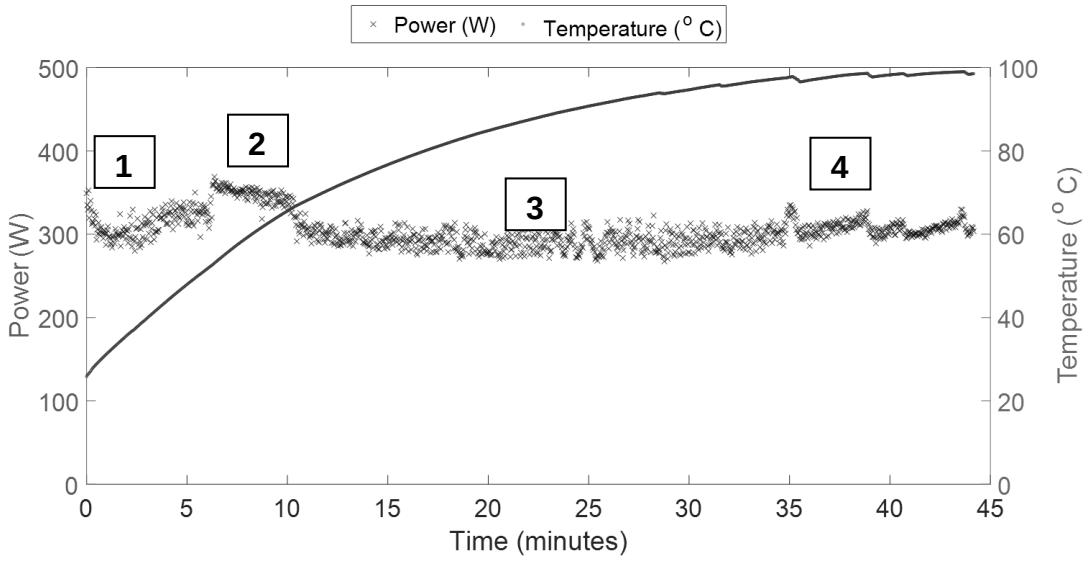

Figure 4.2: Power Draw and Temperature Evolving Over Batch Milling at 9.8 m s^{-1} (72 wt% Calcium Carbonate Slurry in Mullite 0.8-1.2 mm Grinding Media)

It can be observed from Figure 4.2 that there are four characteristic sections of the power draw curve during batch grinding:

1) Initial period of power decrease as the packed grinding media beads become fluidised, moving out of their packed positions.
2) Temporary increase in power draw followed by a decrease.
3) Power draw remains flat.
4) Power draw increases rapidly when the temperature is very high due to evaporation, which causes the solids fraction of the slurry to increase – water is added to counteract evaporation.

The curve shape observed in Figure 4.2 is similar to that observed in previous literature works by Zheng et al.[153] which look at torque and grinding time in a transparent vessel and suggest that the initial torque decrease occurs as the packed solids are loosened.

A subsequent torque increase results from the viscosity increase (see section 4.3.1 for details of the viscosity change as both particle size and temperature change). As motion changes and beads start to form a stationary layer above the impeller pins, the torque decreases and remains flat.

Overall, it appears that the power draw is relatively flat during grinding, with some fluctuations. The rate of energy consumption is close to linear due to the variations in power draw being small. In terms of the practicality of predicting power draw, the ideal scenario would be to be able to predict an average power draw for batch grinding.

4.3. Predicting Power Draw Using the Power Number and Reynolds Number

In typical fluid mixing applications, the relationship between Power number and Reynolds number is used to predict power draw. This relationship depends on the flow regime. As the Reynolds number increases and flow regimes develop, the dependency of Power number on Reynolds number decreases until the turbulent region where Power number is constant and hence independent of Reynolds number. This was discussed in greater detail in Literature Review (Chapter 2). The presence of grinding media beads makes this more complex for stirred media mills. When plotting the Po-Re (Power number-Reynolds number) curves, two scenarios have been considered:

1) Method 1: The grinding media are a part of the set-up (like baffles) and so are considered within the Power number (Po) term itself rather than by including them in the viscosity and density terms. This method was first proposed by Weit

and Schwedes in 1987 where it was tested for Newtonian fluids[83] and is discussed in Literature Review (Chapter 2).

2) Method 2: The grinding media are a part of the fluid being mixed and are hence included through their effect on the density and viscosity terms. This method remains a challenge due to difficulties in measuring the viscosity of the grinding media and slurry combination.

The determination of viscosity for calculation of Reynolds number is an important part of predicting power draw. For method 1, the slurry viscosity is required, whilst for method 2, a combined viscosity of the slurry and grinding media is required. Sections 4.3.1 and 4.3.2 outline the viscosity measurement methods used in this chapter.

4.3.1. Measuring Slurry Viscosity

A suitable measurement geometry is essential for reliable viscosity measurements. With traditional cone and plate or parallel plate rheometer geometries, the gap size is highly dependent on the particle size and the solids content - for suspensions with solids contents up to 50 vol% like calcium carbonate slurries, a gap size of 100 times the maximum particle size is required[45]. Since it is not practical to have a gap large enough for slurries with particles as large as 50 μm, a vane geometry (28 mm diameter vane in a 30 mm diameter cup) was utilised instead to eliminate wall slip. Viscosities were found experimentally for slurries which have been ground to different extents and hence have different particle sizes, shown in Figure 4.3.

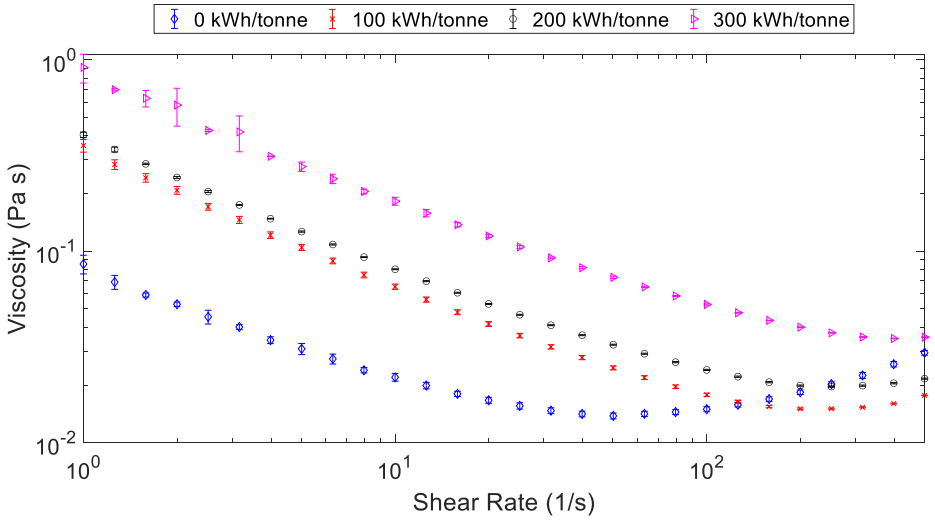

Figure 4.3: 72 wt% Slurry Viscosity Over the Course of a Batch Grind Using 0.8-1.2 mm Mullite Grinding Media Measured Using 28 mm Vane in a 30 mm Diameter Cup at 25 ° C. Error Bars Indicate the Standard Deviation of Three Consecutive Flow Ramps.

From Figure 4.3, it can be seen that viscosity profiles change significantly with particle size. The viscosity data for fluids at all stages of grinding can be fitted to the power law equation up to a limiting shear rate. The flow behaviour index, n, varies between approximately 0.3 and 0.5, suggesting that the slurries are highly shear thinning at all stages of grinding. At the start of grinding, the slurries were of low viscosity and showed a lower degree of shear thinning behaviour (n=0.5) across the range of shear rates considered. After significant grinding had occurred, a stronger shear thinning effect was observed for higher viscosity slurries, which have more particle-particle interactions as there are a larger number of particles present.

For 0 kWh tonne^{-1}, there appears to be shear thickening behaviour at high shear rates. This could be a measurement artefact caused by sedimentation increasing the measured torque – at higher shear rates, viscosity is lower which causes increased sedimentation and the onset of 'shear thickening'. This was also observed by Yang[33]

measuring similar slurries using a cone and plate rheometer. The shear thickening observation was attributed to the sedimentation of particles, as was also suggested by Greenwood et al.[29]. However, if sedimentation were the cause of this apparent viscosity increase, an increased viscosity would be expected in subsequent flow sweeps, leading to large error bars. Since error bars are low, sedimentation is unlikely the cause of this. An alternative reason for the apparent viscosity increase is vortexing and slip in the rheometer. This suggests that the use of the vane does not improve on the measurement method at high shear rates, despite vanes generally being suitable for high solids content slurries due to the elimination of wall slip issues. Hence, when a quantitative relationship for viscosity is suggested, such as for calculating Reynolds number, the relationship before this area of viscosity increase is used. This increases the error of viscosity since extrapolation above the measurement range is required.

4.3.1.1. The Effect of Temperature

The temperature effect during batch grinding is important since over the course of a 300 kWh tonne^{-1} batch grind, the temperature increases from room temperature to approximately 99 °C with some water evaporating. This temperature increase is likely to have a significant impact on viscosity. To investigate this, the viscosity was measured at the temperature during milling in Figure 4.4. It should be noted that the measurements at elevated temperatures are challenging at low shear rates because of the low viscosities and hence low torque measurements close to the lower measurable limit of the equipment. Additionally, although the solvent trap prevents some evaporation, it is not a perfect system and some water still evaporates leaving solid calcium carbonate particles on the shaft of the rheometer after long

measurements. Hence, measurements were limited to shear rates above 50 s^{-1} and only one flow sweep was conducted per sample.

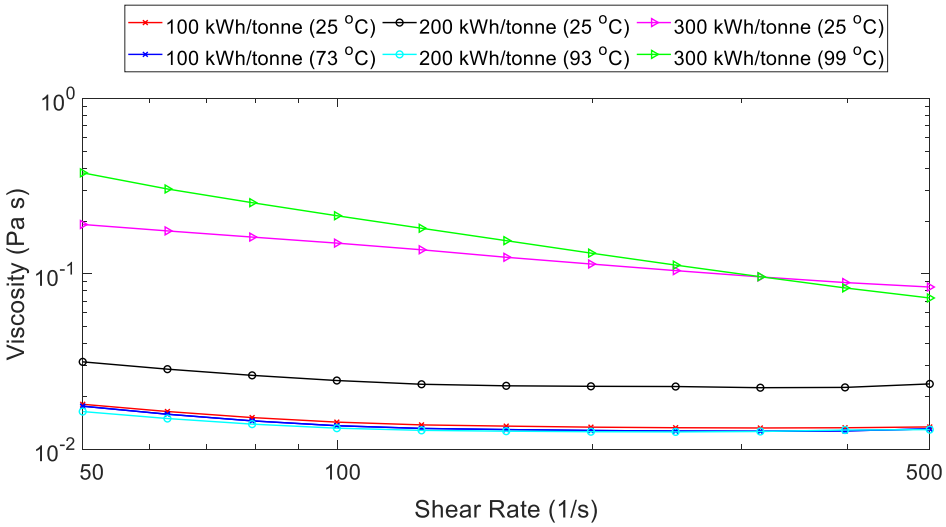

Figure 4.4: 72 wt% Slurry Viscosity Over the Course of a Batch Grind Using 0.8-1.2 mm Mullite Grinding Media Measured Using 28 mm Vane in a 30 mm Diameter Cup Measured at Approximate Mill Temperature When Slurry Sample Was Taken and At 25 °C

From Figure 4.4 it is observed that temperature does have an effect on viscosity when compared with the 25 °C measurements. Viscosities are generally lower at higher mill temperatures. The 300 kWh $tonne^{-1}$ slurry at low shear rates is an exception for this – this could be due to small amounts of evaporation in the rheometer caused by solvent trap inefficiencies.The 300 kWh $tonne^{-1}$ slurry at 99 °C remains the most viscous, despite being at the highest temperature, confirming that slurries get more viscous during batch grinding. This suggests that the particle size impact is more important than the temperature impact when comparing fluids and considering viscosity.

4.3.1.2. The Effect of Slurry Solids Content

The solids content of the slurry has an impact on grinding efficiency[22]. Lower solids content slurries are expected to behave differently since there are fewer particles and

hence fewer particle interactions. When measuring and comparing slurry viscosities, ground 72 wt% calcium carbonate slurries were diluted as opposed to grinding lower solids content slurries to ensure that only the solids content changed, keeping the particle size distribution constant. Figure 4.5 shows the reduction in viscosity occurring as slurries are diluted.

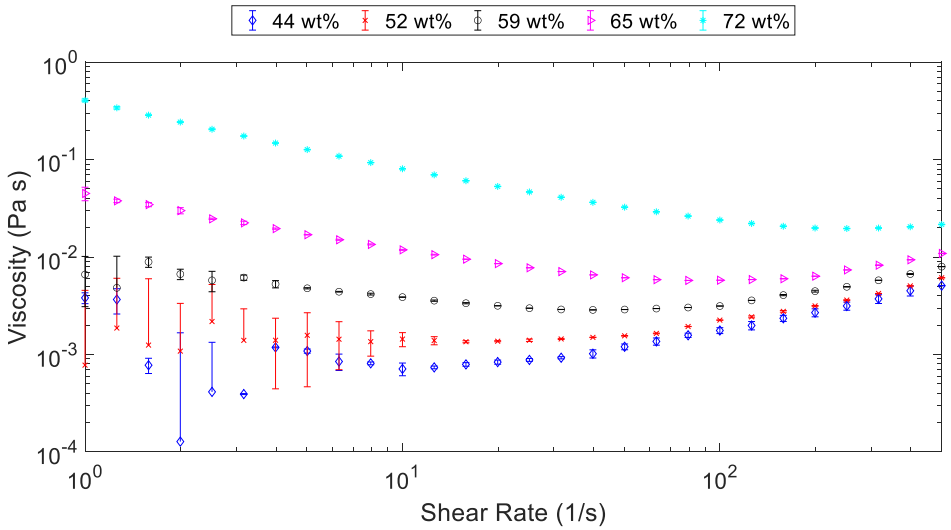

Figure 4.5: Slurry Viscosity with Same Particle Size but Different $CaCO_3$ Solids Content (Ground Samples Diluted by Water Addition) Measured Using Vane Geometry at 25 ˚C - 200 kWh/tonne (2.8 µm d_{80}). Error Bars Indicate the Standard Deviation of Three Consecutive Flow Ramps.

From Figure 4.5, it is observed that lowering the solids content significantly reduces viscosity. At high shear rates, the viscosity appears to increase with shear rate, implying shear thickening behaviour. This could potentially be explained as a measurement artefact caused by the sedimentation of particles in the rheometer, as was discussed in section 4.3.1. This thickening behaviour occurs at lower shear rates for slurries with a lower solids content, which could be explained by hindered settling, where there is viscous resistance in slurries with high solids concentration, resulting in slower settling than would be suggested by Stokes law[154]. Due to the repeatability of flow sweeps measured on the same sample making sedimentation an unlikely

explanation, an alternative reason suggested for the apparent increase in viscosity at high shear rates is vortexing.

Error bars are large for low solids contents at low shear rates. In some cases, the downwards error bar cannot be shown on the log scale as it includes some negative viscosity measurements. In theory, negative viscosity values are not possible; they stem from negative torque measurements caused by the torque being very close to the lower measurable limit of the equipment. The viscosity of these slurries with larger error bars is close to 10^{-3} Pa s, which is close to the viscosity of water, which is a challenge to measure using any rheometer geometry. However, the most commonly used slurries in grinding are high solids content and suited to being measured with the vane geometry. This shows that although the vane provides a suitable method of measuring high solids content slurries, it has its downfalls when measuring lower solids content fluids and becomes less reliable.

As well as influencing the viscosity at individual shear rates, the slurry concentration has an effect on the behaviour type observed. This behaviour can be observed more clearly from the power law equations shown in Table 4.1, which were fitted to data points before the apparent shear thickening was observed. The power law equations demonstrate the relationship between shear stress (τ) and shear rate ($\dot{\gamma}$).

Table 4.1: Power Law Equations for 200 kWh tonne^{-1} Ground Calcium Carbonate Slurries with Different Solids Contents

Mill Concentration/Milling Energy	Relationship	R^2
49 vol% (72 wt%)	$\tau = 0.386\dot{\gamma}^{0.33}$	0.99
45 vol% (65 wt%)	$\tau = 0.0247\dot{\gamma}^{0.45}$	0.99
40 vol% (59 wt%)	$\tau = 0.0074\dot{\gamma}^{0.73}$	0.80
35 vol% (52 wt%)	$\tau = 0.0026\dot{\gamma}^{0.76}$	0.59
30 vol% (44 wt%)	$\tau = 0.0011\dot{\gamma}^{0.77}$	0.06

Data in Table 4.1 shows the expected trends; slurries with higher solids contents are more highly shear thinning because there are more particles and a greater attractive potential. Higher shear rates can break the flocs down and release the water, decreasing the viscosity[155]. Fluctuation at low shear rates for the solids contents less than 59 wt% (observed in Figure 4.5) significantly reduces the R^2 value, reducing the certainty of the power law equation. This means that errors associated with the calculated Reynolds number will be larger for the lower solids content slurries.

The power law nature of slurries makes it difficult to relate viscosity to the power draw during milling. The shear rate throughout the mill is both variable and unknown. To relate viscosity to milling power draw in initial tests in section 4.3.3.1, Newtonian glycerol-water solutions were used in the mill in place of calcium carbonate slurries. In subsequent tests, the Metzner-Otto correlation was used to estimate an apparent shear rate.

4.3.1.3. Using Newtonian Mimic Fluids in Place of Slurries

To ensure glycerol-water solutions are comparable with calcium carbonate slurries, the glycerol-water content was selected as to ensure the viscosity was in the same range as calcium carbonate slurries. From Figure 4.3 and Figure 4.4, it can be seen that the range of slurry viscosities is likely to cover the range 0.02 – 0.35 Pa s. Hence, glycerol-water solutions with glycerol contents of 71 – 95% were selected. Table 4.2 shows the glycerol-water solution concentrations selected and justification for their use.

Table 4.2: Glycerol Concentrations Selected and Justification for Use

Glycerol Concentration	Newtonian Viscosity (Pa s)	Reason for Selection
71%	0.02	Lower limit - calcium carbonate slurries at the start of batch milling.
87%	0.1	Similar to high shear viscosities for highly ground slurries.
95%	0.35	Upper limit - highly ground slurries at low shear rates and high temperatures.

4.3.2. Measuring Combined Fluid + Grinding Media Viscosity

Since both the fluid and grinding media properties influence power draw, it is useful to consider an overall viscosity. This is a challenge since rheometers typically exhibit wall slip with large particles and are not designed to measure viscosities of such large particles. However, the possibility of using the vane geometry with a wide gap to measure a combined viscosity is explored. The fluid and grinding media were measured in the rheometer with a wide gap (28 mm vane, 50 mm cup diameters). When fluid and mullite grinding media were measured in the rheometer at grinding media concentrations typically used during milling, shear-thinning viscosity profiles

were observed, shown in Figure 4.6. This was the case for both slurry and glycerol with grinding media, despite glycerol-water solutions being a Newtonian fluid.

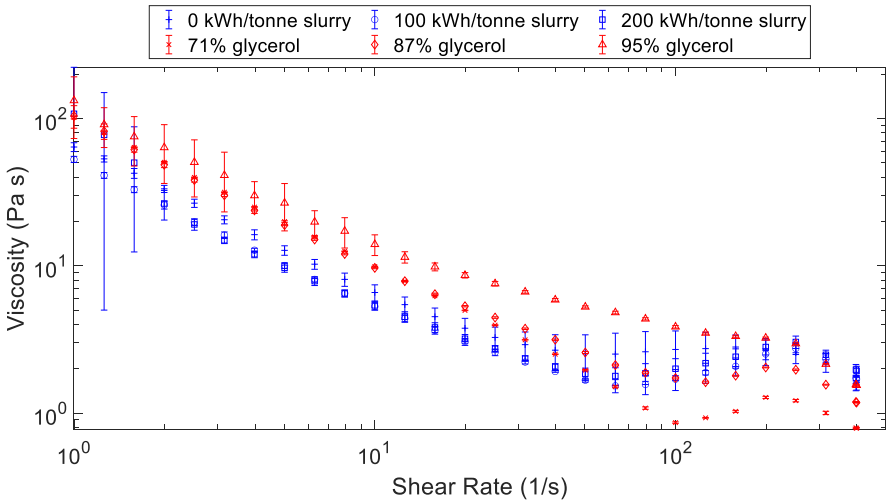

Figure 4.6: Viscosity of 72 wt% Surries or Glycerol-Water Solutions with 52 vol% Mullite Grinding Media 0.8 – 1.2 mm at 25 ˚C. Error Bars Show Standard Deviation of Three 'Up' Flow Sweeps

From Figure 4.6, it can be seen that when grinding media are used, the viscosity of the fluid itself is not as important as the interactions between the grinding media. This is due to the high solid content and density of the grinding media, making the combined viscosity over 250 times higher than that of the glycerol alone at low shear rates. Higher shear rates (> ~ 100 s^{-1}) were observed to cause extreme vortexing in the rheometer and also wall slip, where the grinding media at the walls start to move. The point at which this vortexing and wall slip is qualitatively observed corresponds to the area in which the viscosity profile changes and hence data above ~100 s^{-1} is deemed to be a measurement artefact. Nevertheless, this is a repeatable measurement, with relatively small error bars shown in Figure 4.6. Error bars are largest at low shear rates where the fluid may not be well distributed throughout the beads. Due to reliable measurements not being possible above approximately 100 s^{-1} it is necessary to

extrapolate outside of the range of measured viscosities when determining the viscosity in the stirred media mill, where shear rates are expected to be high. This is a drawback of this method and future improvements to the viscosity measurement method could improve the validity of the method of using this combined fluid and grinding media viscosity in power draw predictions.

When comparing glycerol with slurries, it was observed that when measured in the vane rheometer with mullite grinding media, glycerol-water solutions have a higher viscosity than slurries. Further research should be conducted with a wider range of fluids to determine how the viscosity with grinding media is affected. Although the slurries at different stages of grinding were shown to be of very different viscosities at room temperature in Figure 4.3, the viscosity of the slurries combined with grinding media are very similar in Figure 4.6, suggesting that the large amount of grinding media reduces the importance of the slurry particle size.

The viscosity of fluids with grinding media is shear thinning. This is in agreement with other findings in literature, where high solid content slurries (> 70 wt%) showed shear thinning behaviour.[54] The viscosity profiles were fitted to shear thinning profiles for the area before this vortexing and wall slip is observed in Table 4.3.

Table 4.3: Power Law of Different Glycerol-Water Solutions and Slurries with 0.8-1.2 mm Mullite Grinding Media

Fluid	Power Law Equation	R^2 of Fitted Equation
71% Glycerol	$\tau = 100.7\dot{\gamma}^{0.01}$	1
87% Glycerol	$\tau = 93.5\dot{\gamma}^{0.04}$	1
95% Glycerol	$\tau = 108\dot{\gamma}^{0.14}$	0.99
0 kWh/tonne Slurry	$\tau = 59.8\dot{\gamma}^{0.1}$	0.99
100 kWh/tonne Slurry	$\tau = 47.2\dot{\gamma}^{0.09}$	0.99
200 kWh/tonne Slurry	$\tau = 39.3\dot{\gamma}^{0.17}$	0.99

Power law equations in Table 4.3 are similar to typical power law fluids found in literature, and the high R^2 shows that the fluid and grinding media combinations fit well to this model. However, the flow behaviour index, n, for a shear thinning fluid typically lies between 0.3 and 0.7, where 1 would be the flow behaviour index for a Newtonian fluid[156]. The lower exponents in Table 4.3 imply that the grinding media in glycerol solutions are more highly shear thinning. Other authors have found shear thinning exponents of less than 0.2 for soils[157] and polymer type drilling fluids[158]. These fluids have in common that they contain large amounts of solids or polymers, which decrease the dependency of shear stress on shear rate.

The low Power number exponent indicates that the shear stress of the rheometer is close to being independent of shear rate. This was originally hypothesised to be a result of some sort of secondary motion in the mill pushing the blades of the vane. To test this hypothesis, the raw torque and rotational speed data from the rheometer was analysed along with data from a second, custom 3D printed rheometer geometry, which is similar to the pin impeller of the mill. By using a pin impeller, it is unlikely that

the pins will be as impacted by motion of the grinding media beads. The torque data for the vane and the 3D printed pin impeller is shown in Figure 4.7.

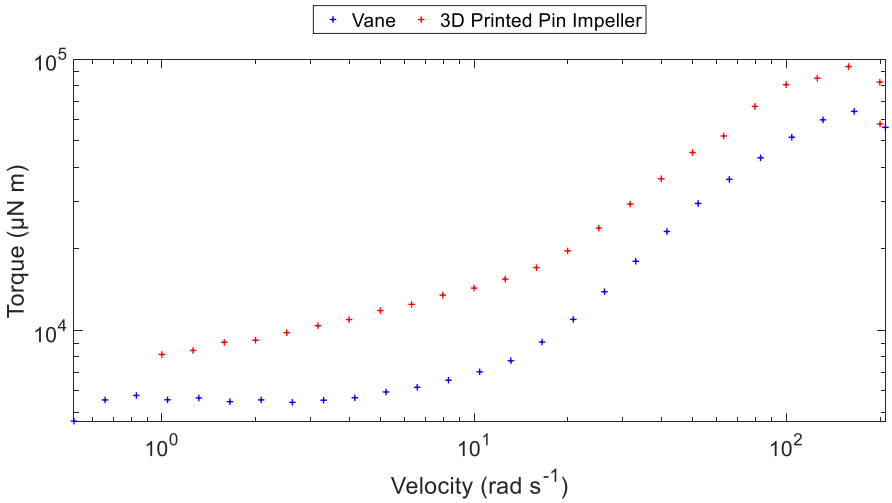

Figure 4.7: Rheometer Torque for Vane Impeller and Custom 3D Printed Pin Geometry at Constant Rheometer Fill Level – 0 kWh/tonne 72 wt% $CaCO_3$ Slurry with 52 vol% 0.8-1.2 mm Mullite Grinding Media

From Figure 4.7, it is observed that for the vane geometry at low velocities, the torque does not change significantly with increasing velocity. A more significant change in torque is observed at low velocities using the custom impeller, suggesting that secondary motion of the beads pushing the impeller could be partially contributing to the low rate of torque increase seen with the vane geometry. At higher speeds where the torque begins to change more rapidly, a vortex was observed to have developed in the rheometer and the level in the vessel changed significantly because there is a large amount of air within the slurry and grinding media combination for both the vane and custom geometry. These secondary flow effects makes viscosity measurements unreliable at high shear rates.

As the pin impeller is not a standard geometry, it is difficult to relate the torque to a shear stress and calculate the viscosity from this. However, the torque measured using this impeller in the rheometer is discussed with respect to scale-up in Chapter 6.

It has been shown that there are small changes in torque in the vane rheometer at low shear rates for 72 wt% calcium carbonate slurries. However, the power law exponent is significantly lower for 71% and 87% glycerol water solutions, where the torque shows very little increase with increasing shear rate in the low shear rate range. The glycerol-water solutions are highly lubricating and it was observed that at low shear rates, some of the glycerol sits on top of the grinding media beads. It is hypothesised that this low power law exponent is a tribological effect. At low speeds the beads are in direct contact and have a high friction coefficient, whilst at higher speeds, the beads are separated by a layer of lubricating liquid which reduces the friction coefficient[159] and hence minimises the increase in torque with increasing impeller speed.

To further test the reliability of the vane geometry viscosity measurements, tests were conducted to determine whether hysteresis is important and ensure equilibrium is reached before a viscosity measurement is made. Six alternating up and down flow sweeps were conducted, as shown in Figure 4.8.

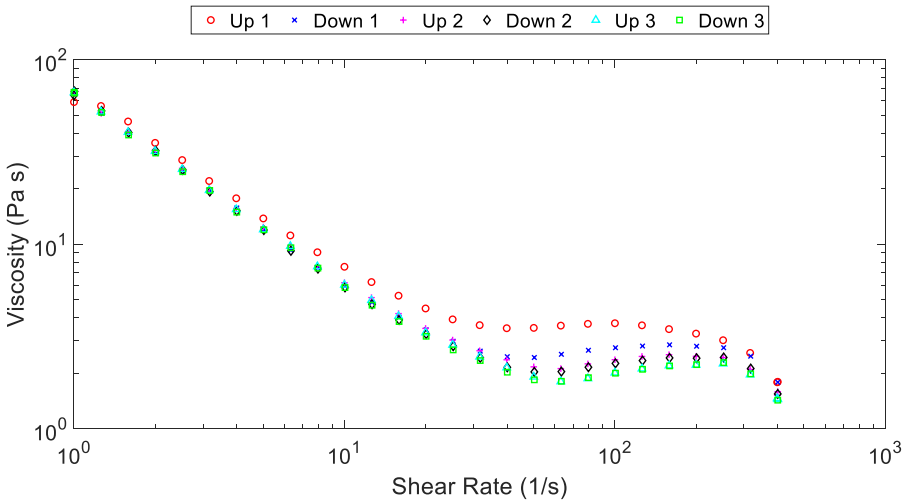

Figure 4.8 Consecutive Up and Down Flow Sweeps Conducted Using Vane Geometry – 0 kWh/tonne 72 wt% $CaCO_3$ Slurry with 52 vol% 0.8-1.2 mm Mullite Grinding Media

From Figure 4.8 there was little observable difference between up and down sweeps or consecutive sweeps. The first flow sweep gives a slightly higher viscosity than consecutive sweeps. However, this is due to some of the grinding media escaping the bulk flow and sticking to the vessel walls from where the level in the rheometer has increased at high speeds and then dropped at low speeds.

Overall, the viscosity measured at low shear rates is selected as being most suitable for use in calculating Reynolds number; this is before the vortex and secondary flow effects are having significant impact on the measurements.

4.3.2.1. Comparing Grinding Media Types

A key aim of measuring the fluid and grinding media combination in the rheometer is to infer information on how grinding media beads of different sizes and types behave differently. The viscosity for three commonly used grinding media types is shown in Figure 4.9.

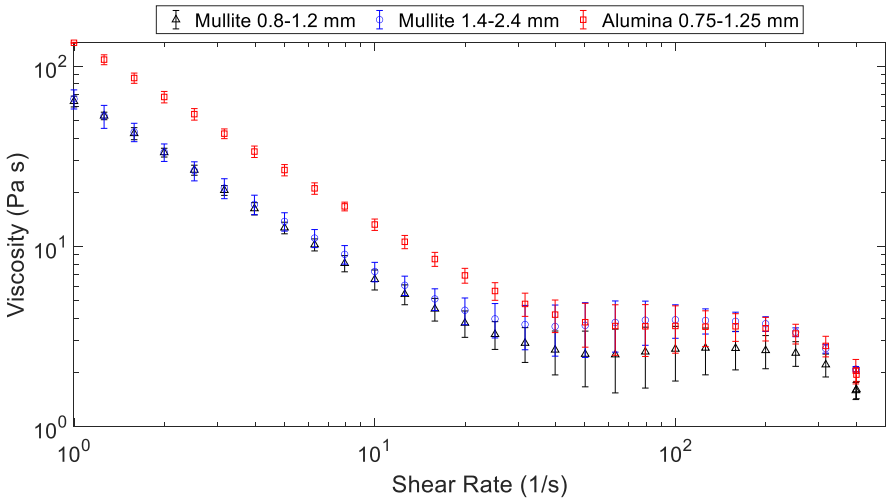

Figure 4.9: Viscosity of 0 kWh/tonne 72 wt% Surry with Different Grinding Media Types at 25 ˚C. Error Bars Show Standard Deviation of Three 'Up' Flow Sweeps

From Figure 4.9, it is evident that the two sizes of mullite bead show very little difference in viscosity, despite the differences observed in power draw when the two bead types are used. As is predicted, the denser alumina beads result in a higher apparent viscosity due to the higher torque requirement for the greater grinding media mass.

4.3.3. Predicting Power Draw: Assuming Grinding Media are a Part of the Equipment

When the grinding media are assumed to be part of the equipment, only the fluid is considered in density (ρ_f) and viscosity (μ_f) terms of the Reynolds number and Power number, as is illustrated in Equation (4.1) and (4.2).

$$Re = \frac{\rho_f N D^2}{\mu_f} \tag{4.1}$$

$$Po = \rho_f N^3 D^5 \tag{4.2}$$

In the simplified case of Newtonian glycerol-water solutions, the Po-Re curve is easily produced because the viscosity is constant and known. In the case of calcium carbonate slurries, the power law nature of the fluids and unknown and variable shear rates within the mill increase complexity – this is considered in section 4.3.3.2. Error bars throughout this section show the power fluctuation during milling by representing the standard deviation of 10 measurements, measured at a rate of one per second.

4.3.3.1. Glycerol-Water Solutions

The Po-Re curve was plotted for the three glycerol-water solutions combined with 52 vol% grinding media of two size ranges and materials in Figure 4.10.

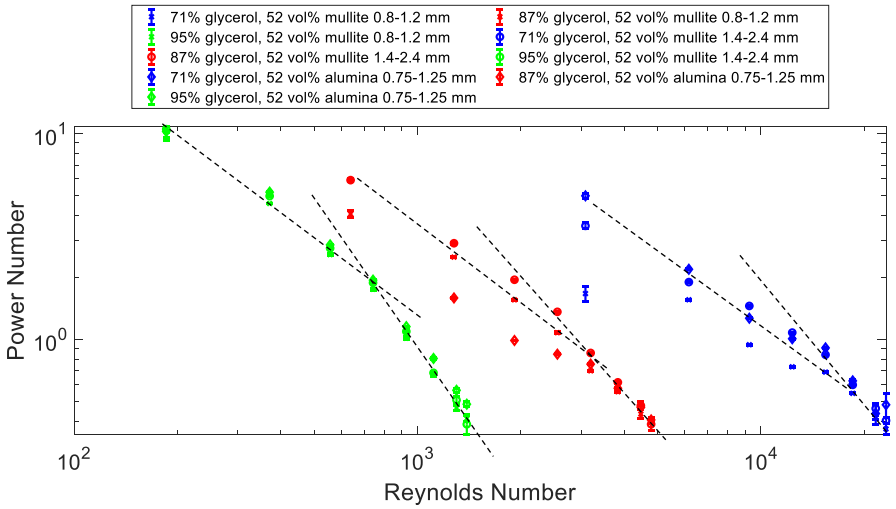

Figure 4.10: Po-Re Curve for Glycerol-Grinding Media Systems with 52 vol% Grinding Media, Assuming the Grinding Media are a Part of the Tank Set-Up. Dashed lines indicate the transition to the vortexing region.

Figure 4.10 follows the expected trend for an unbaffled system - Power number decreases with increasing Reynolds number, even at high Reynolds numbers[82]. This is likely to be due to the vortex formation at high tip speeds. The vortexing action in the batch lab-scale unbaffled mill is investigated further using positron emission particle

tracking (PEPT) and high-speed imaging (HSI) in Chapter 5. The area of interest in this work is the vortexing region since this contains the impeller speeds that are likely to be most effective for grinding; high speeds are required to ensure that grinding media beads collide with enough force to break calcium carbonate particles. In literature there is much debate over whether high tip speeds give increased grinding efficiency[33]. The link between tip speed and the grinding media bead velocities is considered using HSI and PEPT in Chapter 5.

Ideally, all glycerol concentrations with the same grinding media should lie on one curve. However, this is not the case in Figure 4.10. Where there are two conditions with the same Reynolds number, very different Power numbers were measured for the same grinding media. An example is shown in Table 4.4.

Table 4.4: Mill Conditions for Mullite 1.4 – 2.4 mm Grinding Media with Glycerol at Reynolds Number 3000

	Point 1	**Point 2**
Reynolds number	3000	3000
Power Number	1	5
Glycerol Viscosity (Pa s)	0.1	0.02
Impeller Speed (m s^{-1})	5.9	1.3

From Table 4.4, it can be seen that although the points have the same Reynolds number, the impeller speed is very different. The theoretical Power number concept is only valid when the contents of the vessel are homogeneously distributed. In this case, it is likely that at 1.3 m s^{-1}, most of the grinding media are settled at the bottom of the vessel and the impeller is slowly pushing them around. Whereas at 5.9 m s^{-1}, the vessel contents are more homogeneously distributed as the grinding media are being lifted

off the bottom of the vessel. At higher impeller speeds, as well as the grinding media being lifted off the bottom of the vessel they tend to centrifuge and form a vortex, leading to a higher concentration of grinding media at the wall[17]. The different distributions of the grinding media leads to differences in the density of fluid being mixed. The bulk density increases as more grinding media beads are suspended until all beads are suspended. This concept was observed by Shah[160], who looked at the suspension of glass beads up to 27 wt% in a stirred vessel. They assessed the level of suspension by measuring the power draw for a given impeller speed as once all of the solid particles are suspended, there was no further increase in bulk density and the gradient of the increase of power draw with impeller speed decreased. It should however be noted that in this milling work, the grinding media concentration is much higher than was used in the literature example.

The transition point in the Po-Re curve where the slope changes due to vortexing was also identified for fluids in unbaffled stirred tanks by Scargiali et al.[82], who introduced the dimensionless Froude number (Equation (4.3)(2.11)), taking the ratio of inertial to gravitational forces into account. The Froude number is dependent on the impeller speed (N), impeller diameter (D) and acceleration due to gravity (g).

$$Fr = \frac{N^2 D}{g} \tag{4.3}$$

It has been shown that for unbaffled liquid systems, the vortex depth is a linear function of the Froude number[161], which makes it a suitable dimensionless term to include to predict power draw. Mannheim et al.[112] used dimensional analysis to conclude that

the Froude number and Reynolds number are key dimensionless variables in predicting the power draw in a stirred media mill after the transition region.

The data was assumed to fit to a relation in the form of Equation (4.4).

$$Po = A\, Re^{x}\, Fr^{y} \tag{4.4}$$

Excel's non-linear regression analysis toolbox was used to find optimal values for constants A, x and y, which result in a minimum value of the squared error (where the error is the difference between fitted and experimental Power number). Results from evolutionary and generalised reducing gradient (GRG) solving methods were compared and found to be in close agreement, suggesting that a true optimum was determined in both cases. Evolutionary analysis takes longer than other regression analysis methods in Excel but is more likely to ensure a global optimum is found as opposed to a local optimum. However, the amount of time the Evolutionary analysis is allowed to run for affects the results. Other literature work testing Excel's regression analysis methods and comparing them with other methods found error to be low and concluded that they are suitable tools for finding optimal engineering solutions[162]. For more in depth regression analysis with more datasets, the use of statistical software packages is recommended. However, there is a high cost associated with this.

To compare empirical correlations, errors defined in equation (4.5) were considered.

$$Error = abs\left(\frac{Predicted\ power - experimental\ power}{experimental\ power}\right) \times 100 \tag{4.5}$$

Determining the range of parameters over which the correlations are valid is important. Restricting the range can reduce the associated errors, whilst having a smaller range means the practical uses of the equation are limited. For example, in stirred tanks turbulent correlations are typically applicable when the Reynolds number is greater than 10,000. The Froude number is likely to be important in stirred mills. At low impeller speeds, the grinding media beads are packed closely together so there is more friction for smaller beads than larger beads and hence a higher power draw. Whereas at higher speeds when the bed is fluidised, smaller grinding media have less mass so less power is needed to move them compared to larger beads. Data points with lower Froude number (and hence higher power number) do not fit as well to the correlation, as indicated in Figure 4.11.

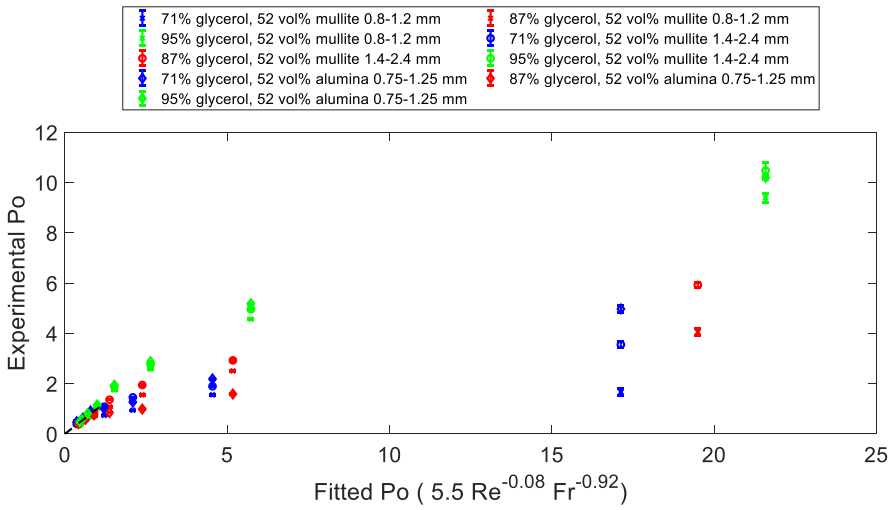

Figure 4.11: Best Fit Relation Between Power Number and Reynolds and Froude Numbers for Glycerol and 52 vol% Grinding Media Systems, Entire Range of Fr

From Figure 4.11, it is evident that the correlation is a significantly better fit for lower Power numbers and hence higher Froude numbers when beads are fluidised and there

is some vortex formation. In this Chapter, data was restricted to Fr >0.5 to consider the high impeller speeds that are after the transition zone (Figure 4.12).

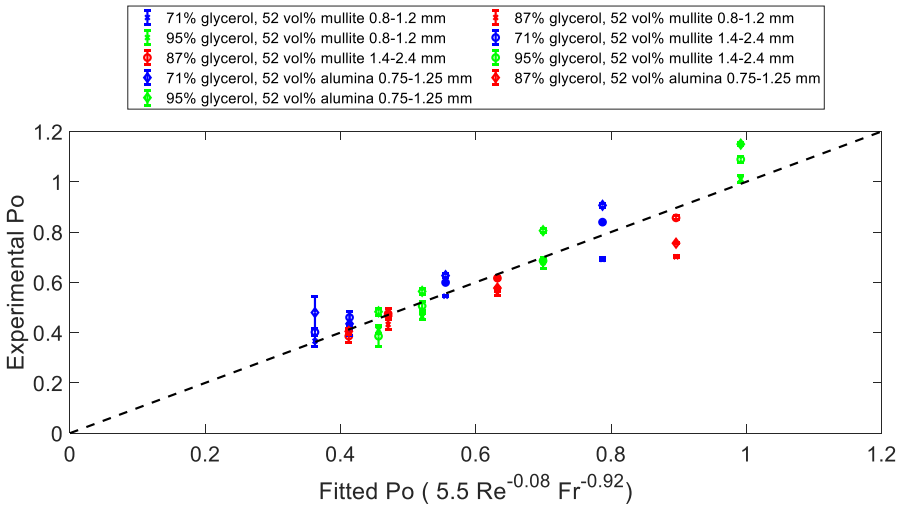

Figure 4.12: Best Fit Relation Between Power Number and Reynolds and Froude Numbers for Glycerol and 52 vol% Grinding Media Systems, Fr >0.5

Although this model appears to be a good fit for predicting power draw, with the average error at 8% and the maximum error 28%, there is no way to differentiate when the ratio of grinding media to glycerol is varied or the grinding media properties are changed. Hence, a new curve is required for each grinding media type or fill ratio. To account for the grinding media properties and how well they follow the flow of the fluid, it is proposed that the Stokes number (Equation (4.6)) is added to the empirical relation. The Stokes number assesses how well the grinding media follow the flow of the fluid and considers the grinding media diameter, d_{GM}, the density difference between the fluid and grinding media, ρ_{GM-f}, impeller speed, N, and fluid viscosity, μ_f.

$$St = \frac{d_{GM}^2 \rho_{(GM-f)} N}{18\mu_f} \tag{4.6}$$

The best fit relation incorporating the Stokes number is shown in Figure 4.13.

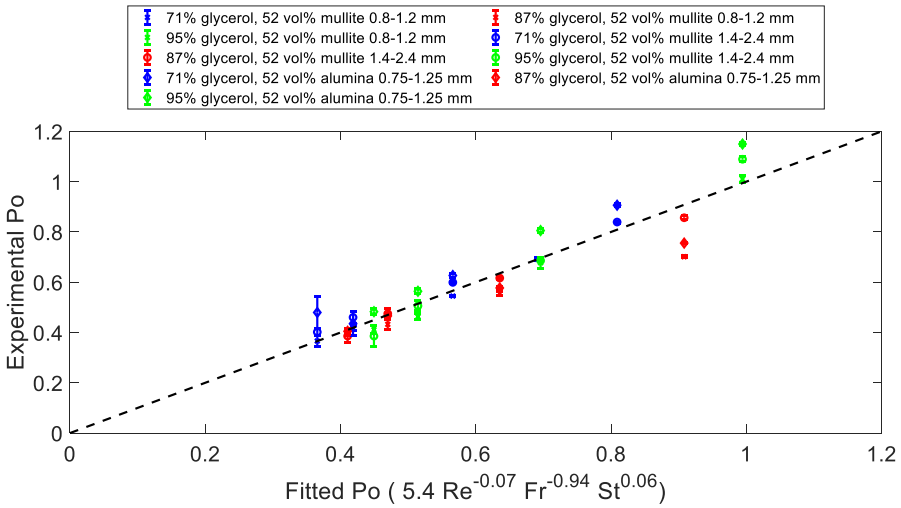

Figure 4.13: Best Fit Relation Between Power Number, Reynolds Number, Froude Number and Stokes Number for Glycerol and 52 vol% Grinding Media Systems

The exponent for Stokes number in Figure 4.13 is very low, suggesting that the power draw has a low dependency on Stokes number in this case. Additionally, the error is approximately the same as the case when just the Reynolds number and Froude number were considered. This suggests that the Stokes number is not an important parameter for predicting power draw in the case of glycerol-water solutions. However, it is shown in section 4.3.3.2 that in the case of slurries with grinding media, the power draw is more dependent on the grinding media properties and the Stokes number is of greater importance. This is likely be due to the frictional effects of the calcium carbonate particles interacting with the grinding media beads.

Another parameter to consider is the density of the grinding media beads. The beads are being moved by the impeller, which means that the mass of beads is likely to have a significant impact on torque. By including the grinding media within the density term when calculating the Reynolds number and Power number (i.e. the density is the

weighted density of the fluid and grinding media), as is indicated in Equation (4.7) and (4.8), the amount and density of the grinding media beads used is considered.

$$Re = \frac{\rho_{f+GM} N D^2}{\mu_f} \tag{4.7}$$

$$Po = \rho_{f+GM} N^3 D^5 \tag{4.8}$$

The resulting Po-Re curve is illustrated in Figure 4.14.

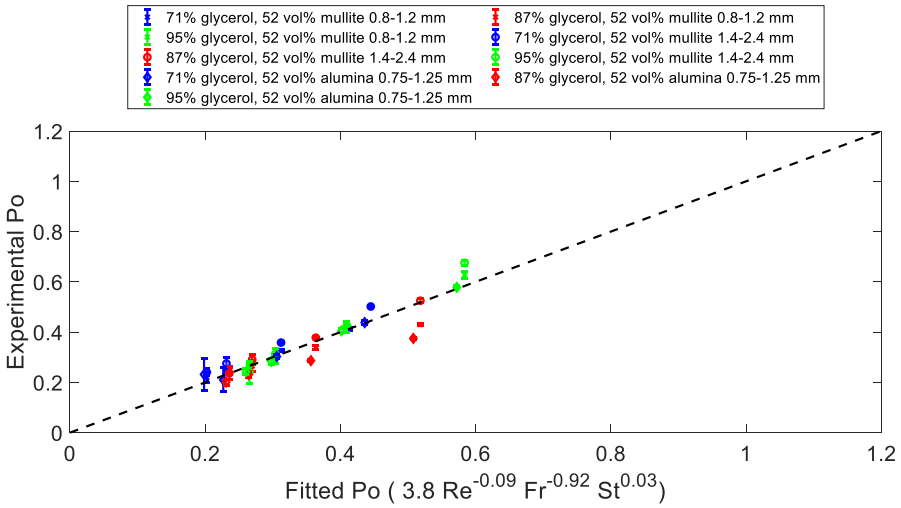

Figure 4.14: Best Fit Relation Between Power Number, Reynolds Number, Froude Number and Stokes Number for Glycerol and 52 vol% Grinding Media Systems – Grinding Media are Included in Density Terms

The inclusion of the grinding media in these terms does not significantly improve the correlation in this case – the average and maximum errors are similar. However, the amount of grinding media used is the same in each of these cases; it is likely that the grinding media density would play a bigger role when differentiating between Power numbers with different amounts of grinding media in the mill.

Glycerol-water solutions are not used in milling scenarios and were used as a model Newtonian fluid to investigate the effect of viscosity on power draw. The case of calcium carbonate slurries is more challenging due to their non-Newtonian behaviour. The methodology applied to glycerol-water solutions was applied to real milling scenarios with calcium carbonate slurries to determine the effectiveness of the model.

4.3.3.2. Calcium Carbonate Slurries

The aim of forming an empirical correlation is to be able to predict the power draw for batch grinding. As the particle size and temperature change with batch grinding, slurry viscosity changes significantly. It was shown in section 4.2 that the turbulent power draw is relatively constant over the course of batch grinding, i.e. as the particles get smaller and the temperature increases, the power draw is approximately constant. This is verified in Figure 4.15.

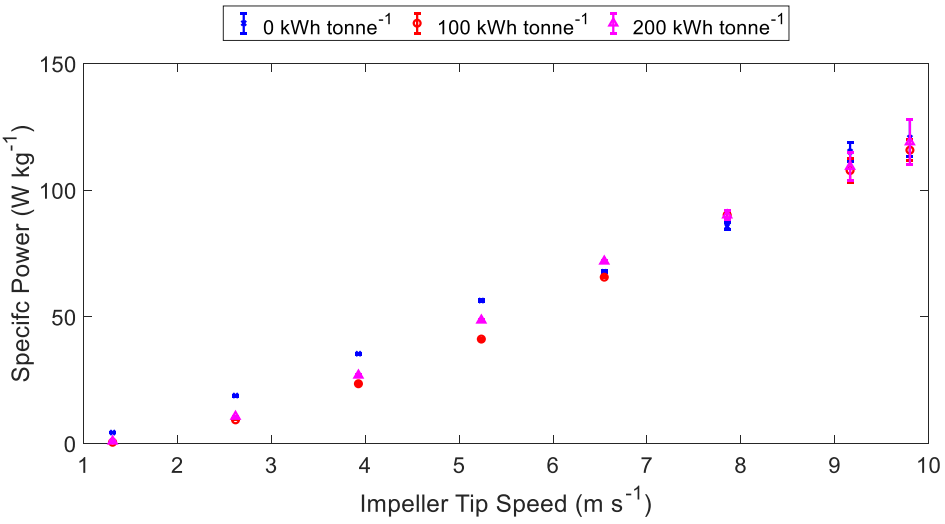

Figure 4.15: Power Draw for Grinding of 72 wt% Calcium Carbonate Slurry in 52 vol% Mullite 0.8 – 1.2 mm Grinding Media

In Figure 4.15, the power draw at a given impeller speed has low dependency on the stage of grinding (kWh/tonne), particularly at higher impeller speeds. This is despite changes in both particle size and temperature occurring at each kWh/tonne. This implies that it is reasonable to assume the same power number at each stage of grinding, despite the viscosity differences. Hence, the most practical method of determining viscosity for use in calculating the Reynolds number to predict power draw is to measure the viscosity of an unground slurry at 25 ^{o}C in the vane rheometer. To plot a Po-Re curve for calcium carbonate slurries, an average shear rate has to be estimated in the mill since slurry viscosity is dependent on shear rate.

4.3.3.3. The Metzner-Otto Correlation

To find an apparent viscosity for calculating the Reynolds number at each mill speed, the Metzner-Otto correlation was applied. This assumes that the apparent shear rate, $\dot{\gamma}_e$, is proportional to the rotational speed of the mill, N, as described in Equation (4.9) with a proportionality constant, k_s.

$$\dot{\gamma}_e = k_s N \tag{4.9}$$

The Metzner-Otto correlation was established to be applied only within the laminar regime and does not work as well in the transitional and turbulent regimes. The shear rate is likely to be much higher in the turbulent regime as a result of eddies and local regions of high shear and therefore be underestimated by the Metzner-Otto correlation. It is possible that the presence of large amounts of grinding media dampens the effect of turbulence in stirred media mills. A more detailed modelling analysis of shear rates in the mill is suggested in Further Research Chapter 8 to determine the validity of using

the Metzner-Otto correlation. However, the modelling of both the fluid and grinding media simultaneously remains a challenge, making shear rates difficult to compute.

The calculated Reynolds number is dependent on the constant, k_s, used to estimate the shear rate. For power law fluids, some authors propose a dependency of k_s on the fluid's power law exponent, n[73]. However, in this case, assuming k_s is constant and independent of the fluid properties works well; a k_s of 13 gives a good model fit (and was determined from the regression analysis). A k_s of 13 is also similar to other similar impeller types in literature[75]. Assuming k_s is dependent on the shear thinning exponent gives little improvement on the best fit of the correlation.

4.3.3.3.1. Using Metzner-Otto in Power Number Correlations

The range of slurry-grinding media combinations from which the empirical correlation was derived were selected to ensure that a range of slurry concentrations, grinding media amounts, grinding media sizes and grinding media materials were included, since these parameters all have a significant impact on power draw and should therefore be considered in any correlation developed. The Po-Re curve for calcium carbonate slurries is shown in Figure 4.16.

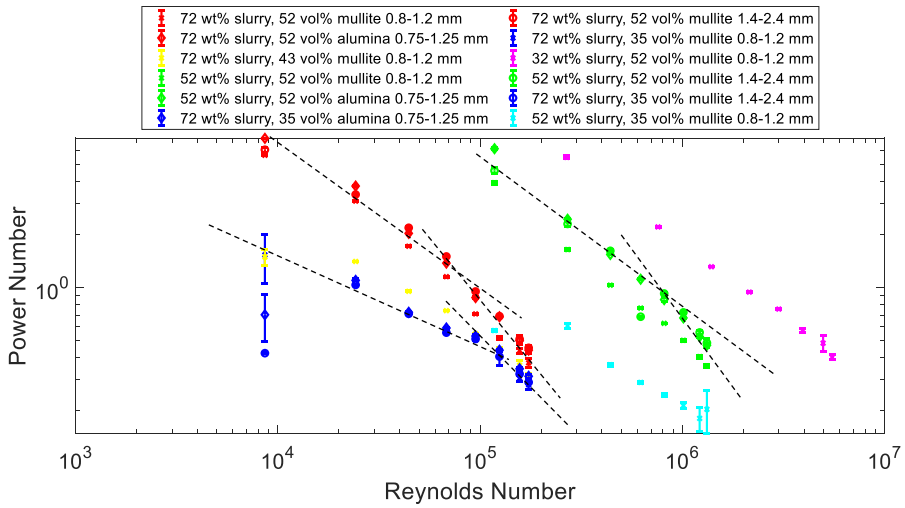

Figure 4.16: Po-Re Curve for Slurry-Grinding Media Systems, Assuming the Grinding Media are a Part of the Tank Set-Up, k_S=13

From Figure 4.16, it can be observed that slurries show a similar trend to glycerol-water solutions, where each slurry viscosity has a distinct line on the plot and there is a gradient change where significant vortexing occurs. It should however be noted that the Reynolds number of each data point is sensitive to the choice of k_S used in the Metzner-Otto correlation. The Reynolds numbers are significantly higher than glycerol-water solutions; the density of slurries is over 2.5 times that of glycerol-water solutions and the choice of selection of k_S also has an impact on this. Similarly to glycerol-water solutions, the distinct lines for each fluid viscosity suggest that the Froude number is again important in this case. This is backed up by the observation of vortexing from occupancy plots in Chapter 5. Predicting the power draw based off the Reynolds number does not work well when the grinding media are part of the fluid, as is confirmed in Figure 4.17.

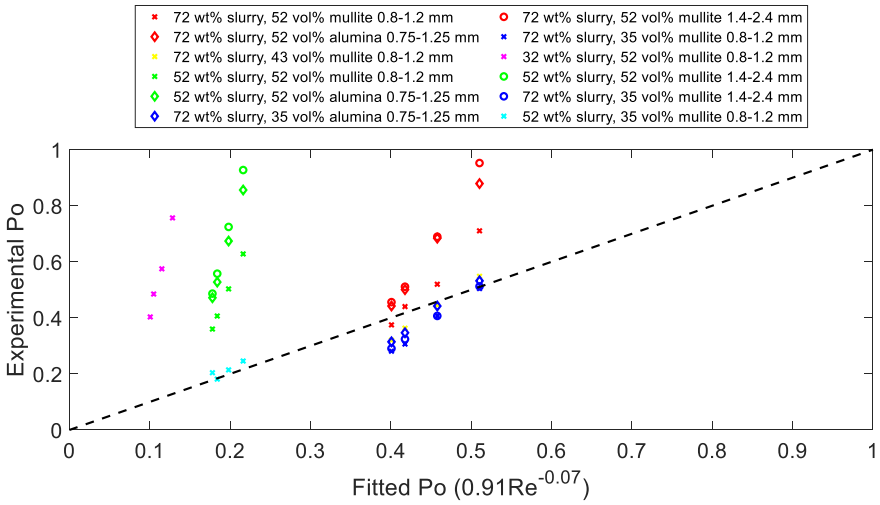

Figure 4.17: Best Fit Relation Between Power Number and Reynolds Number for Calcium Carbonate Slurries with Grinding Media, k_s=13

The method of creating empirical correlations for power draw using the Froude number and Stokes number was repeated from section 4.3.3.1, again for data points where Fr >0.5. The relationship between Power number and the Reynolds and Froude number is shown in Figure 4.18.

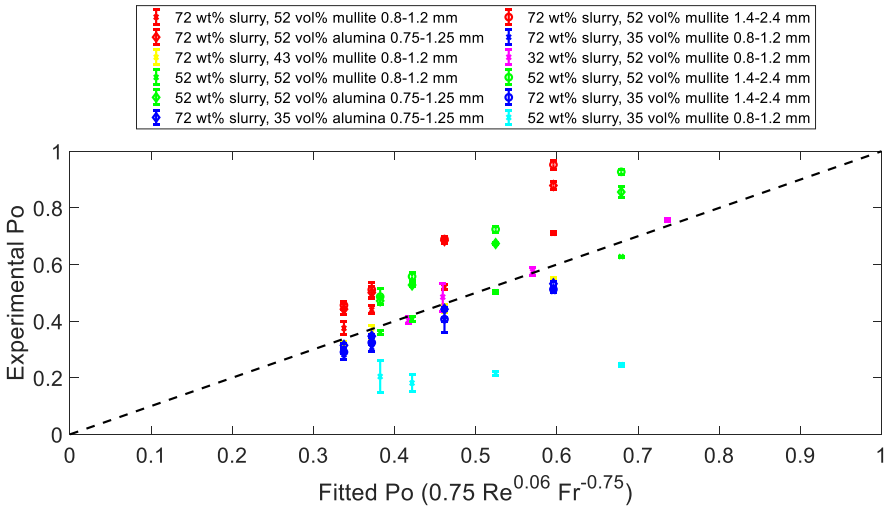

Figure 4.18: Best Fit Relation Between Power Number and Reynolds and Froude Numbers for Calcium Carbonate Slurries with Grinding Media, k_s=13

From Figure 4.18, it is seen that the Power number can again be more accurately estimated when the Froude number is introduced. However, the relationship between the Power number, Reynolds number and Froude number is not the same as it was for glycerol-water solutions ($Po = 5.5\ Re^{-0.08}\ Fr^{-0.92}$). Additionally, it appears that for slurries, the grinding media properties have a greater impact on power draw than they did with glycerol-water solutions. This is likely due to the particle-grinding media interactions that occur in slurries but not glycerol-water solutions. Calcium carbonate slurry and glycerol-water solutions are compared in greater detail in section 4.3.6.

The case of using 52 wt% slurry and 35 vol% mullite 0.8-1.2 mm does not appear to be a good fit to the trend in Figure 4.18. This is likely to be due to the low viscosity fluid and lower grinding media amount causing further vortexing, this increased vortexing was confirmed using PEPT in Chapter 5.

In Figure 4.19, the Stokes number was introduced to the empirical correlation to account for the flow of the grinding media beads as well as the slurry.

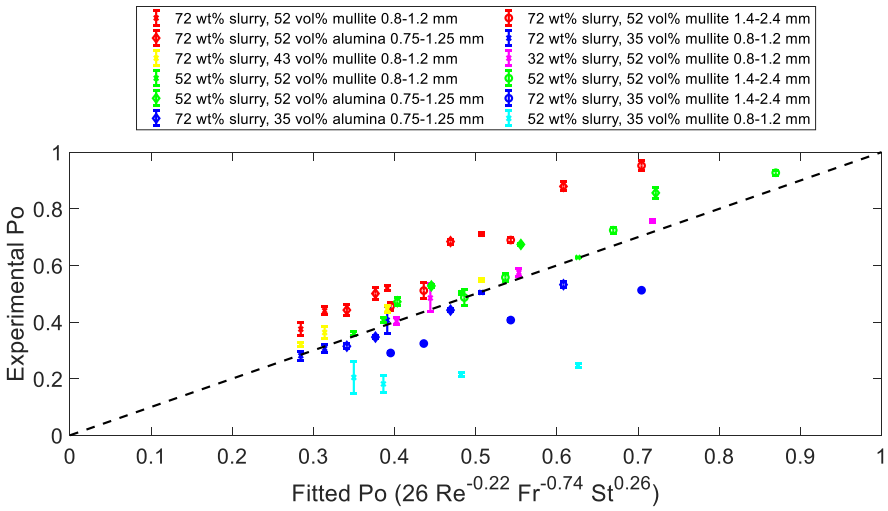

Figure 4.19: Best Fit Relation Between Power Number, Reynolds Number, Froude Number and Stokes Number for Slurry and Grinding Media Systems, Grinding Media Assumed to be Part of System, $k_s = 13$

The Stokes number has a higher exponent than in the case of glycerol-water solutions due to the grinding media properties having a bigger impact when slurries are used. This is likely to be caused by particle-grinding media interactions and friction. To enable the amount of grinding media to be accounted for, the grinding media are included in the density terms for the Power number and Reynolds number in Figure 4.20.

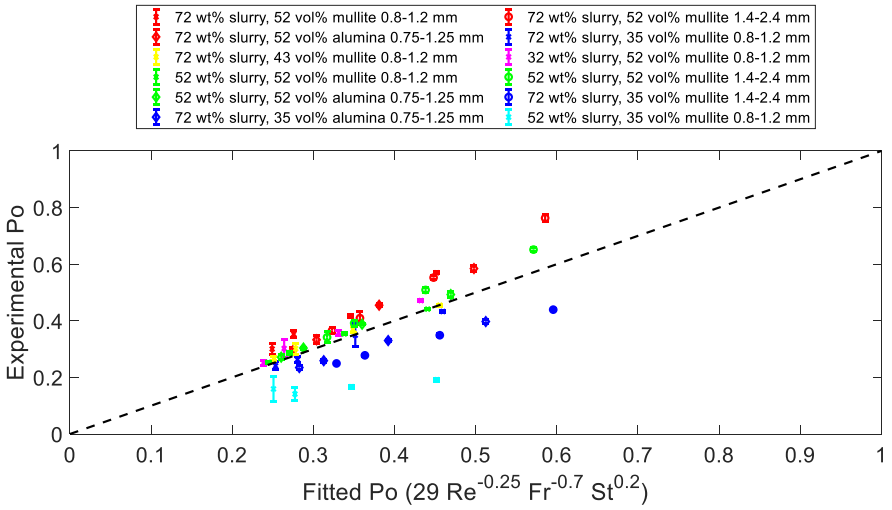

Figure 4.20: Best Fit Relation Between Power Number, Reynolds Number, Froude Number and Stokes Number for Slurry and Grinding Media Systems - Grinding Media are Included in All Density Terms, Grinding Media Assumed to be Part of System, $k_s = 13$

From Figure 4.20, it can be seen that the correlation is improved by including the grinding media in the Power number and Reynolds number density terms. The error is still unacceptably high for the case of the 52 wt% slurry with 35 vol% grinding media, which is described by the different shape of the vortex, as was investigated using PEPT in Chapter 5.

Due to the processing methods used in producing grinding media and advantages of using grinding media of a range of sizes, grinding media typically have a monomodal size distribution. Both the width of the distribution and mean particle size vary

depending on the grinding media type. This makes predicting the effect of grinding media size on power draw difficult. Through the inclusion of the Stokes number, the mean particle size can be considered. However, using this method, there would be no way of considering mixed or bimodal grinding media distributions, which have been shown to increase grinding efficiency in some cases[25]. However, this remains a research concept with mixed grinding media types having little application to industry, potentially due to the increased wear rates of the smaller grinding media beads. Industrial stirred media mills are commonly operated as a series of continuous mills, which often have different grinding media sizes in adjacent mills. This could potentially be compared to batch grinding with mixed grinding media.

Since the greatest errors in Figure 4.20 still result from lower slurry solids contents and grinding media amounts, an alternative method of accounting for the presence of the grinding media and the high solids content of the slurries was tested. The slurry solids content, SC, and grinding media amount, GM, were directly included in the correlation, as shown in Figure 4.21**.**

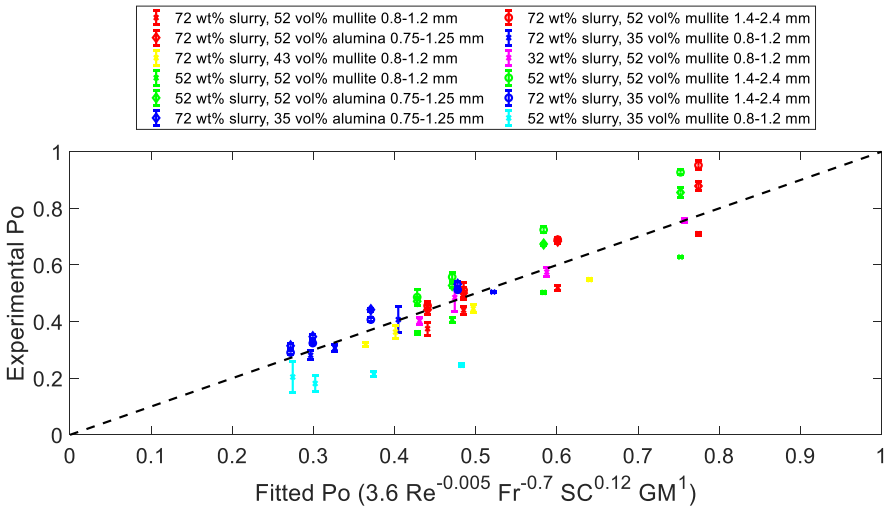

(a)

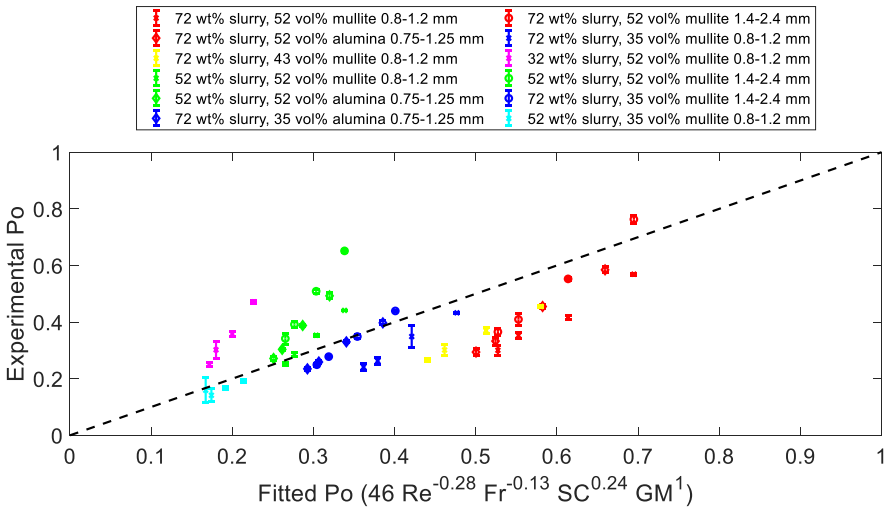

(b)

Figure 4.21: Best Fit Relation Between Power Number, Reynolds Number, Froude Number, Grinding Media Amount and Slurry Solids Content for Slurry and Grinding Media Systems, k_s = 13 (a) Grinding Media Excluded From Density Term (b) Grinding Media Included In Density Term

From Figure 4.21, it is shown that when the amount of grinding media and the solids content of the slurry are included, the correlation is improved when the grinding media beads are not included in the density term. It should be noted that the exponent of the grinding media quantity term is significantly higher than the slurry solids content term. This suggests that this is the most important parameter to include, which is expected since they are large and occupy a substantial volume of the mill.

Similar research was outlined by Kwade[85], where the Reynolds number as linked to the power number along with other important milling parameters with the exponents being determined experimentally. This is however laborious and relies on a quantitative measure of the most important parameters being determined. It also does not allow for the consideration of parameters that may overlap.

In order to compare the errors associated with each power prediction method when the grinding media are assumed part of the system, the average and maximum errors are displayed in Table 4.5 and Table 4.6 respectively.

Table 4.5: Error Associated with Power Number Correlations, Assuming Grinding Media are a Part of the System

	$Po = A\,Re^x$	$Po = A\,Re^x\,Fr^y$	$Po = A\,Re^x\,Fr^y\,St^z$	$Po = A\,Re^x\,Fr^y\,GM^aSC^b$
Average error (%)	35	25	23	15
Max error (%)	83	176	155	96

Table 4.6: Error Associated with Power Number Correlations, Assuming Grinding Media are a Part of the System – Grinding Media Included In Density Terms Only

	$Po = A\,Re^x$	$Po = A\,Re^x\,Fr^y$	$Po = A\,Re^x\,Fr^y\,St^z$	$Po = A\,Re^x\,Fr^y\,GM^aSC^b$
Average error (%)	30	21	13	28
Max error (%)	133	146	136	75

The errors in Table 4.5 and Table 4.6 compare the correlations developed to predict power draw based on a slurry viscosity measured using the vane rheometer. Including the grinding media in the density term improves the correlation in cases where the grinding media amount is not considered separately as a term. A 15% error is deemed good - a 0% error is neither expected nor possible since there is some fluctuation of power draw caused by mill vibrations and viscosity changes throughout milling. However, the maximum error is in some cases unacceptable. The reasons for correlations being a better fit at high solids content could be related to the viscosity measurement errors; at low solids content, the error associated with the viscosity measurements is very high due to the low torque measured on the rheometer (see

section 4.3.1.2). This leads to an unreliable Reynolds number being calculated which impacts the power prediction. The maximum error typically stems from the case of both low slurry solids concentration and a low grinding media amount. The correlations work best at a constant grinding media content and high slurry solids content. In Chapter 5, it was shown using PEPT that the vortex shape is highly dependent on the solids content and the grinding media amount, and that the combined effect of changing both of these parameters is difficult to uncouple due to the interaction of the fluid and grinding media. Hence, this method is best used with a new correlation created for each grinding media amount and each solids content, which is time consuming and laborious.

To overcome some of the problems of this model and consider the grinding media properties, the grinding media can be considered to be a part of the fluid and hence included in viscosity measurements.

4.3.4. Predicting Power Draw: Assuming Grinding Media are a Part of the Fluid

To consider grinding media as part of the fluid, the viscosity measured using the vane rheometer in section 4.3.2 was used alongside the Metzner-Otto correlation, as described in section 4.3.3.3. The modified Reynolds number used in this section includes the grinding media in density and viscosity terms, as is indicated in Equation (4.10) where ρ_{f+GM} is the density of the fluid and grinding media and μ_{f+GM} is the combined viscosity of the fluid and grinding media. The Power number also includes the combined density of the fluid and grinding media, as is illustrated in Equation (4.11).

$$Re_{mod} = \frac{\rho_{f+GM} N D^2}{\mu_{f+GM}} \tag{4.10}$$

$$Po = \rho_{f+GM} N^3 D^5 \tag{4.11}$$

It is possible that the Metzner-Otto term, k_s, is dependent on the power law index, n, particularly in very highly shear thinning fluids[72]. Based on analysis of the experimental results, the following relations between k_s and n have been proposed:

- k_s is constant
- $k_s = A(1-n)$
- $k_s = An^B$

Different k_s relations were tested and as part of the regression analysis, the k_s constants were optimised. A power law relationship between n and k_s gives the best fit between Reynolds and Power number. This fits with literature findings - Govender et al.[79] estimated shear rates using PEPT for a tumbling mill and found that shear rates were higher for lower solids concentrations since there is more space available for particle shearing when the solids content is lower. This means that k_s is dependent on the power law exponent, n. The resulting Po-Re plot is shown in Figure 4.22.

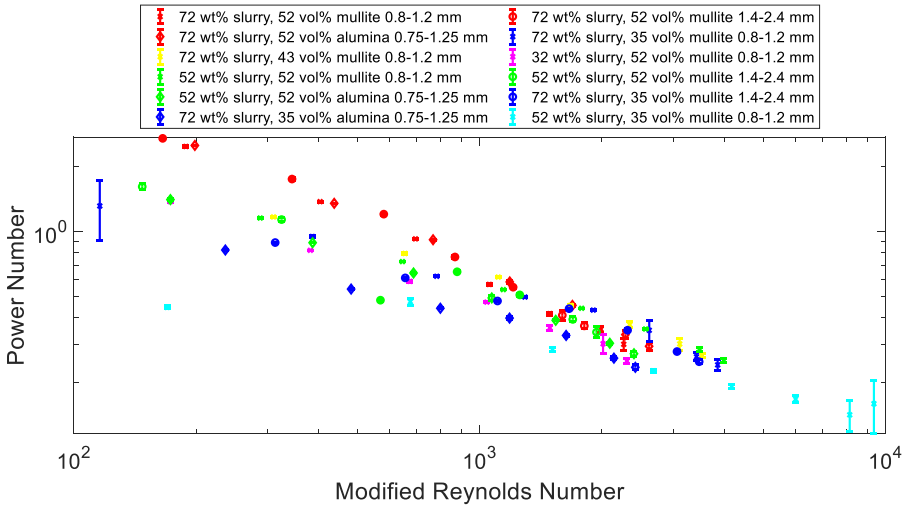

Figure 4.22: Po-Re Curve for Slurry-Grinding Media Systems, Assuming the Grinding Media are a Part of the Fluid, Metzner-Otto Constant, $k_S = 10.7\ n^{-0.15}$

From Figure 4.22, the data points lie closer to one line than in method 1 (Figure 4.16), which assumed the grinding media to be a part of the tank as opposed to the fluid. The 52 wt% slurry with 35 vol% mullite beads did not fit well to the power predictions that exclude the grinding media from the viscosity term, with power draw being largely over predicted in Figure 4.16. However, they are a significantly better fit to this correlation. The low power draw is predicted since the low viscosity measured for the grinding media and fluid combination leads to the calculation of a high Reynolds number. The power prediction fit for this model is shown in Figure 4.23.

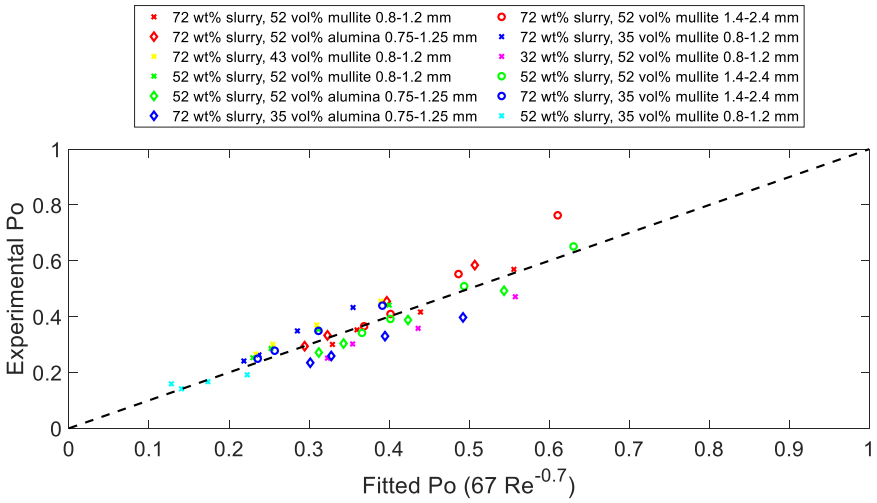

Figure 4.23: Best Fit Relation Between Power Number and Reynolds Number for Slurry and Grinding Media Systems, $k_s = k_s = 10.7\ n^{-0.15}$

Figure 4.23. confirms that in the case of the grinding media being considered as part of the fluid, predicting the power number based off of the Reynolds number works well. However, due to evidence of there being some vortexing behaviour in Chapter 5, empirical relations were fitted using the Froude number and Stokes number to determine if the fit could be further improved, as shown in Figure 4.24 and Figure 4.25. Since the viscosity data in section 4.3.2 showed that the viscosity does not change significantly between the two sizes of mullite grinding media beads but the power draw is still very different for these, the potential use of the Stokes number was still considered.

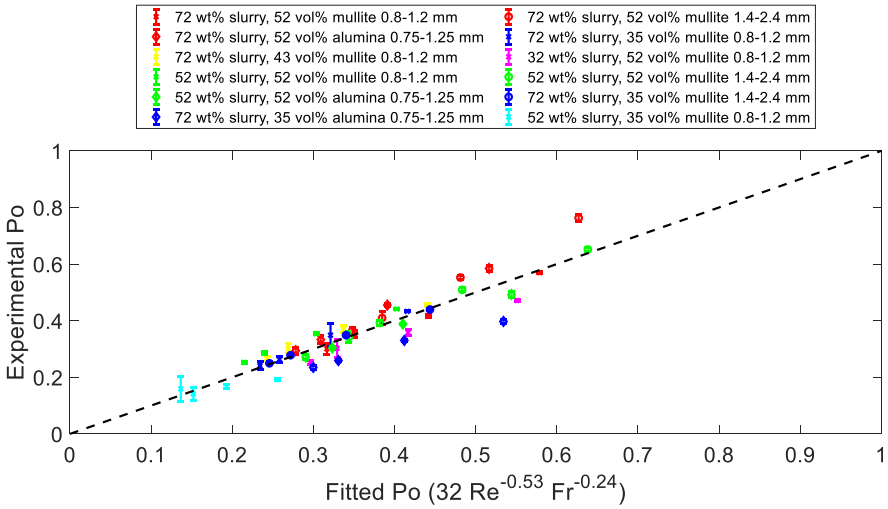

Figure 4.24: Best Fit Relation Between Power Number, Reynolds Number and Froude Number for Slurry and Grinding Media Systems, $k_s = k_s = 10.7\ n^{-0.2}$

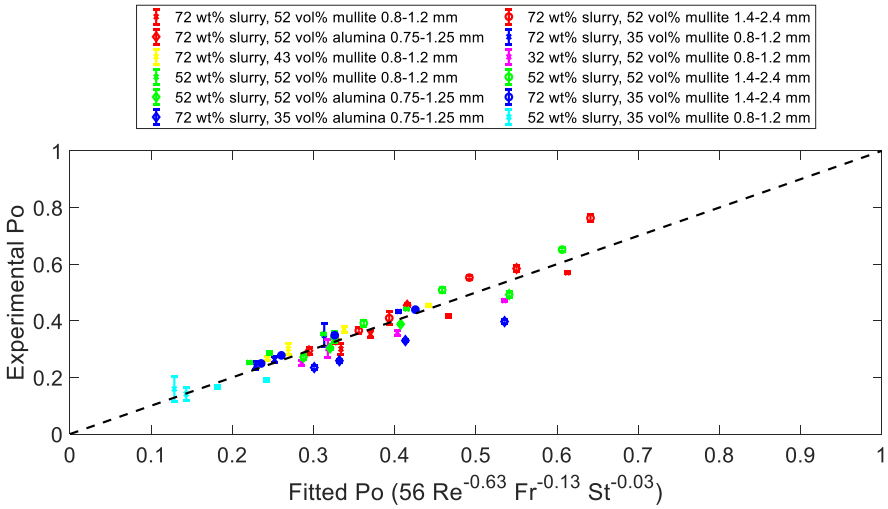

Figure 4.25: Best Fit Relation Between Power Number, Reynolds Number, Froude Number and Stokes Number for Slurry and Grinding Media Systems, for slurry and grinding media, $k_s = 12\ n^{-0.12}$ for slurries only, $k_s = 13$

In Figure 4.25, the exponent of the Stokes number is close to zero, suggesting that when the grinding media have already been included in density and viscosity terms, how well they follow the flow of the fluid is less important for the power draw prediction. The percentage errors for the different models are summarised in Table 4.7.

Table 4.7: Error Associated with Power Number Correlations, Assuming Grinding Media are a Part of the Fluid

	$Po = A\,Re^{x}$	$Po = A\,Re^{x}\,Fr^{y}$	$Po = A\,Re^{x}\,Fr^{y}\,St^{z}$
Average error (%)	12%	10%	10%
Max error (%)	34%	33%	34%

Unlike in the first method which assumed the grinding media beads are a part of the tank set up and hence excluded from the viscosity term, the addition of Froude Number and Stokes number to the correlation does significantly not improve the average error of the correlation. The maximum error is similar in all cases. This largest error is associated with the 72 wt% slurry with 35 vol% 0.75-1.25 mm mullite beads, where the correlation over predicts the power draw. With 52 wt% slurry and 35 vol% mullite beads, it was observed using PEPT that the shape of the vortex was different to other cases, extending below the impeller and reaching the lid of the vessel. However, the vortex shape observed using PEPT for 72 wt% slurry with 35 vol% alumina beads was close to the expected shape, making the vortex shape unlikely to be the reason for the power draw being over predicted in this case.

The findings in Table 4.7 suggest that when grinding media are included in the measured viscosity and the fluid density, it is not necessary to include additional dimensionless numbers in the Po-Re plot.

4.3.5. Testing and Comparing the Models

To test the models, a series of experiments were conducted to compare the power draw predicted using the different models with the experimentally measured power

draw. The aim of the tests is to consider different grinding media amounts and slurry solids contents within the range tested and to consider an additional size range of mullite grinding media and determine how well they fit to the different models proposed. The tests conducted are summarised in Table 4.8.

Table 4.8: Summary of Tests Conducted to Test Model

Test	Grinding Media Type	Grinding Media Amount (vol %)	Slurry Solids Content (wt%)
a	Mullite 0.8 – 1.2 mm	42	56
b	Mullite 1.4 – 2.4 mm	40	52
c	Mullite 1.2 – 1.6 mm	50	70
d	Alumina 0.75 – 1.25 mm	44	60

A comparison between the experimentally measured power draw and the power draw predicted using each model is shown in Figure 4.26. When the grinding media beads are not included in the viscosity term, the models including the Froude number and a method of considering the grinding media beads are evidently notably better than methods excluding these terms. However, when grinding media are included in the viscosity term, the three models provide similar results and so the predictions using all three methods with grinding media include in the fluid are included in the comparison.

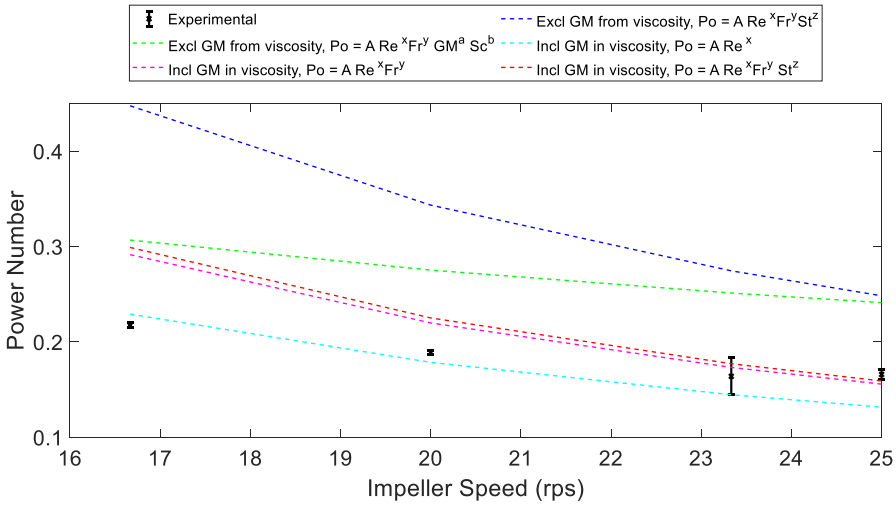
Experimental
Excl GM from viscosity, Po = A Re ^x Fr^y GM^a Sc^b
Incl GM in viscosity, Po = A Re ^x Fr^y
Excl GM from viscosity, Po = A Re ^x Fr^y St^z
Incl GM in viscosity, Po = A Re ^x
Incl GM in viscosity, Po = A Re ^x Fr^y St^z
Power Number
Impeller Speed (rps)
0.1
0.2
0.3
0.4
16
17
18
19
20
21
22
23
24
25

(a)

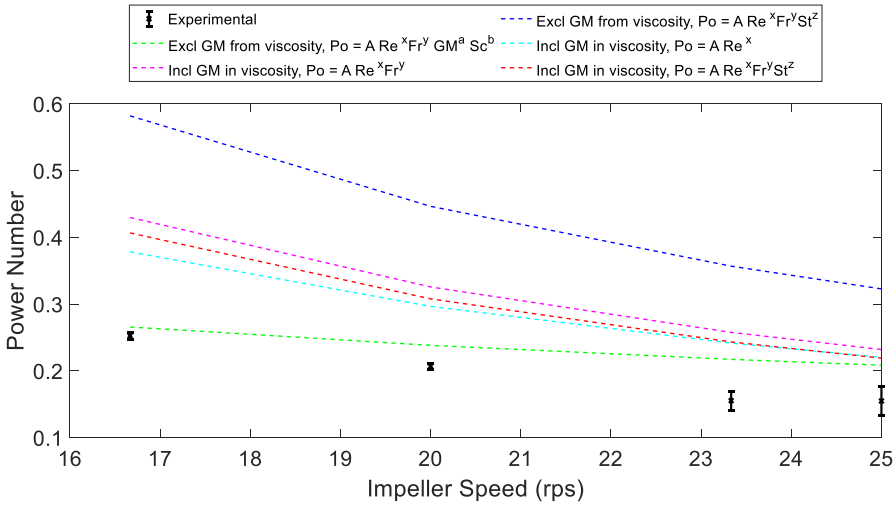
Experimental
Excl GM from viscosity, Po = A Re ^x Fr^y GM^a Sc^b
Incl GM in viscosity, Po = A Re ^x Fr^y
Excl GM from viscosity, Po = A Re ^x Fr^y St^z
Incl GM in viscosity, Po = A Re ^x
Incl GM in viscosity, Po = A Re ^x Fr^y St^z
Power Number
Impeller Speed (rps)
0.1
0.2
0.3
0.4
0.5
0.6
16
17
18
19
20
21
22
23
24
25

(b)

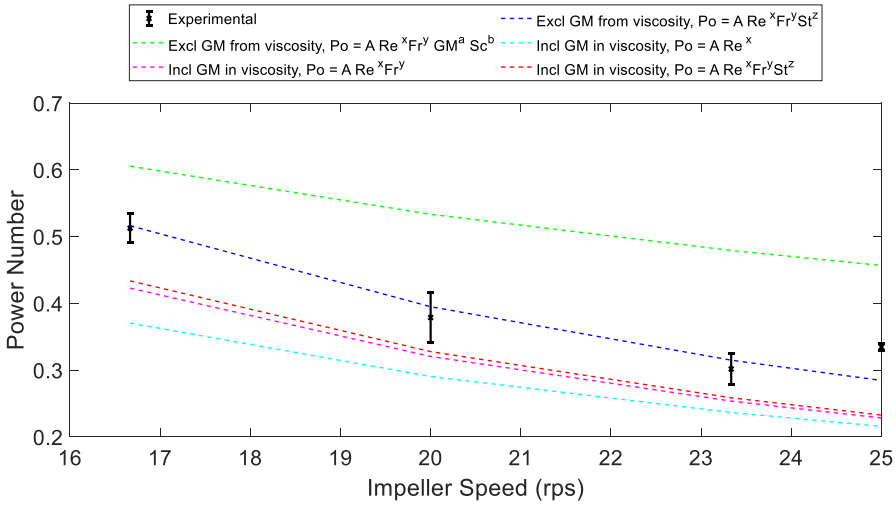
Experimental
Excl GM from viscosity, Po = A Re ^x Fr^y GM^a Sc^b
Incl GM in viscosity, Po = A Re ^x Fr^y
Excl GM from viscosity, Po = A Re ^x Fr^y St^z
Incl GM in viscosity, Po = A Re ^x
Incl GM in viscosity, Po = A Re ^x Fr^y St^z
Power Number
Impeller Speed (rps)
0.2
0.3
0.4
0.5
0.6
0.7
16
17
18
19
20
21
22
23
24
25

(c)

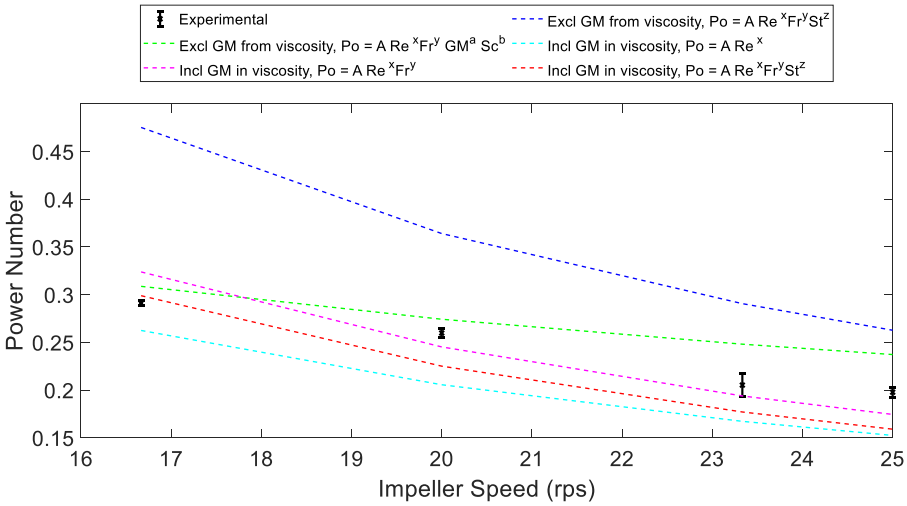

(d)

Figure 4.26: Experimental Power Number and Power Number Predicted Using Each Model (Model Test Conditions Defined in Table 4.8 for (a) to (d)). Error bars indicate fluctuations over a 10 second measurement

From Figure 4.26, it can be deduced that the models that excludes the grinding media from the viscosity term are good in certain but limited circumstances. The new method of including grinding media in the viscosity term is a better fit for a wider range of cases than methods associated with using a viscosity of the fluid only. In section 4.3.4, where grinding media were included in the density and viscosity terms, the three correlations ($Po\ \alpha\ Re^a$, $Po\ \alpha\ Re^a\ Fr^b$ and $Po\ \alpha\ Re^a\ Fr^b\ St^c$) gave approximately the same average power prediction errors, suggesting that it may be favourable to use a simple equation where $Po\ \alpha\ Re^a$. However, in cases (c) and (d), where grinding media types differ, the models including the Froude number and Stokes number provide an improvement to the power prediction.

In Figure 4.26(c), the correlations excluding grinding media from the viscosity terms fit best to the experimental power draw. Although the size of grinding media used is different to those used in the model development, the slurry concentration and grinding

media amount are very close to the values most commonly used in making the correlation. Hence, this illustrates that the correlation with no grinding media consideration works well in a limited range of cases, where conditions are similar to those used in building the correlation.

As can be seen from the model tests, each of the models has their own advantages and disadvantages and producing one model to fit to every scenario in a stirred media mill is difficult due to the interactions between the fluid and the grinding media and the complex flow patterns seen in Chapter 5. The average % error using each model for each test is summarised in Table 4.9.

Table 4.9: Average % Error Using Each Model for Each Test

		Grinding Media Excluded from Viscosity		Grinding Media Included in Viscosity		
Grinding Media Type/Amount	**Solids Content (wt%)**	$Po = A\,Re^x\,Fr^y\,St^z$	$Po = A\,Re^x\,Fr^y\,GM^aSC^b$	$Po = A\,Re^x$	$Po = A\,Re^x\,Fr^y$	$Po = A\,Re^x\,Fr^y\,St^z$
42 vol% 0.8 – 1.2 mm Mullite	56	76	46	10	15	17
40 vol% 1.4 – 2.4 mm Mullite	52	121	24	47	60	52
50 vol% 1.2 – 1.6 mm Mullite	70	6	39	27	20	18
44 vol% 0.75 – 1.25 mm Alumina	60	44	13	18	8	11
Average of 4 Tests		**62**	**31**	**26**	**25**	**30**

From Table 4.9, it is clear that the measurement of the fluid and grinding media together in the vane rheometer offers an improvement on power prediction methods. The method of including the Stokes number whilst the grinding media are considered a part of the fluid does not improve the model. This is because of the very low exponent

of the Stokes number and the beads already being considered within the viscosity measurement. Hence, for the practicality and simplicity of predicting power draw, the Stokes number should be discounted when using the correlations.

4.3.6. Comparing Glycerol-Water Solutions and Calcium Carbonate Slurries

To investigate the effect of changing the fluid, glycerol-water solutions were compared with calcium carbonate slurries. When the Po-Re curve is plotted for glycerol-water solutions in Figure 4.27, it is evident that the Power number is consistently lower than for slurries, even at the same Reynolds number. The same equation linking k_s to the Power number exponent was used for both slurries and grinding media in finding a viscosity to use in calculating the Reynolds number.

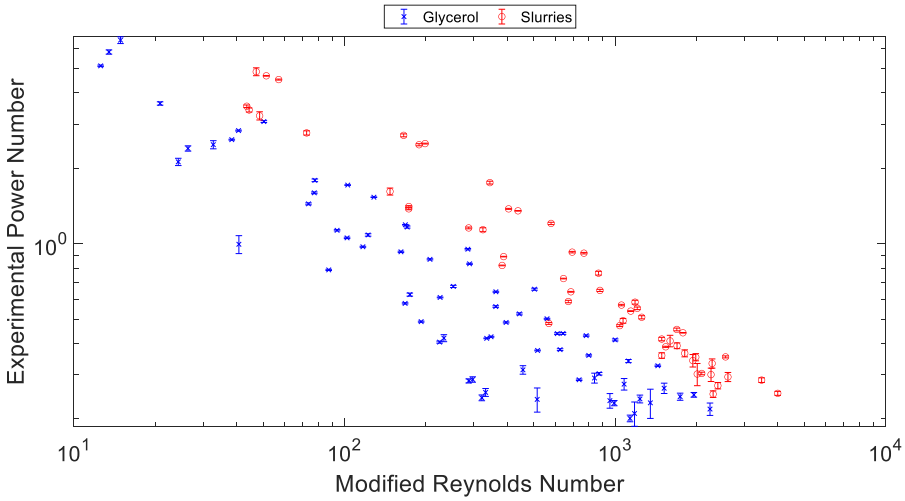

Figure 4.27: Power – Reynolds Number Curve for Slurries and Glycerol-Water Solutions with 52 vol% Grinding Media – Viscosity of Fluid and Grinding Media Combination Measured with Vane Rheometer Geometry

From Figure 4.27, the Power number at a given Reynolds number for glycerol-water solutions is generally lower than for slurries. This suggests that the fluid type is

affecting the power draw of the mill. The only fluid term considered in the Power number is density. The viscosity in the Reynolds term affects the horizontal position; the glycerol and grinding media bead have a higher viscosity at a given shear rate than the slurry and grinding media.

The power draw at a defined Reynolds number is higher for slurries. It is possible that the high friction of the solids in the slurries compared with the lubricating action of the glycerol-water solutions affects the power draw. This term is partially accounted for in the viscosity term, since the interaction of the fluid and grinding media is measured in the vane rheometer. From Chapter 5, which uses PEPT to look at flow patterns, the vortex shape is similar whether glycerol-water solutions or calcium carbonate slurries are used.

The method of predicting Power number is only valid for calcium carbonate slurries; further tests are required before applying it to other materials being ground in stirred media mills.

4.4. Tribology

Whilst some important milling parameters are relatively simple to quantify and include in power prediction correlations, others are more complex due to the range of measurement methods available. One parameter that is expected to be important but is a challenge to quantify directly is the friction between the fluid and grinding media beads. As an initial investigation into the frictional differences between fluids, a

minitraction machine (MTM) was used, applying a constant force of 3 N at a range of entrainment speeds, with the resulting Stribeck curves shown in Figure 4.28.

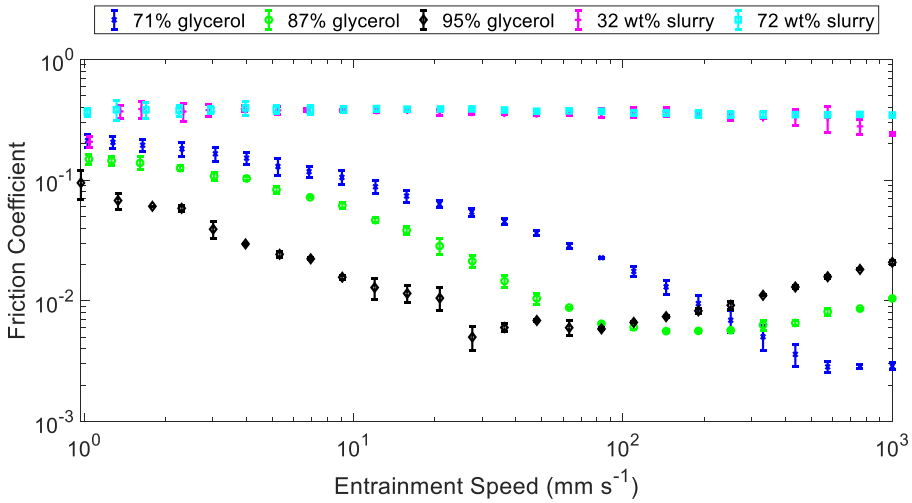

Figure 4.28: Stribeck Curves at 3 N for Glycerol-Water Solutions and Slurries with Stainless Steel Ball and Plate. Error bars show the standard deviation of 6 sweeps of entrainment speed

Figure 4.28 shows the expected Stribeck curves for glycerol-water solutions between a steel ball and plate – these are in agreement with other literature sources[163], which show three main regimes:

- Boundary regime - there is initially high friction where the surfaces come into contact due to the speed not being sufficient to entrain a lot of the fluid, friction is constant with speed in this small region.
- Mixed regime - at higher speeds, there is some fluid entrained but still some contact between the surfaces.
- In the hydrodynamic regime, due to the even higher speeds there is a thick film of glycerol completely separating the surfaces, which means that the friction between the surfaces is determined by drag, which is influenced by the viscosity

of glycerol; the glycerol-water solutions with higher water content have lower friction due to their significantly lower viscosity.

For the calcium carbonate slurries, there was actually very little difference observed in the friction coefficient between samples of different solids concentrations. The curves are very flat as the rolling speed has very little effect on the measured friction coefficient, indicating that interactions between the solids are dominating; even at low entrainment speeds, the calcium carbonate particles are large enough to keep the ball and plate apart.

The behaviour of grinding media beads with glycerol in the vane rheometer and stirred media mill at high speeds relevant to milling is likely to be most comparable with friction factors at high entrainment speeds because of the thick film of glycerol between grinding media beads. This difference in friction could explain the difference in behaviour observed between different glycerol-water solutions with grinding media.

This method of using rolling friction between a ball and plate gives initial data on frictional properties of the fluids, and the higher friction coefficient for slurries at all entrainment speeds compared with glycerol-water solutions suggests why the power draw of the mill may be higher for slurries than glycerol-water solutions. However, it neglects the grinding media; interaction between the grinding media pushing past each other with fluid in the gaps is likely to result in different frictional properties. To consider the sliding motion of grinding media, a Forceboard could be used where a grinding media bead is pushed along a ceramic surface with fluid between. However, this

method only produces an average friction value at a given speed as opposed to a Stribeck curve. The overall friction in the mill is likely to occur at a wide range of forces and a wide range of speeds due to the flow patterns in the mill. These forces and speeds are highly dependent on the impeller speed and flow regimes; friction is greater at lower speeds when the beads are all in a packed bed than when they are fluidised.

Additionally, although initial tests were conducted at a force of 3 N, forces in the mill are likely to cover a wide range since the grinding media beads are of different sizes and hence different masses and there are also a range of grinding media velocities in different regions of the vessel. These factors make it challenging to quantify friction in the mill and directly relate it to power draw.

4.5. Summary

Due to the complex interactions between the fluid and grinding media, producing one empirical correlation for predicting power draw in a wide range of scenarios remains a challenge. All models have their limitations, but some remain useful. An adaptation of existing methods available in literature for stirred tanks was presented, which predicts power draw based on the slurry viscosity to a reasonable degree of accuracy, but falls down with low grinding media amounts or slurry solids contents. Additionally, although different parameters can be accounted for individually in correlations, the overlapping of these parameters is not considered. For the best power predictions, a new correlation would be required for each grinding media type and fill volume, which is impractical. A key issue with this method is the accuracy of the viscosity measurement

method, particularly when solids contents are low because the torque measurement is close to the lower limit of the instrument.

The new proposed method of measuring a combined viscosity of the fluid and grinding media using a vane rheometer predicts the power draw to within a reasonable degree of error for the widest range of cases. The Stokes number and Froude number were less important than in the case of excluding the grinding media from viscosity measurements, as was indicated by their low exponents in the correlations. There remain some potential drawbacks of this method – although it predicts power draw accurately in a wide range of cases, there are some cases with a large error. This method has shown potential but there are further improvements suggested such as using a serrated cup to eliminate wall slip. Excessive vortexing and wall slip in the rheometer at shear rates greater than 100 s^{-1} means that the power law behaviour exhibited below 100 s^{-1} must be extrapolated outside the required range when the estimated shear rate in the mill is greater than this. Additionally, the application of the Metzner-Otto correlation outside of the laminar regime should be used with caution and further research is recommended using CFD to determine how well the Metzner-Otto correlations estimate the effective impeller shear rate.

This section shows that the power draw is, in some cases, challenging to predict using correlations commonly applied to stirred tanks. In Chapter 5, PEPT is used to compare flow patterns when different operating parameters are changed and link this to the observed differences in power draw.

5. GRINDING MEDIA MOTION IN STIRRED MEDIA MILLS

5.1. Introduction

The flow pattern inside stirred media mills is important to understand since it affects grinding media collisions and hence the breakage rate. In existing literature, Positron Emission Particle Tracking (PEPT) is typically used to look at flow patterns[33,118,164]. However, the measurement time to collect enough data for good time averaging (i.e. the grinding media has had time to travel throughout each region of the mill) is relatively long (approximately 10-20 minutes when one grinding media bead is irradiated). The calcium carbonate particle size decreases with grinding, meaning that there are changes in slurry viscosity (See Chapter 4). This may cause changes in flow pattern. These sort of changes cannot be observed from the time averaged PEPT data.

Another technique commonly used to look at flow patterns is particle image velocimetry (PIV), which allows a central plane of the vessel to be observed over a much shorter timescale (a few seconds). However, the requirement for transparency makes it impractical to apply to stirred media mills. Even if a transparent vessel is used with refractive index matched glass beads and fluid, the high speeds results in vortex formation, which leads to air being drawn into the fluid, making it cloudy and obscuring visibility. As an alternative to PIV, a transparent vessel and the usual stirred media mill set-up can be used to observe the grinding media motion using a high-speed camera, but only at the wall of the vessel. This provides information about the instantaneous flow pattern at the wall and from this data, flow patterns in other parts of the vessel can be inferred.

This chapter aims to investigate the potential usefulness of high-speed imaging in understanding more about the flow patterns in stirred media mills. To compare this with the motion of the grinding media in all regions of the vessel and assess the shape of the vortex, PEPT was used. Motion was compared when a range of grinding media amounts and fluid types are used to investigate reasons for power draw differences in Chapter 4.

5.2. High Speed Imaging (HSI)

HSI was used to observe the motion of grinding media at the wall of a transparent vessel. Glycerol-water solutions were initially used in place of calcium carbonate slurries to determine the extent to which fluid viscosity affects flow pattern. This was subsequently compared with calcium carbonate slurries.

5.2.1. Grinding Media Motion at the Wall in a 71% Glycerol-Water Solution (0.02 Pa s)

Using glycerol in place of calcium carbonate slurries enables the observation of how the viscosity of a fluid affects the motion of grinding media since it is Newtonian. The glycerol-water solutions identified as being in the same viscosity range of calcium carbonate slurries in Chapter 4 were used.

Grinding media move at different velocities in different regions of the mill wall, as shown in Figure 5.1. Dimensionless velocities (with respect to tip speed) enable comparability between runs at different impeller speeds since the transfer of energy to bead motion is important. Velocities were split into horizontal ‘U’ and vertical ‘V’ components.

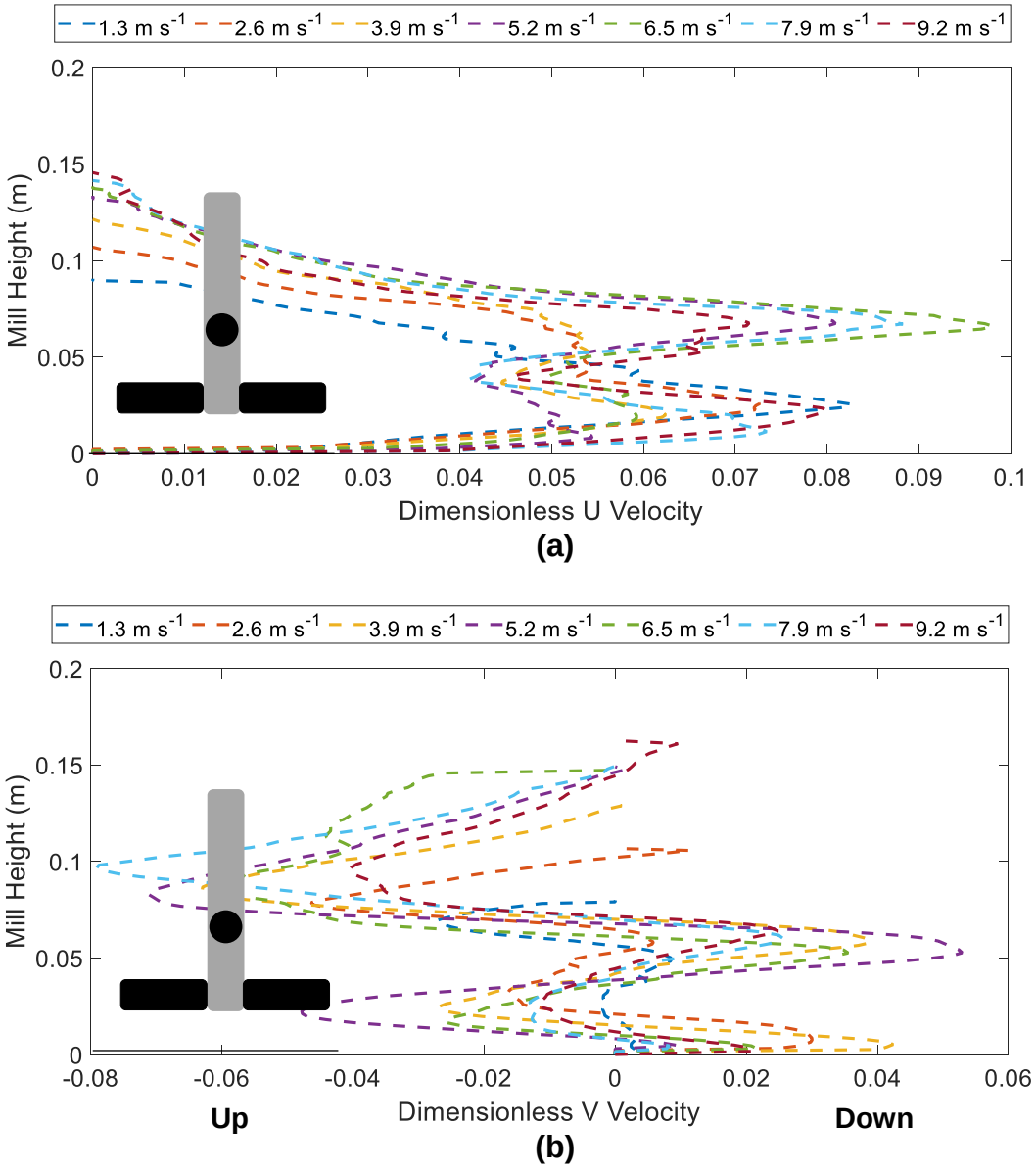

Figure 5.1: Average Dimensionless Velocity of 52 vol% 0.8-1.2 mm Mullite Beads in 71% Glycerol at the Vessel Wall Over One Complete Impeller Revolution at Increasing Impeller Speeds (a) Horizontal 'U' Velocity and (b) Vertical 'V' Velocity (Note that –ve 'V' velocity indicates upward motion)

The areas of higher and lower velocity seen in Figure 5.1 suggest that the rates and effectiveness of grinding media collisions may vary throughout the mill. However, this is difficult to infer from the HSI data directly since the direction of motion of each bead is important - if the beads are moving in the same direction at the same speed then they will not collide. It can be seen that the relative velocity and the height that the

grinding media reach up the wall changes with the impeller speed in the mill and that the velocity is generally dominated by the horizontal ‘U’ velocity; vertical ‘V’ velocities are smaller. Due to the vortex and fluidisation, the height that the grinding media reach at the impeller wall increases with increasing tip speed.

Figure 5.1(a) shows that the highest ‘U’ velocities are encountered approximately level with the impeller pins. At all impeller speeds, two clear peaks can be seen where the velocity of the grinding media beads at the wall is significantly higher adjacent to each impeller arm and lowest at the top and bottom of the vessel. However, this is less prominent at lower impeller speeds below 3.9 m s^{-1}, suggesting that below this speed the beads move around almost as a solid body, which has not yet been fluidised.

In terms of vertical ‘V’ velocities, Figure 5.1(b) shows that whether the grinding media beads at the wall move in an upward or downward position depends on their height relative to the impellers. Beads above the top impeller are moving in an upwards direction, whilst beads below the impellers move in a downwards direction. Within the impeller region, beads adjacent to the top impeller move in an upwards direction whilst beads adjacent to the bottom impeller move in a downwards direction. To examine the direction and magnitude of the grinding media bead velocities at the wall of the vessel, vector plots are shown in Figure 5.2. It should be noted that this is the average motion over one complete impeller revolution – section 5.2.1.1 considers whether the motion of the beads changes significantly when the impeller is in different angular positions.

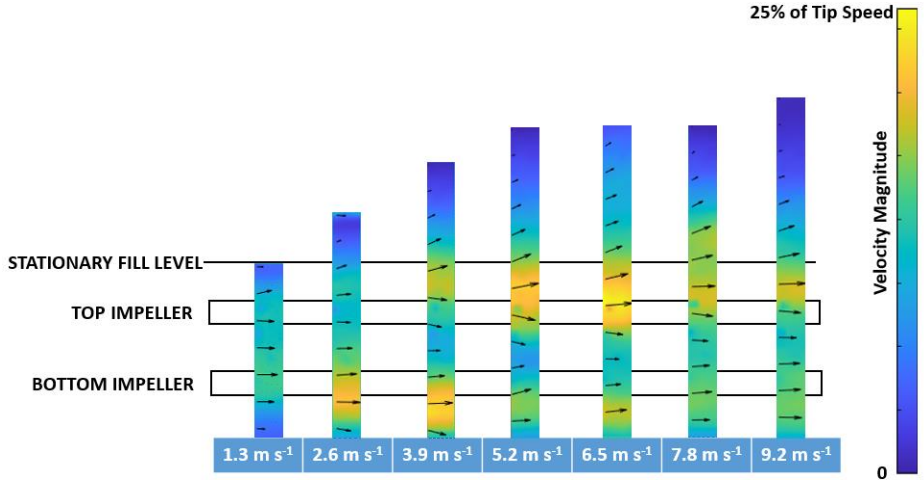

Figure 5.2: Velocity Vectors of Grinding Media at Vessel Wall for 52 vol% 0.8 – 1.2 mm Mullite Beads in 71% Glycerol at Different Impeller Tip Speeds – Average Over One Complete Impeller Revolution

From Figure 5.2, it is shown that although the beads have vertical velocity components, motion is predominantly close to horizontal at all heights at the wall of the vessel. The overall directions of motion observed in Figure 5.2 are in close agreement with published research by Barley et al.[28], which shows upwards motion above the impellers and downwards motion below the impellers. However, bead motion in the area between the impellers is suggested to be close to horizontal by Barley et al. From Figure 5.1b, due to the two large 'V' velocity peaks in opposite directions in this region, the average 'V' velocity in this region is expected to be close to zero and can be assumed to be zero as a simplification. However, further detail can be obtained by splitting this into separate regions for each impeller. This may be more complex in the case of larger scale industrial stirred media mills, where often many more impellers stacked on top of each other are used in larger scale mills. In this small-scale lab case, the difference could be caused by the base effects of the vessel; the beads at the bottom of the vessel and close to the bottom of the impeller are slowed down by the base, whereas those higher up are not as influenced by this.

There are multiple peaks in Figure 5.1b, with the vertical 'V' velocity being more dependent on the location of the bead with respect to the impellers than the horizontal 'U' velocity, which only shows a clear velocity peaks adjacent to each impeller. In Figure 5.3, the maximum 'U' velocity in the region adjacent to each impeller has been plotted. To estimate errors associated with this, the average peak value of five consecutive impeller revolutions was plotted with the error bars representing the standard deviations from the five revolutions. Although a true average turbulent value would require many more revolutions, five was deemed to be sufficient for looking for the point where behaviour becomes random. Five revolutions is a compromise of camera memory and processing time vs number of revolutions analysed.

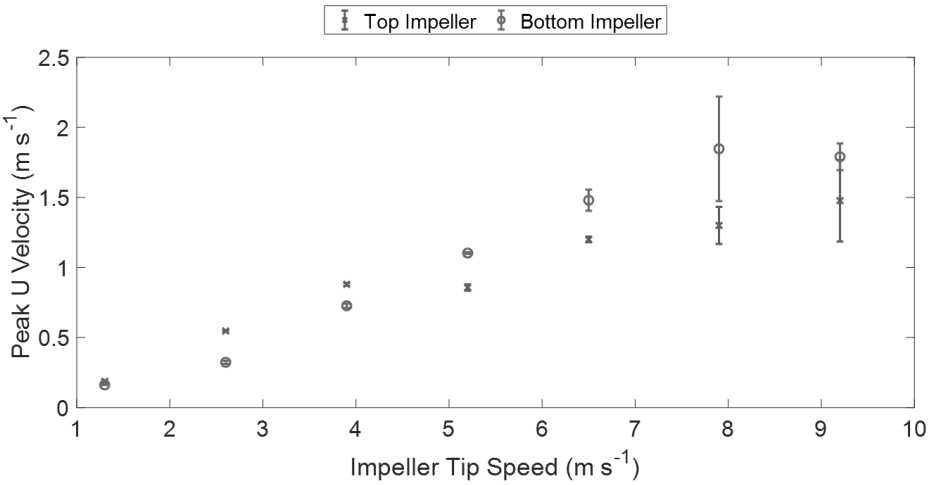

Figure 5.3: Average Peak Dimensionless 'U' Velocity Over One Full Impeller Revolution for 52 vol%0.8-1.2 mm Mullite Beads in 71% Glycerol in the Wall Regions Adjacent to the Top and Bottom Impellers. Error bars represent one standard deviation for 5 impeller revolutions. The absence of error bars indicates that the standard deviation is very low

From Figure 5.3, it can be seen that as the tip speed of the impeller increases, the 'U' velocity of grinding media beads at the wall adjacent to the impeller increases with increased tip speed, until it starts to plateau at a critical value, whilst also becoming significantly more variable. At lower impeller tip speeds, grinding media near the top

impeller move faster, whereas at higher impeller tip speeds, those near the bottom impeller move faster. This could be attributed to the packing and fluidisation of the grinding media beads; at lower speeds, the grinding media beads are moving as a fixed body whilst at higher speeds, fluidisation has occurred and the grinding media beads are less impacted by beads on top compressing them.

The peak velocity value is not the only contributing factor when considering grinding media motion; the width of this peak also varies, which means that the number of grinding media beads moving at these high speeds increases. To consider this impact, the total kinetic energy (KE) reaching the grinding media at the vessel wall was calculated using Equation (5.1), from the mass of beads at the wall, (m), and the bead velocity at the wall, (v). It was assumed that the beads at the wall cover a 1 mm thickness and that the wall is uniformly covered at the same packing fraction at each impeller speed.

$$KE = \frac{1}{2}mv^2 \tag{5.1}$$

The kinetic energy has been plotted in Figure 5.4. Since it is important to compare this to the amount of energy put into the mill, the measured power draw of the mill from Chapter 4 is plotted on the x-axis instead of impeller speed.

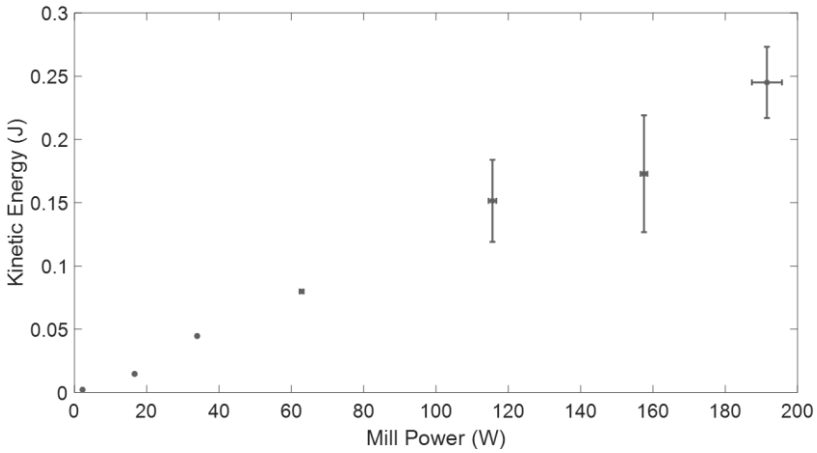

Figure 5.4: Kinetic Energy at Wall for 52 vol% 0.8 – 1.2 mm Mullite Beads in 71% Glycerol. Horizontal error bars represent fluctuation in power over 10 seconds. Vertical error bars represent standard deviation of velocity for 5 impeller revolutions

From Figure 5.4, the kinetic energy of the beads at the wall of the mill increases less rapidly with power draw once higher power is reached. This could be a result of more energy being dissipated as heat, noise and vibration or due to other beads moving faster and the energy not being transferred to the beads at the wall of the vessel. It should also be noted that there is significantly more variation in velocity at high speeds, shown by the larger error bars. This is investigated further in section 5.2.1.2.

5.2.1.1. Surface Plots – Considering the Impeller Position

Using an average velocity of one impeller revolution does not completely describe what is happening inside the mill; the grinding media beads move differently when an impeller pin directly passes them than when they are in the region between two pins. This is important because the acceleration and direction change of grinding media is likely to result in collisions that cause particle breakage. To investigate this, the motion of the grinding media beads was assessed in conjunction with the impeller position, as is shown in Figure 5.5 for horizontal motion.

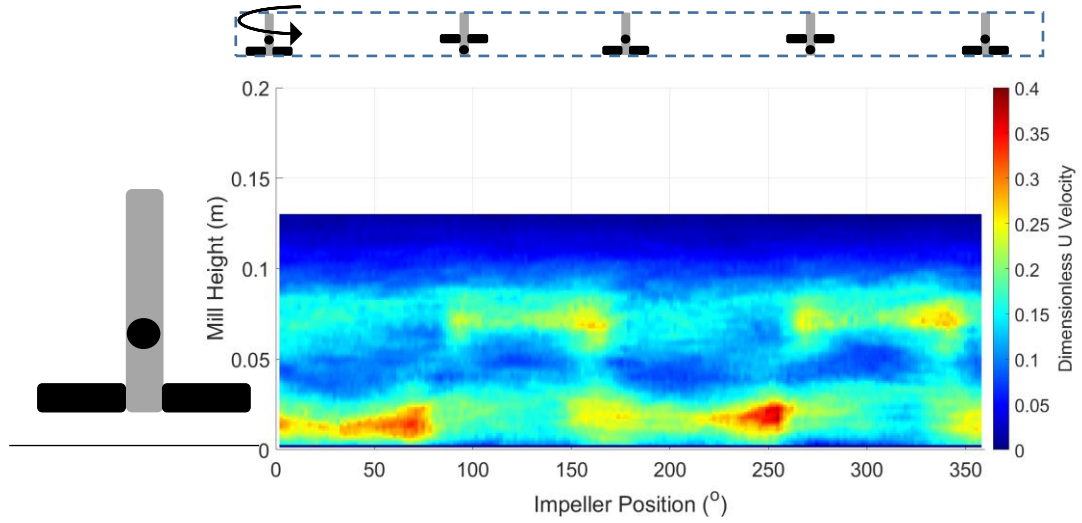

(a)

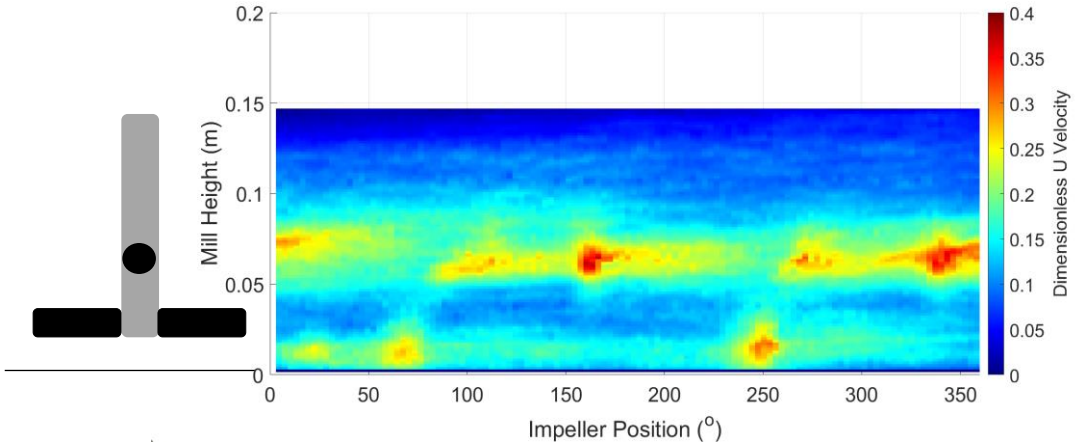

(b)

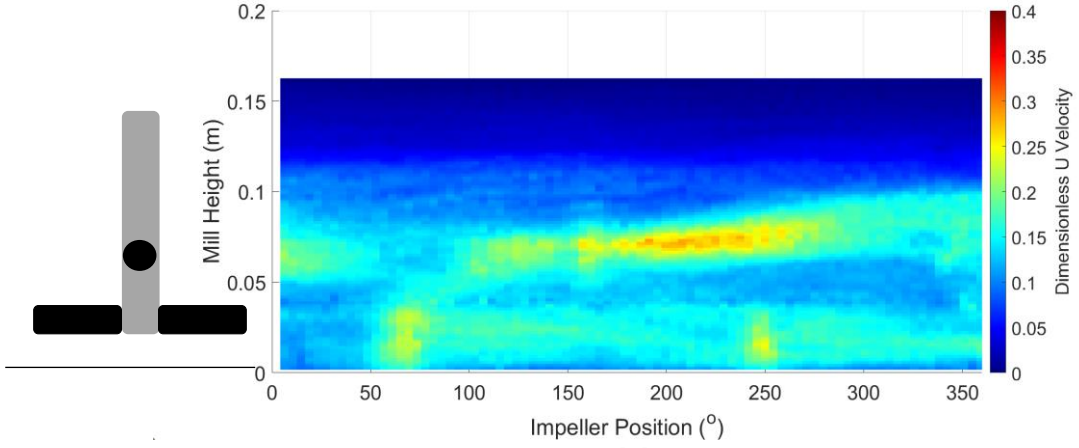

(c)

Figure 5.5: Surface Plots Demonstrating Change in Dimensionless 'U' Velocity at Wall as Impeller Rotates for 52 vol% 0.8 – 1.2 mm Mullite Beads in 71% Glycerol at Impeller Tip Speeds (a) 3.9 m s^{-1} (b) 6.5 m s^{-1} (c) 9.2 m s^{-1}

It can be seen from Figure 5.5 that when the impeller directly passes grinding media beads, it accelerates those beads, leaving a tailing velocity behind it. There are some differences between the two top impeller pins (at 0 and 180 °). However this is most likely due to wear of the impeller pins which cause differences in how the grinding media move as each pin passes - one of the impeller arms shows a dent at the edge. These differences are greater at high speeds where the motion becomes more chaotic and less repetitive; this repeatability is investigated further in section 5.2.1.2. At the highest impeller speeds, less of the energy from the impeller is transferred to the grinding media beads at the wall of the vessel; dimensionless velocities at the wall are lower and the passing of the impeller pins has less of a defined effect on the motion of the grinding media beads.

To describe vertical motion, surface plots in the ‘V’ direction are displayed in Figure 5.6.

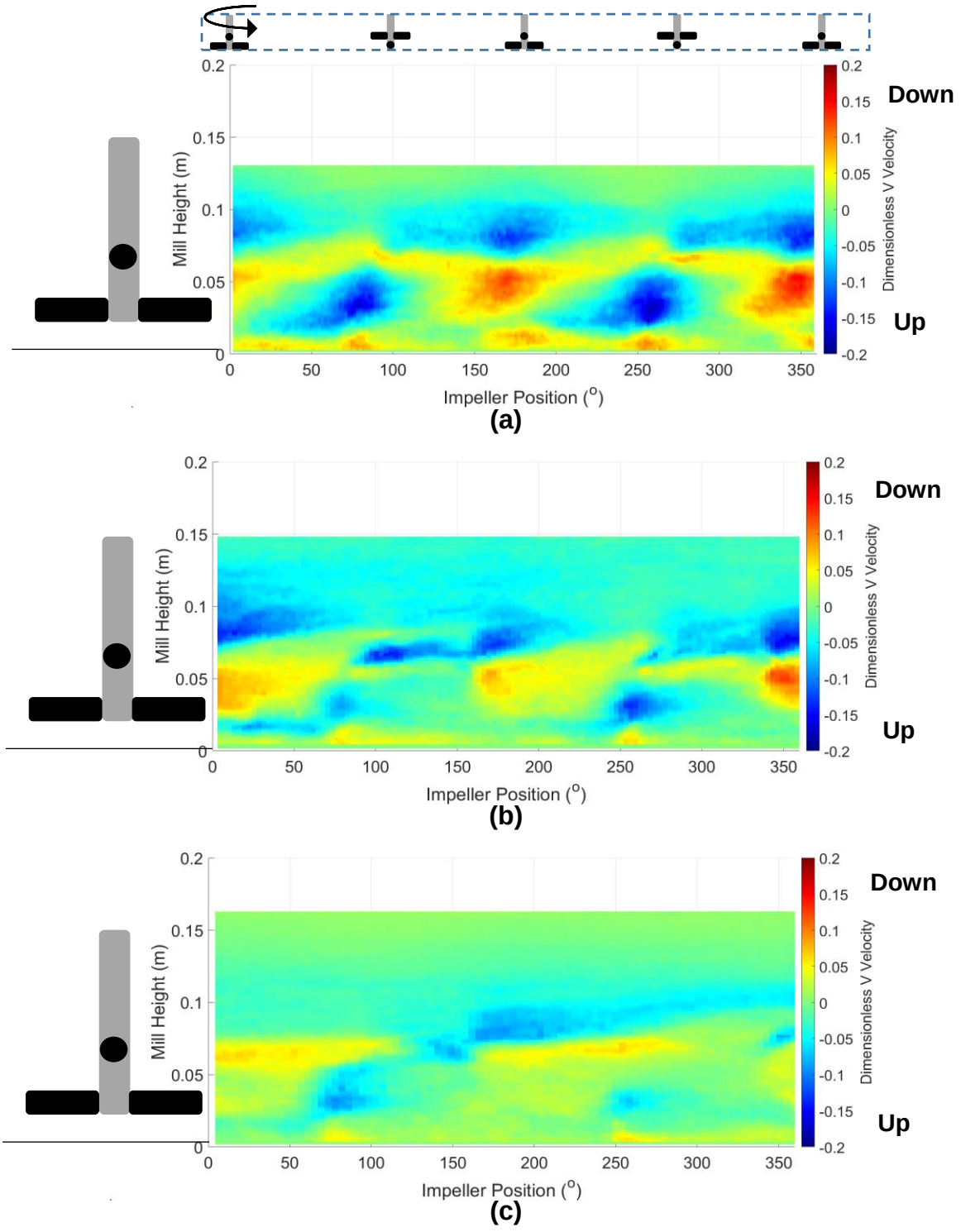

Figure 5.6: Surface Plots Demonstrating Change in Dimensionless 'V' Velocity at Wall as Impeller Rotates for 0.8 – 1.2 mm Mullite Bead Velocity in 71% Glycerol at Impeller Tip Speeds (a) 3.9 m s^{-1} (b) 6.5 m s^{-1} (c) 9.2 m s^{-1}

From Figure 5.6, it can be seen that as an impeller pin passes in line with the grinding media beads, it pushes the beads upwards. For beads around the bottom impeller, it appears that they get pushed downwards by the passing of the top impeller, particularly at lower speeds. At higher speeds, this downwards motion is greatly reduced and vertical motion at the wall is predominantly close to zero or in a slow upwards direction. This net upwards motion means that the grinding media beads in the vortex in the centre of the vessel must be moving in a net downwards motion. This was confirmed using PEPT in section 5.3. The up and down motion as the impellers rotate is accompanied by the level at the wall oscillating whilst the mill is in operation.

The overall direction of motion is highly dependent on the impeller position, as is shown in Figure 5.6 where the vertical velocity and direction changes significantly over one impeller revolution. To assess the general direction of motion at the vessel wall, vector plots were produced in Figure 5.7.

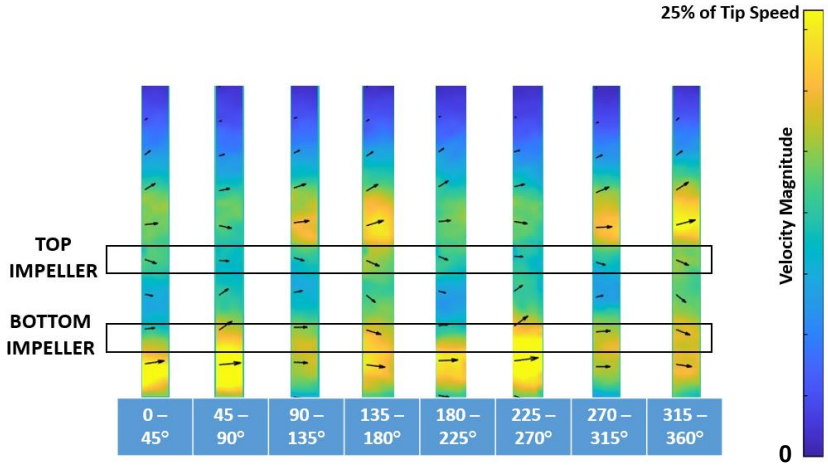

(a)

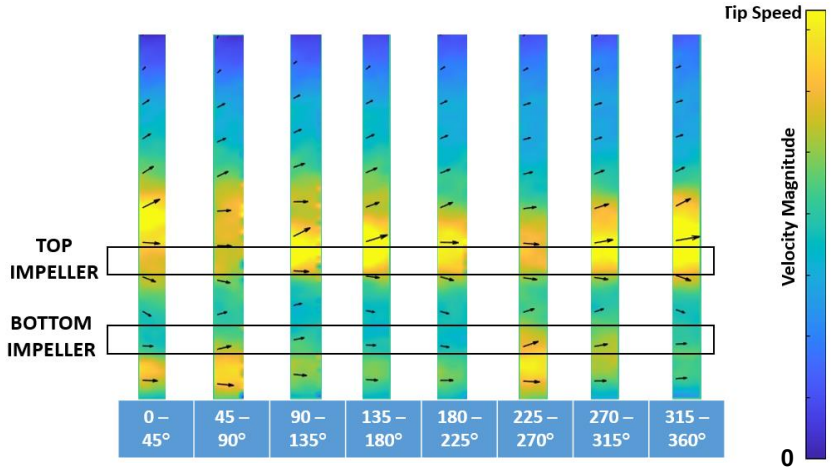

(b)

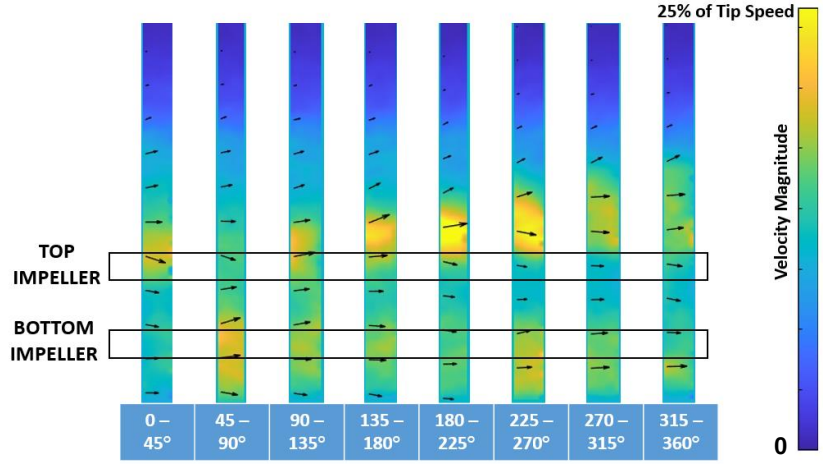

(c)

Figure 5.7: Vector Plots for Grinding Media Beads at Wall for 0.8 – 1.2 mm Mullite Bead Velocity in 71% Glycerol at Impeller Tip Speeds (a) 3.9 m s^{-1} (b) 6.5 m s^{-1} (c) 9.2 m s^{-1} Note that 0 ° is where the top impeller directly passes the window of beads being observed.

From Figure 5.7, the difference in direction of motion when the impeller is in different positions is apparent. The largest impact is on beads close to the impeller, and there is very little impact on the beads above the impeller. As motion is consistently close to horizontal, the direction changes are relatively subtle. Nevertheless, they exist and are likely to lead to particle collisions.

5.2.1.2. Investigating the Transition Zone

There appears to be a transition zone in the stirred media mill, where the flow goes from being steady to unsteady. This is evidenced in the surface plots in Figure 5.5 and Figure 5.6, where the velocity profile appeared to be more random and less strongly influenced by the passing of the impeller at high speeds. For initial quantification of the extent of the velocity fluctuations at the wall of the mill, error bars were plotted on the average velocity in the entire strip of the mill for a complete revolution, shown in Figure 5.8. The error bars show the standard deviation for five impeller rotations. As they are the standard deviations of the average velocity in each revolution, they negate the velocity differences occurring due to the cyclical motion of the impeller.

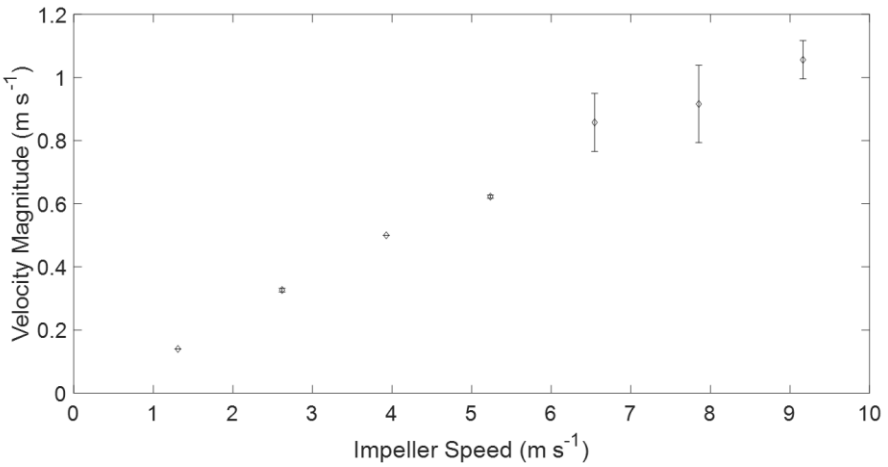

Figure 5.8: Average Velocity Magnitude at Vessel Wall for 52 vol% 0.8 – 1.2 mm Mullite Beads in 71% Glycerol at Vessel Wall Over 5 Impeller Revolutions

Athough Figure 5.8 does not give a true average turbulent velocity, this can be considered close to it. To obtain a true turbulent velocity, around 200 images would be required with the external trigger being in the same position for each image. This is a significantly large data amount for processing and also relies on the use of an external

trigger linked to the camera; due to the high shaft speed and the vibrations of the mill, external triggers do not work effectively.

From Figure 5.8, it can be inferred that there are flow instabilities at impeller tip speeds greater than 6.7 m s^{-1}. This suggests that speeds above this are most useful in grinding; the fluctuations in speed and turbulent behaviour will result in the most particle breakages. It may not actually be the highest tip speeds that give the most efficient grinding; it is inferred from the plateau that the lower tip speeds that result in turbulent flow may lead to more efficient grinding. This fits with findings in literature - Altun et al.[27] showed that increasing stirrer speed increases the efficiency of milling due to the larger amount of energy in collisions but only up to a critical impeller speed. After this point, energy is wasted and dissipated as heat as the energy in collisions is greater than that required to break particles, creating new surfaces.

To assess when and where the greatest instabilities happen, the grinding media ‘U’ velocities within the impeller region for three subsequent impeller revolutions were plotted for a range of impeller speeds. Since it is the repeatability at each speed as opposed to comparing between impeller speeds that is important, the curves were separated by adding an arbitrary y value to each point of each curve for any given impeller speed. The ‘V’ velocities show the same trends as ‘U’ velocities but are much smaller values and so data for V velocities can be found in Appendix C (section 10.3).

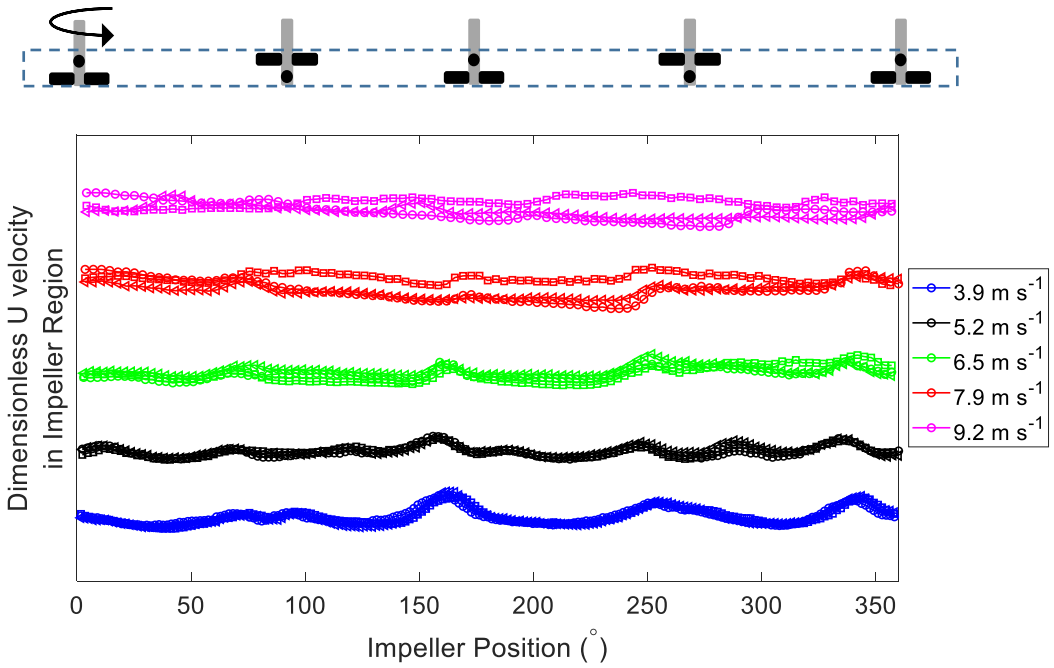

Figure 5.9: 'U' Velocities at Vessel Wall for 52 vol% 0.8 – 1.2 mm Mullite Beads in 71% Glycerol in the Impeller Region – Variation Over Three Impeller Revolutions

Figure 5.9 shows that for lower impeller speeds, the pattern of grinding media average 'U' velocity at the wall of the vessel is periodic, repeating each time the impeller shaft completes a revolution. As higher impeller speeds are reached, the periodicity reduces due to secondary flow effects occurring. It is hypothesised that the secondary flow effects could be caused by the impeller disrupting the vortex at high speeds. To investigate whether the effect on grinding media velocities around the top and bottom impeller are the same, this data was separated into looking only at the beads in the top and bottom impeller regions in Figure 5.10.

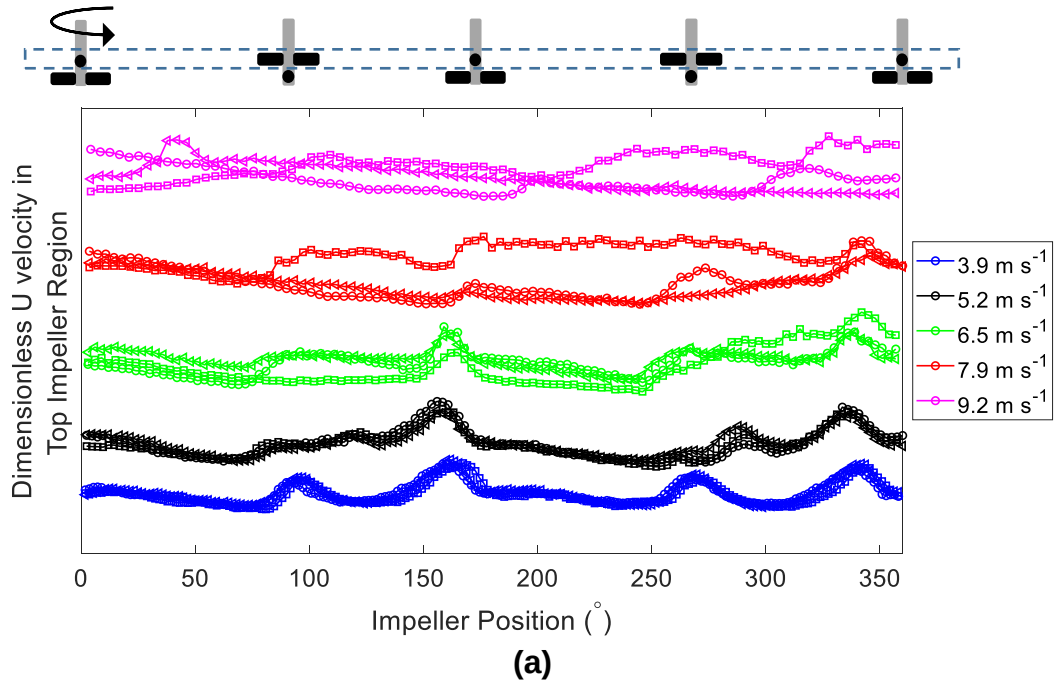

(a)

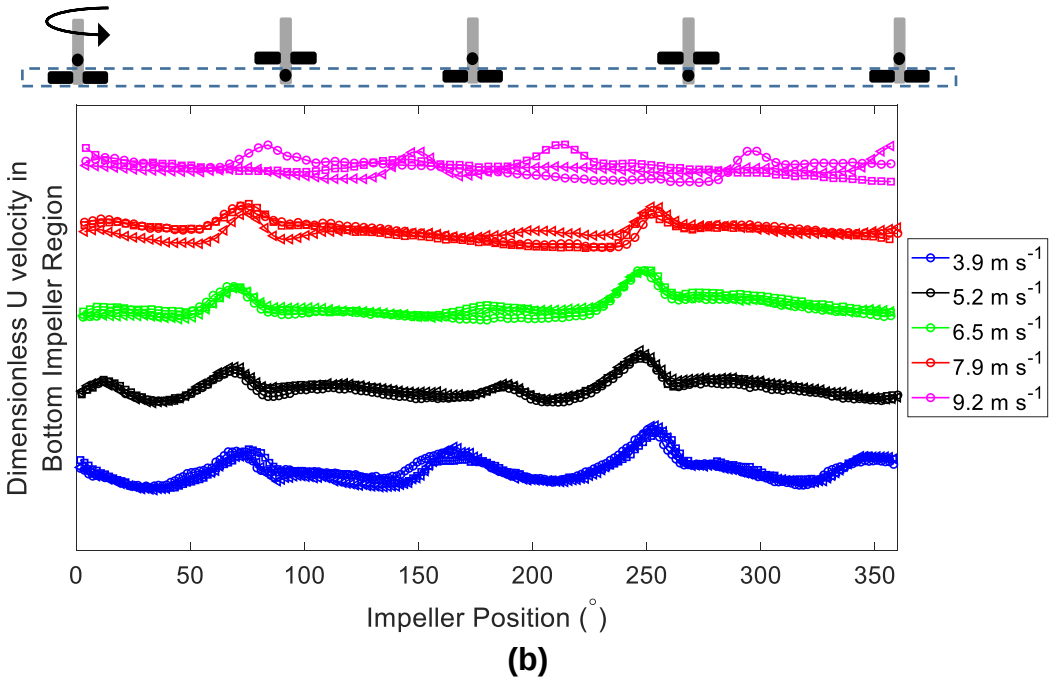

(b)

Figure 5.10: 'U' Velocities at Vessel Wall for 52 vol% 0.8 – 1.2 mm Mullite Beads in 71% Glycerol– Variation Over Three Impeller Revolutions (a) in Top Impeller Region (b) in Bottom Impeller Region

For the grinding media beads adjacent to the top impeller (Figure 5.10a), the periodicity of the grinding media bead motion is significantly influenced by impeller speed, with bead motion at 7.9 and 9.2 m s^{-1} varying greatly between each impeller revolution. This supports the theory that secondary flow effects caused by the impeller breaking up the vortex cause the grinding media bead motion to vary between impeller revolutions. This was verified using PEPT; it is observed that the vortex does get larger with increasing velocity and extends below the top impeller pin in section 5.3.5. However, even at the slowest experimental speeds used, the vortex extends below the top impeller pin, with the key difference being that the vortex is wider (i.e. further from the shaft) at higher speeds.

For grinding media beads adjacent to the bottom impeller (Figure 5.10b), the speeds of the beads still repeats with each passing of the impeller at higher speeds, with the exception of 9.2 m s^{-1}. This suggests that they are not as affected by the disruption of the vortex, potentially because the vortex does not extend down as far as the bottom impeller, as was observed using PEPT in section 5.3.5.

In order to further investigate the hypothesis that the reduction in periodicity and more random grinding media bead motion is that the secondary flow effects are caused by the impeller disrupting the vortex, images and videos were captured using an endoscopic camera, as shown in Figure 5.11.

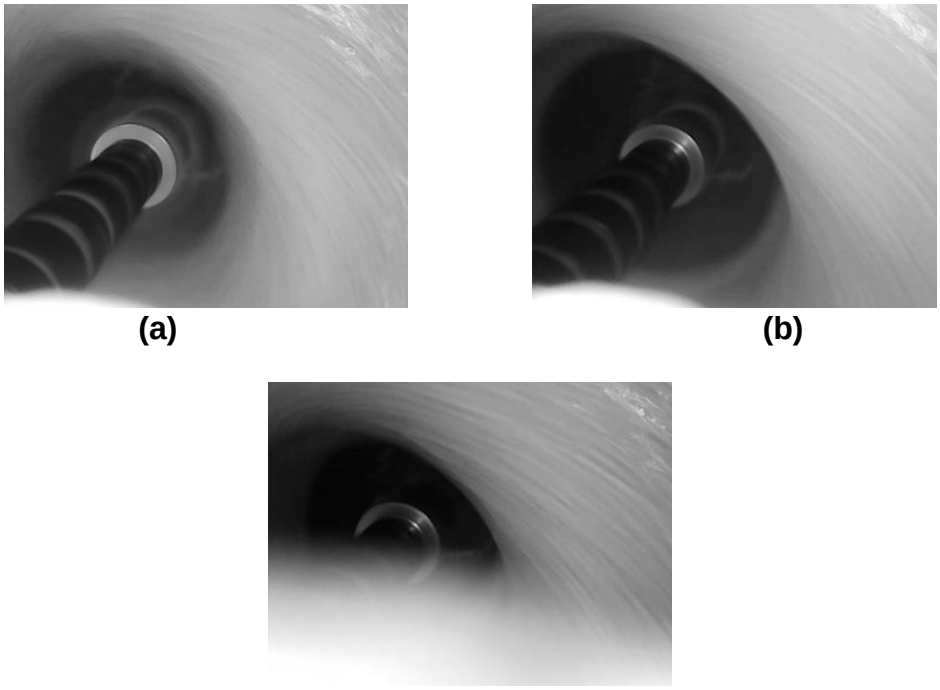

(a) **(b)**

(c)

Figure 5.11: Endoscope Images of Vortex with 52 vol% 0.8 – 1.2 mm Mullite in 71% Glycerol Grinding Media at Tip Speeds (a) 3.9 m s^{-1}, (b) 6.5 m s^{-1} and (c) 7.9 m s^{-1}

Figure 5.11 shows that for higher impeller speeds, the vortex is much larger and extends down below the top impeller. Due to the vortex position, the secondary flow effects have a bigger effect on beads that are around the top impeller and in the vortex region. This is more easily observed in videos captured using the endoscopic camera than still images as the stability of the vortex can be more easily observed. At 7.9 m s^{-1} and higher, it is evident from the videos that the vortex is unstable; it is no longer following a repeatable cylindrical movement pattern, as the lower impeller speeds do, explaining the lack of periodicity observed in Figure 5.10.

Vortex behaviour is difficult to quantify using an endoscopic camera; it is best observed using PEPT. However, PEPT only shows time-averaged data, meaning that instantaneous changes and vortex fluctuation cannot be seen.

5.2.2. The Effect of Changing Fluid Properties on Bead Motion

The motion of grinding media beads at the wall was compared for glycerol-water solutions of different concentrations and also for calcium carbonate slurries, since changing the fluid type was shown to have significant effect on power draw in Chapter 4. In order to compare bead velocities for slurries and glycerol-water solutions broadly, the average grinding media bead velocity magnitude at the wall was plotted for all fluid types in Figure 5.12. The associated variation was considered using error bars showing the standard deviation occurring over five consecutive impeller revolutions.

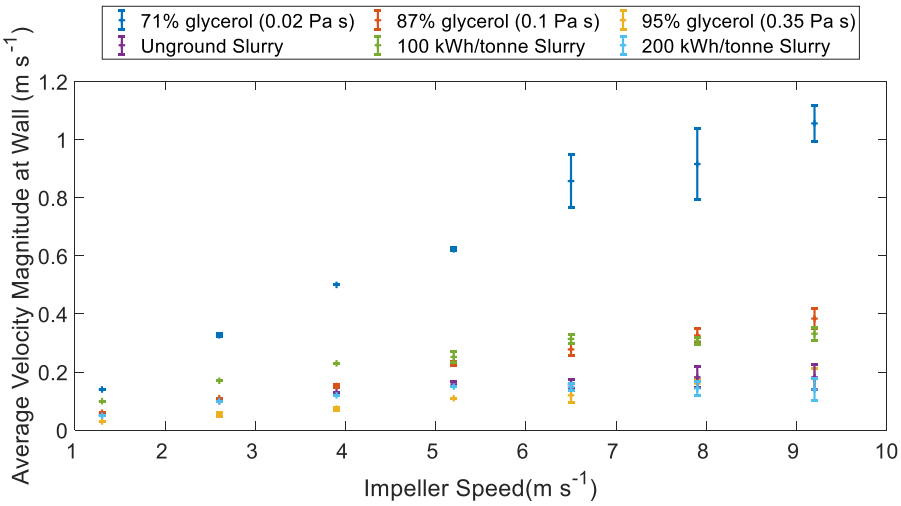

Figure 5.12: Velocity Magnitude at Vessel Wall for 52 vol% 0.8 – 1.2 mm Mullite Beads in Glycerol-Water Solutions of Different Viscosities and a 72 wt% Calcium Carbonate Slurries at Different Stages of Grinding

From Figure 5.12, all fluid types show the similar trend of having an initial linear increase followed by a transition point where the rate of change of velocity with impeller speed decreases. This consistently occurs at an impeller speed of approximately 6.5 m s^{-1}. The velocity at the wall and the amount of velocity fluctuation is much greater for 71% glycerol-water solutions than higher viscosity fluids and slurries. This implies that there is less dissipation in the bulk of the fluid and more at the wall of the vessel for the

low viscosity lubricating fluid. When calcium carbonate is ground, the dimensionless velocity magnitude actually decreases slightly with increasing impeller speed in the plateau region; this suggests that more energy is dissipated into the fluid at higher speeds as opposed to being transferred all the way to the grinding media at the wall.

Figure 5.12 does not take into consideration the different height that the grinding media reach up the wall of the vessel. To compare the total amount of energy reaching the wall at different stages of grinding, the kinetic energy of the beads at the wall was calculated from the average velocity at the wall and plotted in Figure 5.13, assuming the wall is uniformly covered at the same packing fraction for each experimental run. The energy efficiency of milling is important. Hence, the power draw of the mill was plotted on the x-axis as opposed to the impeller speed.

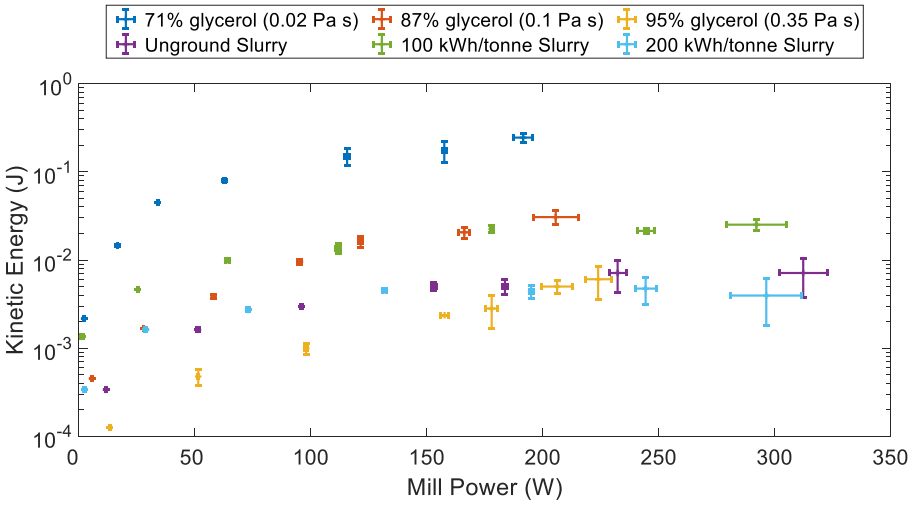

Figure 5.13: Kinetic Energy at Vessel Wall for 52 vol% 0.8 – 1.2 mm Mullite Beads at Vessel Wall in Glycerol-Water Solutions and Calcium Carbonate Slurries at Different Stages of Grinding. Y direction error bars show the standard deviation in velocity measurements occurring over 5 consecutive impeller revolutions. X direction error bars show power fluctuation occurring over 10 seconds.

Figure 5.13 illustrates that the kinetic energy of grinding media beads at the wall slurries is within the range of glycerol-water solutions of 71-95% and shows a similar trend. With grinding for 100 kWh/tonne, the behaviour is very different to 0 kWh/tonne and 200 kWh/tonne. This is investigated further in section 5.2.2.2.1 by considering the change in power draw and temperature of the mill.

From Figure 5.12 and Figure 5.13, it appears that the increase in viscosity greatly affects the velocity and hence kinetic energy of the grinding media beads at the wall of the vessel, constricting them to move more slowly and in a more ordered fashion at all impeller speeds when the viscosity is higher. A lot more of the energy from the impeller is dissipated due to the high viscosity as opposed to making grinding media at the wall move more quickly. These velocity differences between different fluid types were investigated further by analysis of the surface plots, which show how the beads at different heights in the mill move when the impeller is at different angular positions. In section 5.2.2.1 surface plots for glycerol-water solutions of different concentrations are compared and in section 5.2.2.2 surface plots for slurries with different particle size distributions are compared.

5.2.2.1. Comparing Fluids of Different Viscosities – Glycerol-Water Solutions

The way that this energy is distributed over the height of the mill as the impeller rotates differs for different fluid viscosities, as is illustrated in the surface plots in Figure 5.14 and Figure 5.15 for 87% and 95% glycerol respectively for comparison with 71% glycerol surface plots in Figure 5.5.

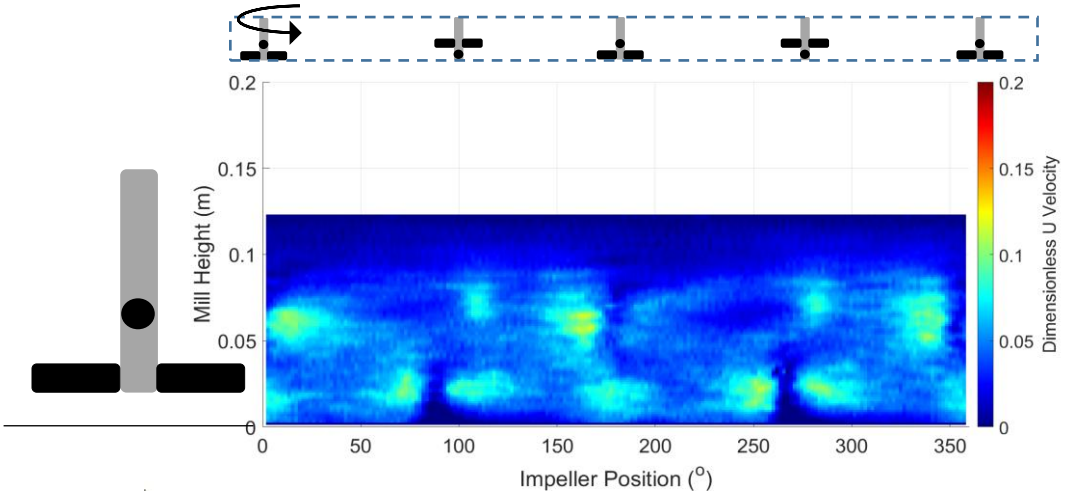

(a)

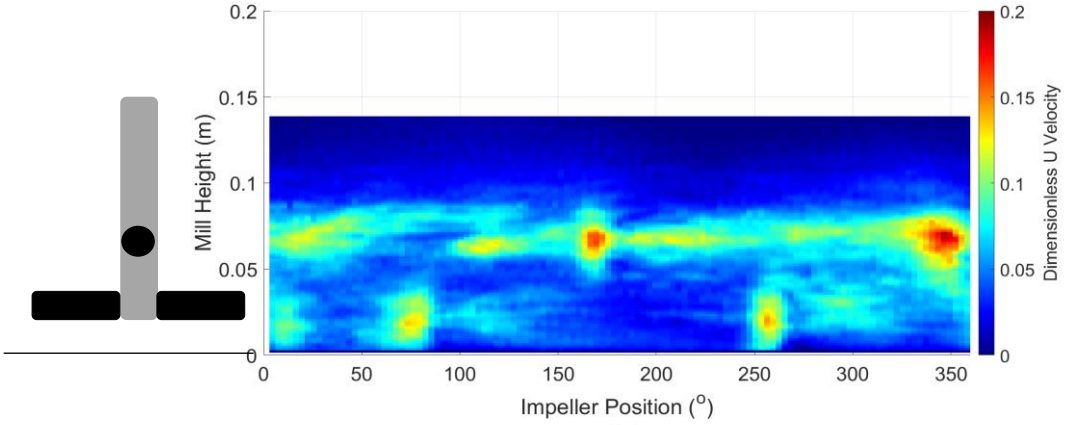

(b)

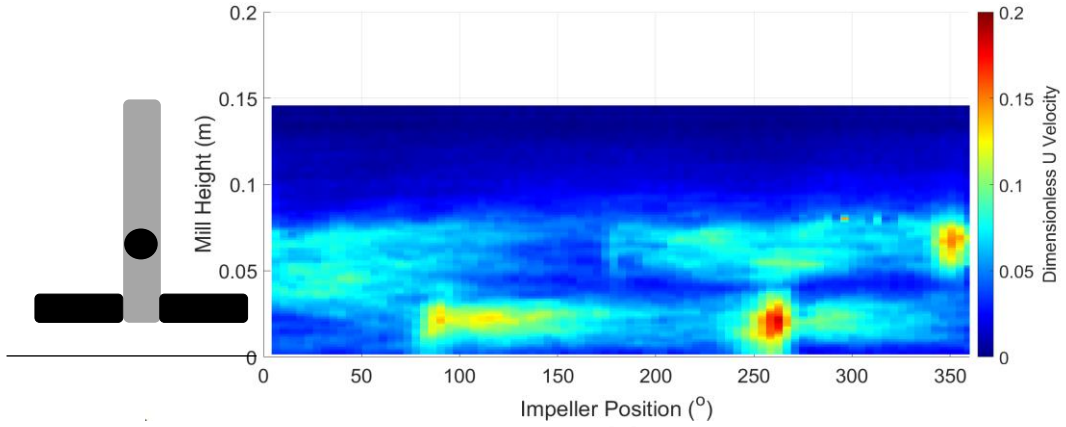

(c)

Figure 5.14: Surface Plots Demonstrating Change in Dimensionless 'U' Velocity at Vessel Wall for 52 vol% 0.8 – 1.2 mm Mullite Beads in 87% Glycerol at Impeller Tip Speeds (a) 3.9 m s^{-1} (b) 6.5 m s^{-1} (c) 9.2 m s^{-1}

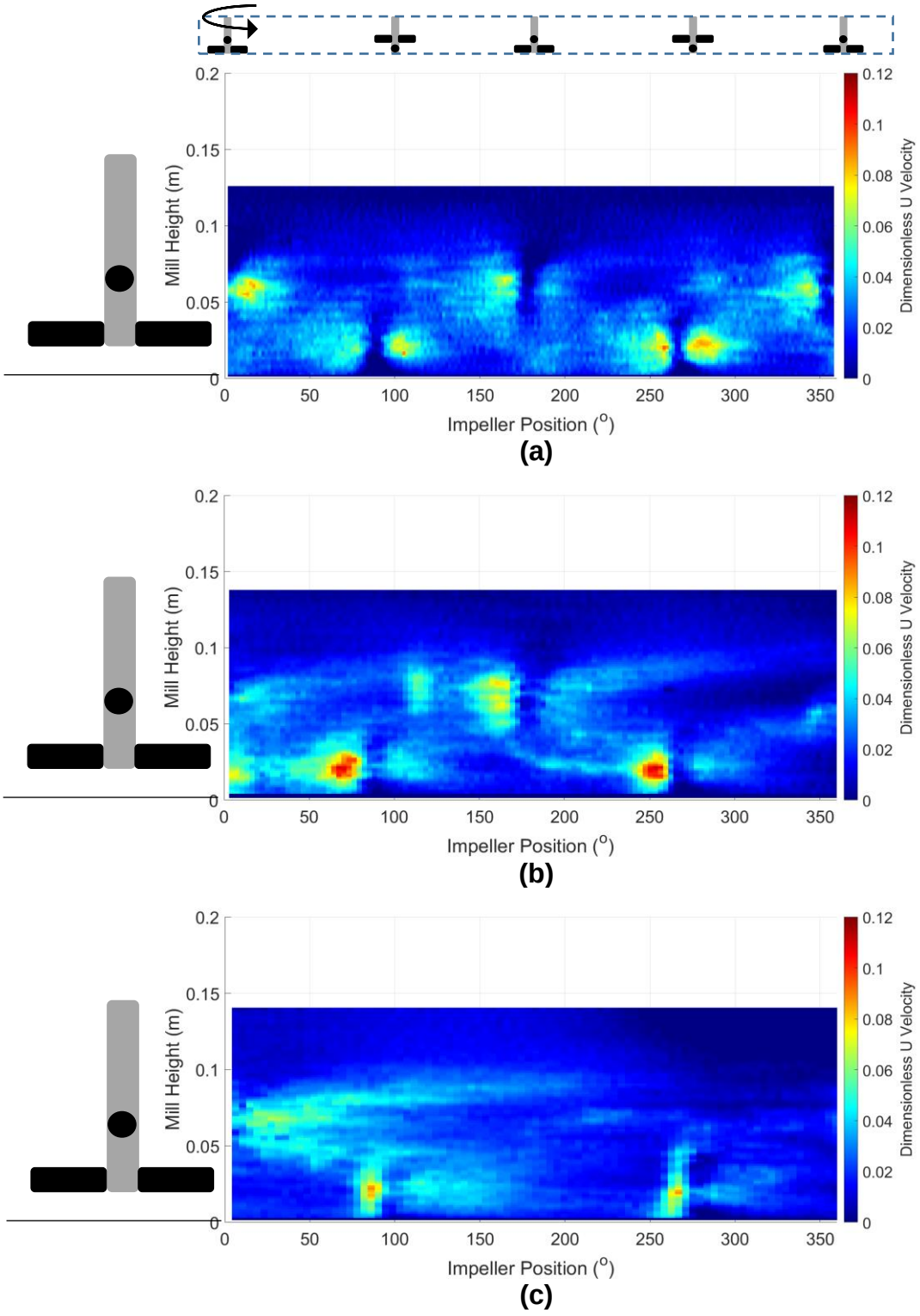

Figure 5.15: Surface Plots Demonstrating Change in Dimensionless 'U' Velocity at Vessel Wall for 52 vol% 0.8 – 1.2 mm Mullite Beads in 95% Glycerol at Impeller Tip Speeds (a) 3.9 m s^{-1} (b) 6.5 m s^{-1} (c) 9.2 m s^{-1}

From Figure 5.14 and Figure 5.15, it is observed that that for the higher viscosity fluid, as well as velocities being significantly lower than with 71% glycerol (Figure 5.5), there are also shorter tailing velocities; there is a temporary velocity increase directly as the impeller passes but the increased velocity dissipates quickly afterwards. At 9.2 m s^{-1}, very little of the energy reaches the wall; even less than with 71% glycerol. The more random motion caused by the vortex at high speeds explains why the pins cannot be directly identified in Figure 5.14c and Figure 5.15c.

5.2.2.2. Comparing Slurries at Different Stages of Grinding

When non-Newtonian calcium carbonate slurries are used in the mill, as in typical grinding scenarios, there appears to be more velocity fluctuations than with glycerol-water solutions. Due to the size reduction process occurring in the mill, separate surface plots were considered at intermediate stages during grinding. The surface plots for calcium carbonate slurries are shown in Figure 5.16 for 3.9 m s^{-1}.

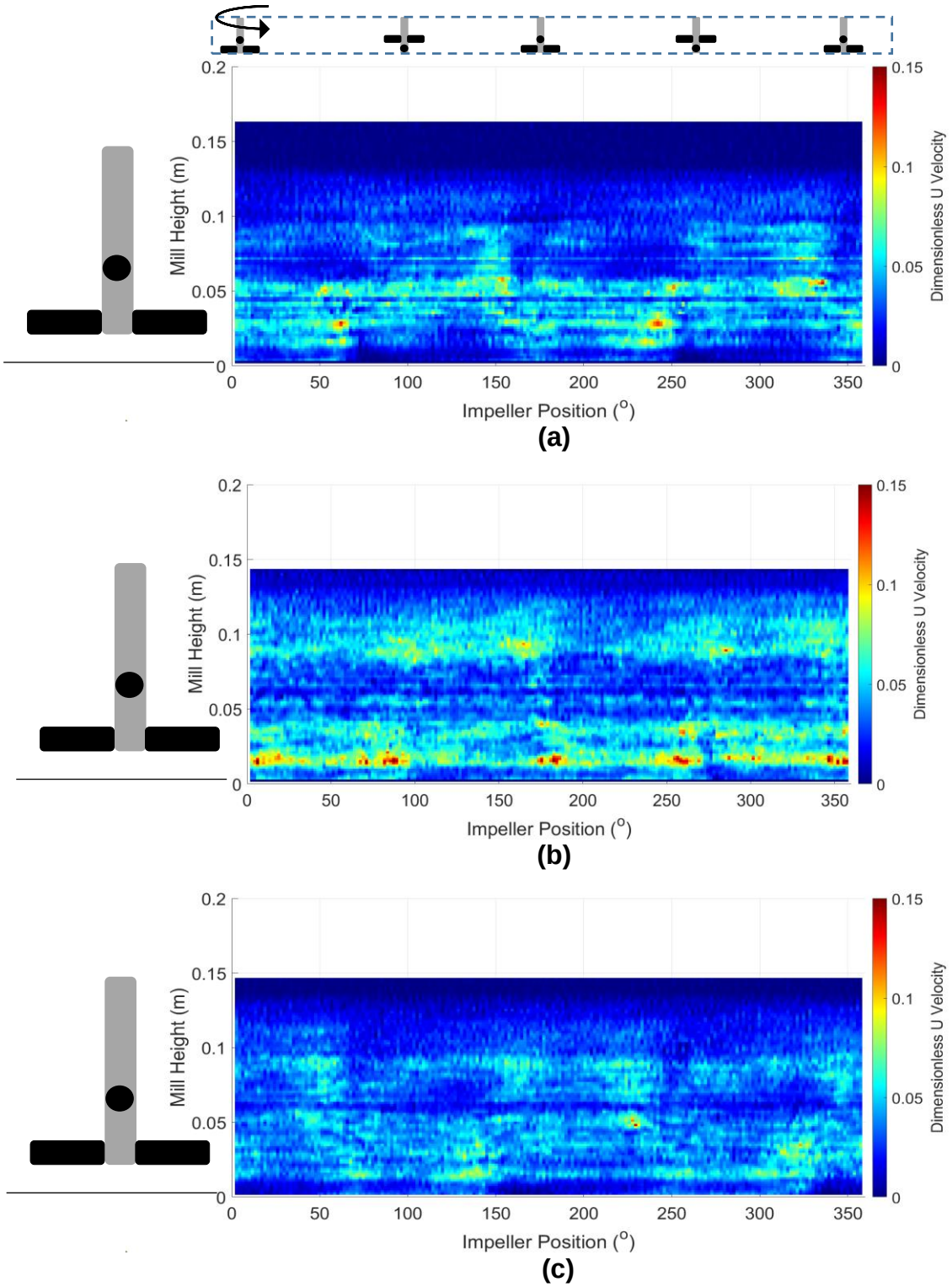

Figure 5.16: Surface Plots Demonstrating Change in Dimensionless 'U' Velocity at Vessel Wall for 52 vol% 0.8 – 1.2 mm Mullite Beads in Calcium Carbonate Slurries at 3.9 m s^{-1} - (a) Start of milling, (b) 100 kWh/tonne, (c) 200 kWh/tonne

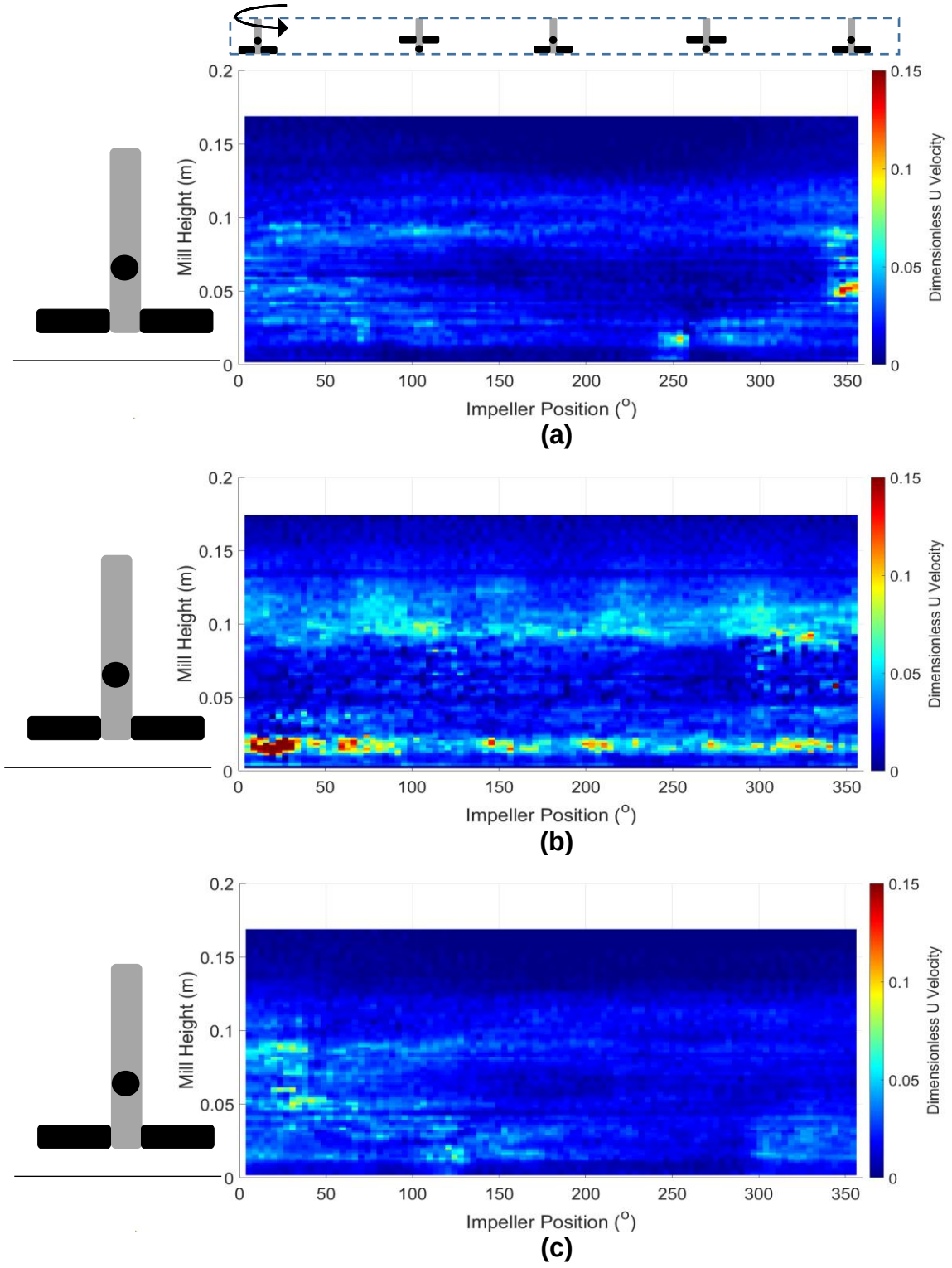

Figure 5.17: Surface Plots Demonstrating Change in Dimensionless 'U' Velocity at Vessel Wall for 52 vol% 0.8 – 1.2 mm Mullite Beads in Calcium Carbonate Slurries at 6.5 m s^{-1} - (a) Start of milling, (b) 100 kWh/tonne, (c) 200 kWh/tonne

As with grinding media in glycerol, Figure 5.16 shows higher velocity regions when the impeller directly passes the beads at the wall. When the impeller speed is increased in Figure 5.17, the impact of the impeller on the bead velocity at the wall is less significant, suggesting that more energy is dissipated in the fluid than with glycerol. This is expected due to the greater frictional properties of particulate slurries than lubricating glycerol-water solutions. As milling progresses, the bead velocities at the wall appear to change significantly. This is explored further in section 5.2.2.2.1 by considering the average velocity at the wall every three minutes during batch grinding.

From Figure 5.16 and Figure 5.17, it is also observed that the surface plots for slurries are less smooth than for grinding media in glycerol-water solutions. This could be due to the opacity of the calcium carbonate slurries; the grinding media beads are more difficult to see due to the layer of white slurry at the wall. Alternatively, the roughness of the slurry due to the presence of large amounts of solids could cause less smooth motion. To test this hypothesis, micron sized glass beads (of similar size to the slurry particles) were added to the glycerol in the mill in different amounts. These beads are not refractive index matched to the fluid but the beads do not obscure the view of the grinding media beads at the wall. The findings of this can be found in section 5.2.2.2.2.

5.2.2.2.1. Changes During Batch Grinding

Due to the changes observed in surface plots at 0, 100 and 200 kWh/tonne, the average bead velocity was plotted every three minutes during grinding alongside associated power and temperature measurements in Figure 5.18.

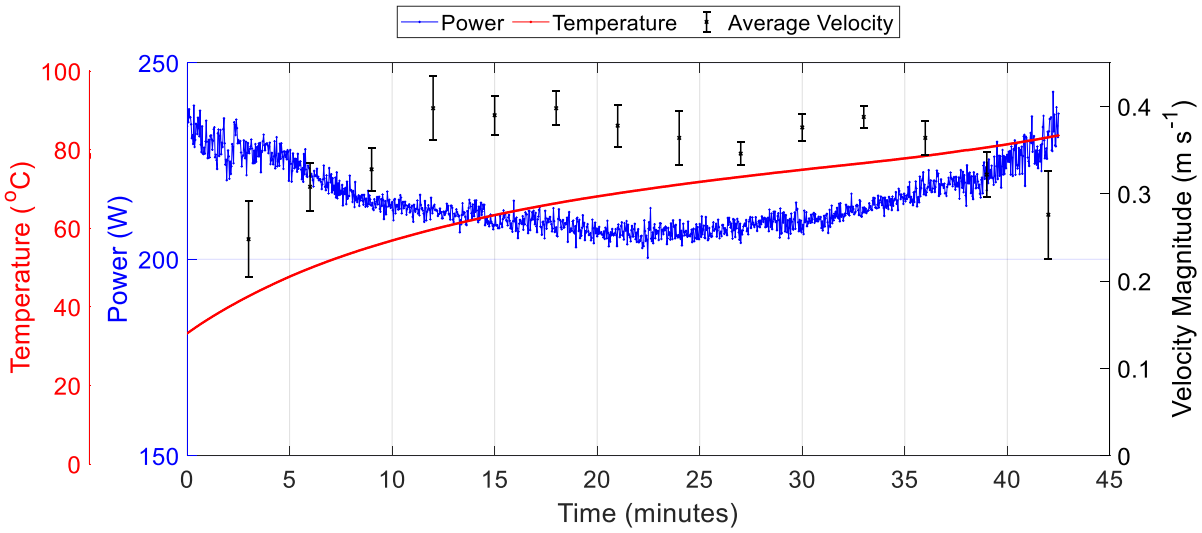

Figure 5.18: Average Bead Velocity at Wall During Batch Milling with Temperature and Power Draw. 52 vol% 0.8 – 1.2 mm Mullite Beads in 72 wt% Calcium Carbonate Slurry at 7.8 m s^{-1}. Error Bars Show the Standard Deviation of 5 Consecutive Impeller Revolutions

From Figure 5.18, it is observed that there is an initial increase in the velocity of the beads at the wall before it is fluctuating but closer to constant. This velocity increase stops when the power is close to constant and the temperature is approximately 60 ˚C. The changes in velocity and power draw could be attributed to the following:

- The temperature increase causing a viscosity decrease
- The particle size change causing a viscosity increase.

The simultaneous particle size decrease and temperature rise make it difficult to determine the precise nature of the changes occurring. The viscosity changes affect the flow patterns of the fluid and the vortex shape – this was confirmed using PEPT in section 5.4. For further investigation into the reasons for the varied velocity during batch grinding, the viscosity of the slurry could be assessed frequently throughout

grinding, e.g. every three minutes, which matches the frequency of the velocity measurements. This is discussed further in Chapter 8.

5.2.2.2.2. Micron Sized Glass Beads in 71% Glycerol

Calcium carbonate particles obscure the view of the beads at the wall due to the opaqueness of the slurry. To improve the view of the grinding media beads at the wall and investigate the impact of the amount of particles in a fluid, 0 – 50 μm SiLi glass beads were added to 71% glycerol-water solution in different amounts, keeping the total volume of glycerol plus particles constant. They are in the same size range as the slurries and do not obscure the motion at the wall as much as the slurries (demonstrated in Figure 5.19). By adding particles to glycerol, it may provide a better representation of motion in the mill due to less obscuration at the wall. It should be noted that within PIV lab, filtering such as CLAHE (contrast-limited adaptive histogram equalisation) is applied to these images to enhance the contrast [150].

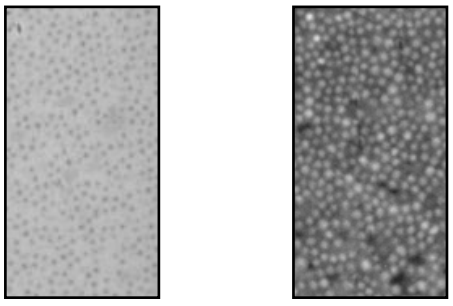

Figure 5.19: Raw High Speed Camera Images at 6.5 m s^{-1} (a) 100 kWh $tonne^{-1}$ Calcium Carbonate Slurry (49 vol%) (b) Glass Beads in 71% Glycerol (40 vol%)

Surface plots are shown for different glass bead amounts in 71% glycerol in Figure 5.20 and Figure 5.21 for two different speeds.

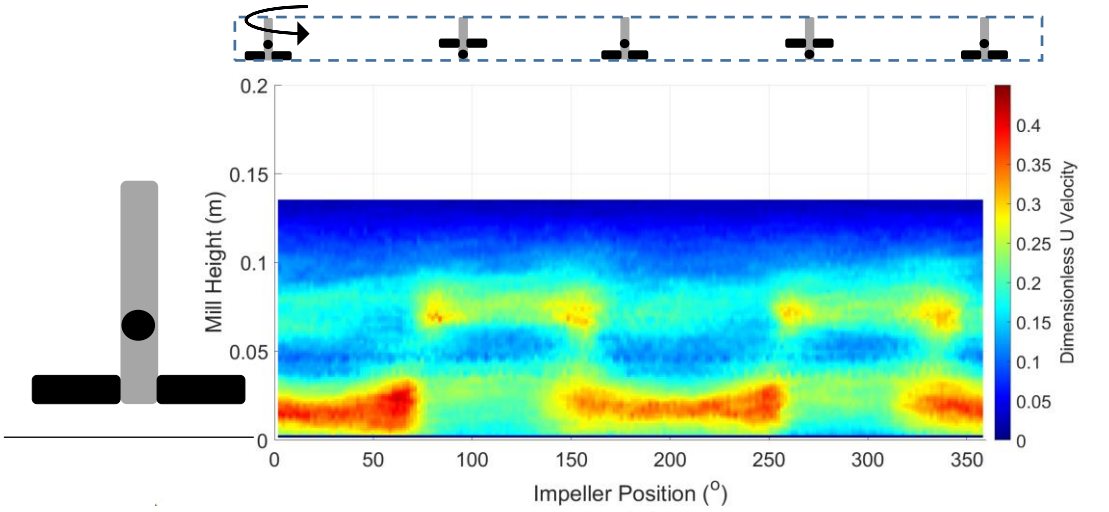

(a)

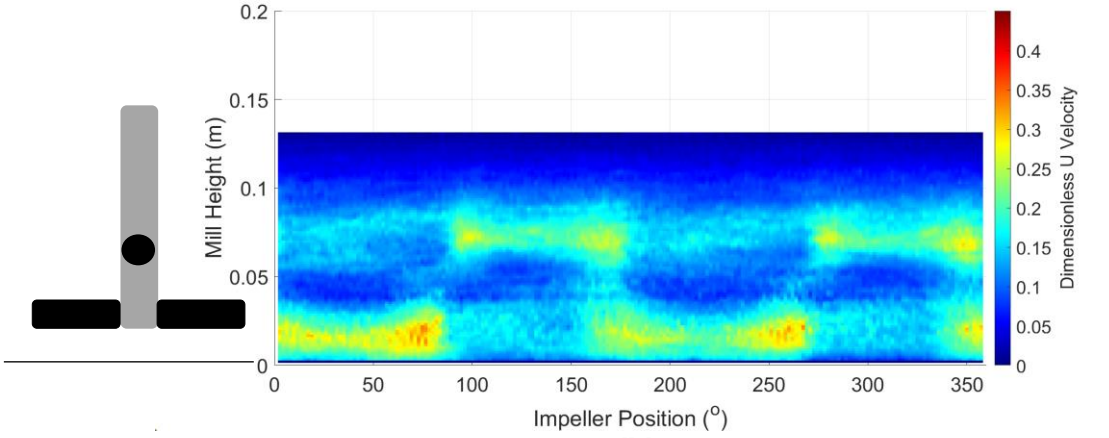

(b)

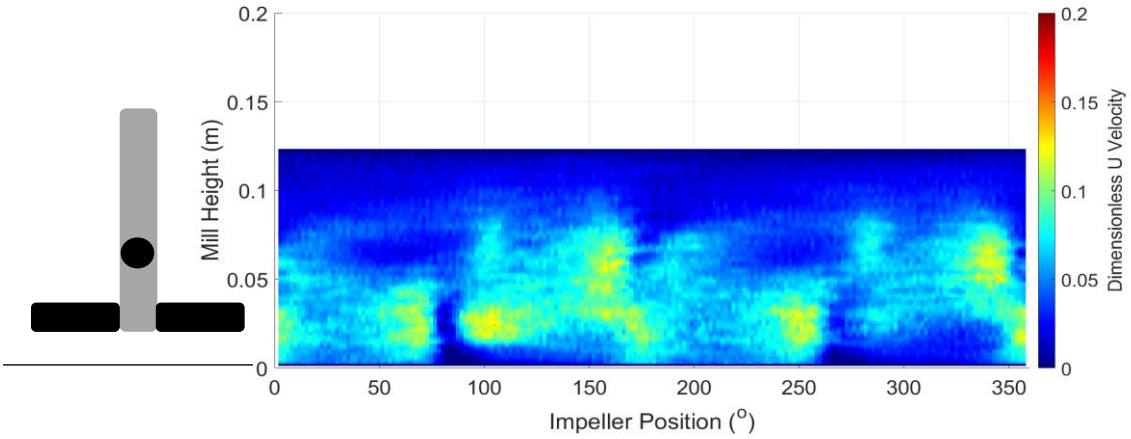

(c)

Figure 5.20: Surface Plots for 71% Glycerol-Water Solutions with Different Glass Particle Contents at 3.9 m s^{-1} – (a) 5 vol% (b) 20 vol% (c) 40 vol%

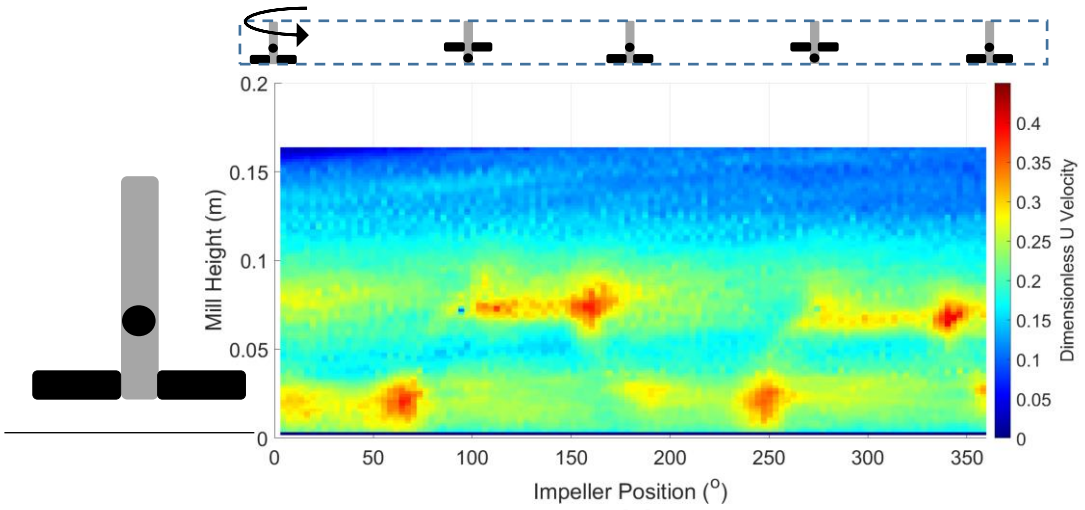

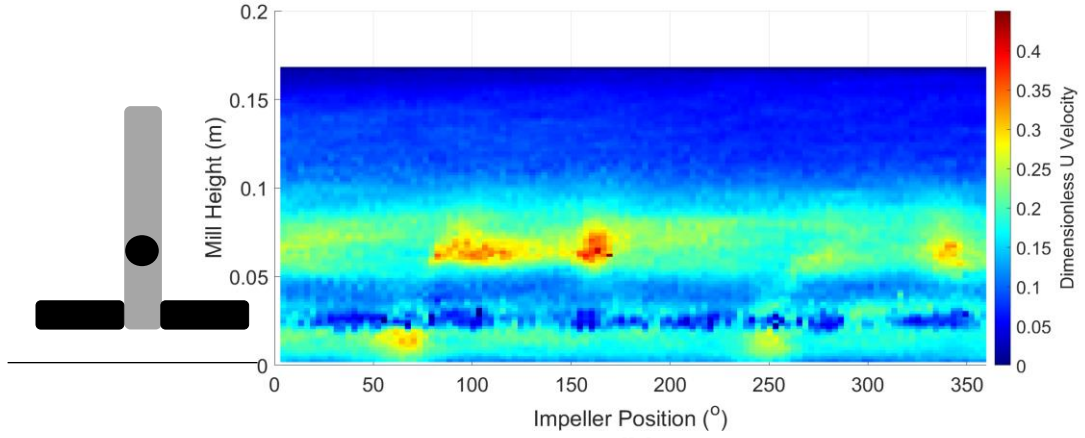

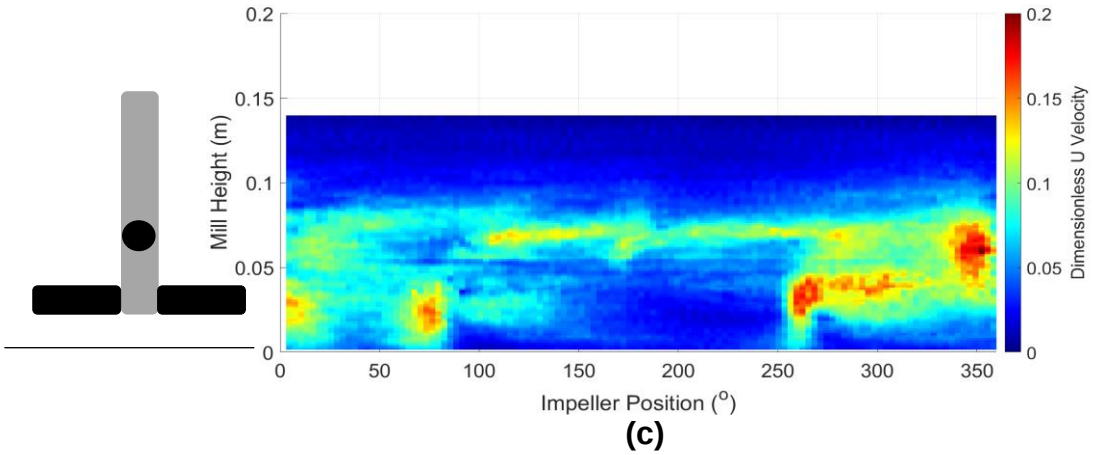

Figure 5.21: Surface Plots for 71% Glycerol-Water Solutions with Different Glass Particle Contents at 6.5 m s^{-1} – (a) 5 vol% (b) 20 vol% (c) 40 vol%

From Figure 5.20 it can be seen that as the amount of solids increases, the high velocity region in line with the impeller at the wall is less intense and the extent of the speed increase caused by the direct passing of the impeller is reduced. Figure 5.21 shows similar trends to Figure 5.20. However, it appears that the highest glass particle content has a lower height of grinding media beads at the vessel wall. The total fill level of the mill remains the same, suggesting that the solids content influences the height/shape of the vortex. The motion with larger amounts of glass beads is closer to the motion observed for calcium carbonate slurries in section 5.2.2.2, suggesting that the addition of particles to glycerol makes the motion of grinding media at the beads more similar to slurries without compromising the visibility of the grinding media beads at the wall. Nevertheless, the presence of the same features in the surface plots suggests that the white appearance of the slurry does not render the calcium carbonate data unreliable and with PIVlab, it is observed that the software has little difficulty in identifying the grinding media beads as particles in either case.

5.3. PEPT

PEPT provides useful information about the flow velocities of grinding media beads (velocity plots) and the regions of the mill in which they spend the most time (occupancy plots). This can be used to infer information about flow patterns and the shape of the vortex. The shape of the vortex has a significant impact on the power draw of the mill and hence the efficiency of milling.

5.3.1. Flow Pattern Development During Batch Grinding

As batch grinding occurs and slurry viscosity increases (see Chapter 4), the flow pattern may also change with time – it was observed in section 5.2 that the grinding media bead velocities at the wall vary with batch grinding time. Although only one tracer bead is used in PEPT experiments, which means that the mill must be run for long enough that the tracer has had time to pass through each region of the mill to obtain meaningful data, it is still possible to get an approximate idea of flow pattern development with time. It should be noted that the mill was allowed to run for 1 minute before recording the PEPT data to ensure the beads were moving at steady state and that the grinding media and calcium carbonate powder were fully mixed with the water and dispersant. The time averaged occupancy and velocity plots at different time segments during batch grinding are shown in Figure 5.22. The dimensionless velocity plotted is the 3D velocity divided by the impeller tip speed.

	Occupancy	Velocity
0 – 20 minutes	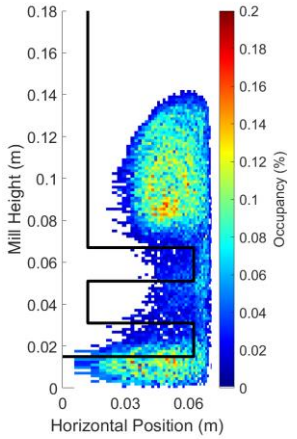	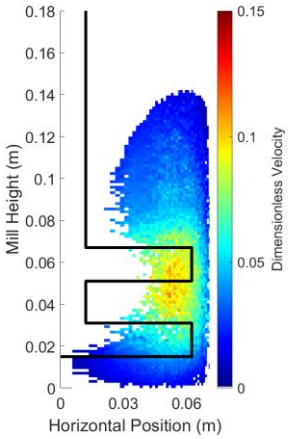
10 – 30 minutes	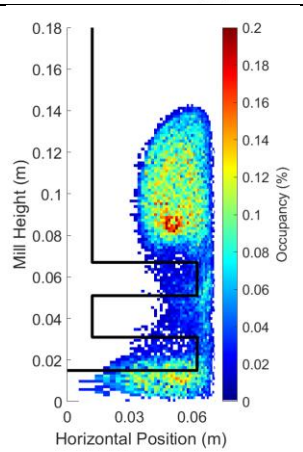	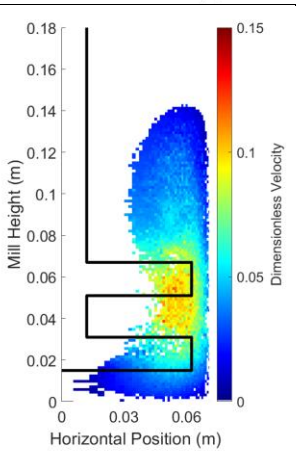
20 – 40 minutes	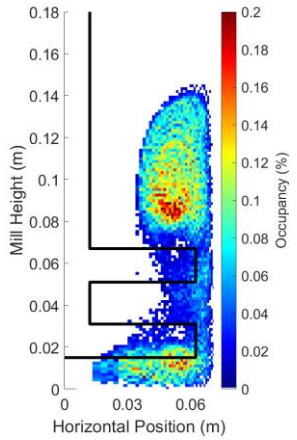	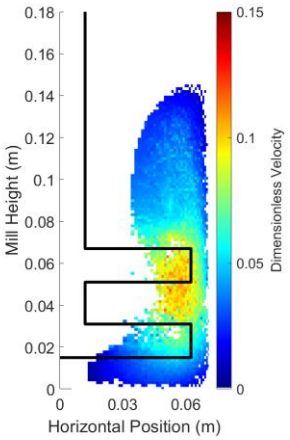

Figure 5.22: Occupancy and Velocity Plots for 52 vol% 0.8 – 1.2 mm Mullite Grinding Media with 72 wt% Calcium Carbonate Slurry at 6.5 m s^{-1}

From Figure 5.22, it can be seen that when the calcium carbonate has been milled for different amounts of time, there are minimal changes in velocity distribution. However,

there is also some change in the size of the vortex due to the viscosity of the fluid in the mill increasing; the height the fluid reaches does not change significantly but the width and shape of the vortex does change with increased grinding. The aim of this chapter is to compare vortex shapes and sizes and hence for consistency, the first 20 minutes of grinding (after 1 minute to reach steady state) were analysed for every scenario, minimising the impact of changes occurring with time.

Other methods of assessing motion changes occurring with time could be employed to allow further comparisons with HSI results, such as using multiple tracers to obtain more data about a smaller time frame or repeating experimental runs several times to get more data about smaller time periods. This is suggested in Chapter 8.

5.3.2. Bead Motion with Time

To understand the occupancy plot and why the bead spends more time above and below the impellers than within the impeller region, bead motion with time in the vertical ‘y’ direction was analysed in Figure 5.23. For figure clarity, only 400 seconds of data is shown in this plot. However, similar trends were observed over the complete run time.

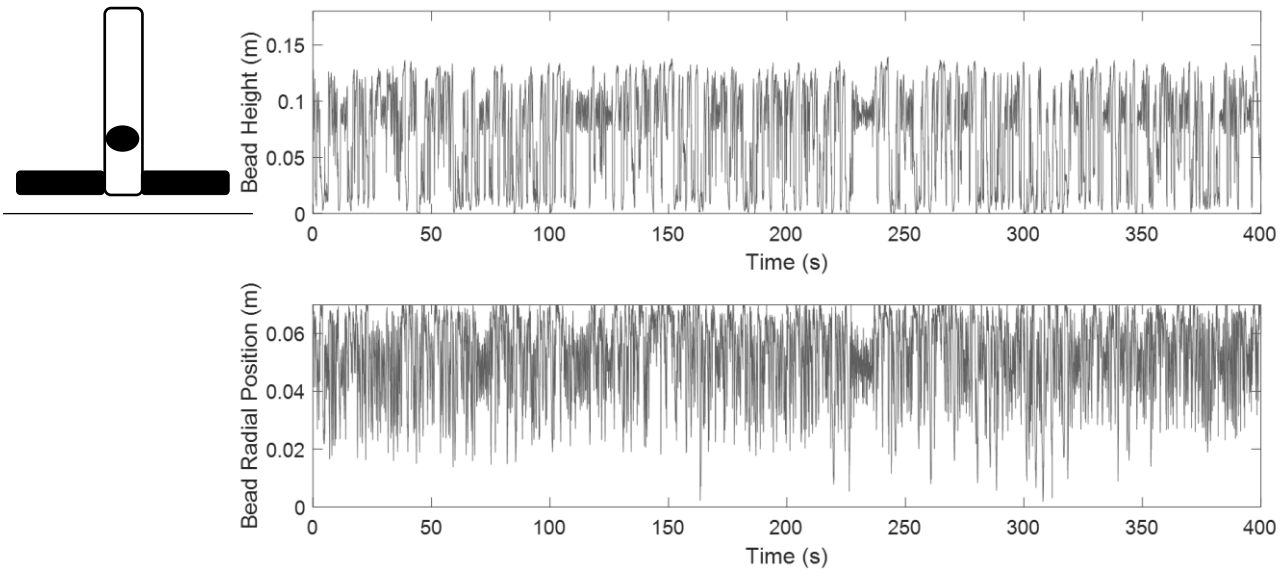

Figure 5.23: Height and Radial Position of Irradiated Bead Over 400 Seconds of Milling for 52 vol% 0.8 – 1.2 mm Mullite Grinding Media with 72 wt% Calcium Carbonate Slurry at 6.5 m s^{-1}

From Figure 5.23, it is seen that the bead quickly moves up and down in the mill. However, once it reaches a height of around 0.08 m (just above the second impeller), the bead often centrifuges around the mill at this height for a few seconds before quickly dropping again, demonstrating the higher occupancy of the bead above the impeller. These changes in height are not accompanied by a typical behaviour in the radial position. The radial position data shows that the bead rarely reaches close to the impeller shaft and when it does, it moves away quickly towards the vessel wall, as is expected based on the shape of the vortex in Figure 5.22. To further assess the amount of time the bead spends in the top flow loop before dropping down below the impeller, a histogram is shown in Figure 5.24.

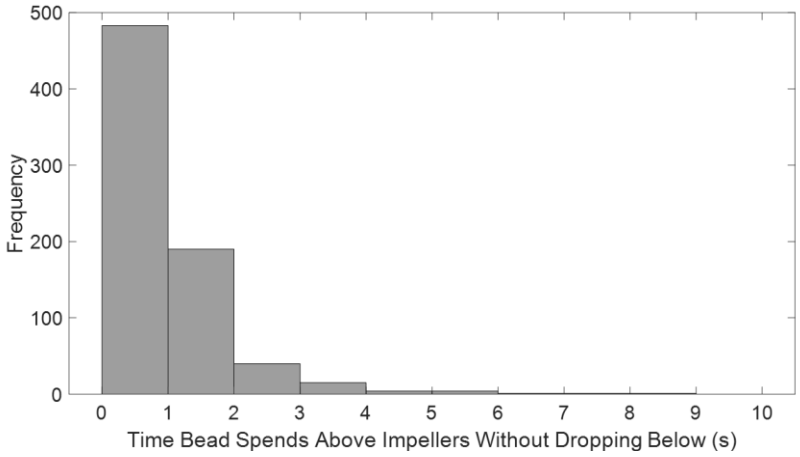

Figure 5.24: Histogram Showing the Amount of Time the Irradiated Bead Spends Above the Impellers Before Dropping into the Bottom Flow Loop – For 72 wt% Slurry in 52 vol% 0.8 – 1.2 mm Mullite Grinding Media

From Figure 5.24, it is observed that the grinding media bead typically spends less than 2 seconds above the impeller before dropping down past the impeller and into the bottom flow loop. However, there are some occurrences where the bead circulates around the top flow loop for up to 8 seconds. It is expected that the grinding media dropping between flow loops is important; this means that the bead passes the high velocity region where beads are moving in different directions and more likely to collide.

5.3.3. Visualising the Vector Flow Field

To understand the flow of grinding media beads and the direction of motion in each region of the mill, a vector flow field was produced, as illustrated in Figure 5.25.

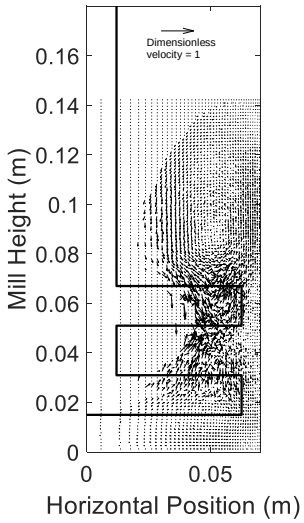

Figure 5.25: Velocity Vectors (Radial and Vertical) for 52 vol% 0.8 – 1.2 mm Mullite Grinding Media with 72 wt% Calcium Carbonate Slurry at 6.5 m s^{-1}

From Figure 5.25, it can be seen that there are three distinct flow regions: above the top impeller, between the impellers and below the impellers. This is in agreement with the flow patterns suggested by Barley et al.[118]. Above the impeller, beads move upwards at the wall of the vessel and drop down the central vortex, whilst at the bottom of the vessel the beads are lifted in the centre by the impeller and travel down at the vessel walls. In the region in the centre of the vessel and between the impellers, the beads can easily move from there into either the top or bottom flow loop. It is suggested that a large proportion of the collisions occur around the impeller region, since this is where the beads move in different directions as the change between flow loops and are hence more likely to collide.

It is also noted that there is a small region by the wall between the impeller tips which has different motion to the rest of the vessel. This region was identified in Figure 5.22 as being of relatively high velocity, yet this is not illustrated by the vectors, implying that the motion is occurring in the tangential direction, not displayed in the vector plot.

5.3.4. The Effect of the Irradiated Bead Size

Since only one grinding media bead is irradiated and the grinding media beads in the mill cover a normal distribution of sizes, it is possible that the smaller and larger grinding media beads within a sample move differently due to their different masses and the effect of gravity. This was investigated using 1.4-2.4 mm mullite grinding media beads since they cover a wide range of sizes, with velocity and occupancy plots shown in Figure 5.26.

	Occupancy	Velocity
Small Bead (~ 1.4 mm)	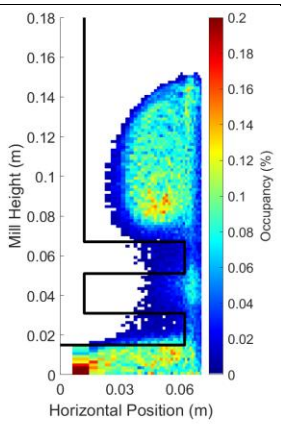	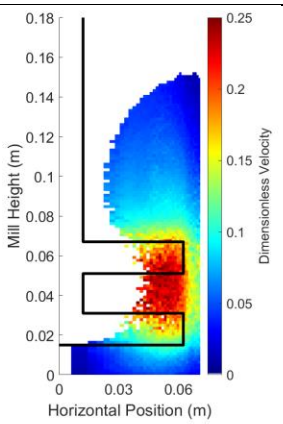
Large Bead (~ 2.4 mm)	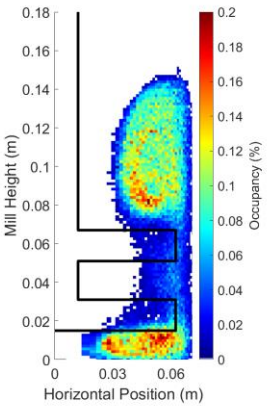	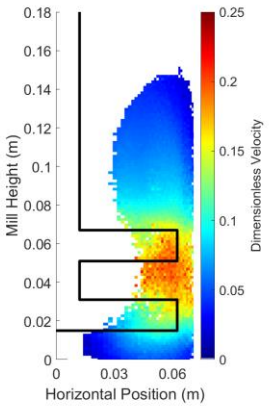

Figure 5.26: Occupancy and Velocity Plots for 52 vol% 1.4 – 2.4 mm Mullite Grinding Media with 72 wt% Calcium Carbonate Slurry at 7.9 m s^{-1}

From Figure 5.26, it can be seen that the smaller bead travels faster in the impeller region than the larger bead; this is expected since the smaller bead is a lower mass so can be accelerated more by the force of the impeller. The occupancy of the small and large beads remains similar, with the bead spending more time above and below the impeller and only a small amount of time in the impeller region. There is a small difference in the vortex width above the impellers. To investigate in more detail whether the beads of different sizes move significantly differently, the bead positions with time are plotted for each bead in Figure 5.27 and Figure 5.28.

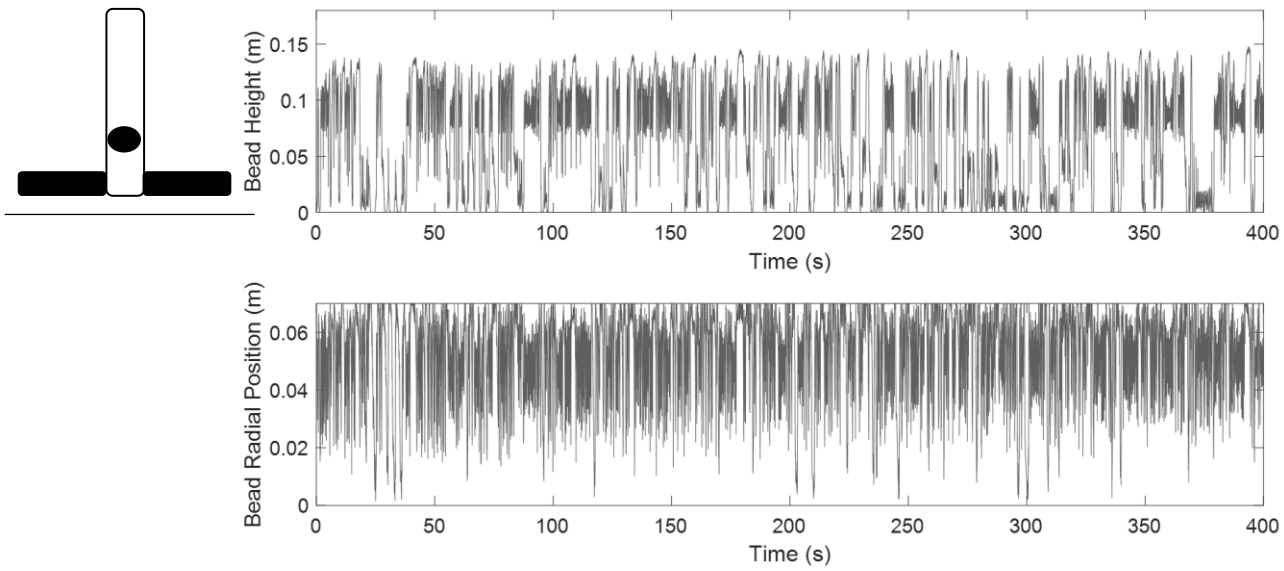

Figure 5.27: Height and Radial Position of Irradiated Small Bead Over 400 Seconds of Milling for 52 vol% 1.4 – 2.4 mm Mullite Grinding Media with 72 wt% Calcium Carbonate Slurry at 7.9 m s^{-1} Note that for radial position, 0 m is centre of vessel and 0.07 m is wall of vessel.

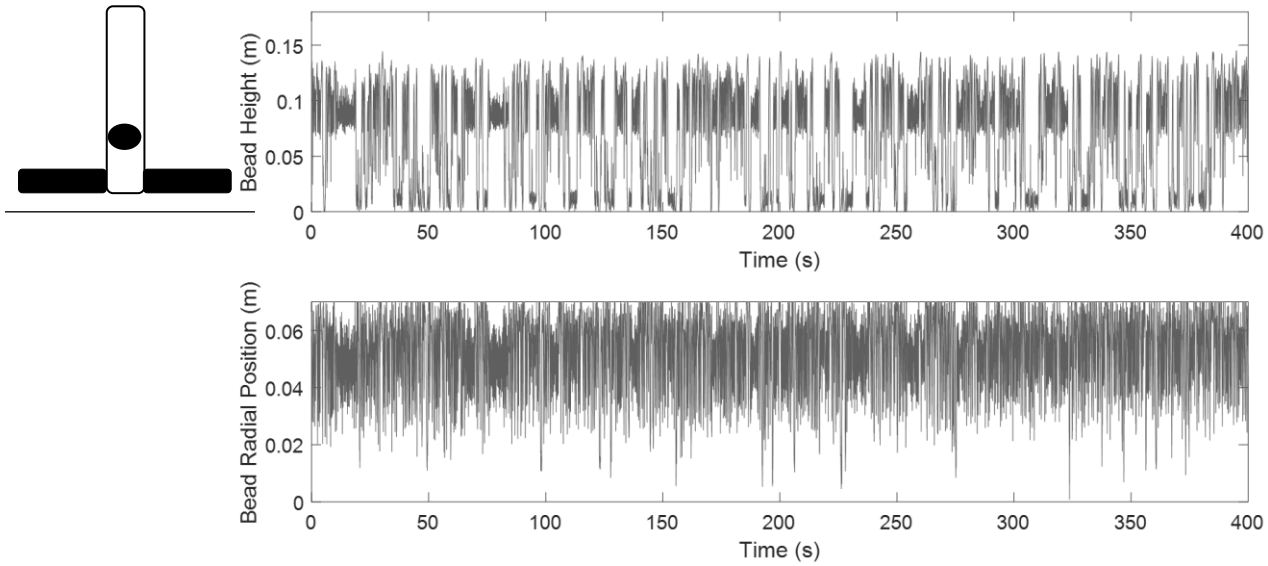

Figure 5.28: Height and Radial Position of Irradiated Large Bead Over 400 Seconds of Milling for 52 vol% 1.4 – 2.4 mm Mullite Grinding Media with 72 wt% Calcium Carbonate Slurry at 7.9 m s^{-1}

From Figure 5.27 and Figure 5.28, the motion of the small and large beads in both the radial and vertical directions follows the same trend, of moving up and down the mill, sometimes spending a few seconds moving around the upper region before dropping down again. The amount of time each bead spends above the impellers before dropping down was plotted in histograms in Figure 5.29.

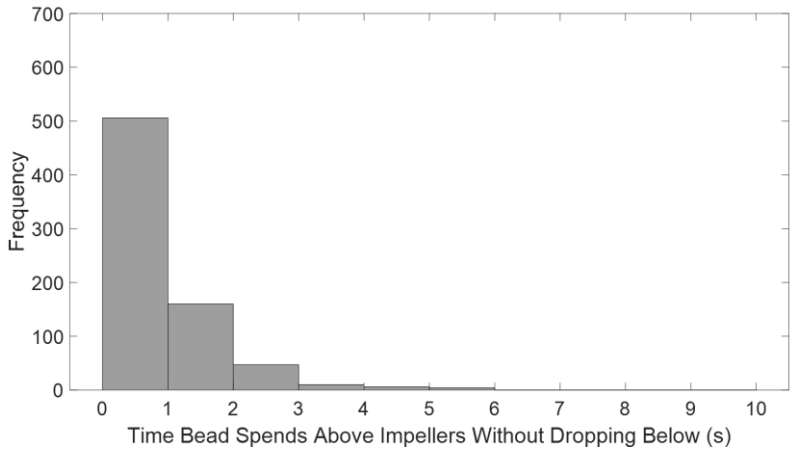

(a)

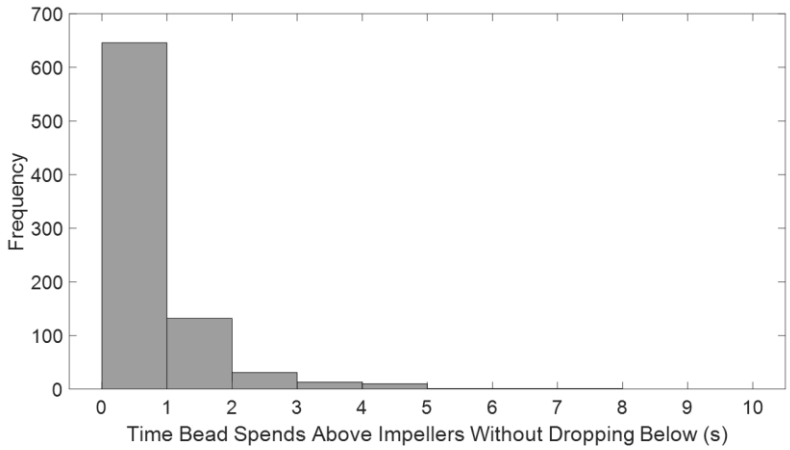

(b)

Figure 5.29: Histogram Showing the Amount of Time the Irradiated Bead Spends Above the Impellers Before Dropping into the Bottom Flow Loop – For 72 wt% Slurry in 52 vol% 1.4 – 2.4 mm Mullite Grinding Media (a) Small Bead Tracer (b) Large Bead Tracer

From Figure 5.29, it is confirmed that the motion of the small and the large bead is very similar; both beads predominantly spend up to two seconds in the upper flow loop before dropping down below the impeller. The time the bead spends in the region of the mill above the impeller is also approximately the same; the small bead spends 59% of time above impellers, whilst large bead spends 60% of time above impellers. The difference is not statistically significant.

To examine and compare the flow patterns, velocity vector plots are illustrated for the small and large bead in Figure 5.30.

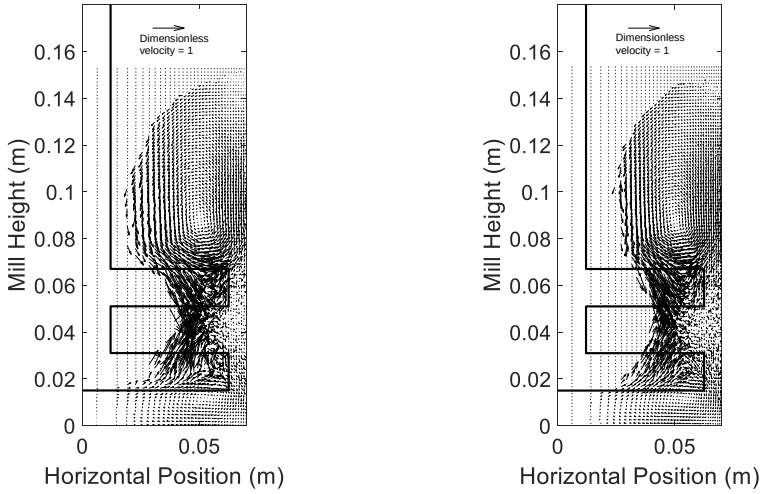

Figure 5.30: Velocity Vectors for 52 vol% 1.4 – 2.4 mm Mullite Grinding Media with 72 wt% Calcium Carbonate Slurry at 7.9 m s^{-1} - (a) Small Bead (b) Large Bead

Figure 5.30 shows that the small and large beads follow close to the same flow pattern within the mill. This confirms that the choice of the irradiated bead in PEPT stirred media mill experiments has little impact on the findings; the beads of different sizes travel equally in each region of the mill and there is little stratification of beads. In experiments throughout this section, an average (median) bead size was selected for each experiment.

5.3.5. The Effect of Impeller Speed

Impeller speed is an important parameter in milling as it affects the speed and acceleration of grinding media beads and hence the number of and forces in grinding media collisions, which determines if calcium carbonate particles will break. Occupancy and velocity plots in Figure 5.31 show the change in velocity and occupancy plots at different impeller speeds.

	Occupancy	Velocity
3.9 m s^{-1} **Power = 96 W**	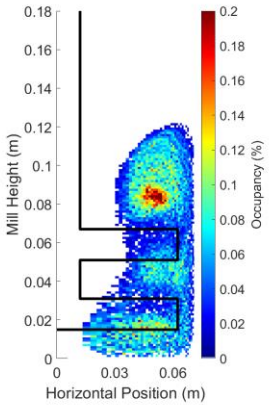	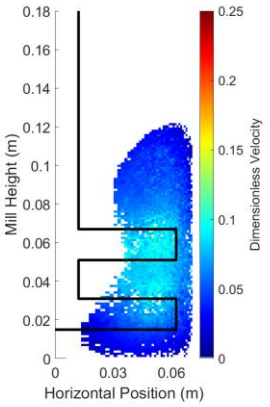
5.2 m s^{-1} **Power = 152 W**	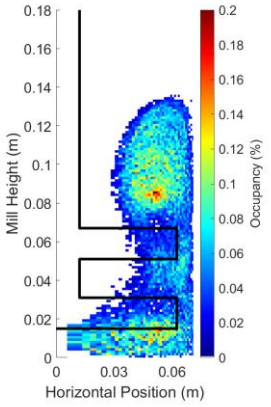	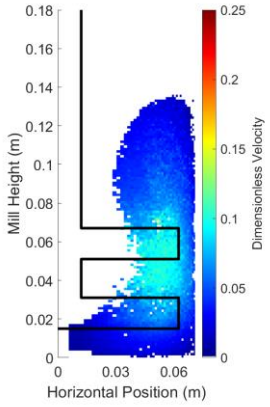
6.5 m s^{-1} **Power = 183 W**	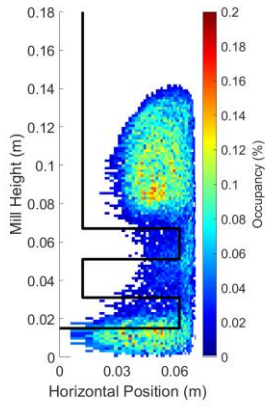	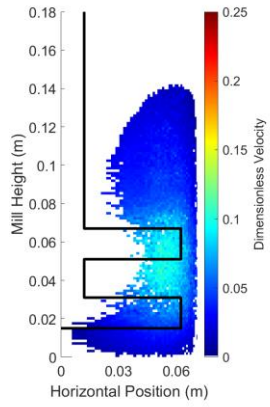
7.8 m s^{-1} **Power = 232 W**	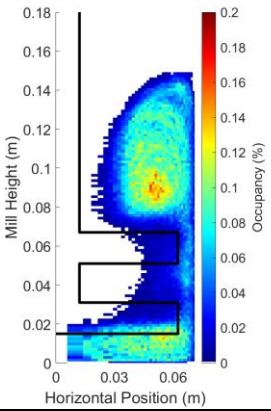	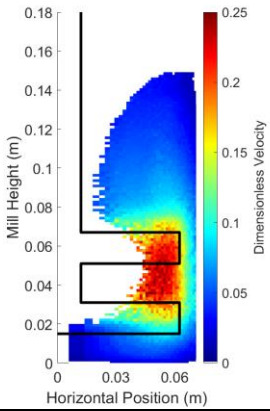

	Occupancy	Velocity
9.2 m s^{-1} **Power = 312 W**	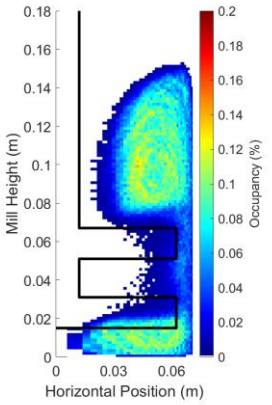	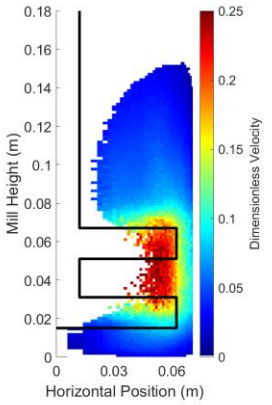

Figure 5.31: Occupancy Plots for 52 vol% 0.8 – 1.2 mm Mullite Grinding Media with 72 wt% Calcium Carbonate Slurry at Different Tip Speeds

From Figure 5.31, it can be seen that as the impeller speed increases, the velocity increases, as is the expected trend due to the increased energy in the system. In terms of the dimensionless velocity plotted, the velocity distribution remains similar for impeller speeds of up to 6.5 m s^{-1}. There is a transition, where at higher speeds the dimensionless velocity is significantly higher within the impeller region. This could be due to the lifting of grinding media; there are fewer grinding media in the impeller region, as can be seen from the occupancy plot. Hence, the impeller is moving more freely in this region meaning that the small number of beads here move much more quickly. However, as the bead spends more time in the regions above and below the impeller rather than in this high velocity (and hence high breakage force and collision rate) region, it is unlikely to provide optimum grinding performance. This has also been observed in literature cases for other stirred media mills, where high speeds do not necessarily result in the production of smaller particles[27]. In terms of flow patterns and direction of bead motion, all beads follow the same general flow patterns with no distinguishing features, as can be seen in Appendix D (section 10.4).

In typical liquid applications, the vortex height is approximately proportional to the Froude number[161]. The only operating parameter in the Froude number calculation is the impeller speed. For this case of stirred media milling, the vortex height is plotted against the Froude number in Figure 5.32.

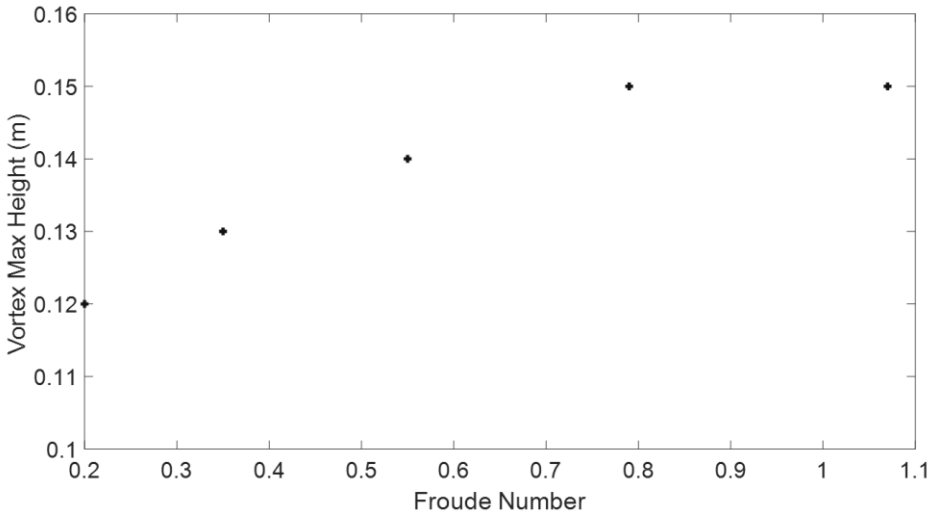

Figure 5.32: Maximum Height of Vortex at Increasing Froude Number – 72 wt% Calcium Carbonate Slurry in 52 vol% 0.8-1.2 mm Mullite Grinding Media

In Figure 5.32, it can be seen that at the highest speeds, the vortex appears to have reached its maximum height for this fluid level and stops increasing with impeller speed. This is not the full height of the vessel. The Froude number relationship is important when predicting power draw since the vortex shape has significant effect on the rotational torque required, as was discussed in Chapter 4.

Although the vortex height increases linearly with the Froude number for this case, apart from at the maximum impeller speed, the vortex height is also dependent on other factors including the grinding media type, amount and the solid content of the slurry/ properties of the fluid phase – this is investigated in section 5.3.6. Due to the

apparent importance of the vortex shape on power draw, the investigation of the relationship between the Froude number and the vortex height at other solids and grinding media contents is suggested as further research in Chapter 8.

5.3.6. The Effect of Grinding Media Amount and Solids Content

To investigate the effect of changing the grinding media amount and the slurry solids content on the vortex size, they were systematically changed whilst keeping the Froude number (impeller speed) constant. An impeller speed of 6.5 m s^{-1} was selected as this is in the vortex region that is typically used for grinding.

5.3.6.1. Varying Slurry Solids Content

The slurry solids content affects the non-Newtonian viscosity as well as the frictional properties. Occupancy and velocity plots for different slurry solids contents are displayed in Figure 5.33. It should be noted that as well as the fluid rheological properties changing with increasing slurry solids content, the total mass of fluid being mixed increases, which will affect the velocity since the force of the impeller provides less acceleration when the fluid mass is greater.

	Occupancy	Velocity
32 wt% slurry **Power = 134 W**	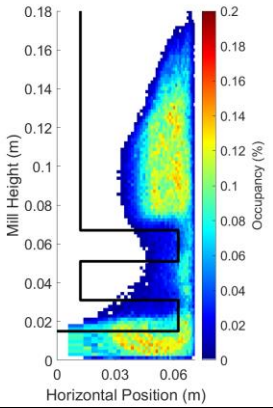	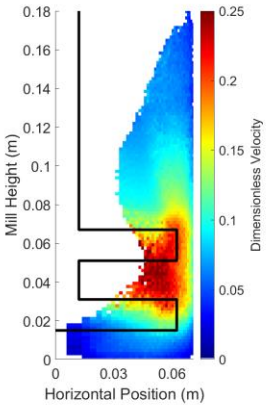
52 wt% slurry **Power = 132 W**	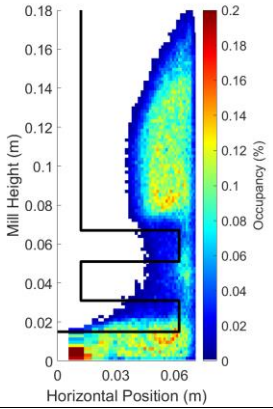	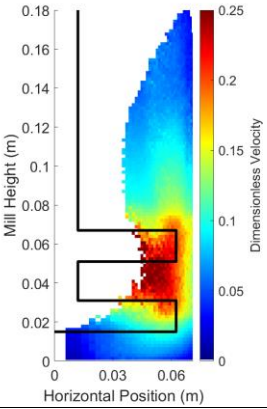
72 wt% slurry **Power = 184 W**	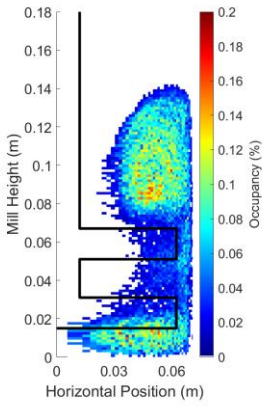	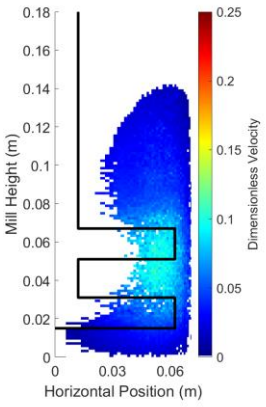

Figure 5.33: Occupancy and Velocity Plots for Slurries of Different Solids Contents with 52 vol% 0.8-1.2 mm Mullite Grinding Media at 6.5 m s^{-1}

Figure 5.33 shows that for 32 and 52 wt% solids in the slurry, there is minimal change in the shape and height of the vortex; in both cases the vortex reaches close to the lid of the vessel and the velocity distribution is similar. However, when the solids content is increased to 72 wt%, there is a significant change; the beads do not reach as high

in the vessel and the top surface of the beads is flatter. This is likely due to the viscosity of the fluid phase; when this is higher viscosity, there is less momentum to push the beads in an upwards direction to the top of the vessel. A viscous dampening effect is also apparent from the velocity distribution where the velocities are notably lower, particularly in the impeller region. This makes it a less optimum condition for particle breakage. As well as it being just due to viscosity, the rheological properties change when the solids content is increased; in Chapter 4 it was shown that calcium carbonate slurries are significantly more highly shear thinning for the higher solids content (72 wt%) slurries. This difference in flow behaviour could further explain the significant flow pattern changes occurring between 52 and 72 wt% slurries. In standard mixing applications, the extent to which a fluid is shear thinning can have a significant impact on flow patterns since the viscosity is affected by shear rate, which is highest at the impeller. Hence, the distribution of viscosities in the system differs greatly. Shear thinning fluids in unbaffled tanks can form caverns because the low shear rate at the wall of the vessel means that the fluid viscosity is at its highest in this region[165].

When considering how this translates to milling efficiency, existing literature research shows that lower solids contents can lead to more efficient grinding since higher solids contents have a higher viscosity and hence a higher power draw[33]. This higher power draw is not used usefully since collisions are cushioned by the higher viscosity fluid. There are also more particles trapped in each grinding media collision, making them more difficult to break. Jankovic[22] found that the efficiency of grinding increased with solids content, but suggested that this was due to the range of solids contents considered and that there is an upper limit to the point at which increasing solids

content increases grinding efficiency. Skuse[32] investigated solids concentrations between 65 and 75 wt% for a similar milling set-up and found the lowest solids content to provide the optimal milling results. In the system studied in this chapter, the optimal operating solids content is likely to lie between 52 and 72 wt% where the transition in occupancy plot occurs. This could be confirmed using batch grinding tests and measuring the particle size distribution for different energy inputs as further research.

5.3.6.2. Varying Newtonian Fluid Viscosity - Glycerol

To eliminate the effect of fluid type, the occupancy and velocity plots for glycerol-water solutions with grinding media are shown in Figure 5.34. Although the glycerol temperature does change with time due to friction, which leads to viscosity changes, it enables a comparison between glycerol-water solutions of different viscosities.

	Occupancy	Velocity
71% glycerol **Power = 116 W**	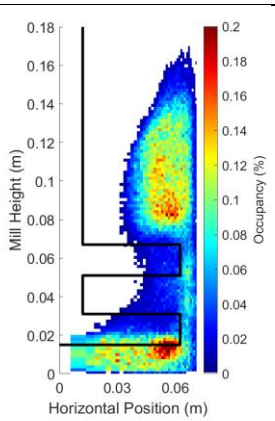	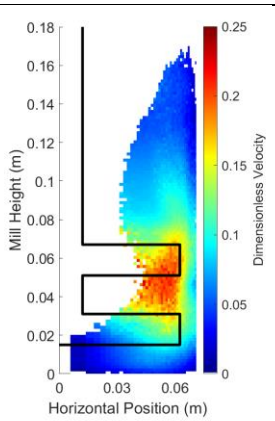
87% glycerol **Power = 122 W**	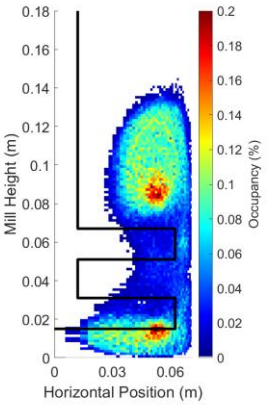	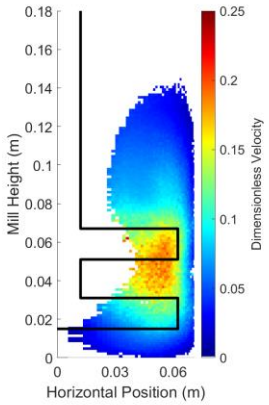
95% glycerol **Power = 178 W**	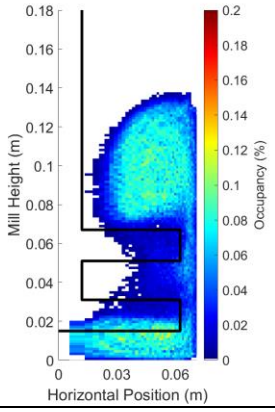	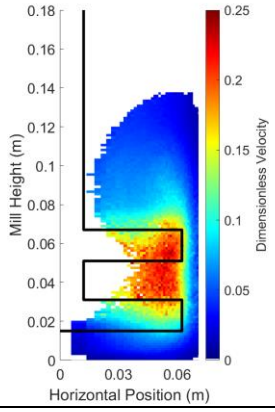

Figure 5.34: Occupancy and Velocity Plots for Glycerol-Water Solutions of Different Concentrations with 52 vol% 0.8-1.2 mm Mullite grinding Media at 6.5 m s^{-1}

From Figure 5.34, the occupancy plots show that with a Newtonian fluid, there is a significant vortex shape change with different viscosities within the range of viscosities of calcium carbonate slurries. This confirms that the viscosity of the fluid is important

in determining the shape of the vortex rather than just the extent to which the fluid is shear thinning (described by the power law index, n) or the solids content. The shape of the vortex is very similar for 87% glycerol and 72 wt% calcium carbonate slurries (Figure 5.33), despite velocities being higher for 87% glycerol.

Although it is difficult to assess the velocities of the beads at the wall directly with PEPT, it is evident from Figure 5.34 that the beads at the wall are of significantly greater velocity in 71% glycerol than with higher glycerol concentrations. This is in agreement with HSI findings in section 5.2.2.1, which shows significantly more energy reaching the beads at the wall for 71% glycerol. This could be attributed to the lack of viscous dampening in the low viscosity fluid. Viscosity in other regions of the mill is not significantly higher for the lowest glycerol concentration; velocities in the impeller region are highest for the most viscous glycerol-water solution.

5.3.6.3. Varying Grinding Media Amount

The amount of grinding media has a large effect on the total mass of material being mixed and hence has significant impact on velocity and flow patterns, shown by occupancy and velocity plots in Figure 5.35.

	Occupancy	Velocity
35 vol% grinding media **Power = 131 W**	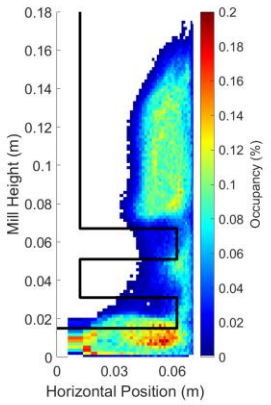	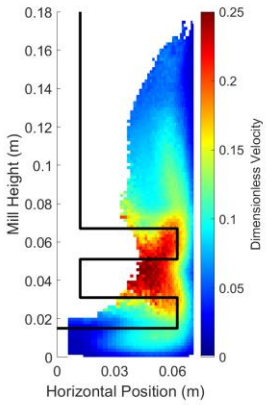
43 vol% grinding media **Power = 142 W**	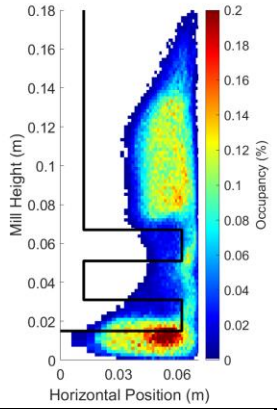	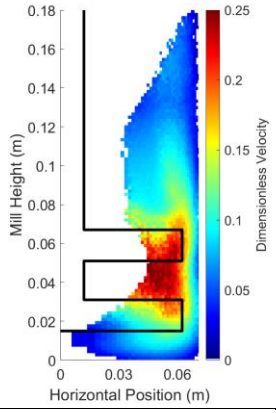
52 vol% grinding media **Power = 184 W**	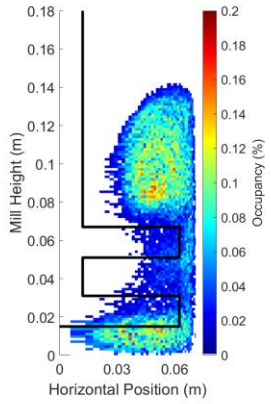	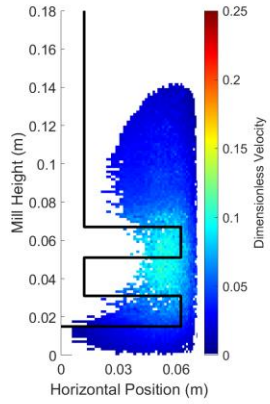

Figure 5.35: Occupancy and Velocity Plots of 72 wt% Slurries with Different Amounts of 0.8-1.2 mm Mullite Grinding Media at 6.5 m s^{-1}

Figure 5.35 shows that increasing the amount of grinding media has a similar impact to increasing the viscosity of the fluid - the vortex extends lower up the vessel walls when more grinding media are present. This implies that the greater mass of grinding media means that there is less momentum to lift the grinding media beads further

above the height of the impeller. When this larger amount of grinding media beads is used, the velocity in the impeller region also decreases, which again is likely to be due to the mass of beads packed into the vessel.

There is limited comparable literature for systems with a large amount of solids and a vortex (unless literature directly regards stirred media mills) since fluid mixing typically operates without a vortex by employing baffles since it leads to inefficient mixing when most of the vessel contents are moving in close to solid rotation[166].

5.3.6.4. The Coupling of Fluid Properties and Grinding Media Amount

The vortex shape has been shown to be affected by both the slurry properties and the grinding media amount. To investigate if these parameters are strongly coupled, the vortex shape for 52 wt% calcium carbonate slurry with 35 vol% 0.8-1.2 mm mullite grinding media was examined in Figure 5.36. An additional reason for assessing the vortex shape for this condition as it was found in Chapter 4 that for these parameters, the power draw correlation did not fit as well.

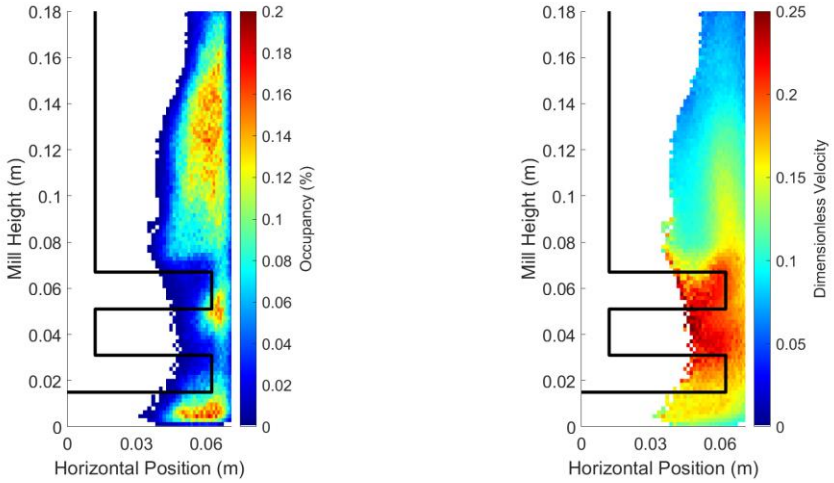

Figure 5.36: (a) Occupancy and (b) Velocity Plots for 35 vol% 0.8-1.2 mm Mullite Grinding Media Beads with 52 wt% Calcium Carbonate Slurry at 6.5 m s^{-1} (Power = 52 W)

From Figure 5.36a, both the solids content and grinding media amount are low, which causes the grinding media to reach the lid of the vessel and the vortex extends below the bottom impeller in the vessel. This is likely a result of momentum; there is less viscous dampening and a smaller mass of grinding media beads to be moved, resulting in them travelling further. The flow vectors were visualised in Figure 5.37.

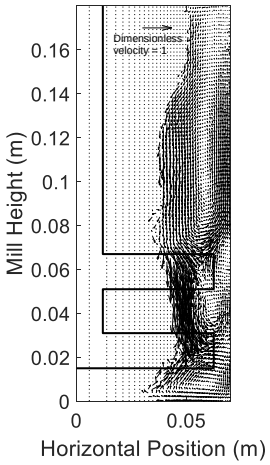

Figure 5.37: Velocity Vector Plot for 35 vol% 0.8-1.2 mm Mullite Grinding Media Beads with 52 wt% Calcium Carbonate Slurry at 6.5 m s^{-1}

The velocity vectors in Figure 5.37 show the expected trend of the beads travelling up the wall and down the centre of the vessel in the vortex, suggesting that the direction of motion is not greatly affected when compared with standard milling scenarios. However, the top and bottom motion loops appear to be more separate, with the crossover region being closer to the centre of the vessel and not extending to the vessel walls.

5.3.7. Using Higher Density Grinding Media Beads

Alumina grinding media beads were used to investigate the effect of changing the density and material of the grinding media beads. Investigations were conducted using a range of grinding media amounts and fluid types. When 87% glycerol is used as the fluid type, flow velocities and occupancy is very similar for the two bead types, as is shown in Figure 5.38.

	Occupancy	Velocity
52 vol% 0.8-1.2 mm MULLITE **ρ = 2700 kg m^{-3}** **Power = 121 W**	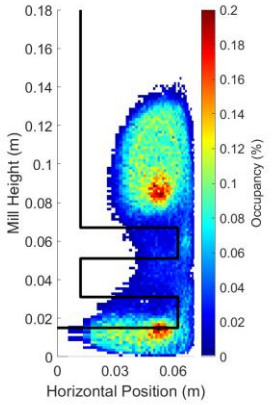	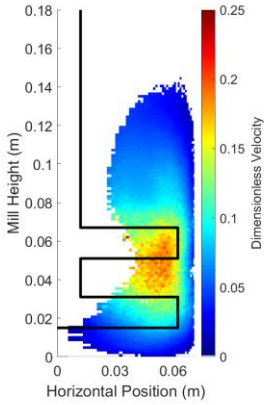
52 vol% 0.75-1.25 mm ALUMINA **ρ = 3600 kg m^{-3}** **Power = 130 W**	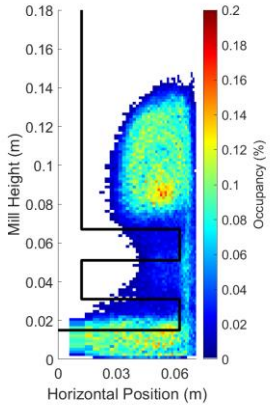	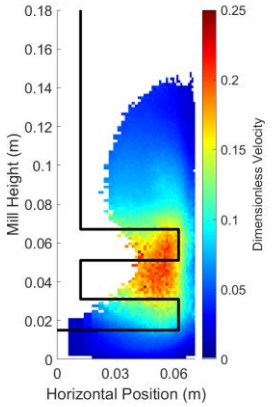

Figure 5.38: Occupancy and Velocity Plots of 87% Glycerol-Water Solutions with 52 Different Grinding Media Types at 6.5 m s^{-1}

From Figure 5.38, although the grinding media tend to move in similar regions of the mill and with a similar velocity profile. The alumina grinding media beads have a higher density, making the mass of each grinding media bead greater. However, as the impeller speed of the mill is fixed, the power draw of the mill is greater for alumina beads, as was discussed in Chapter 4.

It was also shown in Chapter 4 that the interaction between the fluid and grinding media is important. Hence, occupancy and velocity plots were compared for alumina and mullite beads with a range of grinding media amounts and fluid types in Figure 5.39.

	Occupancy	Velocity
72 wt% slurry + 52 vol% 0.8 – 1.2 mm MULLITE **Power = 184 W**	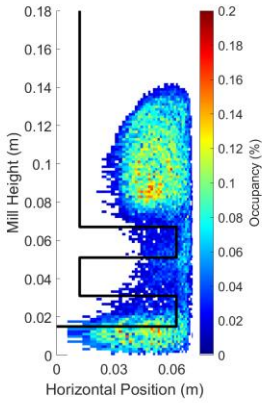	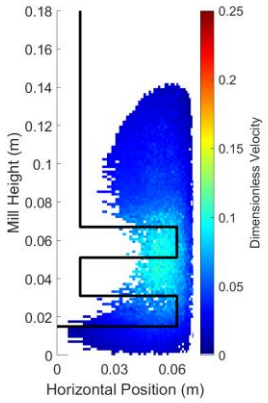
72 wt% slurry + 52 vol% 0.75-1.25 mm ALUMINA **Power = 227 W**	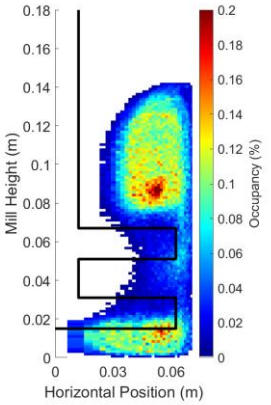	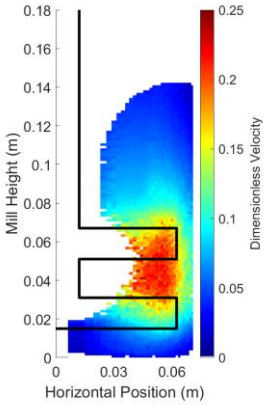
72 wt% slurry + 35 vol% 0.8 – 1.2 mm MULLITE **Power = 131 W**	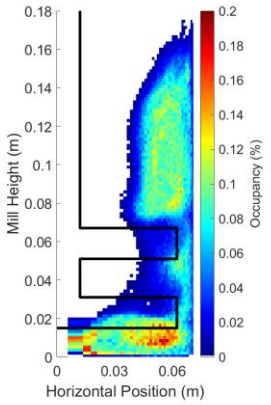	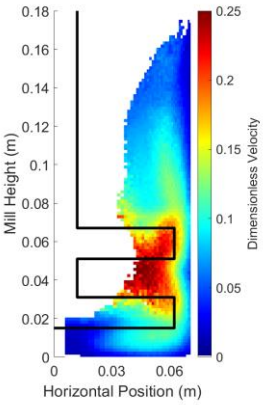
72 wt% slurry + 35 vol% 0.75-1.25 mm ALUMINA **Power = 138 W**	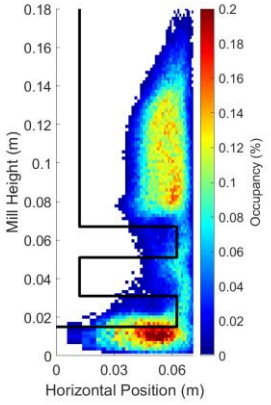	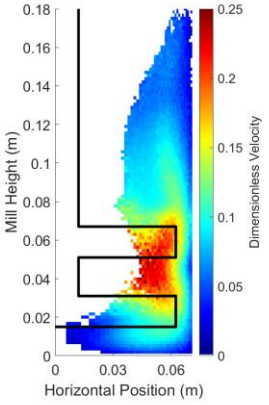

	Occupancy	Velocity
52 wt% slurry + 35 vol% 0.8 – 1.2 mm MULLITE **Power = 52 W**	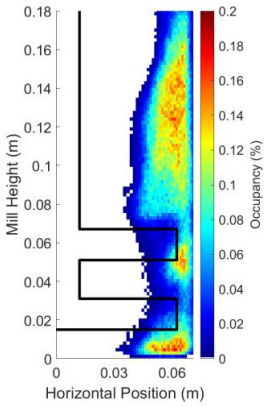	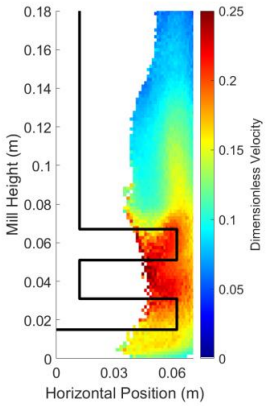
52 wt% slurry + 35 vol% 0.75-1.25 mm ALUMINA **Power = 64 W**	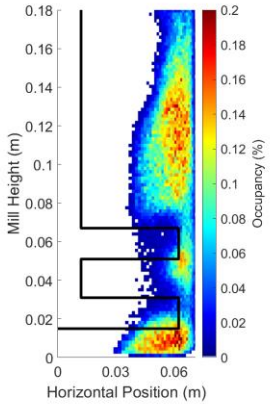	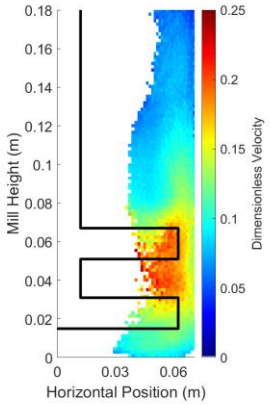

Figure 5.39: Occupancy and Velocity Plots of Different Fluids and Grinding Media Amounts at 6.5 m s^{-1}

From Figure 5.39, it is evident that changing the grinding media type from mullite to alumina does not have a significant impact on the shape or size of the vortex. It does however have an impact on the velocity profile, which is the expected result since the beads are of different densities and the power draw for each grinding media type is different as a result of this. In the impeller region, the mullite beads generally have the higher velocity. However, this is not the case for the 72 wt% slurry in 52 vol% grinding media, where the mullite beads move much slower, particularly in the impeller region. This could be due to the frictional forces between the fluid and grinding media but further tribology tests would be required to confirm this. In section 5.3.5 where

occupancy plots and velocity plots were compared for mullite grinding media at different speeds, it was shown that there is a jump in velocity occurring between tip speeds of 6.5 and 7.8 m s^{-1}. For a full comparison of the two bead types, the comparison should be made at other impeller speeds to determine if there is also a transition point where there is a jump in velocity around the impeller for alumina beads. This is discussed in more detail in further research Chapter 8.

5.4. Comparison of PEPT and HSI

Although PEPT and HSI both provide information about flow patterns, the information obtained is different. HSI data focuses on the motion of the beads at the wall of the vessel and less than 0.1 seconds of data provides enough information to infer the flow velocities at the wall, making it fairly instantaneous, whilst with PEPT, 20 minutes of data is required to obtain sufficient data since the motion of only one bead is tracked. In terms of observing changes occurring with time, this can be done over much shorter time periods with HSI than with PEPT, but both PEPT and HSI are in agreement that there are some changes in how the beads move at different stages of batch grinding.

With HSI, it is possible to confirm the orientation of the impeller visually by using a luminous strip at the top of the impeller shaft as a visual marker. From using this together with knowledge of the rotational speed of the shaft, the impeller position at any time can be inferred. This is more difficult with PEPT experiments since the impeller is not visually observed. It is possible to install an optical trigger. However, due to the vibration of the mill, producing this set-up to run accurately remains a challenge. The potential for future installation and use of a trigger for PEPT

experiments is discussed in further research Chapter 8. Additionally, since only one impeller bead is tracked, there will be limited amounts of data for each bead position relative to each impeller position. Hence, only the average data can be compared for PEPT and HSI. This method is also dependent on the resolution of PEPT - since the impeller moves quickly, excellent spatial and time resolution is required to determine the impeller position accurately for a particular tracer location.

Although PEPT and HSI give very different information, the same overall flow patterns in the mill are inferred from each technique. These flow patterns are both in agreement with those of Barley[28] illustrated in Figure 5.40, showing three main regions of motion:

- The region above the impeller pins
- The region surrounding the impeller pins
- The area beneath the impeller pins

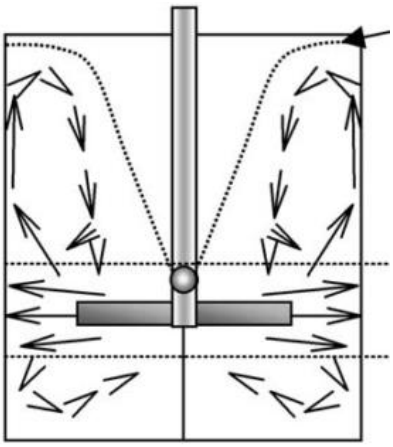

Figure 5.40: Diagram of the Three Regions in a Stirred Media Mill Proposed by Barley[28]

To compare HSI and PEPT data directly, only the wall motion can be compared. However, using PEPT it is difficult to assess the motion at the wall for two key reasons:

- It is difficult to determine when a grinding media bead is at the edge of the vessel as opposed to just close to the wall – it is expected that grinding media beads at the vessel wall move differently to those close to the wall.
- From HSI, it is shown that the beads at the wall tend to move around the edge of the vessel for a long time rather than being well mixed with the fluid, so the irradiated bead is unlikely to spend significant, if any time in this region.

Vortex plots at the edge of the vessel can be used to show motion close to the wall using PEPT, as illustrated in Figure 5.41, which shows radial and vertical motion only.

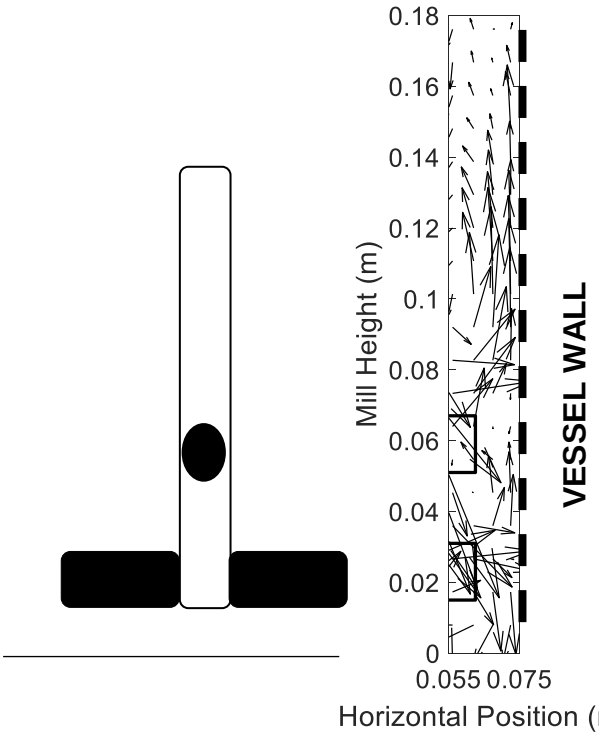

Figure 5.41: Vector Plot for Vessel Edge for 0.8 – 1.2 mm Mullite Beads in Calcium Carbonate Slurries at 6.5 m s^{-1} from PEPT Data

Figure 5.41 suggests similar vertical motion to the HSI data. The beads closest to the wall move in an upwards direction above the impeller and a downwards motion below the impellers, with motion being closer to horizontal between the impellers. The trend is similar for several layers of grinding media nearest the wall. Using PEPT, it is not possible to see the difference in the behaviour of the beads at the wall adjacent to the top and bottom impellers; this level of detail is best achieved using HSI.

5.5. Summary

Motion in a stirred media mill differs to that in a stirred tank, predominantly due to the action of the vortex; very few mixing applications exhibit vortexing. The shape and size of the vortex in the lab-scale stirred media mill changes significantly with changes in operating parameters, which in turn has a significant effect on power draw.

Using both HSI and PEPT, information on how the grinding media beads in the mill move has been obtained. These techniques suggest the same flow patterns, but the two techniques are very different, with HSI giving near instantaneous wall velocities whilst PEPT gives time-averaged data over a period of 20 minutes for all regions of the mill. Using PEPT and HSI together, a more in depth understanding of grinding media motion can be obtained.

Previous literature in this area utilises PEPT to visualise flow. Using HSI, it has been shown that the motion of the beads is highly dependent on the position of the bead relative to the impeller. This is important in milling because as a small amount of beads are accelerated by the impeller, they are more likely to be involved in collisions that

result in particle breakage. Additionally, the amount of energy reaching the vessel wall can be obtained, which is useful when considering how efficiently a mill is operating. There is a transition region where the addition of more energy by increasing the impeller speed no longer translates into faster motion of beads at the wall of the vessel, which suggests that more energy is dissipated in the bulk fluid.

Glycerol-water solutions exhibit similar flow patterns to calcium carbonate slurries, despite calcium carbonate slurries demanding a higher power draw of the mill. Using glycerol-water solutions, it was shown that the fluid viscosity has a significant effect on the shape of the vortex and the amount of energy reaching the grinding media beads at the wall of the vessel. However, the presence of solid particles in the fluid also has significant shape on the distribution of energy throughout the mill; adding micron sized SiLi beads to glycerol-water solutions had significant impact on the velocity distribution for grinding media beads at the vessel wall. Furthermore, the effects of grinding media amount and fluid viscosity are coupled, making it difficult to predict the vortex depth using the Froude number alone, which in turn effects power predictions.

In terms of comparing flow patterns in stirred tanks and lab-scale stirred media mills, the key difference is the vortexing. Stirred tanks do not typically operate with a vortex since it does not improve mixing behaviour. Additionally, HSI is not suitable for stirred tank applications since it is rare that there are a large number of particles present at the wall that can be clearly observed by the camera. Stirred tank flow patterns are commonly determined using modelling such as CFD or DEM, which is simpler to apply to single-phase or low solids concentration systems than stirred media mills.

6. COMPARING STIRRED MEDIA MILLS AT THREE SCALES

6.1. Introduction

Scale-up is important because conducting experiments at lab-scale provides the most efficient use of time and resources. It is crucial to have an understanding of the key differences between different scales to be able to predict what happens at a large-scale based on small-scale results. This chapter focuses on comparing the power draw of stirred media mills of different sizes and discussing key reasons for differences, as well as considering whether scale-up methodologies typically applied to mixing applications are applicable to stirred media mills.

6.2. Comparing Batch and Continuous Operation

Industrial mills typically operate semi-continuously, whereas lab-scale mills often operate as a batch. To directly compare batch and semi-continuous set-ups, a lab-scale semi-continuous set-up was created (see Chapter 3 for description). There are differences in particle size distributions (PSDs) between batch and continuous operations. PSDs resulting from continuous milling are also dependent on the number of mills in series or the number of passes through the mill – a narrower PSD closer to the batch PSD is achieved with more passes[90]. To investigate whether there are also differences in power draw, the lab-scale power draw is plotted for batch and semi-continuous lab-scale operation in Figure 6.1.

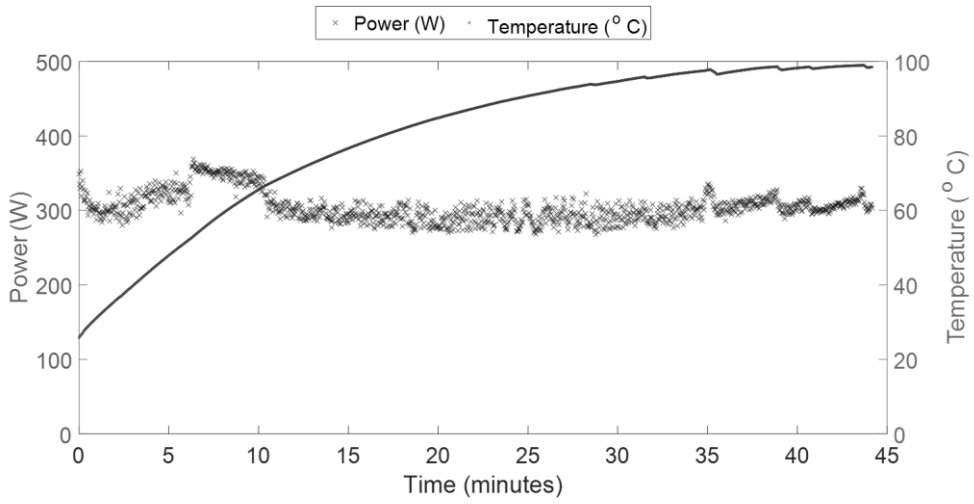

(a)

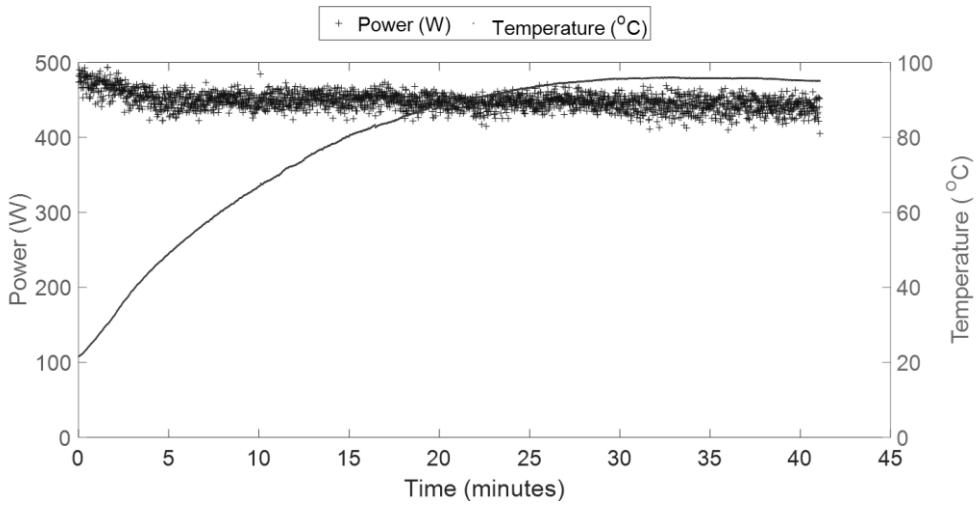

(b)

Figure 6.1: Power Draw and Temperature During Lab-scale Grinding at Impeller Tip Speed 9.8 m s^{-1} and Flowrate 1 ml s^{-1} (a) Batch Operation (b) Continuous Operation

From Figure 6.1, it is observed that for both batch and continuous lab-scale grinding, there is an initial decrease in power draw as the initial mixing and fluidisation of the calcium carbonate, water, dispersant and grinding media occurs. After this, the power draw for continuous grinding remains much flatter for continuous operation than batch, despite the temperature change being very similar for both modes of operation. This is likely due to the lack of particle size change occurring in continuous grinding at steady

state. For continuous grinding, the power draw was recorded from start-up, which mean that initial fluctuations are during the transition to steady state. Steady state is reached after approximately three residence times (30 minutes), which is similar to the time estimated to reach steady state in mixing applications (3-5 residence times).

The average power draw was approximately 50% higher for continuous grinding. This could be due to the control mechanisms of the continuous mill. The outlet flowrate and hence the level in the mill was controlled using elevated outlet tubing, as illustrated in Chapter 3. However, due to the large vortex observed in the mill using PEPT in Chapter 5, this method may not ensure the level remains the same as during batch grinding, which results in both differences to the average residence time and the ratio of media to fluid. The constant power draw over the run time suggest that the outlet and inlet flowrates were approximately the same and that there was no significant accumulation of slurry with time once steady state was achieved. However, for further analysis, the mill should be placed on a balance to continually measure the mass of material in the mill, as is suggested in Chapter 8.

6.3. Lab-scale Residence Time Distributions (RTDs)

Stirred media mill RTDs are important since they can be used to relate the product particle sizes from batch and continuous milling. If RTD characteristics are known, the PSD can be predicted for any flowrate from the batch particle size distribution[89].

To measure RTDs, a continuous set-up is required. This was not possible at the small rheometer scale due to the low flowrates required being difficult to control. Pilot-scale

RTD experiments were not possible due to pilot plant commitments and material constraints amongst Covid travel restrictions. However, lab-scale methods of assessing RTDs have been tested and compared to determine the feasibility of conducting future RTD experiments at pilot-scale.

RTDs were measured at lab-scale using the two methods described in Chapter 3:

- Using a Nigrosin dye tracer in a glycerol-water solution with grinding media.
- Using a titanium dioxide tracer in a calcium carbonate slurry with grinding media.

Each method has its advantages and drawbacks, which are discussed in this section, as well as the potential for application to a larger scale system.

6.3.1. Glycerol RTDs in Stirred Media Mill

Using a Nigrosin dye tracer, the RTDs for glycerol-water solutions in the lab-scale stirred media mill with varying amounts of mullite grinding media were determined. The total fill volume of the mill was the same for all trials, meaning that when less grinding media was used, more glycerol was added to counteract the change in total fill volume. The grinding media appear to supress the vortex in the mill. When the mill is operated without the grinding media, the vortex is so large that the fluid comes out the top of the mill. Hence, the grinding media amount in experiments is kept greater than or equal to 35 vol%. This change in vortex shape with different grinding media amounts was confirmed using PEPT in Chapter 5. The resulting RTDs for 71% glycerol-water solutions are shown in Figure 6.2.

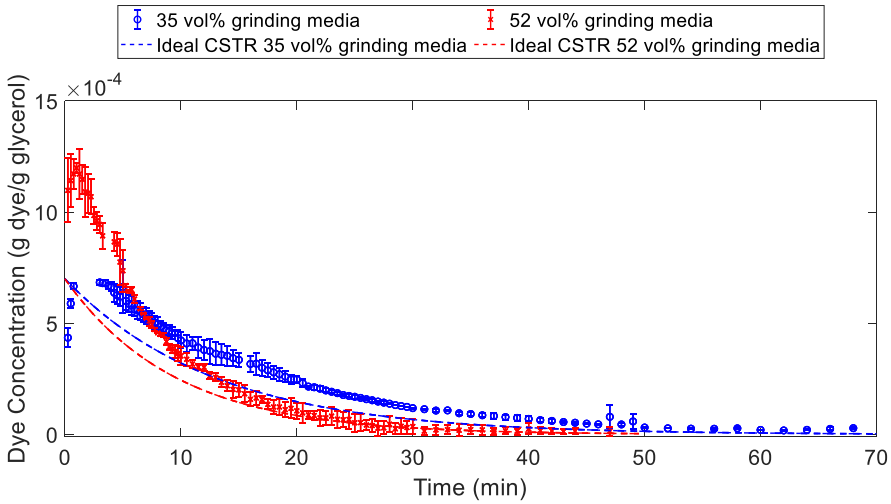

Figure 6.2: RTDs of a Dye Tracer in 71% Glycerol with Varying Amounts of 0.8-1.2 mm Mullite Grinding Media in the Stirred Media Mill. Error bars indicate the standard deviation from the average of three tracer pulses added to mill

Error bars in Figure 6.2 are relatively low and show reasonable experiment repeatability using the Nigrosin dye tracer method. The data does not appear to fit perfectly to the ideal continuous stirred tank reactor (CSTR) equations. To investigate this further, the data was fitted to the ideal CSTR equation for a C-curve Equation (6.1).

$$Ca = Ca_0 e^{\frac{-t}{\tau_t}} \tag{6.1}$$

Ca_0 (initial concentration) and τ_t (average residence time) values resulting in the best model fit are shown in Table 6.1 alongside the theoretical values based off the experimental set-up (τ_t was calculated from the volume of fluid in the mill and the flowrate).

Table 6.1: Actual and Experimentally Fitted Values for Constants in Ideal CSTR RTD – Dye Tracer in Glycerol

Case	Calculated Ca_0 (g/ml)	Fitted Data Ca_0 (g/ml)	Calculated τ_t (s)	Fitted Data τ_t (s)	Fitted Data R^2
35% Grinding Media	0.0006	0.00074	770	811	0.99
52% Grinding Media	0.0006	0.0015	570	441	0.99

All of the data is a good fit to an exponential decay equation, giving an R^2 of > 0.99 in all cases. However, the initial concentration, Ca_0 is significantly higher than the concentration of dye added to the mill, which would not be possible if the mill were perfectly mixed. The high initial tracer concentration could be attributed to one of the following reasons:

- The total volume of glycerol in the mill is lower than expected due to the size of the vortex. The flowrate out of the mill is controlled by an outlet tubing held at such a height as to keep the fluid height in the mill constant and is also dependent on how easily the fluid can exit through the mesh. When different fluids and amounts of grinding media are used, the size of the vortex changes. This means that the volume of fluid in the mill may differ, leading to a different initial concentration of dye in the mill. This could be measured if the mill were situated on a load cell and is suggested in Chapter 8.
- There are dead zones in the mill, where the dye does not reach, meaning that the volume of fluid containing dye is smaller than the volume of fluid in the mill.

The fitted τ_t is also different to the expected value. This average residence time inside the mill was calculated from the total volume of glycerol in the mill and the steady state flowrate out of the mill. Differences in fitted and calculated τ_t , could be due to:

- Flowrate fluctuations – steady state operation is much more difficult to maintain for such a small-scale continuous mill.
- The volume of glycerol in the mill is different to expected as a result of the vortex, as described for the initial concentration variation.

The C-curves for different amounts of grinding media are expected to differ due to the different volume of glycerol in the mill. Hence, to normalise the data with respect to the total tracer concentration measured, E-Curves were produced using Equation (6.2). The area under the C-curve was calculated using the trapezium rule as a simplification to integration. All of the measured concentrations had reached zero at the end of sample taking, and hence it is acceptable to sum the concentrations between zero and the end of the experimental run as opposed to zero and infinity.

$$E(t) = \frac{C(t)}{\int_0^\infty C(t)dt} \tag{6.2}$$

The area underneath the C-curve in an ideal system is related to the total mass of dye in the pulse and the flowrate of the mill, as indicated in Equation (6.3).

$$\int_0^\infty C(t)dt = Area\ Under\ C\ Curve = \frac{Mass\ of\ tracer\ (g)}{Flowrate\ from\ mill\ (ml\ min^{-1})} \tag{6.3}$$

The calculated experimental mass of tracer per unit volume flowrate and the summed area beneath the C-curve (taking into account the density of 71% glycerol-water solutions for unit conversion) are compared in Table 6.2.

Table 6.2: Comparing the Experimental and Predicted Amounts of Dye Exiting the Mill Over 5 Residence Times

Grinding Media Amount	Area Under C-Curve (g min ml^{-1})	Calculated Experimental Area (g min ml^{-1})
35 vol%	0.64	0.54
52 vol%	0.52	0.40

Table 6.2 shows that for both grinding media amounts the area under the C-curve is higher than expected; this could be due to the flowrate of the mill being slightly slower than expected due to the challenges of manual process control. The E-Curves calculated using the area under the C-curve are shown in Figure 6.3.

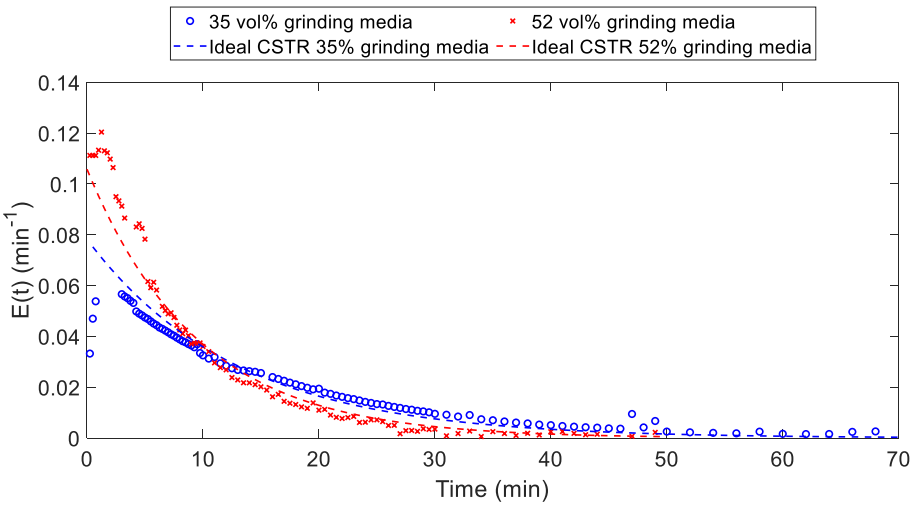

Figure 6.3: Normalised RTDs of a Dye Tracer in Glycerol with Varying Amounts of 0.8-1.2 mm Mullite Grinding Media in the Stirred Media Mill – E Curves

From Figure 6.3, it can be seen that when a larger proportion of the mill volume is filled with grinding media, a greater proportion of the dye exits at the beginning and the RTD is narrower. This is expected because of the lower total glycerol volume inside the mill and the lower average residence time, τ_t .

To further compare the data, the time and concentrations were both normalised using Equations (6.4) and (6.5) to calculate a dimensionless time, $\boldsymbol{\theta}$, and a dimensionless RTD function, $E(\theta)$.

$$\theta = \frac{t}{\tau_t} \tag{6.4}$$

$$E(\theta) = \tau_t \, E(t) \tag{6.5}$$

Dimensionlessly, all perfectly mixed CSTRs should have the same RTD, with the area under the E(θ) curve being 1. Dimensionless RTDs were plotted in Figure 6.4.

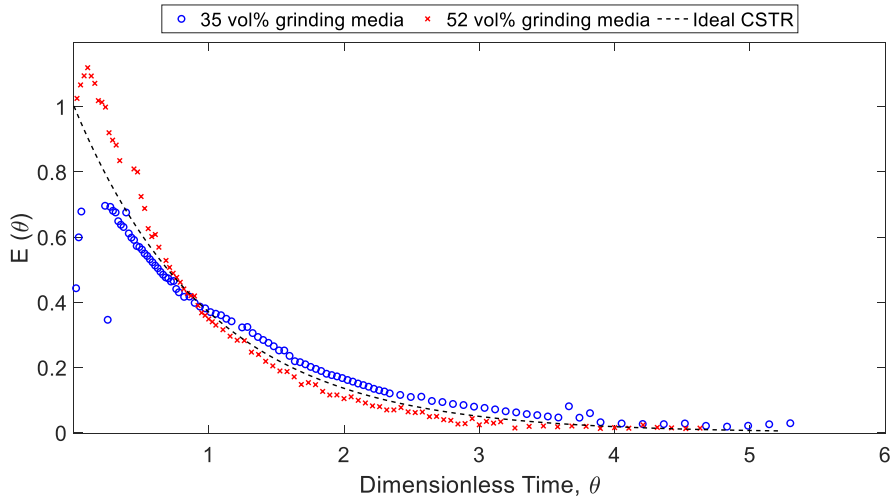

Figure 6.4: Dimensionless Plots of Glycerol RTDs

From Figure 6.4, it can be seen that the experiment using the standard 52 vol% grinding media behaves more closely to a CSTR than that with a smaller proportion of

grinding media. Unlike CSTRs, where the RTD indicates exponential decay, this data demonstrates a unimodal distribution. In Chapter 5, it was shown using PEPT that grinding media flow around either the top flow loop above the impeller pins or the bottom flow loop around and below the impeller pins. The flow of grinding media beads between these regions typically happens in the central region of the vessel. It can be hypothesised that the slurry move similarly to the beads, which means that there are also two flow loops of slurry, which could result in the deviation of the RTD from that of a CSTR. The dye added to the vessel reaches the bottom outlet of the mill quickly by dropping down through the central impellers without travelling through all regions of the mill. The RTD would be a better fit to a model of multiple CSTRs in series; this has been suggested in published research papers looking at RTDs in mills, which show similar RTDs to those presented here[107,167,168]. As the aim of this section is to investigate different methods of measuring the RTDs of stirred media mills and discuss potential differences from RTDs in CSTRs, this data has not been fitted to different models. This is suggested as further study when the RTD measurement methods proposed in this section are applied to larger scale mills such as at the Imerys pilot plant.

6.3.2. Calcium Carbonate RTDs in Stirred Media Mills

RTDs for the lab-scale stirred media mill media were measured using a solid titanium dioxide tracer. In this case, a base level of titanium dioxide was required to be maintained in the mill to ensure the amount of titanium dioxide in the samples remained sufficient to be detectable using X-Ray Fluorescence (XRF) – this is described in

greater detail in Chapter 3. Hence, the tracer concentration was calculated using Equation (6.6), where C_b is the base level constant.

$$Ca = Ca_{measured} - C_b \tag{6.6}$$

RTDs determined using the corrected concentration are shown in Figure 6.5.

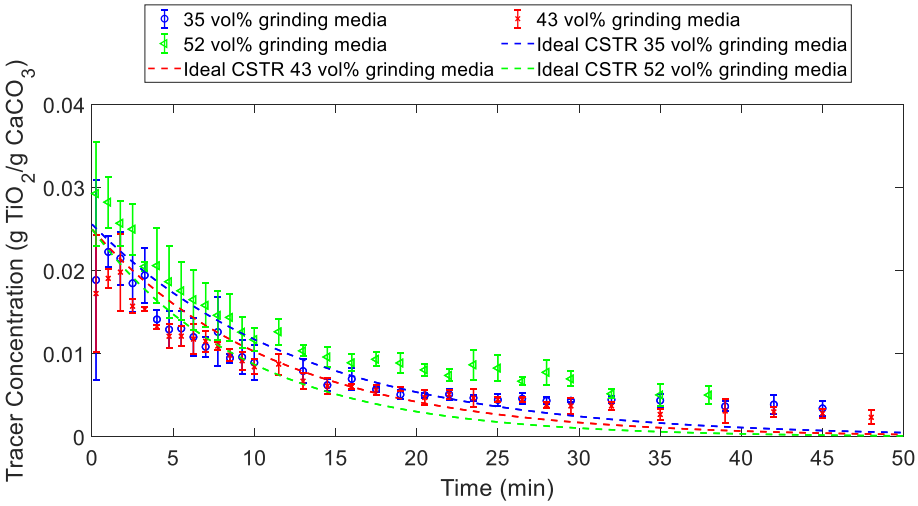

Figure 6.5: RTDs of a Titanium Dioxide Tracer in Calcium Carbonate with Varying Amounts of 0.8-1.2 mm Mullite Grinding Media in the Stirred Media Mill. Error bars indicate the standard deviation from the average of three tracer pulses added to mill.

Variability in Figure 6.5 is larger than for the Nigrosin dye in tracer method, particularly for 52 vol% grinding media, showing less repeatability. The calcium carbonate slurries were fitted to single term exponential decay equations, with the fitted and calculated experimental parameters shown in Table 6.3 to compare the behaviour in a mill to behaviour in a CSTR.

Table 6.3: Actual and Experimentally Fitted Values for Constants in Ideal CSTR RTD – Titanium Dioxide Tracer in Calcium Carbonate

Case	Calculated Ca_0 (g/ml)	Fitted Data Ca_0 (g/ml)	Calculated τ_t (s)	Fitted Data τ_t (s)	Fitted Data R^2
35% Grinding Media	0.025	0.024	770	895	0.9
43% Grinding Media	0.025	0.018	675	960	0.95
52% Grinding Media	0.025	0.026	570	981	0.93

In Table 6.3, the R^2 ranged from 0.9 to 0.96 for the cases with three different grinding media amounts, suggesting that the data is a worse fit to a CSTR model than the Nigrosin tracer in glycerol system. For further analysis, C-curves were normalised to give E-curves in Figure 6.6 and dimensionless plots in Figure 6.7, which could be more easily compared.

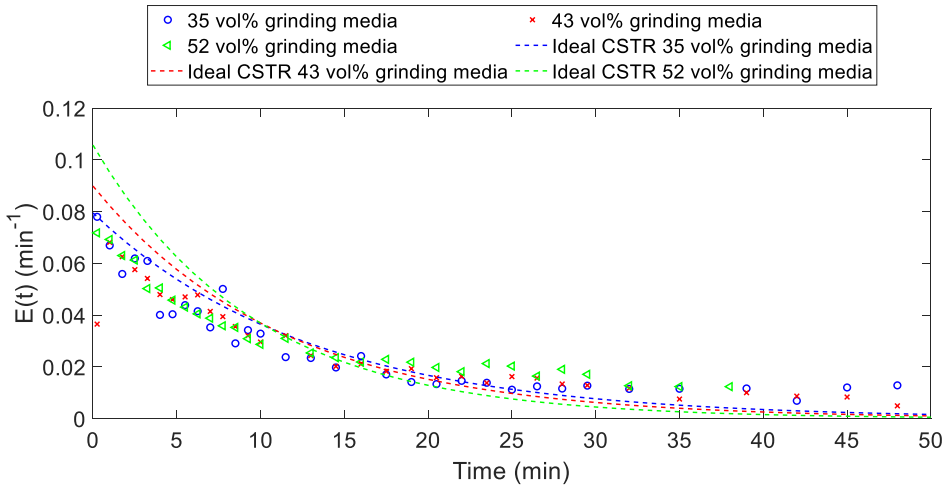

Figure 6.6: Normalised RTDs of a Titanium Dioxide Tracer in Calcium Carbonate with Varying Amounts of 0.8-1.2 mm Mullite Grinding Media in the Stirred Media Mill – E Curves

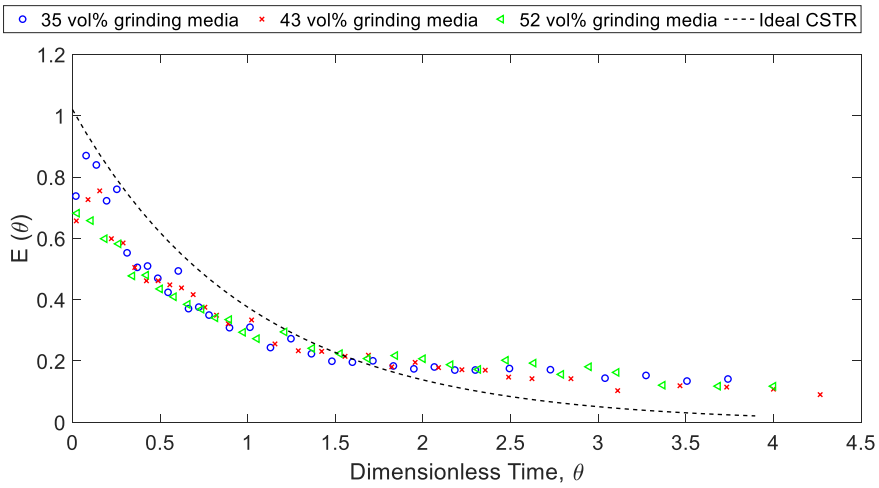

Figure 6.7: Dimensionless Plots of Calcium Carbonate RTDs Using Titanium Dioxide Tracer

In Figure 6.6 and Figure 6.7, the final concentration does not reach zero at the end of the milling, which suggests that a model with the addition of a constant (Equation (6.7)) would be a better fit – this indicates that mass is not conserved, which is likely due to process control inaccuracies.

$$Ca = Ca_0 e^{\frac{-t}{\tau t}} + \text{constant} \tag{6.7}$$

Adapting the model to include a constant gives a higher R^2 value in all cases, as is illustrated in Table 6.4 with the parameters fitted to the new model.

Table 6.4: Actual and Experimentally Fitted Values for Constants in Ideal CSTR RTD + Constant – Titanium Dioxide Tracer in Calcium Carbonate

Case	Calculated Ca_0 (g/ml)	Fitted Data Ca_0 (g/ml)	Calculated τ_t (s)	Fitted Data τ_t (s)	Constant	Fitted Data R^2
35% Grinding Media	0.025	0.019	770	480	0.003	0.96
43% Grinding Media	0.025	0.017	675	593	0.003	0.98
52% Grinding Media	0.025	0.024	570	453	0.006	0.99

The curves are a better fit to the equation with a constant, which suggests that the initial base level concentration of titanium dioxide may be higher than initially estimated due to the control methods associated with the system. The offset is unlikely to be related to the measurement method (XRF) since the calibration of this instrument was checked using samples of known concentration and shown to have minimal error. Due to the lower detectable limit of titanium dioxide in the XRF being approximately 0.01 g TiO_2/g $CaCO_3$, a base level of 0.01 g titanium dioxide was added to the mill with within the water and dispersant stream. Even a small variation in the pumped liquid flowrate compared with the powder fed calcium carbonate would cause a different amount of titanium dioxide to be measured than is expected. However, again due to the tests conducted to ensure the flowrates are as expected, this is unlikely to lead to errors of this scale. It is probable that the tail of the RTD is long in these cases and if measurements were continued for longer, 0 concentration would be reached. A long tail on an RTD is indicative of a dead zone that the tracer diffuses into, meaning that a small amount of the tracer remains in the mill for a long time.

The fitted C_{A0} and τ_t in Table 6.4 are lower than the calculated values. Due to the improvement in the curve fitting being small when a constant is added and the fitted C_{A0} and τ still being far from the experimental values, it is deemed that the stirred media mill does not deviate significantly from a standard CSTR in these cases. Due to the unimodal shape of the distribution at the start, it could also be fitted to a multiple CSTRs in series model, as discussed in section 6.3.1.

6.3.3. Comparing Glycerol and Calcium Carbonate RTDs in Stirred Media Mill

Dimensionless residence distributions determined using Nigrosin dye (in glycerol) and titanium dioxide (in slurry) tracer methods are compared in Figure 6.8.

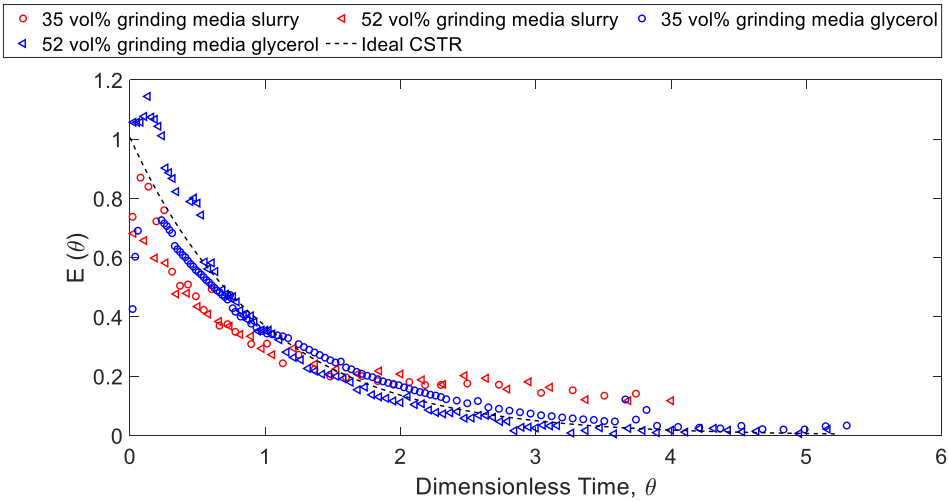

Figure 6.8: Dimensionless RTDs – Comparison Between Nigrosin Dye in Glycerol and Titanium Dioxide in Slurry

Dimensionless RTDs in Figure 6.8 lie close to that expected for a CSTR, which suggests that despite the large vortex observed in the mill, mixing is good. The solid and liquid residence distributions lie close to one another and are hence likely to be the same. This is in agreement with other literature sources finding solid and liquid

RTDs to be almost identical in a stirred mill[168]. Furthermore, flow patterns for glycerol and slurries in stirred media mills with grinding media were found to be similar in Chapter 5. There remains conflict on the effect of the amount of grinding media in a stirred media mill; initial concentrations were higher for the larger grinding media amount when a dye tracer was used, but lower when the titanium dioxide tracer was used. It was concluded that the amount of beads does not have significant impact on the RTD model. The unimodal distributions suggest that a multiple CSTRs in series model would be a better fit to the data[107].

Average residence times found using each tracer method are compared in Table 6.5 along with the average residence time calculated from the fluid volume and the volume flowrate.

Table 6.5: Average Residence Times Measured Using the Two RTD Methods

Case	Calculated τ_t (s)	τ_t Nigrosin Tracer in Glycerol (s)	τ_t Titanium Dioxide Tracer in Slurry (s)
35% Grinding Media	770	811	895
52% Grinding Media	570	441	981

From Table 6.5, τ_t is similar using both tracers for 35 vol% grinding media but differs greatly for the two tracer methods with 52 vol% grinding media. If a constant is added to the CSTR equation when titanium dioxide is used, τ_t is reduced significantly to 453, which is very similar to that obtained using the Nigrosin dye in water method.

Mixing at a small-scale is less demanding than at a large-scale. Hence, ideally the RTDs should be measured at larger scale. Literature sources suggest that a multiple

tanks in series model is suited to industrial mills, with the area around each impeller pin essentially representing a tank of compartmentalised flow[107,168]. This is particularly relevant to larger scale milling where more impellers are present and stacked in more layers rather than the lab-scale mills equipped with four impeller pins across two rows. The potential application of RTD measurement methods to the pilot plant mill is considered in section 6.3.4 and further research is suggested in Chapter 8.

6.3.4. Potential Application of RTD Measurement Methods to Pilot-Scale

The method of using glycerol in the mill is less feasible at large-scale than lab-scale since large amounts of glycerol will be wasted leading to high operating costs and disposal issues. At pilot-scale, it may be possible to use the method of using calcium carbonate slurries with a dye in the mill to measure the RTD. Samples will be larger due to the higher flowrate, which means that the slurry can be centrifuged to separate the solid particles from the dyed liquid. However, since it is desirable for calcium carbonate to maintain its very white appearance, contamination of the pilot plant equipment with the dye could be an issue and calcium carbonate cannot be recycled.

Using a titanium dioxide tracer is practically feasible. However, the requirement to maintain a base level of titanium dioxide in the mill to exceed the lower limit of XRF detection results in high operating costs. The pilot-scale tests would require approximately 13 kg to run a single trial with one pulse addition, or approximately 28 kg to run a single trial with three pulse additions to allow for the assessment of errors.

6.4. Investigating Key Parameters Affecting Scale-Up

To consider parameters affecting scale-up of a stirred media mill, three different equipment scales were utilised:

- A four-pin impeller in a 50 mm diameter rheometer vessel operated as a batch.
- A four-pin impeller in a 142 mm diameter lab-scale mill operated as a batch.
- An 18-pin impeller in a baffled octagonal 800 mm diameter mill at Imerys pilot plant in Liege operated semi-continuously.

There are geometrical differences between the mills at different scales. Due to the small size, no baffles and fewer impeller pins are present in the lab-scale mill, whereas to promote efficient use of the entire mill volume at larger scales, baffles and more stacked impeller pins are required. Additionally, even at the smallest scales, the gap between the impeller pins and the wall/base of the vessel must be sufficiently large to allow the grinding media beads to pass through the gap. Geometrical differences should be considered in scale-up approaches.

In batch milling, the PSD changes with time so short experimental run times are desirable. At lab-scale, the time to reach a constant power draw is short and hence an average power draw could be measured over 15 seconds. For continuous milling, operational times can be longer since there is no PSD change occurring with time after steady state has been reached. It takes longer to reach steady state for pilot-scale continuous milling (shown in Figure 6.9), so the power draw was measured and recorded for 15 minutes at each speed to allow sufficient time to reach a new steady state at each speed.

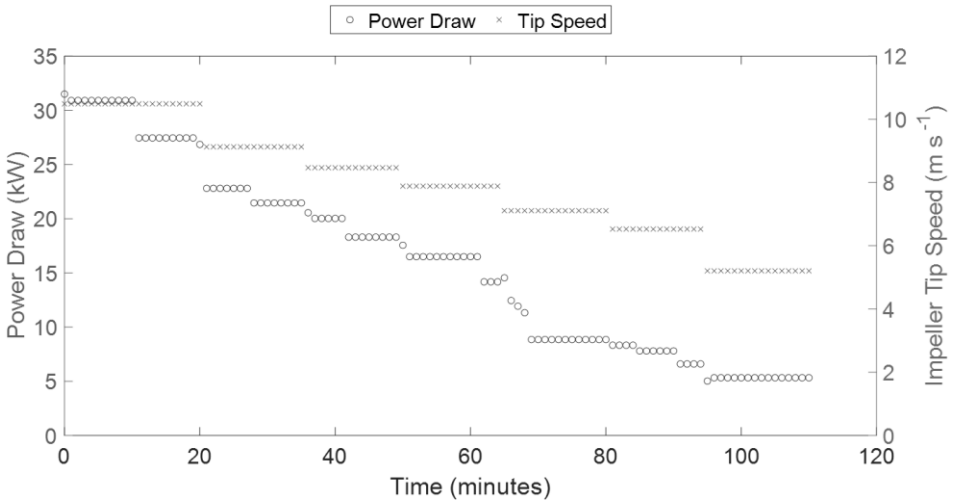

Figure 6.9: Power Draw in Pilot-scale Continuous Operation Milling with approx 42 vol% 0.8-1.2 mm Mullite Grinding Media in 75 wt% Slurry

In typical mixing operations, scale-up is often based on using the same tip speed or power per unit mass, as was discussed in Chapter 4. In terms of understanding the flow and vortexing in the vessel, the Reynolds number and Froude number are important. In terms of particle breakages, stress energy (SE) and stress number (SN) (defined in Chapter 2) are critical. Using power draw data collected experimentally from three different scales, comparisons were made in terms of each of these parameters.

6.4.1. Tip Speed, Torque and Specific Power Draw

Scale-up at a constant tip speed can be a challenge due to the vastly different impeller diameters - high tip speeds are unachievable in very small diameter systems. Nevertheless, the specific power draw at the measurable range of tip speeds is compared for the three systems in Figure 6.10. Experiments with 1.4-2.4 mm mullite grinding media were not possible at the rheometer scale due to the set-up structure; the geometry was not operable with the large grinding media beads due to the high initial torque required.

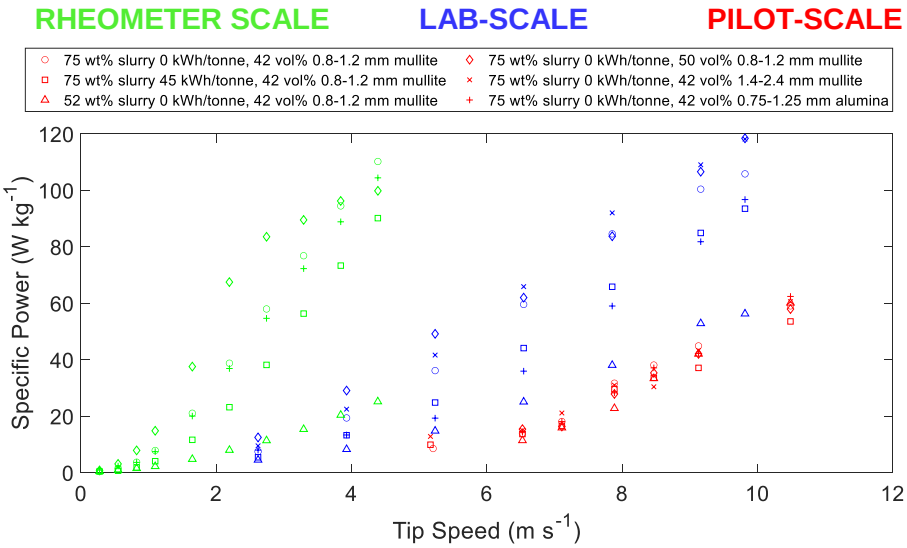

Figure 6.10: Specific Power Draw for Small Rheometer Scale Tests, Lab-scale Batch Milling and Pilot-scale Semi-Continuous Milling

It can be observed from Figure 6.10 that the range of tip speeds covered by the rheometer scale tests are low and the same tip speeds as pilot-scale milling cannot be achieved. A similar range of tip speeds can be achieved in the lab-scale and pilot-scale mills, making them more easily comparable.

The power is indicative of the magnitude of momentum transfer[169]. It should be noted that the power for the rheometer scale and lab-scale operations is calculated based on the actual torque measured, whilst the pilot plant power is the power supplied to the motor. The motor and gearbox do not have 100% energy efficiency, so it is likely that the actual power supplied to the grinding media and slurry is less than indicated. This is discussed further in section 6.4.6. At the lab-scale, the specific power draw is consistently higher than the pilot-scale mill. This is different to typical mixing scale-up, where the same power per unit mass at a larger scale typically requires a lower tip speed in mixing applications[74]. This can be attributed to the lack of geometric similarity

and baffles – baffled tanks are demonstrated in literature to have a higher Power number, and hence power, than a geometrically similar unbaffled tank[170]. The lack of vortexing in a baffled tank allows more power to be delivered to a system at a given impeller speed.

Furthermore, there is more variation in power draw when parameters such as the slurry and grinding media properties are changed at smaller scales. This is likely a result of the flow pattern variation - Chapter 5 showed that the operating parameters have a large effect on the shape of the vortex which affects the power draw. To consider the different vortex sizes at different scales, the Froude number is discussed in section 6.4.3.

When selecting a tip speed for large scale stirred media mills, it is also important to consider the wear of the mill liner, grinding media beads and impeller pins. Wear should be investigated on larger scale mills since wear rates here are greater. Wear is difficult to relate directly to impeller speed and milling parameters since it happens over a relatively long period of time, over which the pilot-scale mill will have operated with a range of impeller speeds and operating conditions[26].

6.4.2. Stress Energy and Stress Number

The ultimate aim of scaling up a stirred media mill is to obtain the same stress energy and stress number since this, in theory, should lead to the same amount of particle breakages and hence the same resulting particle size distribution[112]. The stress

energy is proportional to the maximum stress energy, which is related to the kinetic energy of the grinding media bead and can be calculated using Equation (6.8)[11].

$$SE_{max} = d_{GM}^3 v_t^2 \rho_{GM} \tag{6.8}$$

The maximum stress energy is obtained when the largest grinding media beads are moving at the impeller tip speed. A comparison of maximum stress energies at the three scales is shown in Figure 6.11.

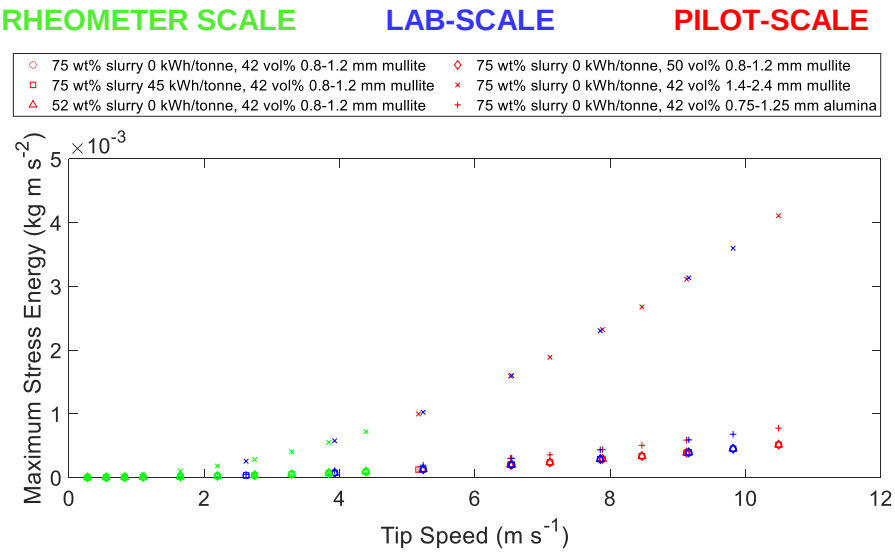

Figure 6.11: Maximum Stress Energy at Each Equipment Scale

From Figure 6.11, it is observed that the range of maximum stress energies at the lab and pilot-scales are very similar. This is because both equipment scales are capable of operating in the same range of tip speeds. Although the maximum stress energy is the same at each scale at a constant tip speed, the distribution of stress energy throughout the mill is likely to differ greatly.

The distribution of stress energies throughout the mill depends greatly on the mill geometry and flow patterns. Stender et al.[171] considered the difference in stress energies in different equipment geometries and scales and found the mean stress energy to be higher in smaller units. This was done by splitting the mill into cells with different stress energies based on knowledge of bead velocities and acceleration from CFD models. As well as literature showing that the energy distribution differs greatly between units of different sizes, the pilot vessel studied in this thesis is equipped with baffles which is likely to affect the stress energy distribution since it affects the flow patterns; flow pattern investigations in baffled vessels using PEPT are suggested as further research to investigate this.

The stress number is the average number of stress events of each feed particle and can be calculated using Equation (6.9)[12].

$$SN \propto \frac{\varphi_{GM}(1-\varepsilon)}{(1-\varphi_{GM}(1-\varepsilon))C_v}\frac{Nt}{d_{GM}^2} \tag{6.9}$$

As the same grinding media type are used at each scale, the grinding media fill volume, packing ratio and size are the same at each scale. The slurry solids content, C_v, also remains constant. Hence, the main difference at scales is the impeller rotational speed, N. Equation (6.9) is generally valid but is less accurate if the slurry particle size (and hence viscosity) varies widely or the grinding media fill ratio changes[12]. This was described by the authors as being due to the grinding media contacts increasing superproportionally with increasing grinding media fill ratio and also as the viscosity is not included in equation (6.9) but does affect the number of collisions.

6.4.3. Froude Number

In literature it is shown that scale-up at constant Froude number (Equation (6.10) where N is the impeller speed, D is the impeller diameter and g is acceleration due to gravity) results in much higher energy requirements than necessary, resulting in overmixing (and hence overgrinding) and potentially poor energy efficiency[116]. Nevertheless, it does have successful application as a scale-up criteria in pharmaceutical granulation systems, the result is similar process temperatures and a similar resulting particle size, since the force pressing the particles against the vessel walls is the same in each process[114].

$$Fr = \frac{N^2 D}{g} \tag{6.10}$$

The Froude numbers at each equipment scale can be seen in Figure 6.12 for the range of tip speeds.

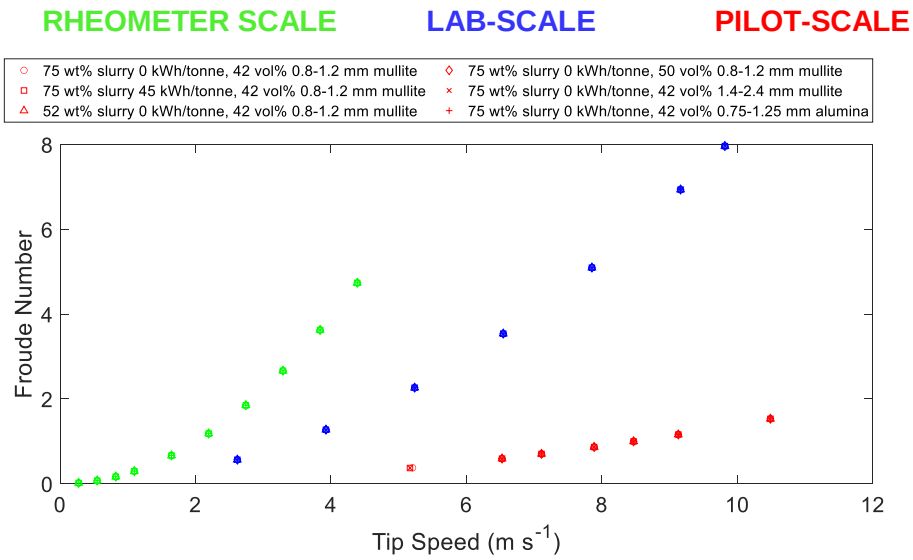

Figure 6.12: Froude Numbers at A Range of Tip Speeds for Each Equipment Scale

Figure 6.12 shows that there is some overlap in the range of Froude numbers at each scale. At larger scale for a given tip speed, the Froude number is lower meaning that the vortex is shallower. The Froude number calculated is independent of the grinding media type and amount. However, in Chapter 5, it was seen that the vortex size is widely affected by these parameters for the lab-scale mill.

As well as the low Froude number at the pilot-scale, baffles are employed which will also further reduce the size of the vortex. The vortex being significantly smaller at the pilot-scale is a likely reason for the changes in grinding media type and amount having a smaller impact on power draw at a given tip speed for pilot-scale milling than lab-scale milling in section 6.4.1. This suggests that analysis using the Froude number is more relevant to predicting power draw at smaller scales that exhibit vortexing behaviour. Power predictions at each scale are discussed further in section 6.4.5.

The shallower vortex and flatter surface at large-scale mean that flow patterns are likely to be different at larger scales, which affects the stress energy distribution and hence the efficiency of particle size reduction. Further detail about flow patterns and turbulence can be obtained by consideration of the Reynolds number and Power number.

6.4.4. Reynolds Number and Power Number

The Reynolds number is important to consider for scale-up since it can be used to predict the power requirement using the Power number. The Reynolds number is

dependent on the viscosity of the fluid. A detailed discussion of the calculation of Reynolds numbers in lab-scale stirred media mills can be found in Chapter 4.

Slurries and also slurry and grinding media combinations used in this work were found to be shear thinning in Chapter 4, which means that an estimate for an apparent shear rate in the mill is required to select a viscosity to use in calculating the Reynolds number. In Chapter 4, the Metzner-Otto correlation was used to estimate an apparent shear rate, $\dot{\gamma}_e$, based on the impeller speed, N and the Metzner-Otto constant, k_s, as shown in Equation (6.11)(4.9).

$$\dot{\gamma}_e = k_s N \tag{6.11}$$

It was found that Metzner-Otto constant, k_s, is important and may be dependent on the power law index of the fluid, n, as is typical of highly shear thinning fluids[73]. However, k_s is unlikely to be the same at each equipment scale due to geometrical differences. Furthermore, in the turbulent regime, the contribution of turbulence to shear rate is sufficiently large that using the Metzner-Otto correlation significantly underestimates the shear rate[72]. In order to consider the Reynolds numbers encountered at different scales, the following assumptions were tested:

- Assume the Metzner-Otto correlation can be applied at all scales with constant k_s (k_s = 13, as was used in Chapter 4). The viscosity term includes slurry only and hence assumes the grinding media are a part of the system like baffles.
- Assume the Metzner-Otto correlation can be applied at all scales with constant k_s (k_s = 13). The viscosity term includes slurry and grinding media (measured

using vane rheometer) and hence assumes the grinding media are a part of the fluid.

- Assume the Metzner-Otto correlation can be applied at all scales with the optimal k_s determined in Chapter 4 ($k_s = 10.7\ n^{-0.15}$). The viscosity includes the slurry and grinding media (measured using vane rheometer).
- Assume the turbulent shear rate is proportional to the square root of the energy dissipation rate[72], which essentially gives a higher dependency of the shear rate on the impeller speed ($\dot{\gamma}_e\ \alpha\ N^{1.5}$).

6.4.4.1. Metzner-Otto $k_s = 13$ – Slurry Only Viscosity

When the grinding media are assumed to be a part of the system (like baffles) and are therefore excluded from the density and viscosity of the fluid, the resulting Po-Re plot for the lab and pilot scales can be seen in Figure 6.13.

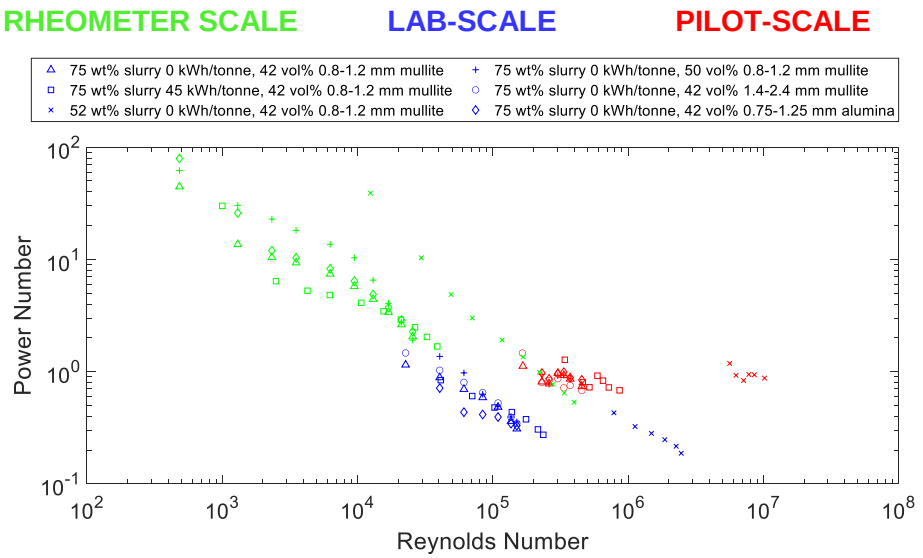

Figure 6.13: Po-Re Plot for Lab and Pilot-scale Milling – $k_s = 13$ - Viscosity and Density Terms Exclude Grinding Media and Assume They are a Part of the System

The Power number is still dependent on the Reynolds number at high speeds at the rheometer and lab-scale, which is expected for unbaffled tanks[82]. For the baffled pilot-scale mill, the dependence of Power number on Reynolds number is low, making the power draw simpler to predict, which is typical of turbulent flow in a fully baffled vessel[172]. This suggests that the pilot mill operates in the turbulent regime, which is expected due to the large impeller diameter and high speeds. For this case, it is likely that the shear rate in the pilot-scale mill is underestimated; the effect of turbulence (eddies and local high shear regions) on shear rate is not considered in the Metzner-Otto correlation. It is useful to be able to estimate shear rate since the viscosity in stirred media mills is often Non-Newtonian and hence dependent on shear rate. The shear rate can be used to infer information about power draw and motion.

For both the lab-scale and the rheometer-scale, the sample with the low solids content slurry does not fit with the overall trends – this is likely to be due to the inaccuracies of measuring low solids content slurries discussed in Chapter 4. This was improved upon by including the grinding media in the measured viscosity.

6.4.4.2. Metzner-Otto $k_s = 13$ – Slurry + Grinding Media Viscosity

When the grinding media are assumed part of the fluid and therefore considered in the density and viscosity terms, the resulting Po-Re plot for the lab and pilot-scales can be seen in Figure 6.15, assuming the Metzner-Otto concept holds and k_s is constant. The density term is the weighted density of the slurry and grinding media and the viscosity

of the slurry and grinding media combination was measured using the vane rheometer, as in Chapter 4.

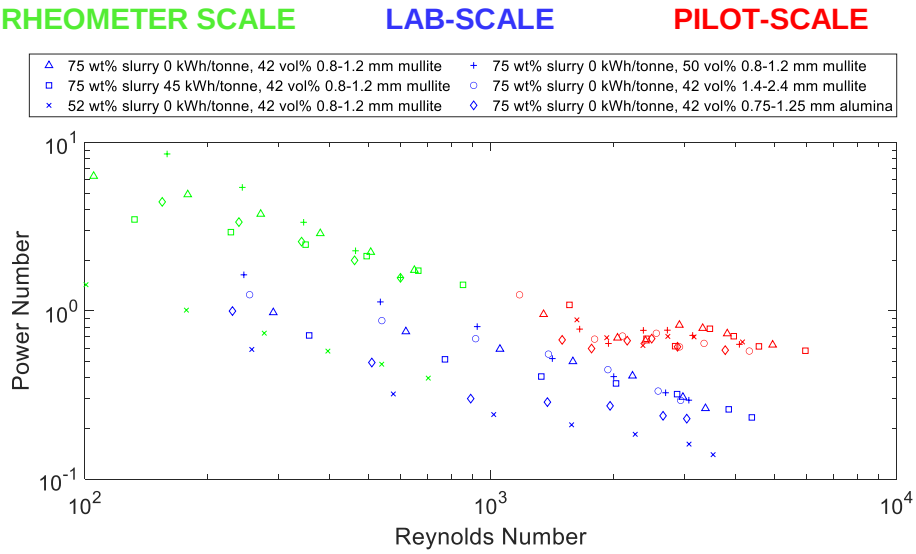

Figure 6.14: Po-Re Plot for Small Rheometer, Lab and Pilot-scale Milling – k_s = 13 - Viscosity and Density Terms Include Grinding Media

Figure 6.14 shows that flow in the pilot-scale mill is turbulent since the Power number again has little dependency on Reynolds number meaning that the choice of k_s is less important. However, it is likely that the Reynolds number is again largely underestimated by the lack of consideration of turbulence when estimating the shear rate.

With the assumption of a constant k_s, there is no clear singular relationship between Power number and Reynolds number at the rheometer and lab scales. To improve upon this, k_s was assumed to be dependent on the power law exponent, n, as is typical of shear thinning fluids[72]. The k_s relationship used is the one found to be optimal in Chapter 4.

6.4.4.3. Metzner-Otto $k_s = 10.7\ n^{-0.15}$ (Optimal k_s from Chapter 4) – Slurry + Grinding Media Viscosity

The choice of Metzner-Otto constant is important since it has a large impact on the Reynolds number. Figure 6.15 shows the Po-Re plot where k_s is the optimal found for the lab-scale mill in Chapter 4.

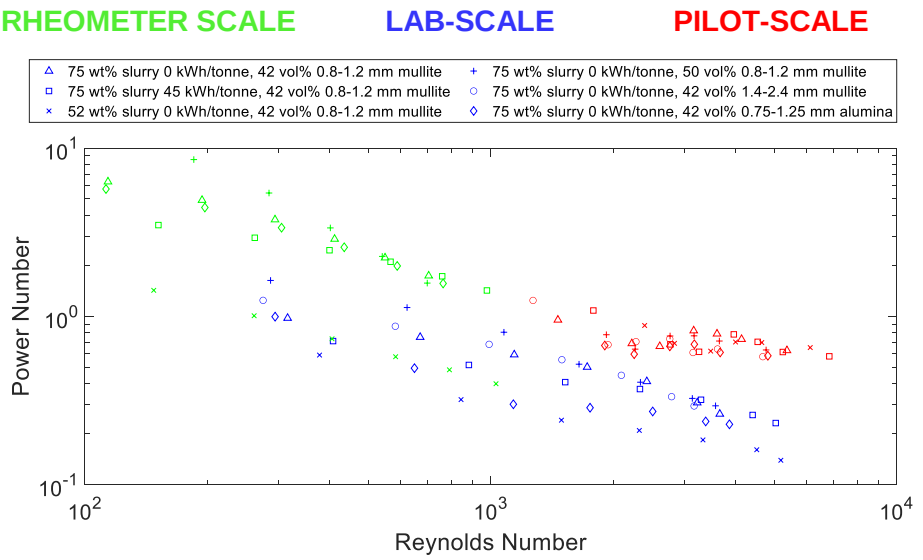

Figure 6.15: Po-Re Plot for Lab and Pilot-scale Milling – $k_s = 10.7\ n^{-0.15}$ (optimal from Chapter 4) -Viscosity and Density Terms Include Grinding Media

From Figure 6.15, it is shown that the optimal k_s found for lab-scale milling in Chapter 4 works relatively well for both rheometer-scale and lab-scale tests. Although the relatively flat Power number observed in Figure 6.15 again suggests that flow is turbulent at the pilot-scale, the Reynolds numbers are not significantly higher than lab-scale. It should be noted that k_s is unlikely to be the same at all scales due to lacking geometric similarity[75], which would have a large impact on the Reynolds numbers.

The Metzner-Otto correlation assumes that the shear rate is dependent only on velocity and neglects the effect of turbulence, which means that shear rates are likely to be

underestimated. Higher shear rates would lead to higher Reynolds number since the fluids are shear thinning.

6.4.4.4. Shear Rate is Proportional to Square Root of Energy Dissipation Rate – Slurry + Grinding Media Viscosity

As an alternative to the Metzner-Otto correlation, the shear rate was assumed to be proportional to the square root of the energy dissipation rate[72,173]. If the turbulent shear rate estimation method of assuming the shear rate is proportional to the square root of the power per unit mass for lab-scale data, the data points are separated and do not fit as close to a straight line, making power draw more difficult to predict, as is illustrated in Figure 6.16.

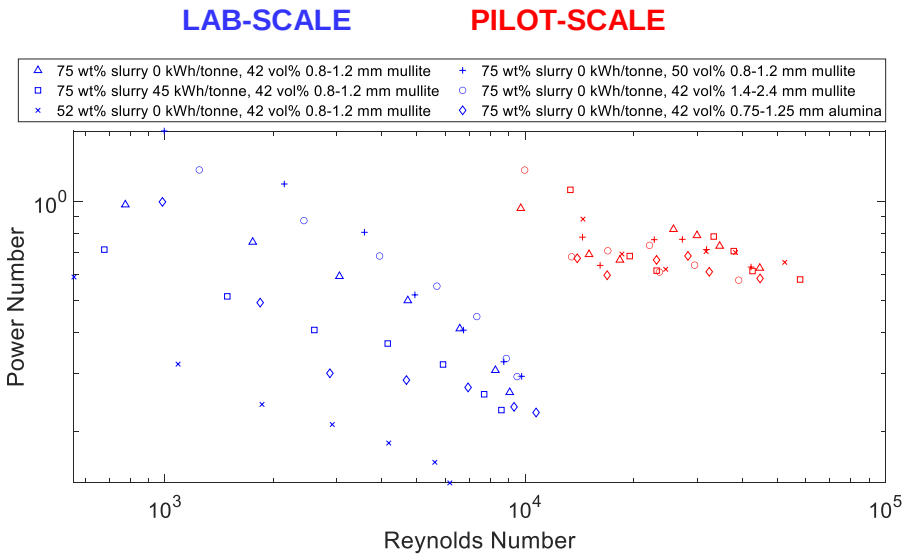

Figure 6.16: Po-Re Plot for Lab and Pilot-scale Milling – Shear Rate Estimated to be Proportional to Square Root of Power per Unit Mass ($shear\ rate = 100\sqrt{power\ per\ unit\ mass}$).

From Figure 6.16, it is evident that a smooth Po-Re curve is not produced when this alternative to the Metzner-Otto correlation, which assumes the shear rate is

proportional to the power per unit mass, is applied to lab-scale data. This could be due to the lack of consideration of the fluid type or the fluid not being fully turbulent at the unbaffled lab-scale. Hence, lab-scale and rheometer-scale data will revert to being estimated using the Metzner-Otto correlation, assuming the Metzner-Otto constant is dependent on shear thinning index, n, as was discussed in Chapter 4.

Po-Re plots produced by assuming the shear rate in the mill for pilot-scale only (turbulent flow) is proportional to the square root of the power per unit mass measured are shown in Figure 6.17.

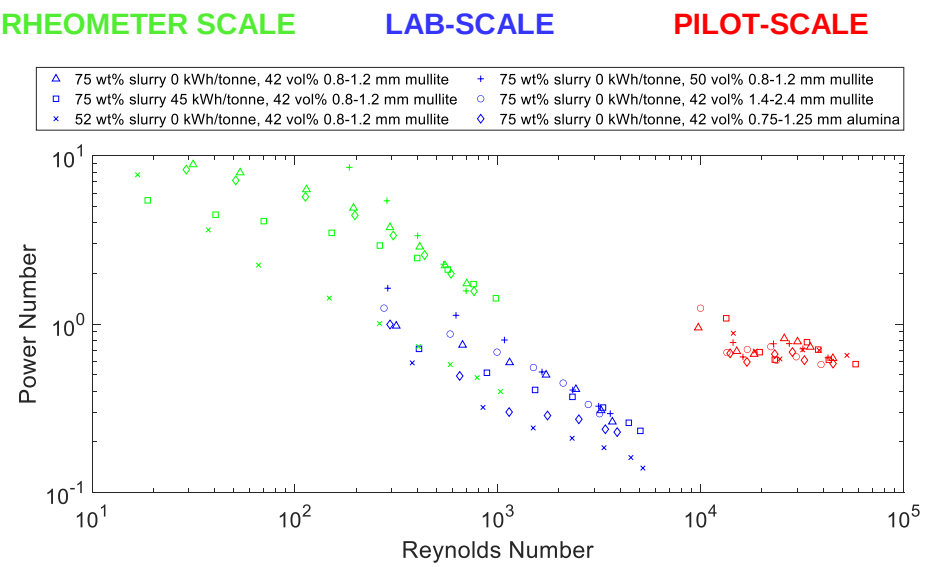

Figure 6.17: Po-Re Plot for Lab and Pilot-scale Milling – Shear Rate Estimated to be Proportional to Square Root of Power per Unit Mass for Turbulent Pilot-scale and Estimated Using Metzner-Otto for Lab and Rheometer Scale - Viscosity and Density Terms Include Grinding Media

An arbitrary constant of 100 was used ($shear\ rate = 100\sqrt{power\ per\ unit\ mass}$). This is useful for showing the trend of the data in Figure 6.17 but may cause the data to be compressed, elongated or shifted left or right depending on the actual constant. Further

research into predicting shear rates in the mill, including by utilising CFD, is recommended in Chapter 8.

This method is less useful than estimating the shear rate based on the tip speed due to the requirement of the power per unit mass being measured and known. The power is related to impeller speed by a cubic relation. This means that when the shear rate is proportional to the square root of the energy dissipation rate, the shear rate could now be related to the impeller speed raised to the power of 1.5, which is easier to apply when predicting power draw. Nevertheless, the constant of proportionality still needs to be determined as further research. It should be noted that other methods of estimating shear rates in the turbulent regime have been proposed in literature and the shear rate is unlikely to be uniform throughout the vessel and will have areas of higher shear rates near the impeller[72].

6.4.5. Predicting Power Draw at Different Scales

In Chapter 4, several methods of predicting power draw were compared for the lab-scale mill. The power draw could be predicted based off the measured slurry viscosity by considering a relationship between the Power number and the Reynolds, Froude and Stokes numbers, or alternatively based off a measured combined viscosity of the slurry and grinding media. Predicting power draw at the larger pilot-scale is simpler because the Power number is less dependent on Reynolds number and hence viscosity.

Predicting the power draw based off a constant Power number (Po = 0.7) gives an average power prediction error for the pilot-scale mill of 12% and a maximum error of 42%. Although the maximum error is high, these high errors occur at the slowest speeds. These slow speeds resulted in the level of the mill rising due to difficulties of the fluid exiting the mesh at the bottom of the mill, as is discussed in section 6.4.7. The fill level is a geometry factor that effects the Power number. A higher fill level would result in a larger measured power draw than predicted. When the slowest speed is eliminated from the analysis, the average error is reduced to 10% and the maximum error 24%, which is more reasonable. The turbulent Power number, 0.7 is typical of other similar impeller types in literature[74].

6.4.6. Comparing Power Measurement Methods at Each Scale

The pilot-scale power draw is measured before the motor and gearbox, which means that frictional heat loss within the motor and gearbox are not considered. The lab-scale and rheometer power draws are calculated from a torque and hence do not have any additional energy losses. This results in the pilot-scale having a higher power draw that is not directly comparable to lab-scale milling.

The efficiency of the motor and gearbox is likely to be a function of the impeller speed, with an optimum at the normal operating range[174]. In order to compare the pilot-scale power draw to lab-scale power directly, a load cell or torque meter could be introduced to measure the torque of the pilot-scale mill.

In terms of predicting power draw, the energy efficiency is likely to be ~ 95% at normal operating impeller speeds[175], which means that the Power number is still close to constant, as is expected in the turbulent regime.

6.4.7. Variability Considerations

To illustrate the repeatability of the power draw measurements at the lab and rheometer scales, variability is illustrated in Figure 6.18 for an example experiment.

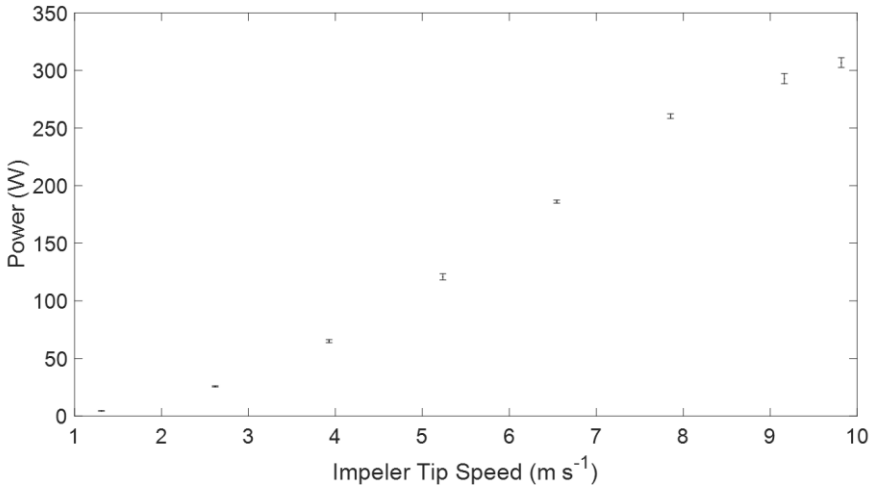

(a)

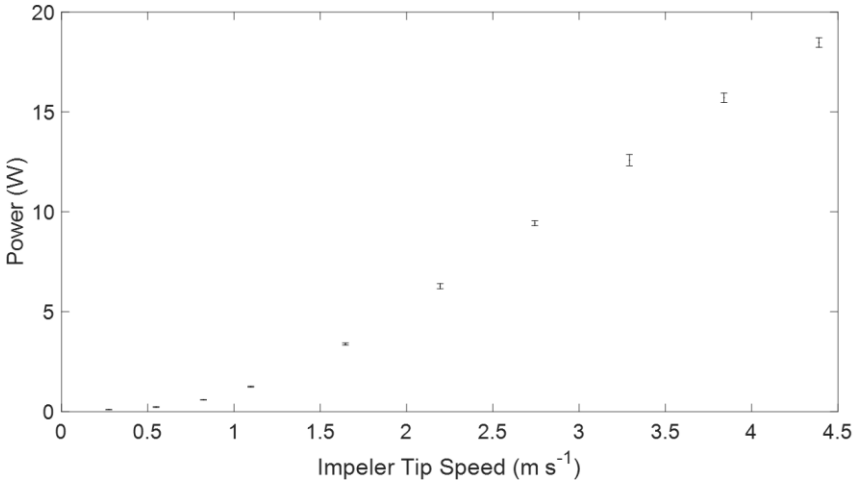

(b)

Figure 6.18: Mill and Rheometer Power Draw Data for 75 wt% Slurry in 42 vol% 0.8-1.2 mm Mullite Grinding Media – Data is Average of 3 Mill or Rheometer Runs, Error Bars Indicate Standard Deviation (a) Mill Lab-scale (b) Rheometer-Scale

At the lab and rheometer scales, errors bars are not visible at low impeller tip speeds due to their small size, suggesting good experimental repeatability. The errors increase at high tip speeds due to increased fluctuations and turbulence, but are still well within the acceptable range.

Repeat experiments were not conducted at pilot-scale due to operating time and material constraints. However, errors are expected to be larger than in smaller scale experiments due to the continuous mode of operation and the change in fill level of the mill occurring due to the ease that the fluid can exit the mill through the mesh on the exit pipes. At pilot-scale, the mill sits on a load cell, continually measuring the mass of material in the mill, as is plotted in Figure 6.19 for a range of impeller speeds.

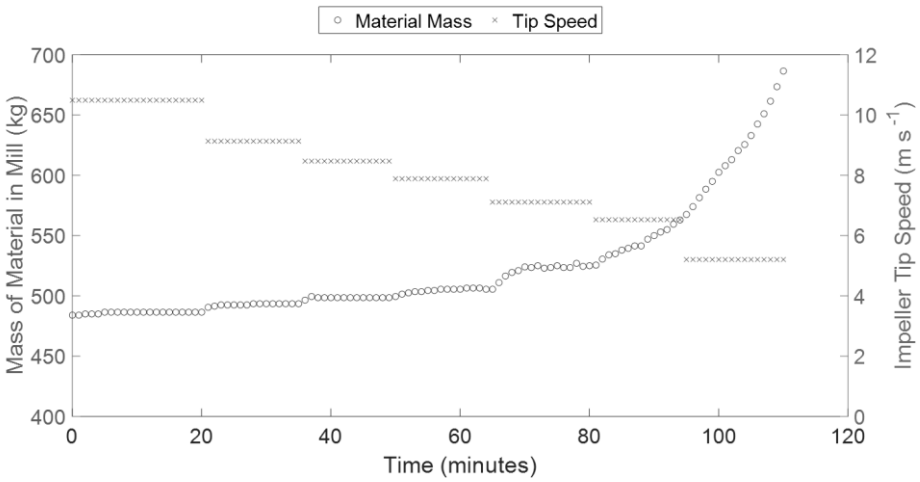

Figure 6.19: Mass of Material in Mill Changes with Impeller Speed During Pilot-Scale Continuous Grinding with approx 42 vol% 0.8-1.2 mm Mullite Grinding Media in 75 wt% Slurry

Figure 6.19 shows that the mass of material in the pilot-scale mill gradually increases with decreasing impeller speed as it becomes more difficult for the slurry to exit the mill through the mesh at the outlet, which is designed to prevent grinding media beads from

exiting the mill. This is caused by a lack of fluidisation of grinding media beads surrounding the exit and means that not only is the fill volume of the mill changing, but also the ratio of slurry to grinding media. At speeds lower than 6.5 m s^{-1}, the mass of material in the mill increases constantly, suggesting that it does not reach steady state. Hence, the power draws measured at lower speeds are less reliable.

6.5. Summary

Lab-scale operation was compared with pilot-scale operation as well as a smaller scale system which makes use of a rheometer set-up with a custom 3D printed geometry. Although small-scale milling utilising a 3D printed impeller with a rheometer set-up has shown potential due to the ease of setting up, fast experimental run time, low resource requirements and good control, the tip speeds covered are significantly lower than the lab-scale and pilot-scale applications, making drawing scale-up conclusions a challenge. These small-scale experiments do provide the major advantage of enabling a lot of impeller types and configurations to be tested easily by 3D printing impellers.

The pilot-scale mill is baffled and flow behaviour is turbulent, with the Power number being close to constant. This makes power prediction simpler than the methods discussed in Chapter 4 for lab-scale milling. The grinding media amount, density and size were shown to have less of an impact on Power number in larger pilot-scale milling than lab-scale milling due to the much flatter surface profile (i.e. no significant vortex at pilot-scale). This means that when selecting the grinding media properties, they can be selected based on which type results in the desired PSD or optimum energy efficiency, which cannot be predicted based on power draw alone.

The Reynolds number remains a challenge to estimate due to challenges in determining an apparent shear rate. However, from initial Po-Re plots, flow is evidently turbulent in these large-scale mills. It has been shown that the Reynolds number is likely to be greatly different at each equipment scale, meaning that flow patterns and the distribution of shear rates and stress energies throughout the mill are likely to differ. Flow patterns measured at lab-scale using PEPT and HSI aid the understanding of stirred media mills but caution should be applied when inferring information about larger scales.

In terms of comparing milling and mixing scenarios, a similar range of parameters are important in the scale-up of both mixers and mills. However, where overmixing can be tolerated in mixers, overmilling results in an off specification product. Hence, the stress energy and stress number must be considered. The distribution of stress energies throughout the mill is linked to flow behaviour and patterns. From initial visual observations, the vortex observed during lab-scale milling is not present at large-scale milling. Hence, there are likely to be more differences in flow patterns across the processing scales than in typical mixing applications. RTDs at lab-scale are reasonably close to those of a CSTR, but would likely be a better fit to multiple CSTRs in series model[107,167,168]. The RTD measurement methods utilised in this section have shown the potential to be utilised at pilot-scale.

7. CONCLUSIONS

Although stirred tanks are similar to stirred media mills, correlations found in literature for stirred tanks generally require adaptation before they can be successfully applied to stirred media mills at the lab-scale. This is due to the large amount of grinding media beads present, which contribute to the formation of a vortex and flow patterns differing to those in stirred tanks.

In stirred tanks, the power draw can be predicted relatively simply based on the relationship between the dimensionless Power number and Reynolds number. To extend this theory to apply to stirred media mills, the grinding media can be considered within the Power number term itself (similar to baffles in a stirred tank) and hence the density and viscosity terms include the slurry only. The important difference between baffles and grinding media beads is that baffles do not move, whilst grinding media beads flow with the slurry. Using this method, it is not possible to form one correlation that predicts power draw accurately in a wide range of cases. The best predictions using this method are achieved when a new Po-Re curve is produced for each grinding media type, fill volume and slurry type.

In this thesis, a new method of predicting power draw was proposed where the viscosity of a fluid and grinding media combination was measured using the vane geometry. Measuring such large particles in a rheometer is a challenge and leads to wall slip and vortexing at high shear rates. It is also likely that there is an impact of tribology on the measurements, where the amount of fluid between grinding media beads at a given rotational speed affects the viscosity measured. Nevertheless, this

method has been shown to be more successful at predicting power draw in a wider range of cases than the method that excludes the grinding media from the density and viscosity terms.

PEPT was used to investigate flow patterns within the mill and explain the power draw changes observed. It was found that fluid viscosity and the amount of grinding media beads have a significant impact on the shape of the vortex. Furthermore, the effect of these parameters is coupled; a low fluid viscosity and low grinding media amount results in a high fluid level and a very wide vortex, which was explained by the large amount of momentum and the small mass of material in the mill. This large vortex results in a lower power draw than expected.

The potential use of HSI to infer information about close-to-instantaneous flow patterns in stirred media mills was investigated. Using this method, bead velocities relative to the impeller position can be determined. The acceleration of beads caused by the passing of an impeller pin is likely to be important since it leads to grinding media collisions. Furthermore, the evolution of bead velocities with batch grinding was investigated. Clear velocity changes were observed as the slurry particle size decreased and the temperature increased. The velocity tends to increase as the power draw decreases, and decrease as the power draw increases. This could be linked to the changes in grinding media packing and slurry viscosity. When a higher power draw is required, more energy is dissipated in the fluid as opposed to being transferred to the beads at the vessel wall.

In terms of scale-up, similar principles are applicable for stirred media mills and stirred tanks. However, more importance is placed on achieving energy efficiency and a desired particle size. In a stirred tank, overmixing can be tolerated since it does not typically affect product quality, whilst overgrinding in a stirred media mill may result in the PSD being different and the product being off specification. Hence, it is important to consider the stress energy and stress number during the scale-up of stirred media mills and be able to predict particle size. RTDs for lab-scale stirred media mills were shown to be similar to a CSTR but would be a better fit to a multiple CSTRs in series model. Methods of measuring RTDs at pilot-scale have been proposed using dye or titanium dioxide tracers. Due to the larger equipment size, it is possible that the RTDs will deviate further from that of a CSTR.

8. FURTHER STUDY SUGGESTIONS

The suggested further research aims to improve upon the proposed methods of predicting power draw, determine shorter time scale occupancy and velocity plots using PEPT to consider changes happening with time during grinding and considering RTDs of larger scale mills.

8.1. Improving Power Prediction Methods

A drawback with predicting power draw based on the Reynolds number is the reliability and accuracy of viscosity measurements and the estimation of the shear rate inside the mill. In this thesis, a new method of measuring the combined rheology of a slurry and grinding media was proposed. However, this was limited to a low shear rate range due to slip and vortexing occurring. Further experimentation of wall slip should be conducted – this could include the use of roughened or serrated rheometer cups. Furthermore, the shear rate in the mill was estimated using the Metzner-Otto correlation, which is only recommended for use in the laminar flow regime since the flow effects of turbulence are negated. Although the value of k_s was optimised to give good power predictions, modelling should be conducted to estimate the shear rates within the mill and determine how good the Metzner-Otto estimate of shear rate is.

Currently the power draw prediction methods are exclusive to calcium carbonate slurries. It was shown that the constants and exponents in power draw prediction equations are very different when glycerol-water solutions are used in place of these slurries, suggesting that the fluid type is important. Further experimentation is recommended to determine the extent to which the mineral or material being ground

affects power draw, enabling this method to be applied to a wider range of fluid types. The difference in properties of fluids is not solely described by viscosity. It is likely that friction also plays an important role. Although frictional properties were investigated in this thesis using tribology, a single term to incorporate into the power prediction has not been determined. Further study in this area could be used to understand further the impact of fluid friction and the incorporation of fluid friction into models is suggested.

8.2. Flow Pattern Analysis Development

In this thesis, HSI was shown to provide the advantage of illustrating close to instantaneous grinding media velocities, which can be assessed in conjunction with the impeller position. It was shown that there are considerable bead velocity changes with time when batch grinding. However, this is limited to the motion of the grinding media beads at the wall of a transparent vessel. Further experimentation with PEPT could be used to observe changes occurring with time during milling more closely. Specifically, an external trigger could be utilised so that the position of the impeller is known at each time a location is known. However, this is difficult with the current time and spatial resolution of the PEPT camera. This could become increasingly possible with new higher resolution camera developments.

Furthermore, to enable smaller time periods of data to be assessed, multiple tracers could be used in PEPT experiments with new and improved algorithms developed to process the data such as a machine learning algorithm developed by Nicusan et al. (2020)[130]. Alternatively, several repeat experimental runs could be conducted and the data sets analysed together so that shorter time periods of data can be assessed

separately. The combined viscosity of the fluid and grinding media should also be measured much more frequently during batch grinding (e.g. every 2 minutes) in an attempt to relate this to the bead velocity changes observed using PEPT and HSI.

It was shown that although the size of the vortex is approximately proportional to the Froude number for a set of operating parameters, the slurry viscosity and amount of grinding media beads have an overlapping impact on the size of the vortex. PEPT experiments should be conducted at a wider range of impeller speeds for different grinding media amounts and different fluid contents to further assess the impact of these parameters on the vortex size and relate this to the power draw.

As well as looking at the power and flow patterns with the mill, it would be beneficial to compare this with particle size data to determine which flow patterns and power draws give the optimal grinding efficiency.

8.3. Further Scale-Up Studies

Although a lab-scale continuous milling set-up was developed, it is difficult to determine the amount of slurry in the mill at any time due to the vortexing action making flowrate control based on fluid level difficult. The installation of a load cell below the mill would enable the mass of fluid to be recorded.

Furthermore, potential methods of measuring RTDs at small-scale were explored and shown to provide useful information. These techniques could be employed on a larger scale. At a large-scale, the Nigrosin dye could be used in the slurry instead of glycerol

since the flowrate is higher, enabling much larger samples to be taken and subsequently centrifuged to separate the dyed liquid phase. Limitations of RTD measurement methods include potential contamination of pilot plant vessels with dye and the high cost of titanium dioxide. Multiple CSTRs in series models could be tested and the model with the best fit to pilot plant data could be determined.

9. REFERENCES

1. Imerys. Activity Report 2018/2019 [Internet]. 2019 [cited 2021 Aug 14]. Available from: https://www.imerys.com/sites/imerys.com/files/2019/06/17/Imerys_AnnualReport_2019_EN.pdf
2. Huwald E. Calcium Carbonate - Pigment and Filler. In: Tegethoff F, editor. Calcium Carbonate. Basel: Birkhauser; 2001. p. 160–70.
3. Mathur NK, Jakhar SR, Mathur R. Calcium carbonate and derived products. Int J Sci Res. 2016;2128–33.
4. Teir S, Eloneva S, Zevenhoven R. Production of precipitated calcium carbonate from calcium silicates and carbon dioxide. Energy Convers Manag. 2005;46:2954–79.
5. Kwade A, Schwedes J. Wet Grinding in Stirred Media Mills. In: Salman AD, Ghadiri M, Hounslow MJ, editors. Handbook of Powder Technology Volume 12. 2007. p. 251–382.
6. Moore P. Dust To Dust. Int Min. 2012;
7. Stehr N. Recent developments in stirred ball milling. Int J Miner Process. 1988;22:431–44.
8. Kelly E., Spottiswood D. Introduction to Mineral Processing. Somerset: John Wiley and Sons; 1982. 117-118 p.
9. Kwade A. Determination of the most important grinding mechanism in stirred media mills by calculating stress intensity and stress number. Powder Technol. 1999;105:382–8.
10. Gao M, Forssberg E. Prediction of product size distributions for a stirred ball mill. Powder Technol. 1995;84:101–6.

11. Stender H, Kwade A, Schwedes J. Stress energy distribution in different stirred media mill geometries. Int J Miner Process. 2004;74:103–17.
12. Kwade A, Schwedes J. Breaking characteristics of different materials and their effect on stress intensity and stress number in stirred media mills. Powder Technol. 2002;122:109–21.
13. Kwade A, Blecher L, Schwedes J. Motion and stress intensity of grinding beads in a stirred media mill. Part 2 : Stress intensity and its effect on comminution. Powder Technol. 1996;86:69–76.
14. Taylor L, Skuse D, Blackburn S, Greenwood R. Stirred media mills in the mining industry: Material grindability, energy-size relationships, and operating conditions. Powder Technol. 2020;369:1–16.
15. Kwade A. Grinding and Dispersing with Stirred Media Mills: Basic Course. 4th ed. Braunschweig; 2018.
16. Kwade A. A Stressing Model for the Description and Optimization of Grinding Processes. Chem Eng Technol. 2003;26:199–205.
17. Hogg R, Cho H. A review of breakage behavior in fine grinding by stirred-media milling. KONA Powder Part J. 2000;18:9–19.
18. Blecher L, Kwade A, Schwedes J. Motion and stress intensity of grinding beads in a stirred media mill. Part 1 : Energy density distribution and motion of single grinding beads. Powder Technol. 1996;86:59–68.
19. Wang S, Li X, Mao E, Cheng Z. Preparation of Plate-Shaped Calcium Carbonate and its Application in the Coating Paper. In: Cao Z, He Y., Sun L., Cao X., editors. Application of Chemical Engineering. Durnten-Zurich: Trans Tech Publications; 2011. p. 1124–7.

20. Ballantyne GR, Peukert W, Powell MS. Size specific energy (SSE) - Energy required to generate minus 75 micron material. Int J Miner Process. 2015;136:2–6.
21. von Rittinger P. Lehrbuch der Aufbereitungskunde in Ihrer Neuesten Entwicklung Und Ausbildung Systematisch Dargestellt. Ernst & Korn; 1867.
22. Jankovic A. Variables affecting the fine grinding of minerals using stirred mills. Miner Eng. 2003;16:337–45.
23. Yue J, Klein B. Effects of Bead Size on Ultrafine Grinding in a Stirred Bead Mill. In: Kawatara SK, editor. Advances in Communution. 2006. p. 87–99.
24. Guo W, Gao P, Tang Z, Han Y, Meng X. Effect of grinding media properties and stirrer tip speed on the grinding efficiency of a stirred mill. Powder Technol. 2021;382:556–65.
25. Patel CM, Chakraborty M, Murthy ZVP. Enhancement of stirred media mill performance by a new mixed media grinding strategy. J Ind Eng Chem. 2014;20:2111–8.
26. Massola CP, Chaves AP, Albertin E. A discussion on the measurement of grinding media wear. J Mater Res Technol. 2016;5:282–8.
27. Altun O, Benzer H, Enderle U. Effects of operating parameters on the efficiency of dry stirred milling. Miner Eng. 2013;58–66.
28. Conway-Baker J, Barley RW, Williams RA, Jia X, Kostuch J, McLoughlin B, Parker DJ. Measurement of the motion of grinding media in a vertically stirred mill using positron emission particle tracking (PEPT). Miner Eng. 2002;15:53–9.
29. Greenwood R, Rowson N, Kingman S, Brown G. A new method for determining the optimum dispersant concentration in aqueous grinding. Powder Technol.

2002;123:199–207.

30. He M, Wang Y, Forssberg E. Parameter effects on wet ultrafine grinding of limestone through slurry rheology in a stirred media mill. Powder Technol. 2006;65:10–20.
31. Wang Y, Forssberg E. Dispersants in stirred ball mill grinding. KONA Powder Part J. 1995;13:67–77.
32. Skuse T. The Use of Positron Emission Particle Tracking (PEPT) to Determine the Grinding Mechanisms within a Vertically Stirred Media Mill. University of Birmingham; 2016.
33. Yang Y, Rowson N, Tamblyn R, Ingram A. Effect of operating parameters on fine particle grinding in a vertically stirred media mill. Sep Sci Technol. 2017;52:1143–52.
34. Altun O, Benzer H, Enderle U. The effects of chamber diameter and stirrer design on dry horizontal stirred mill performance. Miner Eng. 2014;69:24–8.
35. Kwade A. Wet comminution in stirred media mills - research and its practical application. Powder Technol. 1999;105:14–20.
36. Daraio D, Villoria J, Ingram A, Alexiadis A, Stitt EH, Marigo M. Investigating grinding media dynamics inside a vertical stirred mill using the discrete element method: Effect of impeller arm length. Powder Technol. 2020;364:1049–61.
37. Jankovic A, Valery W. Closed circuit ball mill – Basics revisited. Miner Eng. 2013;43:148–53.
38. Silva AC, Silva EMS, de Rezende RA. Circulating load calculation in mineral processing closed circuit operations. IFAC Proc. 2013;46:45–50.
39. Bond FC. Crushing and grinding calculations part 1. Br Chem Eng. 1961;6:378–

85.

40. He M, Wang Y, Forssberg E. Parameter studies on the rheology of limestone slurries. Int J Miner Process. 2006;78:63–77.

41. Senapati PK, Panda D, Parida A. Predicting viscosity of limestone-water slurry. J Miner Mater Charact Eng. 2009;8:203–21.

42. Collyer AA. Time independent fluids. Phys Educ. 1973;8:333–8.

43. Steffe J. Rheological Methods in Food Process Engineering. 2nd ed. USA: Freeman Press; 1996. 21-22 p.

44. Garcia F, Le Bolay N, Frances C. Rheological behaviour and related granulometric properties of dense aggregated suspensions during an ultrafine comminution process. Powder Technol. 2003;130:407–14.

45. Barnes HA. Measuring the viscosity of large-particle (and flocculated) suspensions — a note on the necessary gap size of rotational viscometers. J Nonnewton Fluid Mech. 2000;94:213–7.

46. Barnes HA, Nguyen QD. Rotating vane rheometry — a review. J Nonnewton Fluid Mech. 2001;98:1–14.

47. Estellé P, Lanos C. High torque vane rheometer for concrete: Principle and validation from rheological measurements. Appl Rheol. 2012;22:1–18.

48. Zarraga IE, Hill DA, Leighton DT. The characterization of the total stress of concentrated suspensions of noncolloidal spheres in Newtonian fluids. J Rheol (N Y N Y). 2000;44:185–220.

49. Ferrini F, Ercolani D, de Cindio B, Nicodemo L, Nicolais L, Ranaudo S. Shear viscosity of settling suspensions. Rheol Acta. 1979;18:289–96.

50. Faitli J, Bohács K, Mucsi G. Online rheological monitoring of stirred media

milling. Powder Technol. 2017;308:20–9.

51. Mangesana N. Developing a Methodology for Characterising In-Situ Viscosity Profiles in Tumbling Mills. University of Capetown; 2012.

52. Zheng J, Harris CC, Somasundaran P. A study on grinding and energy input in stirred media mills. Powder Technol. 1996;86:171–8.

53. Fuerstenau DW, Kapur PC, Velamakanni B. A multi-torque model for the effects of dispersants and slurry viscosity on ball milling. Int J Miner Process. 1990;28:81–98.

54. Koltka S, Guevercin S, Ekelik T, Ozdemir O, Sabah E. The Dispersion Properties of Micronized Marble Suspensions in the Presence of Inorganic and Polymeric Dispersants. In: International Porous and Powder Materials Symposium and Exhibition. 2013. p. 686–92.

55. Deng D, Boyko V, Pancera SM, Nestle N, Tadros T. Rheology investigations on the influence of addition sodium polyacrylate to calcium carbonate suspensions. Colloids Surfaces A Physicochem Eng Asp. 2010;372:9–14.

56. Ouattara S, Frances C. Grinding of calcite suspensions in a stirred media mill: effect of operational parameters on the product quality and the specific energy. Powder Technol. 2014;255:89–97.

57. Shi FN, Napier-Munn TJ. Effects of slurry rheology on industrial grinding performance. Int J Miner Process. 2002;65:125–40.

58. Savarmand S, Heniche M, Béchard V, Bertrand F, Carreau PJ. Analysis of the vane rheometer using 3D finite element simulation. J Rheol (N Y N Y). 2007;51:161–77.

59. Mahaut F, Chateau X, Coussot P, Ovarlez G, Mahaut F, Chateau X, Coussot P,

Ovarlez G. Yield stress and elastic modulus of suspensions of noncolloidal particles in yield stress fluids. J Rheol (N Y N Y). 2008;52:287–313.

60. Mahaut F, Mokéddem S, Chateau X, Roussel N, Ovarlez G. Effect of coarse particle volume fraction on the yield stress and thixotropy of cementitious materials. Cem Concr Res. 2008;38:1276–85.

61. Higashi N, Sumita I. Experiments on granular rheology: Effects of particle size and fluid viscosity. J Geophys Res Solid Earth. 2009;114:1–18.

62. Mueller S, Llewellin E, Mader H. The rheology of suspensions of solid particles. R Soc. 2009;466:1201–28.

63. Tangsathitkulchai C, Austin LG. Rheology of concentrated slurries of particles of natural size distribution produced by grinding. Powder Technol. 1988;56:293–9.

64. He M, Wang Y, Forssberg E. Slurry rheology in wet ultrafine grinding of industrial minerals: A review. Powder Technol. 2004;147:94–112.

65. Alderliesten M. Mean particle diameters. Part VII. the Rosin-Rammler size distribution: Physical and mathematical properties and relationships to Moment-Ratio defined mean particle diameters. Part Part Syst Charact. 2013;30:244–57.

66. Delagrammatikas G, Tsimas S. Grinding process simulation based on Rosin-Rammler equation. Chem Eng Commun. 2004;191:1362–78.

67. Shi FN, Napier-Munn TJ. A model for slurry rheology. Int J Miner Process. 1996;47:103–23.

68. Adams LW, Barigou M. CFD analysis of caverns and pseudo-caverns developed during mixing of non-Newtonian fluids. In: Chemical Engineering Research and Design. 2007. p. 598–604.

69. Carreau PJ, Chhabra RP, Cheng J. Effect of rhecological properties on power

consumption with helical ribbon agitators. AIChE J. 1993;39:1421–30.

70. Yap CY, Patterson WI, Carreau PJ. Mixing with helical ribbon agitaors: Part III. Non-Newtonian fluids. AIChE J. 1979;25:516–21.

71. Wu J, Graham LJ, Mehidi NN. Estimation of Agitator Flow Shear Rate. AIChE J. 2006;57:2324–32.

72. Doraiswamy D, Grenville RK, Etchells AW. Two-Score Years of the Metzner-Otto Correlation. Ind Eng Chem Res. 1994;33:2253–8.

73. Delaplace G, Jeantet R, Grenville R, Cuvelier G, Loubiere K. How dimensional analysis allows to go beyond Metzner-Otto concept for non-Newtonian fluids. Rev Chem Eng. 2020;1–23.

74. Hemrajani R, Tatterson G. Mechanically Stirred Vessels. In: Paul E, Atiemo-Obeng V, Kresta S, editors. Handbook of Industrial Mixing: Science and Practice. John Wiley and Sons; 2003. p. 345–89.

75. Chhabra RP. Fluid Mechanics and Heat Transfer with Non-Newtonian Fluids in Mechanically Agitated Vessels. In: Hartnett J., editor. Advances in Heat Transfer. 1st ed. Oxford; 2003. p. 108–24.

76. Ayas M, Skocilas J, Jirout T. Analysis of power input of an in-line rotor-stator mixer for viscoplastic fluids. Processes. 2020;8.

77. Ramírez-Muñoz J, Guadarrama-Pérez R, Márquez-Baños VE. A direct calculation method of the Metzner-Otto constant by using computational fluid dynamics. Chem Eng Sci. 2017;174:347–53.

78. Shi FN, Napier-Munn TJ. Estimation of shear rates inside a ball mill. Int J Miner Process. 1999;57:167–83.

79. Govender I, Mangesana N, Mainza AN, Franzidis J. Measurement of shear rates

in a laboratory tumbling mill. Miner Eng. 2011;24:225–9.

80. Bazin C, B-Chapleau C. The difficulty associated with measuring slurry rheological properties and linking them to grinding mill performance. Vol. 76, International Journal of Mineral Processing. 2005. p. 93–9.

81. Radziszewski P. Towards a Better Understanding of Stirred Milling Technologies -Estimating Power Consumption and Energy Use. 46th Annu Can Miner Process Oper Conf. 2014;55–66.

82. Scargiali F, Tamburini A, Caputo G, Micale G. On the assessment of power consumption and critical impeller speed in vortexing unbaffled stirred tanks. Chem Eng Res Des. 2017;123:99–110.

83. Weit H, Schwedes J. Scale-Up of Power Consumption in Agitated Ball Mills. Chem Eng Technol. 1987;10:398–404.

84. Major-Godlewska M, Karcz J. Power consumption for an agitated vessel equipped with pitched blade turbine and short baffles. Chem Pap. 2017;72:1081–8.

85. Kwade A. Specific Energy Consumption, Stress Energy, and Power Draw of Stirred Media Mills and their Effect on Production Rate. In: Kawatra SK, editor. Advances in Comminution. Society for Mining, Metllurgy and Exploration Inc; 2006. p. 99–114.

86. Mannheim V. Empirical and scale-up modeling in stirred ball mills. Chem Eng Res Des. 2011;89:405–9.

87. Jankovic A, Morrell S. Power Modelling of Stirred Mills. Annu Int Symp Fundam Miner Process Environ. 1997;

88. Radziszewski P. Shear based stirred mill power model - An adimensional

analysis. Miner Eng. 2015;73:16–20.

89. Stehr N. Residence time distributions in a stirred ball mill and their effect on comminution. Chem Eng Process. 1984;18:73–83.

90. Varinot C, Berthiaux H, Dodds JA. Prediction of the product size distribution in associations of stirred bead mills. Powder Technol. 1999;105:228–36.

91. Bel Fadhel H, Frances C, Mamourian A. Investigations on ultra-fine grinding of titanium dioxide in a stirred media mill. Powder Technol. 1999;105:362–73.

92. Menon SH, Madhu G, Mathew J. Modeling residence time distribution (RTD) behavior in a packed-bed electrochemical reactor (PBER). Int J Chem Eng. 2019;

93. Loffill E, Alkhaddar R., Phipps D., Faram MG. Development of residence time distribution measurement techniques to improve reliability and accuract. Novatech. 2010;1–9.

94. Gitis V, Adin A, Nasser A, Gun J, Lev O. Fluorescent dye labeled bacteriophages - A new tracer for the investigation of viral transport in porous media: 2. Studies of deep-bed filtration. Water Res. 2002;36:4235–42.

95. Muhr H, Leclerc JP, David R. Fluorescent UV dye: A particularly well-suited tracer to determine residence time distributions of liquid phase in large industrial reactors. Analusis. 1999;27:541–3.

96. Charlou C, Milhé M, Sauceau M, Arlabosse P. A new methodology for measurement of sludge residence time distribution in a paddle dryer using X-ray fluorescence analysis. Water Res. 2015;69:1–8.

97. Dagadu CPK, Akaho EHK, Danso KA, Stegowski Z, Furman L. Radiotracer investigation in gold leaching tanks. Appl Radiat Isot. 2012;70:156–61.

98. Sugiharto S, Su'ud Z, Kurniadi R, Wibisono W, Abidin Z. Radiotracer method for residence time distribution study in multiphase flow system. Appl Radiat Isot. 2009;67:1445–8.

99. Miskiewicz A, Zakrzewska-Trznadel G, Dobrowolski A, Jaworska-Sobczak A. Using tracer methods and experimental design approach for examination of hydrodynamic conditions in membrane separation modules. Appl Radiat Isot. 2012;70:837–47.

100. Chen C, Cheng G, Sun H, Hou Z, Wang X, Zhang J. Effects of salt tracer amount, concentration and kind on the fluid flow behavior in a hydrodynamic model of continuous casting tundish. Steel Res Int. 2012;83:1141–51.

101. Lange J, Schuetz T, Gregoire C, Elsässer D, Schulz R, Passeport E, Tournebize J. Multi-tracer experiments to characterise contaminant mitigation capacities for different types of artificial wetlands. Int J Environ Anal Chem. 2011;91:768–85.

102. Avidan A, Yerushalmi J. Solids mixing in an expanded top fluid bed. AIChE J. 1985;31:835–41.

103. Sette E, Pallarès D, Johnsson F, Ahrentorp F, Ericsson A, Johansson C. Magnetic tracer-particle tracking in a fluid dynamically down-scaled bubbling fluidized bed. Fuel Process Technol. 2015;138:368–77.

104. Chen L, Zhang G, Wang L, Wu W, Ge J. Zeta potential of limestone in a large range of salinity. Colloids Surfaces A Physicochem Eng Asp. 2014;450:1–8.

105. Medrzycka KB. The effect of particle concentration on zeta potential in extremely dilute solutions. Colloid Polym Sci. 1991;269:85–90.

106. Romero CP, Jeldres RI, Quezada GR, Concha F, Toledo PG. Zeta potential and viscosity of colloidal silica suspensions: Effect of seawater salts, pH, flocculant,

and shear rate. Colloids Surfaces A Physicochem Eng Asp. 2018;538:210–8.

107. Yianatos J, Bergh L, Vinnett L, Díaz F. Modeling of residence time distribution in regrinding Vertimill. Miner Eng. 2013;53:174–80.
108. Danckwerts P V. Continuous flow systems. Distribution of residence times. Chem Eng Sci. 1953;2:3855.
109. Frances C. On modelling of submicronic wet milling processes in bead mills. Powder Technol. 2004;143–144:253–63.
110. Barling D, Morton DAV, Hapgood K. Pharmaceutical dry powder blending and scale-up: Maintaining equivalent mixing conditions using a coloured tracer powder. Powder Technol. 2015;270:461–9.
111. May-Masnou A, Porras M, Maestro A, González C, María Gutiérrez J. Scale invariants in the preparation of reverse high internal phase ratio emulsions. Chem Eng Sci. 2013;101:721–30.
112. Mannheim V, Siménfalvi Z. Determination of Power Consumption for Suspension Mixing in Stirring Equipments and Stirred Ball Mills. J Mater Sci Eng A. 2012;7:572–8.
113. D.Mazzinghy, C.Schneider, P.Faria RG. Predicting the size distribution in the product and the power requirements of a pilot scale vertimill. In: 9th International Mineral Processing Conference. 2012.
114. Jang EH, Park YS, Kim MS, Choi DH. Model-based scale-up methodologies for pharmaceutical granulation. Pharmaceutics. 2020;12:1–51.
115. Rahmanian N, Ng BH, Hassanpour A, Ding YL, Antony J, Jia XD, Ghadiri M, van der Wel PGJ, Krug-Polman A, York D, Bayly A, Tan HS. Scale-up of high-shear mixer granulators. KONA Powder Part J. 2008;26:190–204.

116. Dickey D. Mixer Scale-Up Demands Constant Attention [Internet]. Chemical Processing. 2013 [cited 2021 Aug 1]. Available from: https://www.chemicalprocessing.com/articles/2013/mixer-scale-up-demands-constant-attention/
117. Tamblyn R. Analysis of Energy Requirements in Stirred Media Mills. University of Birmingham; 2009.
118. Barley RW, Conway-Baker J, Pascoe RD, Kostuch J, McLoughlin B, Parker DJ. Measurement of the motion of grinding media in a vertically stirred mill using positron emission particle tracking (PEPT). Miner Eng. 2002;15:53–9.
119. Theuerkauf J, Schwedes J. Theoretical and experimental investigation on particle and fluid motion in stirred media mills. Powder Technol. 1999;105:406–12.
120. Gers R, Anne-archard D, Climent E, Legendre D, Frances C. Two colliding grinding beads: Experimental flow fields and particle capture efficiency. Chem Eng Technol. 2010;33:1438–46.
121. Machin TD, Wei HY, Greenwood RW, Simmons MJH. In-pipe rheology and mixing characterisation using electrical resistance sensing. Chem Eng Sci. 2018;187:327–41.
122. Aw SR, Rahim RA, Rahiman MHF, Yunus FRM, Goh CL. Electrical resistance tomography: A review of the application of conducting vessel walls. Powder Technol. 2014;254:256–64.
123. Milton-McGurk L, Williamson N, Armfield SW, Kirkpatrick MP. Experimental investigation into turbulent negatively buoyant jets using combined PIV and PLIF measurements. Int J Heat Fluid Flow. 2020;82:1–8.

124. Thaker AH, Bhujbal S V, Buwa V V. Effects of sloshing gas – liquid interface on dynamics of meandering bubble plumes and mixing in a shallow vessel : PIV and PLIF measurements. Chem Eng J. 2019;386:1–16.
125. Hu Y, Liu Z, Yang J, Jin Y, Ã YC. Study on the reactive mixing process in an unbaffled stirred tank using planar laser-induced fluorescence (PLIF) technique. Chem Eng Sci. 2010;65:4511–8.
126. Darelius A, Remmelgas J, Rasmuson A, van Wachem B, Björn IN. Fluid dynamics simulation of the high shear mixing process. Chem Eng J. 2010;164:418–24.
127. Pianko-Oprych P, Nienow AW, Barigou M. Positron emission particle tracking (PEPT) compared to particle image velocimetry (PIV) for studying the flow generated by a pitched-blade turbine in single phase and multi-phase systems. Chem Eng Sci. 2009;64:4955–68.
128. Parker DJ, Broadbent CJ, Fowles P, Hawkesworth MR, McNeil P. Positron emission particle tracking - a technique for studying flow within engineering equipment. Nucl Inst Methods Phys Res A. 1993;326:592–607.
129. Parker DJ, Forster RN, Fowles P, Takhar PS. Positron emission particle tracking using the new Birmingham positron camera. Nucl Instruments Methods Phys Res Sect A Accel Spectrometers, Detect Assoc Equip. 2002;477:540–5.
130. Nicuşan AL, Windows-Yule CRK. Positron emission particle tracking using machine learning. Rev Sci Instrum. 2020;91:1–14.
131. Chiti F. Lagrangian Studies of Turbulent Mixing in a Vessel Agitated By a Rushton Turbine : Positron Emission Particle Tracking (PEPT) and Computational Fluid Dynamics (CFD). University of Birmingham; 2007.

132. Bickell M, Buffler A, Govender I, Parker DJ. A new line density tracking algorithm for PEPT and its application to multiple tracers. Nucl Instruments Methods Phys Res Sect A Accel Spectrometers, Detect Assoc Equip. 2012;682:36–41.
133. Wiggins C, Patel N, Bingham Z, Ruggles A. Qualification of multiple-particle positron emission particle tracking (M-PEPT) technique for measurements in turbulent wall-bounded flow. Chem Eng Sci. 2019;204:246–56.
134. Riley M, Pinkney S, Blackburn S, Rowson NA. Spatial distributions of media kinetic energy as measured by positron emission particle tracking in a vertically stirred media mill. Miner Eng. 2016;98:177–86.
135. Cundall PA, Strack ODL. A discrete numerical model for granular assemblies. Géotechnique. 1979;29:47–65.
136. Sinnott M, Cleary PW, Morrison R. Analysis of stirred mill performance using DEM simulation: Part 1- Media motion, energy consumption and collisional environment. Miner Eng. 2006;19:1537–50.
137. Jayasundara CT, Yang RY, Yu AB. Discrete Particle Simulation of Particle Flow in a Stirred Mill: Effect of Mill Properties and Geometry. Ind Eng Chem Res. 2012;51:1050–61.
138. Plochberger T, Avila MB. Development of an Energy Optimized Stirred Media Grinding Mill. BHM Berg- und Hüttenmännische Monatshefte. 2014;159:253–8.
139. Zhao J, Shan T. Coupled CFD-DEM simulation of fluid-particle interaction in geomechanics. Powder Technol. 2013;239:248–58.
140. Jayasundara CT, Yang RY, Guo BY, Yu AB, Rubenstein J. Effect of slurry properties on particle motion in IsaMills. Miner Eng. 2009;22:886–92.
141. Beinert S, Fragnière G, Schilde C, Kwade A. Analysis and modelling of bead

contacts in wet-operating stirred media and planetary ball mills with CFD-DEM simulations. Chem Eng Sci. 2015;134:648–62.

142. Jayasundara CT, Yang RY, Guo BY, Yu AB, Govender I, Mainza A, Westhuizen A Van Der, Rubenstein J. CFD-DEM modelling of particle flow in IsaMills - Comparison between simulations and PEPT measurements. Miner Eng. 2011;24:181–7.
143. Yang Y. A Study of Fine Particle Grinding in Vertically Stirred Media Mills via Positron Emission Particle Tracking Technology and The Discrete Element Method. University of Birmingham; 2018.
144. Rogan KR, Bentham AC, George IA, Skuse DR. Colloidal stability of calcite dispersion treated with sodium polyacrylate. Colloid Polym Sci. 1994;272:1175–89.
145. Ferreira AGM, Egas APV, Fonseca IMA, Costa AC, Abreu DC, Lobo LQ. The viscosity of glycerol. Vol. 113, Journal of Chemical Thermodynamics. 2017. p. 162–82.
146. Swinehart DF. The Beer-Lambert law. J Chem Educ. 1962;39:333–5.
147. Bruker. Handheld XRF: How it Works [Internet]. [cited 2021 Jul 20]. Available from: https://www.bruker.com/pl/products-and-solutions/elemental-analyzers/handheld-xrf-spectrometers/how-xrf-works.html
148. Malvern Panalytical. Selecting an appropiate particle absorption for laser diffraction particle size calculations [Internet]. Technical Note 101104. 2019 [cited 2021 Jul 10]. Available from: https://www.malvernpanalytical.com/en/learn/knowledge-center/technical-notes/TN101104SelectingParticleAbsorbtionLaserDiffractio

149. Instruments P. PCS Instruments MTM [Internet]. 2021 [cited 2021 Aug 24]. Available from: https://pcs-instruments.com/product/mtm/

150. Thielicke W, Stamhuis EJ. PIVlab – Towards User-friendly, Affordable and Accurate Digital Particle Image Velocimetry in MATLAB. J Open Res Softw. 2014;2(E30):1–10.

151. Parker DJ, Fan X. Positron emission particle tracking-Application and labelling techniques. Particuology. 2008;6:16–23.

152. Leadbeater TW, Parker DJ, Gargiuli J. Positron imaging systems for studying particulate, granular and multiphase flows. Particuology. 2012;10:146–53.

153. Zheng J, Harris CC, Somasundaran P. The effect of additives on stirred media milling of limestone. Powder Technol. 1997;91:173–9.

154. Alexander KS, Azizi J, Dollimore D, Uppala V. Interpretation of the hindered settling of calcium carbonate suspensions in terms of permeability. J Pharm Sci. 1990;79:401–6.

155. He M, Forssberg E. Influence of slurry rheology on stirred media milling of quartzite. Int J Miner Process. 2007;84:240–51.

156. Chhabra RP. Non-Newtonian fluids: An introduction. Rheol Complex Fluids. 2010;3–34.

157. Jeong SW, Leroueil S, Locat J. Applicability of power law for describing the rheology of soils of different origins and characteristics. Can Geotech J. 2009;46:1011–23.

158. Nwosu OU, Ewulonu CM. Rheological Behaviour of Eco-friendly Drilling Fluids from Biopolymers. J Polym Biopolym Phys Chem. 2014;2:50–4.

159. Robinson JW, Zhou Y, Bhattacharya P, Erck R, Qu J, Bays JT, Cosimbescu L.

Probing the molecular design of hyper-branched aryl polyesters towards lubricant applications. Sci Rep. 2016;6:1–10.

160. Shah RSSRE, Sajjadi B, Raman AAA, You ST, Ibrahim S, Mok Y. Estimating Just Suspension Speed for Stirred Reactors Using Power Measurement. Res Commun Eng Sci Technol. 2019;1:1–5.
161. Markopoulos J, Kontogeorgaki E. Vortex depth in unbaffled single and multiple impeller agitated vessels. Chem Eng Technol. 1995;18:68–74.
162. Hashemi SH, Mousavi Dehghani SA, Samimi SE, Dinmohammad M, Hashemi SA. Performance comparison of GRG algorithm with evolutionary algorithms in an aqueous electrolyte system. Model Earth Syst Environ. 2020;6:2103–10.
163. Kalin M, Novak S, Vizintin J. Surface charge as a new concept for boundary lubrication of ceramics with. J Phys D Appl Phys. 2006;39:3138–49.
164. Barley RW, Conway-Baker J, Pascoe RD, Kostuch J, McLoughlin B, Parker DJ. Measurement of the motion of grinding media in a vertically stirred mill using positron emission particle tracking (PEPT) Part II. Miner Eng. 2004;17:1179–87.
165. Amanullah A, Hjorth SA, Nienow AW. Cavern sizes generated in highly shear thinning viscous fluids by SCABA 3SHP1 impellers. Food Bioprod Process Trans Inst Chem Eng Part C. 1997;75:232–8.
166. Dickey D. Tackling difficult mixing problems. Chemical Engineering Progress. 2015. p. 35–42.
167. Makokha AB, Moys MH, Bwalya MM. Modeling the RTD of an industrial overflow ball mill as a function of load volume and slurry concentration. Miner Eng. 2011;24:335–40.
168. Weller KR, Spencer SJ, Gao M, Liu Y. Tracer studies and breakage testing in

pilot-scale stirred mills. Miner Eng. 2000;13:429–58.

169. Dickey D. Don’t Get Mixed Up by Scale Up [Internet]. Chemical Processing. 2005 [cited 2021 Aug 1]. Available from: https://www.chemicalprocessing.com/articles/2005/dont-get-mixed-up-by-scale-up/

170. Padron GA. Measurement and Comparison of Power Draw in Batch Rotor-Stator Mixers. University of Maryland; 2001.

171. Stender HH, Kwade A, Schwedes J. Stress energy distribution in different stirred media mill geometries. Int J Miner Process. 2004;103–17.

172. Zheng M. Impeller Power Draw Across the Full Reynolds Number Spectrum. University of Dayton; 2014.

173. Wichterle K, Kadlec M, Žák L, Mitschka P. Shear rates on turbine impeller blades. Chem Eng Commun. 1984;26(1–3):25–32.

174. Korka Z. Efficiency Investigation on a Helical Gear Transmission. ANALELE Univ “EFTIMIE MURGU” REŞIŢA. 2017;55–66.

175. McCoy, Gilbert A.; Douglass JG. Premium efficiency motor selection and application guide - A handbook for industry. Energy Effic Renew Energy [Internet]. 2014;136. Available from: https://www.energy.gov/sites/prod/files/2014/04/f15/amo_motors_handbook_web.pdf

10. APPENDIX

10.1. Appendix A

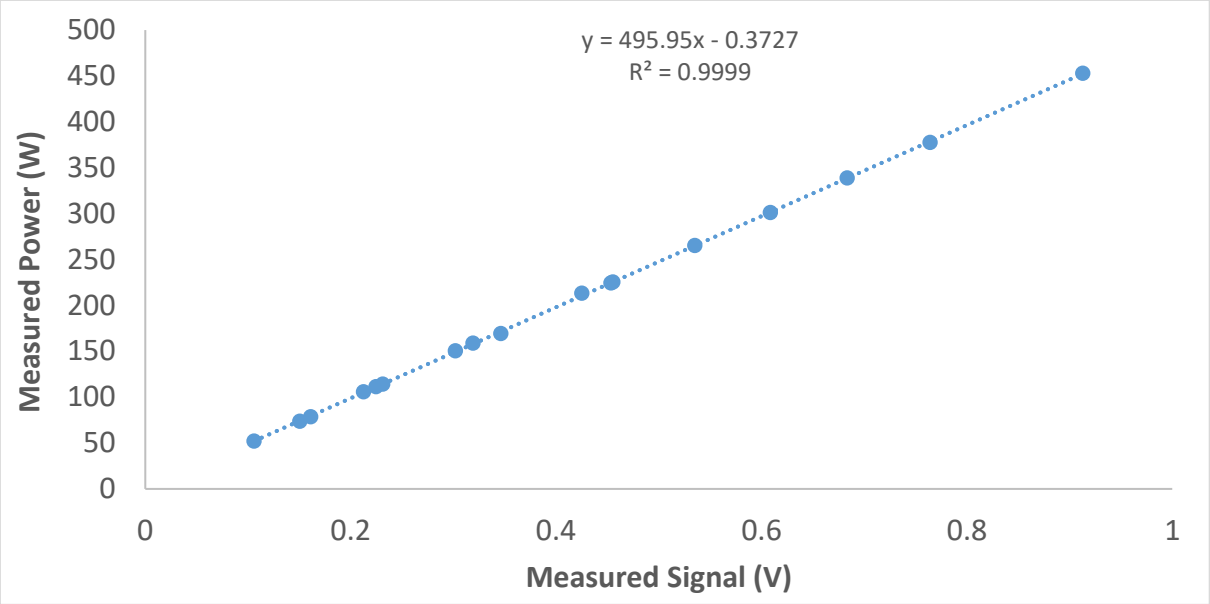

Figure 10.1: A plot Showing the Conversion from Signal to Power Draw Using Picolog

10.2. Appendix B

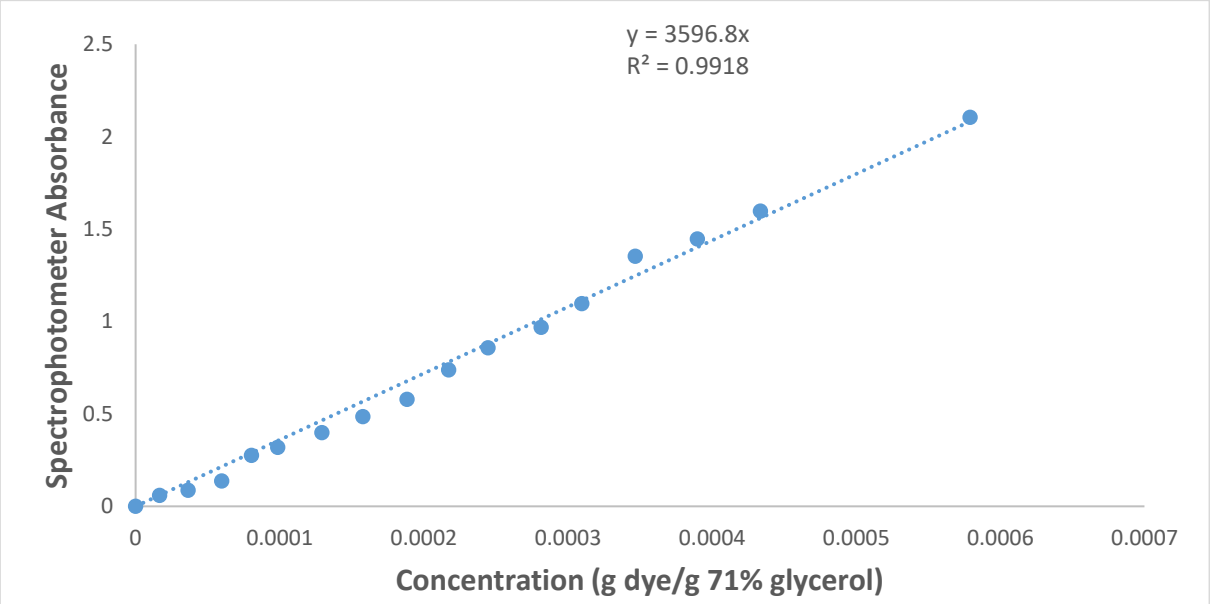

Figure 10.2: Calibration Curve for Spectrophotometer at 910 nm Wavelength

10.3. Appendix C

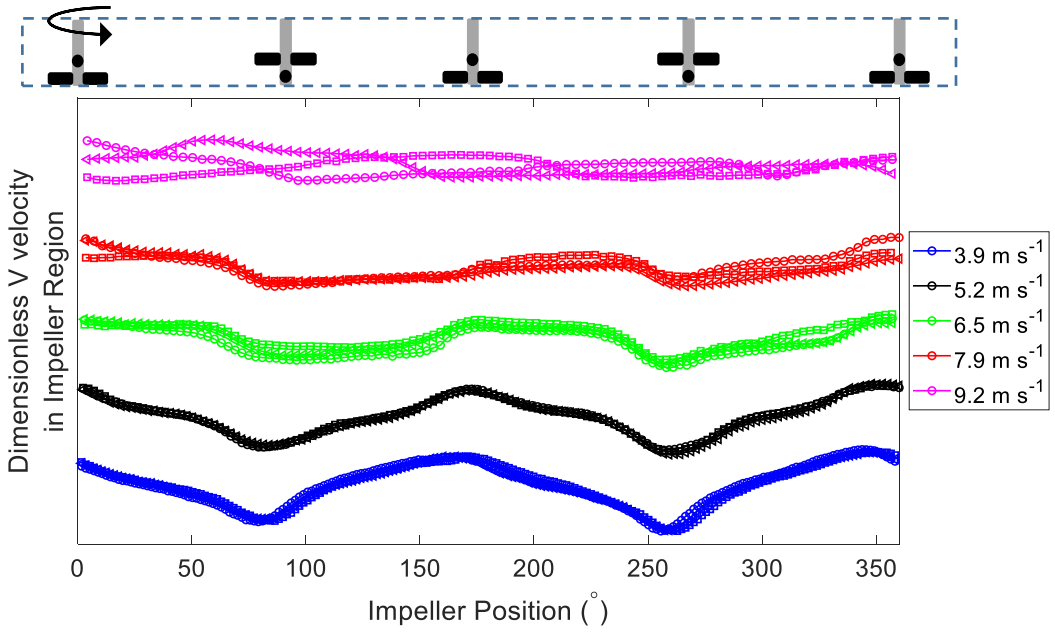

Figure 10.3: 'V' Velocities of 0.8 – 1.2 mm Mullite Beads in 71% Glycerol in the Impeller Region – Variation Over Three Impeller Revolutions

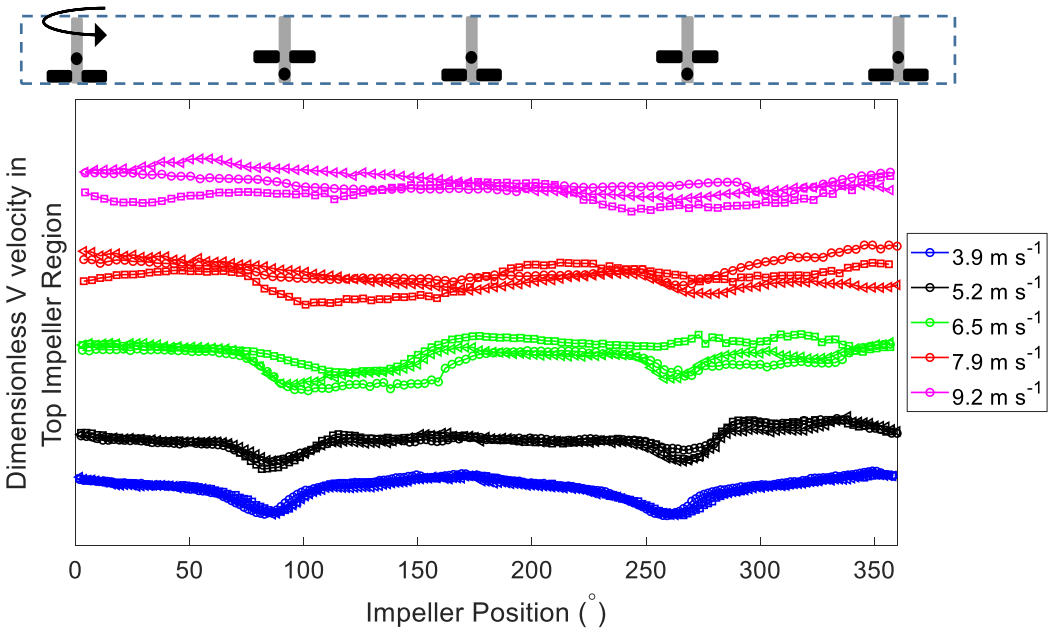

Figure 10.4: 'V' Velocities of 0.8 – 1.2 mm Mullite Beads in 71% Glycerol in Top Impeller Region – Variation Over Three Impeller Revolutions

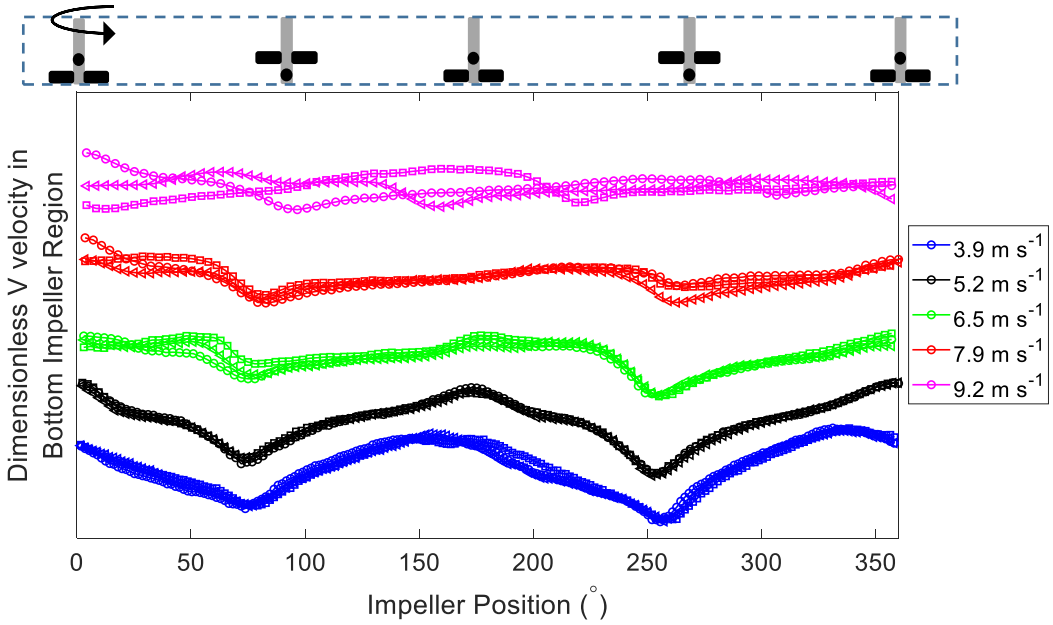

Figure 10.5: 'V' Velocities of 0.8 – 1.2 mm Mullite Beads in 71% Glycerol in Bottom Impeller Region – Variation Over Three Impeller Revolutions

10.4. Appendix D

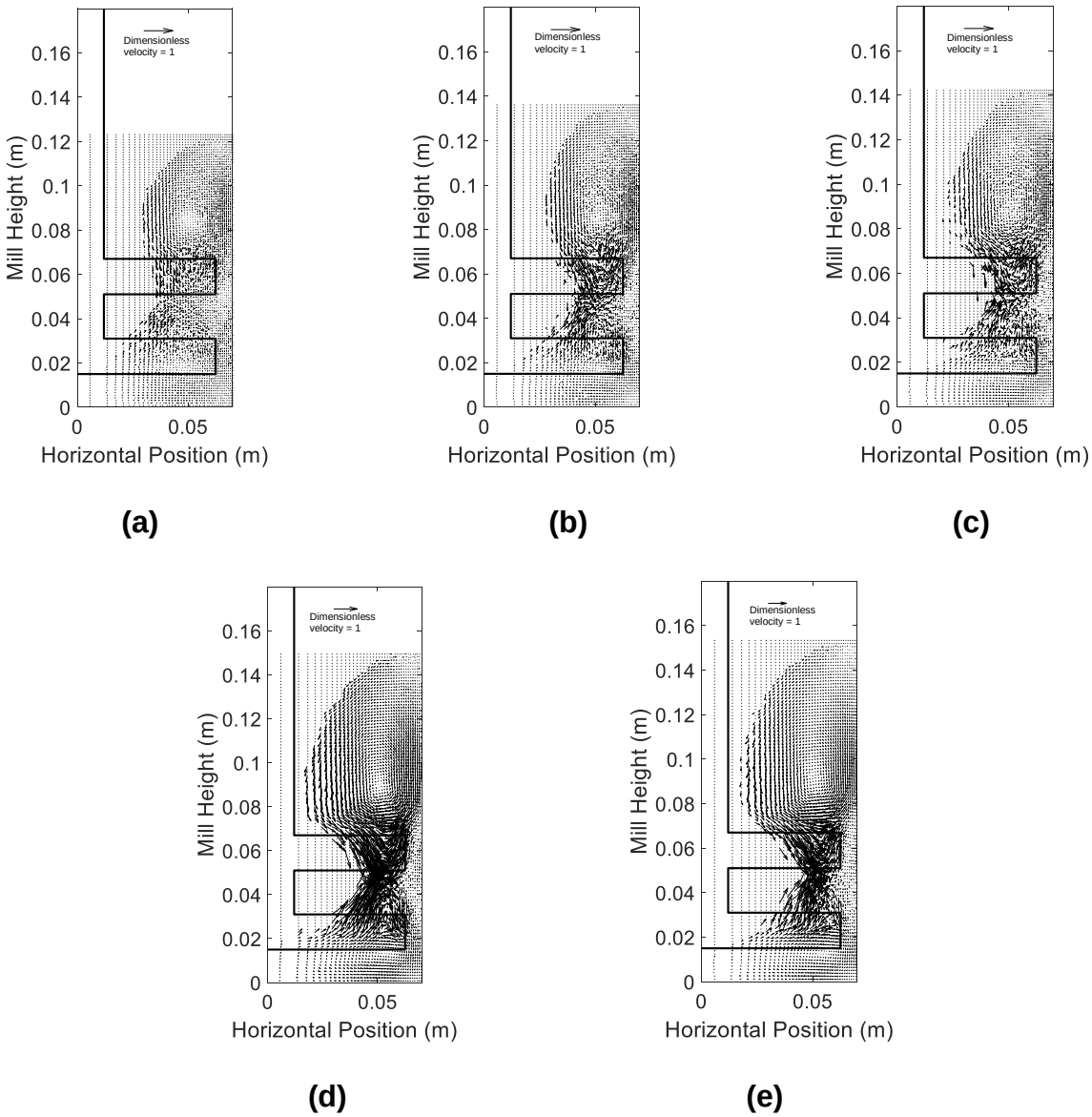

Figure 10.6: Velocity Vector Plots for 72 wt% Calcium Carbonate Slurry in 52 vol% 0.8-1.2 mm Mullite Grinding Media –
(a) 3.9 m s^{-1}, (b) 5.2 m s^{-1}, (c) 6.5 m s^{-1}, (d) 7.8 m s^{-1}, (e) 9.2 m s^{-1}